Inaugural dissertation

for

Obtaining the doctoral degree

of the

Combined Faculty of Mathematics, Engineering and Natural Sciences

of the

Ruprecht – Karls – University

Heidelberg

Presented by

M.Sc. Sophie Luise Winter

Born in: Vancouver, Canada

Oral examination: 28th November 2022

Structural Characterization of Ebola Virus Uncoating

Referees: Prof. Dr. Britta Brügger

Dr. Petr Chlanda

Summary

Viruses initiate infection of host cells by entering through a variety of different pathways. Their entry is concluded by the release of the viral genome into the cytoplasm, where the cellular machinery gets repurposed for virus replication. Prerequisite for genome release is the uncoating of the viral particles, a process which requires the destabilization of interactions established during virus assembly.

Ebola viruses (EBOVs) are highly pathogenic, enveloped RNA viruses of remarkable filamentous morphology. Their shape is dictated by the viral matrix protein VP40, which forms a tubular scaffold underneath the viral envelope and confers stability to the particles during EBOV transmission. EBOVs enter host cells via the endocytic pathway and release their genome into the cytoplasm after fusion of their envelope with the endosomal membrane. The first line of defence against a viral infection is blocking viral entry, and EBOV entry has accordingly been well investigated with respect to receptor engagement and potential membrane fusion triggers. However, key mechanisms governing the final step of virus entry are still unknown, including the central question of how these unusually shaped virions undergo uncoating. Whether and how the VP40 matrix disassembles to enable membrane fusion; whether uncoating involves additional triggers; and finally, how and where the viral genome gets released from the viral particles and nucleocapsids remains to be elucidated. In this thesis, I investigate EBOV uncoating during entry into host cells and shed light on the fate of the most abundant and versatile viral protein, VP40. As a main tool, I use in situ cryo-electron tomography and provide structural insights into EBOV uncoating both in vitro and in infected host cells at molecular resolution. I discover that at low endosomal pH, the VP40 matrix detaches from the viral envelope and disassembles. This is caused by the disruption of electrostatic interactions between membrane lipids and anionic amino acids exposed on the surface of VP40 dimers, which I show are the structural units of the VP40 matrix. The strong effect of low pH on the integrity of the VP40 matrix is a consequence of acidification of the viral lumen, which I further investigate to uncover its mechanism. I show that protons diffuse passively across the viral envelope independently of a dedicated ion channel, which might be relevant for other late-penetrating viruses lacking viroporins. Finally, I provide the first high-resolution images of Ebola virions in endolysosomal compartments of infected cells. These images confirm the disassembly of the VP40 matrix in virions located in acidified compartments while clearly showing that their nucleocapsids remain intact. Together, these findings reveal that VP40 matrix disassembly is an essential step during EBOV uncoating, which precedes membrane fusion and genome release from the nucleocapsids. Overall, this thesis extends the current understanding of virus uncoating and indicates that pH-driven structural remodeling of viral matrix proteins may act as a switch coupling matrix uncoating to membrane fusion during host cell entry of enveloped viruses.

Zusammenfassung

Viren dringen auf verschiedenen Wegen in Wirtszellen ein und beginnen damit ihren Replikationszyklus. Der Viruseintritt in die Zelle ist abgeschlossen, sobald das virale Genom in das Zytoplasma freigesetzt wird, wo die zelluläre Maschinerie der Wirtszelle für die Virusreplikation umfunktioniert wird. Die Freilassung des Genoms von den eindringenden Viruspartikeln erfordert, dass sich die Virushülle öffnet und physikalische Wechselwirkungen, welche während der Virusreifung zwischen dem viralen Kapsid, der Membranhülle (bei umhüllten Viren) und der Nukleinsäure aufgebaut wurden, destabilisiert werden. Ebolaviren sind hochpathogene, umhüllte RNA-Viren mit filamentöser Morphologie. Ihre bemerkenswerte Form wird durch das virale Matrixprotein VP40 bestimmt, das ein zylinderförmiges Gerüst unter der Virushülle bildet und den Partikeln während ihrer Übertragung Stabilität verleiht. Ebolaviren dringen über den endozytischen Weg in Wirtszellen ein und geben ihr Genom nach der Fusion ihrer Hülle mit der endosomalen Membran in das Zytoplasma ab. Die erste Abwehr gegen eine Virusinfektion besteht darin, den Eintritt des Virus in die Zelle zu blockieren. Entsprechend wurde der Eintritt von Ebolaviren im Hinblick auf die Bindung von Rezeptoren und potenziellen Auslösern für Membranfusion eindringlich untersucht. Grundlegende Mechanismen, die diesen letzten Schritt des Viruseintritts steuern, sind jedoch weiterhin unbekannt, einschließlich der zentralen Frage, wie diese ungewöhnlich geformten Viren während des Eintritts in die Wirtszelle ihr Genom freigeben. Bislang ungeklärt ist, ob und wie die VP40-Matrix auseinanderfällt, um die Membranfusion zu ermöglichen; ob für die Enthüllung zusätzliche Auslöser erforderlich sind und schließlich; wie und wo das virale Genom von den Viruspartikeln und den Nukleokapsiden freigesetzt wird. In dieser Arbeit untersuche ich die Enthüllung von Ebolaviren während des Eindringens in Wirtszellen und beleuchte die Rolle des viralen Matrixproteins VP40. Als Hauptmethode verwende ich in-situ-Kryo-Elektronentomographie und gewinne damit hochauflösende strukturelle Einblicke in die Enthüllung von Ebolaviren sowohl in vitro als auch in infizierten Wirtszellen. Ich entdecke, dass sich die VP40-Matrix bei niedrigem endosomalen pH-Wert von der Virushülle löst und zerfällt. Dieser Prozess basiert auf der Unterbrechung der elektrostatischen Wechselwirkungen zwischen Membranlipiden und anionischen Aminosäuren auf der Oberfläche von VP40-Dimeren, die, wie ich zeige, die Struktureinheiten der VP40-Matrix sind. Die starke Auswirkung eines niedrigen pH-Werts auf die Integrität der VP40-Matrix weist auf eine Ansäuerung des viralen Lumens hin, welche ich näher untersuche. Ich weise nach, dass Protonen passiv und ohne spezielle Ionenkanäle durch die Virushülle diffundieren, was auch für andere Viren, die über endosomale Kompartimente in Zellen eindringen, relevant sein könnte. Abschließend nehme ich die ersten hochauflösenden Bilder von Ebolaviren in endolysosomalen Kompartimenten infizierter Zellen auf. Diese Bilder bestätigen den Abbau der VP40-Matrix in Viren, die sich in angesäuerten Kompartimenten befinden, und zeigen deutlich, dass die Nukleokapside intakt bleiben. Zusammengenommen zeige ich, dass der pH-induzierte Abbau der VP40-Matrix ein wesentlicher Schritt während der Enthüllung von Ebolaviren ist, welcher der Membranfusion und der Freisetzung des Genoms aus den Nukleokapsiden vorausgeht.

Table of Contents

Acknowledgements

Throughout the PhD, I have received tremendous support that helped me grow scientifically, maintain my motivation and refocus when I got carried away by the – sometimes overwhelming – whirl of research. I owe my perseverance and endurance and lasting excitement to many people I would like to acknowledge specifically. First and foremost, I am grateful to Petr not only for the opportunity to work on an exciting PhD project, but for his support, supervision, and for sharing his wisdom and transferring his excitement about electron microscopy to me. I started as an absolute beginner and feel at home now in front of the different microscopes. I am also grateful for the scientific input I received during TAC meetings from Britta, Julia and Loan and the numerous conferences I was fortunate enough to attend over the years. Of course, I cherish all the discussions with the members of the Chlanda lab, during (sometimes extensive) lab meetings, and over coffee measured by the litre (drawn from well-selected coffee machines). Thank you, Steffen, for sharing this journey with me from beginning to end. I'm grateful for our discussions in our little (plant-less for a reason) office, the Corona-madness, the conferences we've been to together and all the preparations to get there. I am also thankful to Niki, our first organizing bee in the lab, fun-fact Moritz with his endless programming enthusiasm, Liv and Sarah, who are always curious and questioning, Jana, our lab fairy, and of course Melina, for all the discussions, encouragement, scientific optimism and for the hours spent together in preparation for and during our BSL4 adventure. As a lab, we've been fortunate to have (had) many inspiring master students, and I am really grateful I could supervise some of them: To Tamara, Nick, Lisa, Doro and Keerthi – I hope you learned as much from me as I learned by supervising you. I am equally thankful to the many collaborators I was lucky to work with over the years, especially Gonen for venturing with me into endless discussions about the physics behind biology. Last but not least, I am thankful to my wonderful family and friends, who have supported me in all their different ways. My mum, who seems to never doubt that I will do the right thing – my dad, whose excitement and passion has been a constant source of inspiration since my first day of my bachelor studies – my amazing sisters, who have found their own passions and show me how to find and pursue mine – my friends, who share my lows and highs and who are part of the family – with respect to the PhD times, especially Nic (the most reliable proof-reader), Hanna and Nils: thank you for your support and encouragement and for sharing invaluable (climbing) adventures with me. And finally, I am the luckiest person to share this experience with Dimitris beyond the credit I can give him here: thank you for never being tired of discussing with me at any (inhuman) time of the day, for your patience, support and encouragement. You are my role model in pure scientific excitement and curiosity.

Contributions and Publications

All data presented in this thesis was generated by me if not stated otherwise explicitly throughout the text. Petr Chlanda contributed to the conceptualization of the study and supervised the cryo-ET data collection and analysis. Experiments shown in Figures 21 and 35 were carried out by Keerthihan Thiyagarajah and Lisa Augenstein, respectively, under my supervision. Thomas Hoenen (FLI, Greifswald-Insel Riems) performed all experiments in BSL4, and provided purified EBOVs and EBOV-infected cells shown in Figures 11 and 27. Acquisition of data from EBOV-infected cells was performed together with Melina Vallbracht (Fig. 27). Fabio Lolicato (Nickel lab, BZH Heidelberg) performed MD simulations (Fig. 15), and Gonen Golani (Schwarz lab, ITP Heidelberg) provided the analysis of the time-lapse microscopy data presented in Figure 19. Christian Lüchtenborg and Britta Brügger (Brügger lab, BZH Heidelberg) performed the lipidomics analysis presented in Figure 15. Samy Sid Ahmed (Fackler lab, CIID Heidelberg) acquired and processed the FACS data presented in Figures 22 and 23. Chao Qi (Korkhov lab, PSI Villigen) provided purified NPC1 reconstituted in different liposomes (Fig. 24 and Fig. 25). The cryo-ET dataset, which I used to perform the subtomogram average (Fig. 13) was acquired by Wim Hagen (EMBL Heidelberg). The respective affiliations are: BZH, Heidelberg Biochemistry Center, CIID, Center for Integrative Infectious Disease Research, EMBL, European Molecular Biology Laboratory, FLI, Friedrich-Loeffler Institute, ITP, Institute for Theoretical Physics, PSI, Paul-Scherrer Institute.

The main findings of the work presented in this thesis are currently published as a preprint (Winter et al., 2022). Data acquired by dual-axis Volta phase plate tomography, Figures 14, 30 and 32, are published here (Winter and Chlanda, 2021). I have additionally contributed to the ultrastructural characterization of lamellar bodies (Klein, Wimmer, et al., 2020), and to the publication of the cryo-CLEM workflow established in the lab (Klein et al., 2021), which I applied in Figure 26. Outside the framework of this thesis, I was involved in the ultrastructural characterization of SARS-CoV-2 infected cells and solved the structure of vRNPs within the virions (Klein, Cortese, Winter, et al., 2020).

Winter, Sophie L, Gonen Golani, Fabio Lolicato, Melina Vallbracht, Samy Sid Ahmed, Christian Lüchtenborg, Oliver T Fackler, et al. 2022. "The Ebola Virus VP40 Matrix Undergoes Endosomal Disassembly Essential for Membrane Fusion." BioRxiv. https://doi.org/10.1101/2022.08.24.505067.

Winter, Sophie L., and Petr Chlanda. 2021. "Dual-Axis Volta Phase Plate Cryo-Electron Tomography of Ebola Virus-like Particles Reveals Actin-VP40 Interactions." Journal of Structural Biology 213 (2): 107742. https://doi.org/10.1016/j.jsb.2021.107742.

Klein, Steffen, Benedikt Wimmer, Sophie Winter, Androniki Kolovou, Vibor Laketa, and Petr Chlanda. 2020. "Post-Correlation on-Lamella Cryo-CLEM Reveals the Membrane Architecture of Lamellar Bodies," https://doi.org/10.1101/2020.02.27.966739.

Klein, Steffen, Moritz Wachsmuth-Melm, Sophie L. Winter, Androniki Kolovou, and Petr Chlanda. 2021. "Cryo-Correlative Light and Electron Microscopy Workflow for Cryo-Focused Ion Beam Milled Adherent Cells." In Methods in Cell Biology, 162:273–302. Academic Press. https://doi.org/10.1016/bs.mcb.2020.12.009.

Klein, Steffen, Mirko Cortese, **Sophie Winter**, Moritz Wachsmuth-Melm, Christopher Neufeldt, Berati Cerikan, Megan Stanifer, Steeve Boulant, Ralf Bartenschlager, and Petr Chlanda. 2020. "SARS-CoV-2 Structure and Replication Characterized by in Situ Cryo-Electron Tomography." Nature Communications, 1–10. https://doi.org/10.1101/2020.06.23.167064.

List of Abbreviations

BSL4	biosafety level 4
CCD	charge coupled device
CEMOVIS	cryo-electron microscopy of vitreous sections
CLEM	correlative light and electron microscopy
CTD	C-terminal domain
CTF	contrast transfer function
DED	direct electron detector
DMV	double-membrane vesicle
DRC	Democratic Republic of Congo
EBOV	Ebola virus
EM	electron microscopy
ESCRT	endosomal sorting complex required for transport
ET	electron tomography
EVD	Ebola virus disease
FIB	focused ion beam
GP	glycoprotein
HA	hemagglutinin
HIV	human immune deficiency virus
hpi	hours post infection
MARV	Marburg virus
MD simulations	molecular dynamics simulations
mVP40	MARV VP40
NA	numerical aperture
NMR	nuclear magnetic resonance
NP	nucleoprotein
NPC1	Niemann-Pick Type C transporter-1
NTD	N-terminal domain
ORF	open reading frame
PIP2	phosphatidylinositol 4,5-bisphosphate
RBD	receptor-binding domain
RdRp	RNA-dependent RNA polymerase
SARS-CoV	severe acute respiratory syndrome-coronavirus
SPA	single particle analysis
TIM	T cell immunoglobulin and mucin domain
TMD	tobacco mosaic disease
TMV	tobacco mosaic virus
trVLPs	transcription- and replication- competent virus-like particles
VP	viral protein (e.g. VP24, VP30, VP35, VP40)
VLP	virus-like particle

List of Figures

List of Tables

1 Introduction

Viruses were discovered at the end of the 19th century as the causative agent of diseases, for which no bacterial origin could be identified at the time. Their nature remained a mystery until the development of filtration techniques to isolate bacteria, culturing techniques to observe cell growth and – a milestone in the history of virology – the development of the electron microscope. The first disease of viral origin was identified in 1892 by Dimitri Ivanovsky (Ivanovsky, 1903), who investigated the cause of the mottled browning of leaves of infected tobacco plants, which followed mosaic-like patterns (famously known today as the tobacco-mosaic disease, TMD). Using unglazed porcelain filters with pore sizes designed to retain bacteria (Chamberland, 1884), he investigated the sap of infected plants and excluded bacterial origin. Just a few years later, Martinus Beijerinck independently confirmed his experiments and further extended the study, discovering that the "filterable agent" is liquid and soluble (Sankaran, 2018). Together with his finding that it only replicated in living cells, Beijerinck coined the definition of the newly discovered pathogen as an obligate intracellular parasite. He introduced the term "virus" to describe what he initially referred to as contagium vivum fluidum (Lecoq, 2001), or contagious living fluid. These early studies sparked a debate that lasted for decades on whether viruses are particles or liquids, which was settled only in 1939 with the first electron micrograph of the virus causing TMD (tobacco-mosaic virus, TMV) (Kausche et al., 1939). The first images of TMV confirmed its particulate, highly ordered structure and small size of approximately 15 nm in diameter, while marking a breakthrough for EM as a tool to study microscopic pathogens. Owing to its role in discovering viruses as distinct microbes, its stability when isolated from infected plants and the ability to crystallize easily due to its highly symmetric structure, TMV is still today one of the most studied viruses, overshadowing even the identification of the first animal and human viruses, foot-and-mouth disease virus (Loeffler and Frosch, 1898) and yellow fever virus (whose discovery is reviewed here (Staples and Monath, 2008).

Since the early works on TMV, numerous viruses have been discovered in all kingdoms of life, with an estimated 320,000 viruses infecting mammals alone (Anthony et al., 2013). While differing greatly not only in host species and disease they cause but also in shape, size and structural composition, all viruses share basic properties: they contain an RNA or DNA genome protected by a protein shell and, in some cases, an additional membrane envelope, and they rely on host cells for replication. Virus morphology, size and genome structure are the basis for their classification into different virus families with 26 human virus families known to date (Lefkowitz et al., 2018; Walker et al., 2022). These basic properties further define to a large extent the molecular biology of viruses, revealing important insights into their replication strategy in host cells and pathogenicity of newly emerging or unknown viruses.

1.1 Ebola viruses

Ebola viruses (EBOVs) are highly pathogenic RNA viruses of the order *Mononegavirales*, belonging to the family *Filoviridae* (Fig. 1), the latter of which was introduced after the discovery of the unusually shaped

Marburg viruses (MARVs) and EBOVs (Kiley et al., 1982). Both filoviruses are endemic in Africa and are pathogenic to humans and non-human primates. In 2011, the family was extended by a new member, Cuevaviruses, which were discovered in deceased bats of the species *Miniopterus schreibersii* (Negredo et al., 2011) and have since then been discovered in live and deceased bats in Spain and Hungary (Kemenesi et al., 2018; De Arellano et al., 2019). The latest addition to the *Filoviridae* family infecting mammalian hosts (Kuhn et al., 2019) are Dianloviruses, discovered in pteropodid bats in China (Yang et al., 2019).

EBOVs contain a non-segmented RNA genome of negative sense polarity, are filamentous in shape and contain a membrane envelope. Six EBOV species have been isolated to date, with the most recent member, Bombali virus, discovered in bats in 2018 (Goldstein et al., 2018). Of the other five EBOV species, Zaire, Sudan, Bundigbuyo and Taï Forest are known to cause diseases in humans (ordered from highest to lowest case-fatality rate), while Reston virus has so far only been associated with disease in non-human primates. Due to their high pathogenicity and lack of antiviral treatments, EBOVs are classified as biosafety level-4 (BSL4) pathogens. One of the first EBOV species discovered, the most pathogenic and responsible for the majority of the recurring disease outbreaks, is Zaire EBOV. Having infected a cumulative number of 32867 people in 20 outbreaks from 1976 to 2022 (with recent outbreaks that started in 2021 and are still ongoing) and case-fatality rates up to 90%, it is accordingly the focus of most research on EBOVs to date, including the work presented here.

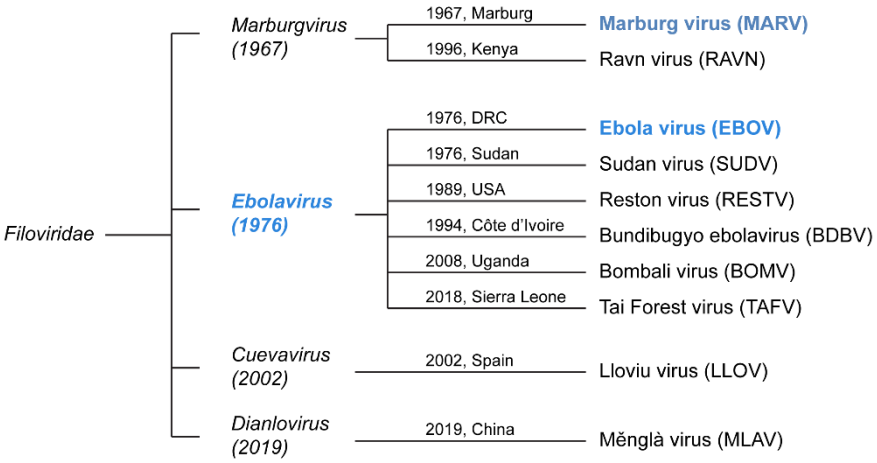

Figure 1: Phylogenetic tree of the virus family *Filoviridae*. The family is composed of five genera infecting mammalian hosts, including marburgviruses, ebolaviruses, cuevaviruses and dianloviruses. Genera and species are listed according to their time of discovery from top to bottom. Data source: (Kuhn et al., 2019).

1.1.1 Discovery and disease

EBOVs were first discovered in 1976 during haemorrhagic fever outbreaks in Sudan and the Democratic Republic of Congo (DRC). The sudden emergence of a disease with unusual symptoms for the typically circulating infectious diseases in Central Africa such as malaria, respiratory diseases, leptospirosis or yellow fever, together with the fast disease onset with high death rates incited immediate investigations into the disease origin. The causative agent was named after the river Ebola, located in proximity to the village in DRC, where it was first discovered.

Analysis of blood samples from infected patients by electron microscopy (EM) quickly revealed the remarkable filamentous structure of the virions (Murphy, 1976), which at the time had only been seen with MARVs, discovered a decade earlier (Siegert et al., 1967). Within three years after its discovery, EM studies of isolated virus particles and infected tissue samples revealed striking structural similarities between MARV and EBOV particles despite their antigenic differences (Johnson et al., 1977; Ellis et al., 1979, 1978): both viruses were found to be primarily filamentous in shape with similar lengths and diameters, and contained similar structural features including the outer coat and an inner "nucleocapsid core" (Ellis et al., 1978).

The pathogenesis of EBOV disease (EVD) including the mode of transmission and disease progression has been well reviewed (Martines et al., 2015; Baseler et al., 2017) and will only briefly be summarized here. Human-to-human transmission occurs via bodily fluids by direct contact of mucous membranes or nonintact skin with infected blood samples or tissue. After incubation times of 6-10 days, mild non-specific symptoms develop and rapidly progress into severe organ injury and often haemorrhagic fever caused by damage inflicted by high levels of EBOV replication and systemic infection. One of the factors involved in the rapid EBOV dissemination throughout the body is its ability to infect a wide range of cell types and tissues. Primary targets upon infection are dendritic cells and macrophages, which transport the virus via the lymphatic vessels to lymph nodes and nodal chains. The virus then enters the bloodstream and gets transported to different organs (with large viral loads found in the liver and spleen), where it replicates quickly. Although lymphocytes appear not to be infected, they have been reported to undergo apoptosis early after infection, contributing to EBOV-induced immune suppression. Both immune suppression and overactivation at later stages of infection have been associated with severe disease progression ultimately resulting in multi-organ failure and death within 6-9 days after the first symptoms occurred.
Humans and non-human primates are dead-end hosts with several intermediate animal hosts suspected to be involved in initial spillover events during zoonotic EBOV transmissions. Extensive efforts to identify the reservoir host all point towards members of the fruit bat family (Leroy et al., 2005; Biek et al., 2006; Pourrut et al., 2009; Olival et al., 2013) and in 2009, the closely related MARVs were isolated for the first time from the Egyptian fruit bat, *Rousettus aegyptiacus* (Towner et al., 2009; Amman et al., 2012). However, live EBOV isolates from any potential reservoir host are still lacking today.

1.1.2 Structure

The EBOV genome encompasses 19 kilobases and contains seven open reading frames (ORFs) coding, from 3' to 5' end, for the structural proteins nucleoprotein (NP), viral protein (VP) 35, VP40, glycoprotein (GP), VP30, VP24 and L (Sanchez et al., 1993). All structural proteins are incorporated into the filamentous virions, which are surrounded by a viral envelope acquired during budding from the plasma membrane of infected host cells. The envelope is studded with a single protein, GP, and is shaped by the viral matrix protein VP40, which forms a tubular scaffold lining the inner viral membrane leaflet. The core of the particles is occupied by the nucleocapsid composed of NP, VP35 and VP24. It encapsidates the viral RNA

genome and is further associated with the viral RNA-dependent RNA polymerase (RdRp) L and the polymerase co-factor VP30.

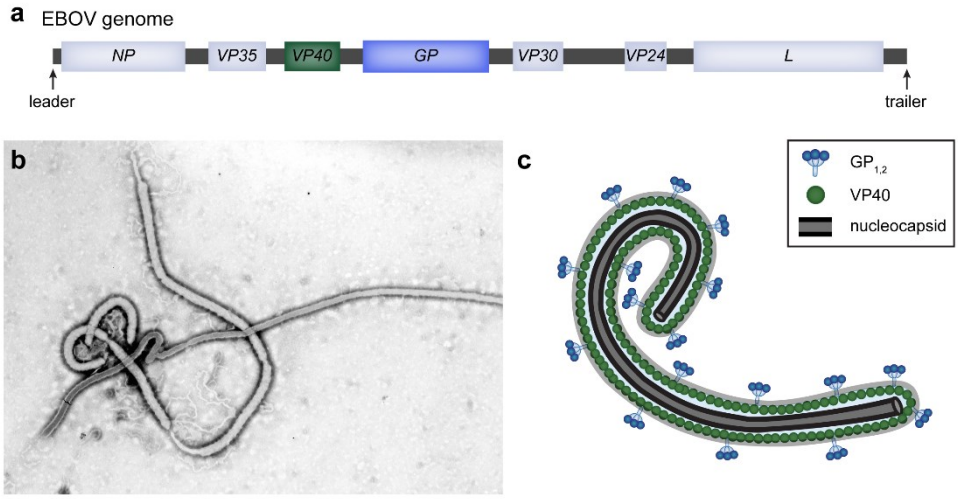

Figure 2: Structural organization of EBOVs. (a) Schematic representation of the EBOV negative-sense RNA genome. The organization of the coding genes including 3' leader and 5' trailer regions are shown approximately to scale. **(b)** First negative stain electron micrograph of an Ebola virion isolated during the outbreak in 1976 in DRC (image credit: Frederick A. Murphy, 1976, image source: https://phil.cdc.gov/Details.aspx?pid=1833). **(c)** Schematic of an EBOV showing the structural components of the virions including from the outside to the particle's core: GPs protruding from the viral membrane, the VP40 matrix and the viral nucleocapsid.

The glycoprotein

The *GP* gene is the only polycistronic gene that gives rise to three known GP variants due to co-transcriptional editing at a poly-adenosine site connecting two ORFs (Lee and Saphire, 2009).

The primary ORF is conserved among EBOV species and encodes a non-structural protein referred to as secreted GP (sGP). Upon expression, sGP is glycosylated and further processed in the Golgi apparatus by furin proteases, resulting in mature sGP and a short 40-amino acid peptide, called delta-peptide (Volchkova et al., 1999). sGP is secreted during EBOV infections and has been detected along with antibodies directed against sGP in the blood of infected patients. Since the antibodies preferentially bind to sGP rather than to virion-bound GP (discussed below), sGP is proposed to act as a decoy during infection, scavenging elicited antibodies and helping virions evade the humoral immune response (De La Vega et al., 2015). The delta-peptide is secreted at a lower rate than sGP and remains largely associated with the cell. Only few studies on the delta-peptide exist, and its functions are still speculative: it has been suggested to prevent re-infection of host cells by blocking EBOV GP-binding to host cell attachment factors (Radoshitzky et al., 2011), and to function as a viroporin (Gallaher and Garry, 2015; He et al., 2017; Pokhrel et al., 2019), a small viral protein composed of amphipathic helices that can insert into membranes and increase their permeability. Recently, the function as a viroporin has been linked to its enterotoxin activity and the gastrointestinal pathology of EVD (Melnik et al., 2022), but the molecular mechanism remains to be elucidated.

The second ORF of *GP* occurs by transcriptional editing at seven consecutive adenosine residues within the gene, which form a hairpin loop and cause the stuttering of the viral RdRp L in 20% of the transcripts (Mehedi et al., 2013). As a result, an additional adenosine gets inserted and full-length GP is produced. Full-

length GP shares the N-terminal amino acids with sGP but contains an additional transmembrane domain and gets inserted into the EBOV envelope after maturation. Similar to sGP, maturation of full-length GP occurs in the Golgi apparatus and involves glycosylation and proteolytic cleavage by furin proteases, resulting in the separation of the two domains GP1 and GP2, which remain connected by a disulfide bridge. Trimeric $GP_{1,2}$ is then transported to the plasma membrane where it is incorporated into budding virions. During the EBOV replication cycle, $GP_{1,2}$ is required for host cell attachment and viral membrane fusion that concludes virus entry into host cells (further discussed below). $GP_{1,2}$ is a class I fusion protein, whose trimeric GP1 structure has been solved in the presence of neutralizing antibodies first (Lee et al., 2008), before the full-length-structure of virion-attached $GP_{1,2}$ was solved in 2017 by cryo-ET (Beniac and Booth, 2017).

The third GP variant of still unknown function is the product of deletion of one, or addition of two adenosines during transcription at the same hairpin loop described above, and results in the expression of a nonstructural, small sGP (ssGP) (Lee and Saphire, 2009).

The nucleocapsid

The EBOV genome is encapsidated by a nucleocapsid primarily composed of NP as well as the transcriptional co-factor VP35 and minor matrix protein VP24. After genome replication in cytoplasmic inclusion bodies and expression of viral proteins, the RNA is bound by multiple copies of NP, which form a loosely coiled helical tube (Bharat et al., 2012). Association of VP35 and VP24 induces condensation of the coiled structure into a left-handed helix composed of a central rigid tubular structure of NP-RNA oligomers and regular, boomerang-shaped VP35-VP24 protrusions (Bharat et al., 2012; Wan et al., 2017). The viral RdRp L and transcriptional co-factor VP30 localize to nucleocapsids in infected cells (Groseth et al., 2009), and ectopic expression of VP30-GFP has been used to fluorescently label nucleocapsid structures (Schudt et al., 2015). However, the position of L and VP30 along the nucleocapsid structure is so far unresolved (Beniac et al., 2012; Dolnik and Becker, 2022). The fully assembled decorated and condensed nucleocapsid is then transported to the plasma membrane in an actin-dependent manner (Dolnik and Becker, 2022) to be incorporated into budding particles.

VP40

The matrix protein VP40 is the most abundant viral protein and indispensable for virus particle formation. Expression of V40 alone leads to the production of virus-like particles (VLPs) of similar dimensions as authentic EBOVs (Noda et al. 2002). VP40 is expressed in the cytoplasm of infected cells and is trafficked along actin filaments to the plasma membrane (Adu-Gyamfi et al., 2012). Through electrostatic and hydrophobic interactions with lipids in the inner plasma membrane monolayer, it then undergoes conformational re-arrangements and oligomerizes to from a tubular scaffold shaping the membrane at budding sites and inducing the formation of filamentous particles (Stahelin, 2014).

The structure of VP40 in solution and within the assembled matrix in virions has long been subject of debate. Several X-ray crystallography studies of purified VP40 in various solvents and using truncations of

the protein to improve crystal packaging have revealed different oligomeric states: First identified as a monomer (Dessen, 2000; Scianimanico et al., 2000; Ruigrok et al., 2000), VP40 was comprehensively shown to be dimeric in solution (Bornholdt et al., 2013b). Each butterfly-shaped dimer is composed of a C-terminal domain (CTD) and an N-terminal domain (NTD) connected by a flexible linker. While the CTD contains two β-sheets and α-helices connected by disordered loops, the NTD is composed of a β-sandwich connected to four α-helices, two of which are involved in forming the dimeric interface (Fig. 3). Furthermore, in the context of virus particles, VP40 was hypothesized to adopt a third conformation upon interaction with lipids in the host cell plasma membrane during budding: in the presence of membrane lipids, low amounts of urea and dextran sulfate that was used to mimic negative charges encountered by VP40 upon membrane binding, VP40 was found to be hexameric (Scianimanico et al., 2000; Ruigrok et al., 2000; Bornholdt et al., 2013b). Hence, the assembled VP40 matrix in Ebola virions was assumed to be composed of hexamers. This structure was recently challenged by cryo-EM studies performed on Ebola VLPs and virions, showing that the VP40 matrix is composed of linearly arranged dimers that are connected via their C-termini (Wan et al., 2020; Winter et al., 2022). Finally, in the presence of RNA, VP40 forms octameric rings with central pores that are occupied by RNA and display inner diameters of 1.7 nm (Gomis-Rüth et al., 2003).

Functionally, VP40 is primarily associated with the assembly and budding of particles, which is supported by the dimeric conformation. In the dimer, so-called late domains encompassing overlapping PTAP and PPXY motifs located in the NTD are accessible and can interact with the host cell endosomal sorting complex required for transport (ESCRT) machinery (reviewed in (Harty, 2009)). The ESCRT machinery is required for efficient scission of budding viral particles from the plasma membrane. Furthermore, the VP40 C-termini contain a basic patch of lysine residues identified to be involved in electrostatic interactions with plasma membrane lipids during membrane association (McCarthy et al., 2007; Bornholdt et al., 2013b; Del Vecchio et al., 2018). Lipid binding is most strongly observed with phosphatidylserines (Soni and Stahelin, 2014; Stahelin, 2014; Adu-Gyamfi et al., 2015; Del Vecchio et al., 2018) and to a lesser extent with phosphatidylinositol 4,5-bisphosphate (PIP2) (Johnson et al., 2016, 2018). Finally, the octameric VP40 structure reveals RNA-binding sites strongly corroborating the postulated role of octameric VP40 in regulating viral transcription and replication (Hoenen et al., 2010a; b).

The different structures of VP40 illustrate its high conformational modularity that is directly linked to its multifunctional character. Determining ultrastructural details of VP40 in different contexts of the viral replication cycle is important to reveal domains and platforms accessible to the viral and host cell machinery.

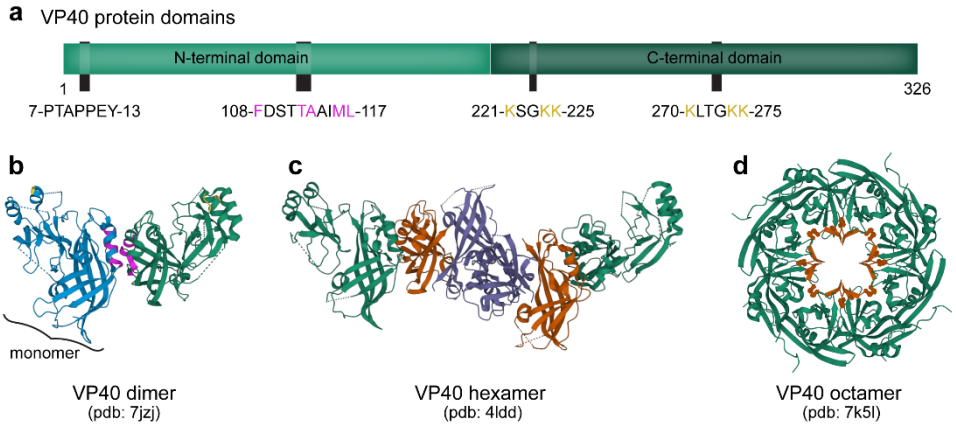

Figure 3: Crystal structures of the EBOV VP40 matrix protein. (a) Schematic representation of the VP40 protein domains. The overlapping late domains PTAP and PPEY are highlighted as well as amino acids that have experimentally been shown to be required for N-terminal dimerization (magenta) and residues involved in electrostatic lipid-interactions (yellow). **(b-d)** Crystal structures of EBOV VP40 solved as a dimer in solution (b), as a hexamer in the presence of dextran sulfate (c) and as an octamer in the presence of RNA nucleotides (d). The same domains (magenta and yellow) highlighted in (a) are highlighted in (b). RNA nucleotides in (d) are marked in brown.

1.1.3 Replication cycle

The viral replication cycle comprises three main steps including (1) entry into host cells, (2) replication and (3) assembly and egress of viral progeny (Fig. 4). As mentioned above, EBOVs can enter a variety of different cell types and tissues owing to their ability to bind to different types of host cell receptors. Due to their large size, they are taken up by macropinocytosis and traffic through the endocytic machinery, before they fuse with the endosomal membrane to deliver the viral genome into the cytoplasm. The EBOV genome is transcribed and replicated in inclusion bodies formed early during infection in the cytoplasm of infected cells (Hoenen et al., 2012), while protein expression presumably takes place in close proximity. Newly formed nucleocapsids containing the viral genome, VP40 matrix proteins and trimeric GP then traffic independently to the plasma membrane to assemble into filamentous virus particles. The replication cycle is concluded with the budding of EBOV particles and transmission of viral progeny to uninfected cells.

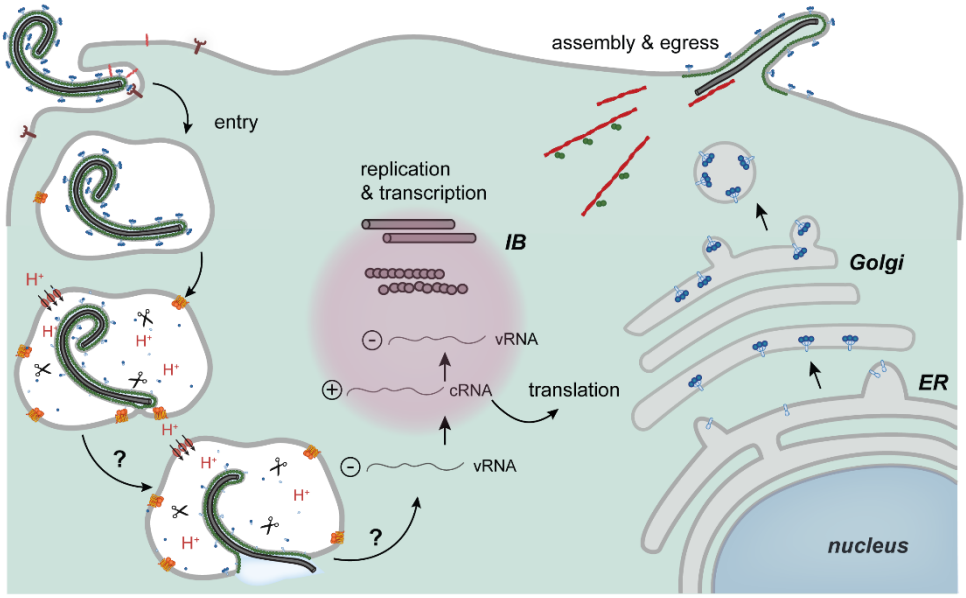

Figure 4: The EBOV replication cycle. Starting with uptake by macropinocytosis, EBOVs enter host cells via the endocytic pathway. After fusion of the viral with the endosomal membrane, the genome is released into the cytoplasm where it replicates and gets transcribed in membrane-less viral factories, the inclusion bodies (IBs). Within inclusion bodies, newly produced viral RNA genomes are encapsidated by nucleocapsids composed of NP, VP35 and VP24 (produced in the cytoplasm), and further associate with the RdRp L and the co-factor VP30. Mature nucleocapsids (grey) are trafficked to the plasma membrane as well as dimeric VP40 (dark green), which is produced in the cytoplasm. Trafficking of both nucleocapsids and VP40 dimers is mediated by actin filaments (red). Translation of the only viral transmembrane protein GP (blue) takes place in the endoplasmic reticulum (ER), after which GP undergoes proteolytic processing in the Golgi and gets transported to the plasma membrane. Budding and assembly of viral progeny occurs at the plasma membrane and is driven by VP40.

Entry into host cells

Virus entry into host cells starts with virus attachment to different receptors, which is mediated in EBOVs by the membrane bound trimeric $GP_{1,2}$, as well as phosphatidylserines exposed on the viral envelope. $GP_{1,2}$ and phosphatidylserine engage two different types of receptors (reviewed extensively here (Davey et al., 2017)), both in a nonspecific manner. Carbohydrate-binding receptors comprising C-type lectins such as DC-SIGN and L-SIGN, and glycosaminoglycans recognize the heavily glycosylated glycan cap of GP1. On the other hand, receptors that recognize phosphatidylserine on the EBOV envelope in a process termed "apoptotic mimicry" (Mercer and Helenius, 2008; Nanbo et al., 2018; Acciani et al., 2021) include members of the T cell immunoglobulin and mucin domain (TIM) and Tyro3/Axl/Mer (TAM) receptor families. Usually, these receptors are involved in the recognition and clearance of apoptotic cells, which expose phosphatidylserine on the external leaflet of their plasma membrane to initiate programmed cell death. Phosphatidylserine-binding is then followed by uptake of the apoptotic cell and eventually its degradation. Since EBOVs acquire their envelope from the plasma membrane, they contain high levels of phosphatidylserine, some of which are flipped in the mature virions by host cell scramblases residing in the viral envelope (Nanbo et al., 2018; Nanbo and Kawaoka, 2019; Acciani et al., 2021). EBOVs can thereby engage phosphatidylserine receptors on a wide range of cell types to initiate viral uptake.

Cellular uptake occurs by macropinocytosis followed by trafficking of the viruses through the endocytic machinery. Endosomal maturation from early- to late endosomes is characterized by a steep pH gradient concomitant with a changing protein composition of the endosomal compartments. EBOVs exhibit

remarkably late entry kinetics compared to other negative-sense RNA viruses (Mingo et al., 2015) and entering EBOVs colocalize with the GTPase Rab7, a late endosomal marker, as well as lysosome associated membrane protein type 1(LAMP1) (Spence et al., 2016) and the Niemann-Pick Type C transporter NPC1, which are present in endolysosomes. NPC1 has been identified as an indispensable intracellular EBOV receptor (Carette et al., 2011; Côté et al., 2011; Miller et al., 2012; Simmons et al., 2015). Furthermore, internalized EBOVs co-localize with endosomal cathepsin proteases, which are involved in lysosomal degradation and are activated by low pH. Cathepsin L and B both cleave the EBOV $GP_{1,2}$, removing the majority of the GP1 domain and leaving a 19 kDa membrane-anchored GP1 core still connected to GP2 via a disulfide bond (Chandran et al., 2005; Schornberg et al., 2006; Brecher et al., 2012). This results in the exposure of a receptor-binding domain (RBD) and fusion peptide consisting of a stretch of hydrophobic residues. The exposed RBD then binds to the C loop of NPC1, which is usually bound by soluble NPC2 during NPC1-mediated cholesterol shuttling (Zhao et al., 2016). Binding to NPC1 is followed by GP-mediated membrane fusion, a process that has so far been postulated based on the similarities of EBOV $GP_{1,2}$ to the founding member and best-studied class I fusion protein to date (White et al., 2008), the influenza A virus hemagglutinin (HA). Membrane fusion involves the extension of the GP2 fusion peptide towards the endosomal membrane, where it gets inserted and forms an extended pre-hairpin structure. It then folds back on itself, thereby distorting the endosomal and viral membrane and forming a hemifusion stalk. Fully backfolded fusion peptides adopt a low energy, postfusion conformation (a coiled-coil six-helix bundle) that further opens the hemifusion stalk, resulting in the formation of a fusion pore. Upon sufficient extension of the fusion pore, the viral genome then passes through and enters the cytoplasm by yet unknown mechanisms, which concludes virus entry.

Virus uncoating

During the final steps of virus entry, the nucleocapsid must dissociate from the virus particle and eventually from the genome to allow its release into the cytoplasm and subsequent replication and transcription of the uncovered genome. These two processes together are referred to as "virus uncoating" and have been well studied for influenza A viruses. In these viruses, the matrix protein M1 plays a critical role. In intact virus particles, M1 binds tightly to the viral membrane, interacts with the cytoplasmic HA tails and is tethered to the viral genome segments (Burleigh et al., 2005; Zhang et al., 2000; Kordyukova et al., 2019, 2021). During entry, it is released from the virus particle to allow membrane fusion, a process that is triggered by low pH and involves the disassembly of the M1 matrix layer leading to overall softening of the virions as determined by atomic force microscopy (Li et al., 2014). Acidification of the viral lumina is achieved by the influenza A virus ion channel M2 and is recognized as a critical step during influenza A virus entry and uncoating (Greber et al., 1994; Yamauchi and Greber, 2016; Moreira et al., 2021). Although matrix proteins of enveloped viruses share no structural homologies, they are functionally related and have been implicated in the same processes: as mentioned for influenza A viruses, they have been shown to interact with nucleocapsids, glycoprotein tails, cellular membranes (Liljeroos and Butcher, 2013) and the cellular host cell machinery, and as such play an important role during assembly and budding of virions (Garoff et al., 1998;

Liljeroos and Butcher, 2013). During virus entry, many interactions that are established during virus assembly are reversed and the detachment of the viral matrix protein from the virions is likely an integral part of virus uncoating.

For EBOVs and filoviruses in general, uncoating is poorly understood and mechanisms driving genome release into the cytoplasm have not been conclusively investigated. Since EBOVs do not encode a dedicated viral ion channel, acidification of the virus core has been disregarded to date, and only limited studies exist addressing the role of low pH during EBOV entry. Especially for the remarkably long EBOVs, matrix disassembly may be pivotal to enable fusion of their membranes during entry.

1.2 Visualizing viruses

With the exception of giant viruses and filoviruses, which reach up to several micrometres in length, most viruses are tiny pathogens ranging from 20 - 250 nm in size. Their small size together with their inability to replicate outside a host contributed to their discovery only in the 1890s with the first virus described as the causative agent of TMD in plants (Lecoq, 2001). At the time, infectious diseases were exclusively associated with bacteria and fungi, which were often isolated by filtration techniques and visualized by optical microscopes (Twort, 1915). Owing to their small size, viruses remained "invisible" (Rivers, 1932) and their nature a mystery until the development of the electron microscope in the 1930s by Ernst Ruska, Max Knoll and Bodo von Borries (Knoll and Ruska, 1932; Ruska et al., 1939). Until then, larger pathogens were characterized using optical light microscopes. The resolution of optical systems is limited by the wavelength of light and the numerical aperture (NA) of the imaging instrument, which is related to the refractive index (n) of the medium through which light passes and the detected angle of the image-forming rays ($NA = n * \sin\alpha$) (Holik, 2001). The maximum achievable resolution of optical systems was first described by Abbé in 1873 as $d = \frac{\lambda}{2\,NA}$ (Abbe, 1873) and is accordingly limited to approximately 200 nm – insufficient to image small viruses. To overcome this limit, microscopes using electrons as illumination source instead of photons were invented in the 1930s. The early microscopes used a cold cathode as electron source, and offered a resolution of 13 nm (Kruger et al., 2000), which was enough to morphologically characterize different viruses and distinguish them from bacteria and one another. Extensive investigation into sample preparation of biological specimen, pioneered by Helmut Ruska (Kruger et al., 2000), soon enabled the first images of viruses, including TMV and the orthopoxviruses mouse extromelia virus, vaccinia virus and rabbit myxoma (von Borries et al., 1938; Kausche et al., 1939). These first images marked the beginning of virology as a distinct field in microbiology and illustrate the interconnected co-evolution of EM and virology.

Rapid improvements in sample preparation, including the introduction of contrast from shadowing techniques and negative staining (Brenner and Horne, 1959), established transmission electron microscopy (TEM) as the main tool to identify viruses and classify them based on morphology. Additionally, the possibility to image unpurified samples including plasma, urine and feces (Goldsmith and Miller, 2009) by TEM together with the development of ultramicrotomes that enabled cutting of biological samples such as infected tissue into ultrathin sections (Pease and Baker, 1948) rendered TEM pivotal for virus diagnostics.

Although gradually replaced by analytical biochemistry assays such as PCR and ELISA for diagnostics in the 1990s (Richert-Pöggeler et al., 2019), TEM is still routinely used when no information regarding the pathogen is known, and no organism-specific reagent is available. Especially relevant for the characterization of emerging viruses, TEM has for example been pivotal in the discovery of the highly pathogenic filoviruses during haemorrhagic fever outbreaks in Central and West Africa in 1976 (Bowen et al., 1977; Johnson et al., 1977), the identification of Nipah viruses causing outbreaks in Malaysia in 1999 (Chua et al., 2007) and the characterization of the causative agent of the severe-acute respiratory syndrome (SARS) outbreak in 2003 (Ksiazek et al., 2003).

Principles of TEM

In TEM, images are created from electrons interacting with a thin sample less than 200 nm thick. Electrons passing through the sample are scattered and focused by electromagnetic lenses to create a magnified image of the sample when collected on a photographic film. The thicker the sample, the less electrons get transmitted resulting in dark images containing less structural details of the specimen. Biological samples are mainly composed of poorly scattering, light atoms (primarily H, O, N and C) that do not provide strong contrast in TEM. To enhance the contrast between the specimen and surrounding environment, negative staining was developed as one of the first sample preparation techniques (Brenner and Horne, 1959). In negative staining, the sample is embedded in a heavy metal salt solution that adsorbs to biological matter and scatters electrons strongly, thereby creating a dark background against which the biological sample is well visible. Since the salt crystals do not penetrate the hydrophobic exterior of the sample, negative staining reveals the surface of the sample but no internal details. Due to the quick sample preparation and high contrast, negative stain EM is widely used to identify unknown pathogens or to assess sample quality prior to performing further experiments. Other techniques used to enhance image contrast without introducing staining solutions are based on the principles of electron interactions with the specimen in TEM (reviewed extensively here (Orlova and Saibil, 2011)) and will briefly be discussed in the following.

Amplitude versus phase contrast

Incident electrons passing through a sample in TEM interact with the sample in different manners: They either get transmitted without changing their paths and thus remain unscattered or they interact with the atoms in the sample, resulting in inelastic and elastic scattering. Inelastic scattering occurs when the incident electrons interact directly with electrons of the sample atoms, thereby transferring some of their energy into the atoms. This can cause the ejection of secondary electrons, ionization, emission of X-rays, and production of free radicals. The energy transfer during inelastic scattering thus induces radiation damage to the sample, which significantly impairs high-resolution imaging (Cosslett, 1978). Elastic scattering, on the other hand, occurs when the incident electrons do not directly interact with the electrons in the sample, but get attracted by the positive charge of the nuclei and subsequently deflected at different angles. They have the same energy as the incident and unscattered electrons and do not cause specimen damage. To create an

image, all scattered electrons are refocused by an objective lens and interfere with the unscattered electrons on the image plane (Fig. 5). Since inelastically scattered electrons have lost some of their energy and have thus longer wavelengths, they are focused by the objective lens on different planes than the elastically scattered electrons, causing a blurring in the final image. To avoid compromising the final image, inelastically scattered electrons can be removed by using energy filters (first introduced in 1987 (Trinick and Berriman, 1987)) that are either placed in-column or post-column and significantly improve the signal-to-noise ratio in the final reconstructed volumes.

Scattering objects lead to the loss of part of the incident electron beam, as some electrons get absorbed by the sample, are not collected or filtered out. This causes a contrast between scattering objects and non-scattering or weaker scattering environments, through which a larger number of electrons get transmitted and consequently recorded on the image plane. This is referred to as amplitude contrast, which can be increased by using heavy metal stains that absorb electrons more strongly than the light atoms found in biological specimen (for example using negative staining). In cryo-EM (discussed below), amplitude contrast is less relevant, since the samples are imaged without staining and the number of recorded electrons after interaction with the sample remains similar to the number of incident electrons. Instead, so-called "phase contrast" dominates and contributes primarily to image formation. Phase contrast is formed by the interference of scattered and unscattered electrons on the image plane. Since scattered electrons follow a longer path and are thus phase-shifted with respect to unscattered electrons, their interference with unscattered electrons changes the amplitude, and hence intensity and contrast, of the electrons recorded on the image plane. Since thin biological specimen scatter weakly, contrast can be improved by collecting images at a slight defocus (further described below), which introduces an additional phase shift.

The contrast that is transferred from the sample to the recorded image is modulated by the contrast transfer function (CTF) of the microscope, which depends on microscope parameters including the accelerating voltage of the microscope, objective defocus, and the spherical aberration. The CTF is a sinusoidal function describing the contrast (or amplitude) of the interfering electron waves plotted against their spatial frequencies (Fig. 5). It thus reflects the contribution of the scattered waves across a spectrum of frequencies to the recorded image. Negative amplitudes at certain frequencies and loss of information at zero-crossings (Fig. 5 b) distort the final image, which can be corrected to restore structural information. This is achieved partly by applying a CTF-correction to the recorded image. Prerequisite is that a CTF can be fitted to the oscillating signal of concentric rings (so called Thon rings, named after F. Thon (Thon, 1966)), which is visible in the reciprocal space of the projection image. A Fourier transform is then applied to the recorded image and divided by the CTF to obtain a CTF-corrected Fourier transform. The inverse of the Fourier transform will then give a CTF-corrected image. Zero-crossings in the CTF cannot be corrected since the information at these spatial frequencies is lost. However, recording images at different defocus values (further described below), changes the frequency of the CTF and thereby the position of the zero-crossings. Therefore, by combining information from these images, the information can be restored.

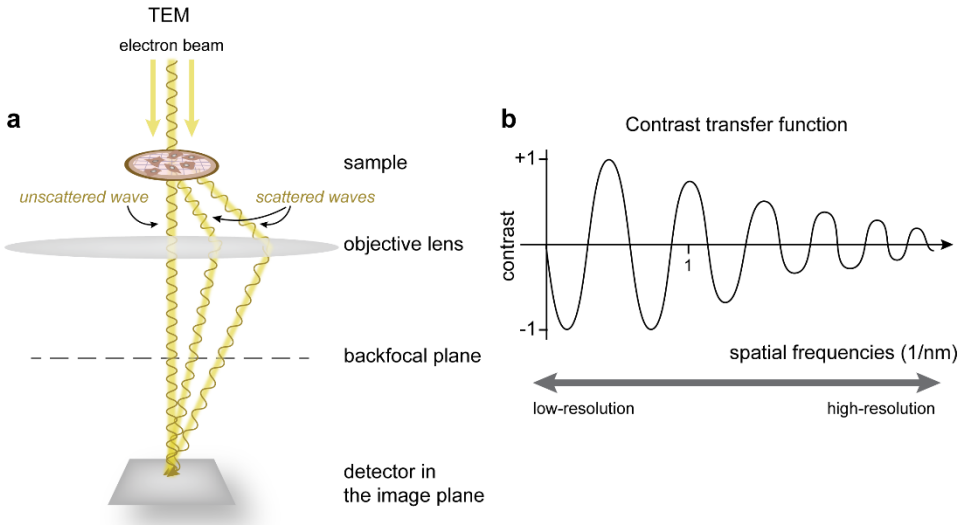

Figure 5: Data collection in transmission electron microscopy (TEM). (a) Schematic depiction of electrons transmitted through a sample in a TEM. The incident electron beam either directly passes through the sample as an unscattered beam, or gets scattered by the electrons in the sample. After refocusing at the electromagnetic objective lens, the scattered and unscattered waves are collected in the image plane, where they interfere. **(b)** Schematic of a contrast transfer function (CTF) plotted against spatial frequencies. Low-resolution details of the specimen imaged by TEM appear close to the origin, whereas high-resolution details are stored at high spatial frequencies.

Defocus phase contrast and phase plates

As mentioned above, introducing a defocus during image acquisition increases the contrast and is referred to as "defous phase contrast". This is achieved by altering the current of the objective lens, which results in a shift of the CTF curve towards low-resolution frequencies. The increased amplitude at low-resolution frequencies is manifested in a higher contrast at the expense of high-resolution details, which are lost at zero-crossings (Fig. 6). Alternatively, to allow data acquisition in focus while providing sufficient contrast, "in-focus phase contrast devices" (Danev et al., 2014), or phase plates, have been developed. Phase plates are typically composed of a thin layer of amorphous carbon and placed in the back-focal plane of the objective lens. Interactions of the electron beam that has passed the sample with the phase plate cause a phase shift between the scattered and unscattered electrons and the conversion of the CTF from a sine to cosine function (Fig. 6). As a result, the amplitude at low-resolution frequencies is enhanced, contributing to a significant increase in contrast, while retaining the signal at high spatial frequencies. The most commonly used phase plates are the Zernike phase plate and the Volta phase plate (Wang and Fan, 2019). The Zernike phase plate contains a hole at the centre through which the unscattered electron beam passes. Scattered waves pass through the carbon film and are slowed down, resulting in an additional phase shift (Danev and Nagayama, 2001). Challenges when using the Zernike phase plate include the optimization of the film thickness for accurate phase shifts, the precise alignment of the central whole through which the unscattered beam needs to pass and charging effects around the edges of the hole (Wang and Fan, 2019). Volta phase plates, on the other hand, are hole-free, uniform carbon films (Danev et al., 2014). The unscattered electron beam passing through the centre of the plate locally generates an electrostatic negative potential, which leads to a phase shift of the scattered waves by 90° (Danev et al., 2014). This allows in-focus imaging of biological samples at high contrast, while eliminating the challenges posed by the Zernike

phase plate: since the incident beam is used to define the centre of the phase plate, where the electrostatic potential is created, precise alignment of the plate becomes less relevant, and the absence of the hole eliminates any charging effects. Since its development in 2014, Volta phase plates have been increasingly used in TEM for high-resolution studies of macromolecules (a list of studies using Zernike or Volta phase plate is published here (Wang and Fan, 2019). Despite the significant increase in contrast allowing to image samples in focus, higher resolution during subtomogram averaging (discussed below) is still achieved when using defocus phase contrast as demonstrated and discussed by a recent benchmarking study (Turoňová et al., 2020a).

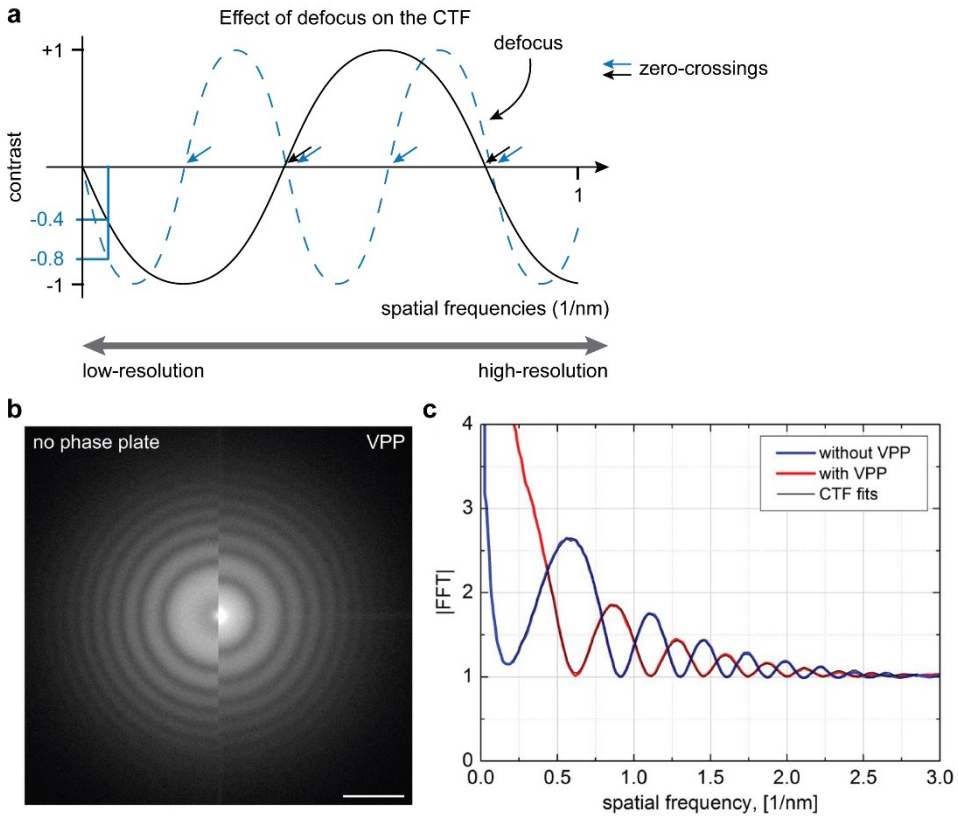

Figure 6: Effect of defocus and the Volta phase plate on the CTF. (a) Schematic of CTFs of images recorded in focus (black line) and at a defocus (dotted line) plotted against spatial frequencies. Applying a defocus shifts the CTF towards low-resolution frequencies, which results in higher contrast at these frequencies (exemplarily shown here at an arbitrary low-resolution spatial frequency where the transferred contrast is double in comparison to the in-focus data). The higher contrast comes at the expense of more frequent zero-crossings at which the information is lost. **(b-c)** Fourier transforms and corresponding CTFs of images acquired at high magnification with and without a Volta phase plate (VPP). The images in (b) ad (c) are taken from (Danev et al., 2014).

1.2.1 Pushing the resolution using cryo-EM

Driven by the quest to reveal further structural details, the field of structural biology rapidly evolved in the 20th century, with X-ray crystallography, nuclear magnetic resonance spectroscopy (NMR) and EM as the main drivers in producing high-resolution macromolecular structures (Curry, 2015). Pivotal for establishing EM as a highly valuable tool to study biological macromolecules at high resolution and in 3D, was the development of cryo-EM, the introduction of direct electron detectors and averaging techniques such as

single particle analysis (SPA). These developments have transformed EM from a low-resolution imaging method to a high-resolution technique contributing considerably to the ultrastructural characterization of macromolecules at atomic resolution (Fig. 7). Today, cryo-EM bridges the resolution gap between light microscopy and high-resolution techniques such as X-ray crystallography and NMR.

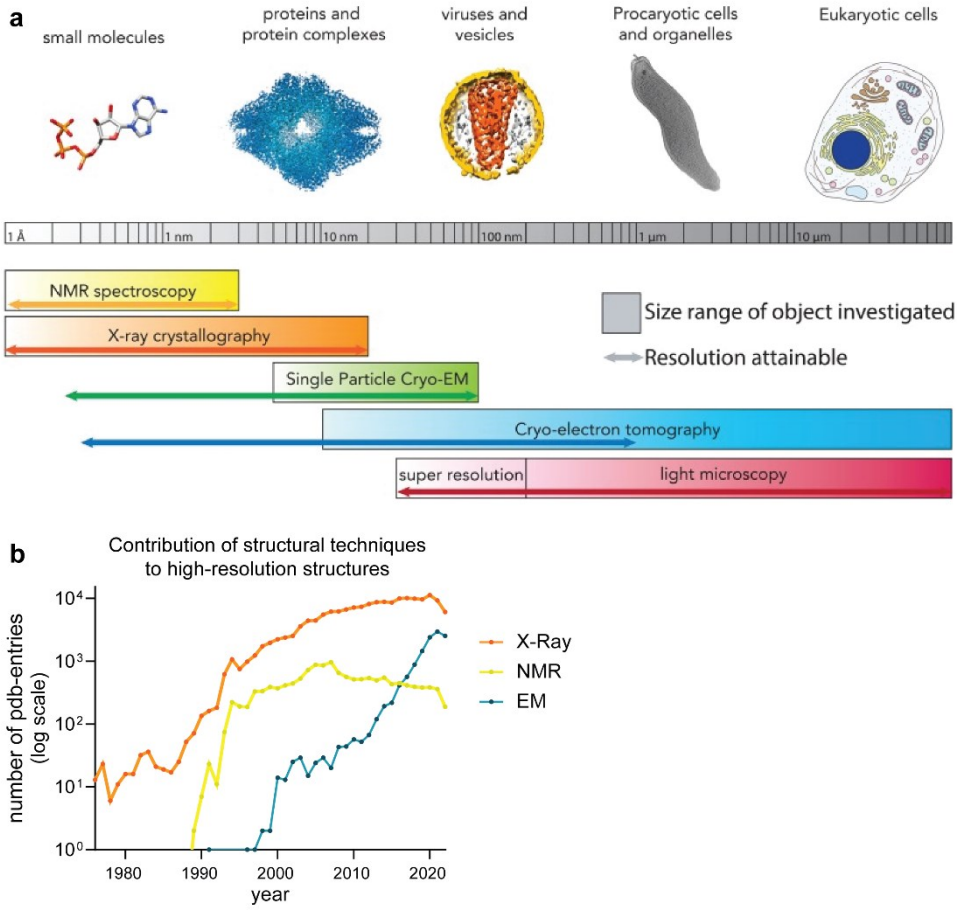

Figure 7: Structural analyses of biological specimen across different size scales. (a) Diagram depicting biological structures of different sizes and respective structural techniques used to study them. The attainable resolution corresponds to the details that can be resolved from atomic bonds to whole cells (from left to right). Cryo-EM including single particle cryo-EM and cryo-electron tomography (discussed below) are bridging the resolution range from light microscopy to NMR. Image source: (Hutchings and Zanetti, 2018). **(b)** Number of high-resolution structures solved by X-ray crystallography, NMR and EM deposited on the protein data bank (pdb) from 1976 until 2022. Source: https://www.rcsb.org/stats/all-released-structures.

Since preservation of samples at cryogenic temperatures, the data collection method and averaging techniques have been instrumental for the advancement of EM, they are briefly discussed in the following.

Cryo-EM and sample vitrification

Cryo-EM was introduced in the 1980s as an alternative to negative staining and was first successfully demonstrated on viruses (Adrian et al., 1984). Instead of embedding the sample in a contrasting solution after dehydration, it is cooled down rapidly such that the water contained in the sample forms amorphous (or vitreous) ice. The cooling process must occur fast enough to avoid the formation of cubic ice, which is crystalline and adsorbs the electron beam strongly, thereby obscuring the sample. Additionally, crystalline ice causes molecule segregation and osmotic changes within the biological sample, thereby damaging its

ultrastructure. Vitreous ice on the other hand is non-crystalline and hence adsorbs the electron beam to lesser extent. Since, similar to water, it is intrinsically disordered, it does not cause diffraction patterns, which would obscure the signal arising from the biological sample (Dubochet et al., 1988). Vitreous ice is thus essentially "invisible" in the electron beam and contrast is formed solely by the difference in density between the ice and biological sample. Thus, when imaging thin samples such as viruses by cryo-EM, their organization inside the outer protein or membrane layer is revealed, albeit at low signal-to-noise ratio compared to stained samples.

Rapidly cooling down biological samples, also referred to as cryo-preservation or vitrification, can be achieved by two main techniques: Samples thinner than 5 μm such as eukaryotic cells, bacteria and viruses are plunge-frozen into liquid ethane cooled down to -180° and transferred to and stored in liquid nitrogen. While liquid nitrogen is cold enough to allow the instant immobilization of water molecules in amorphous ice, its heat capacity is low and at -180°C, it is close to its boiling point. Consequently, when samples at room temperature are immersed in liquid nitrogen, they warm up slightly, slowing down the freezing process and increasing the chances of cubic ice formation. In contrast, ethane exhibits significantly higher heat capacity and is close to its freezing point when cooled down by liquid nitrogen. It hence does not evaporate upon slight temperature changes and allows efficient sample vitrification.

The second vitrification technique is applied to larger specimen (up to 200 μm) such as tissues or small organisms like *Caenorhabditis elegans*. The cooling rate in thick samples is too slow at ambient pressure to allow uniform vitrification, causing the formation of ice crystals. Instead of plunge-freezing the samples, they are vitrified using liquid nitrogen under high pressure, thereby increasing the cooling rate and enabling even vitrification throughout the sample. This technique is referred to as high-pressure freezing (described in more detail here (Dahl and Staehelin, 1989; Studer et al., 2008) and is used in combination with freeze fracturing (Moor and Mühlethaler, 1963), freeze-substitution and resin embeddin, or cryo-sectioning of the samples (Al-Amoudi et al., 2004).

Since vitrified samples are exclusively embedded in thin ice and not treated with staining solutions that lead to structural damages caused by dehydration or interactions with the stain, cryo-EM allows imaging of biological samples close to their native state. Additionally, the low temperatures greatly reduce beam-induced damage (Orlova and Saibil, 2011), further protecting the sample during image acquisition.

Direct electron detectors

Conventionally, images in TEM were recorded using photographic films and needed to be digitalized for further image processing before digital detectors were invented. The most commonly used digital detectors are so-called charge couple devices (CCD), introduced in the late 1960s (Janesick, 2001) but are gradually replaced by direct electron detectors (DEDs), developed two decades later (Milazzo et al. 2011; Faruqi and McMullan 2011; Li et al. 2013). CCD cameras are semiconducting photoelectric conversion devices, which indirectly detect the electrons transmitted through the sample after their conversion to photons. The conversion of electrons to photons is achieved using scintillators, which reduce the detective quantum efficiency (DQE) of the devices. The development of DEDs revolutionized data collection and the

achievable resolution obtained by cryoEM (Hanssen, 2018) by allowing the detection of electrons without prior conversion to photons. This enables faster image acquisition at a significantly higher DQE as demonstrated by several high-resolution studies performed on purified virus particles (Schur et al., 2016; Mattei et al., 2018; Obr et al., 2022) and even ribosomes inside intact cells (O'Reilly et al., 2020; Tegunov et al., 2021).

(Cryo-)electron tomography

High-resolution structures have proven invaluable in basic research to understand the function of macromolecules and particularly in medical research for drug design and development. In EM, high resolution structures can be obtained by averaging multiple two-dimensional projection images of individual particles, also referred to as single particle projections, thereby enhancing the signal-to-noise ratio and revealing ultrastructural details with increasing number of averaged particles. This is the basic principle of SPA (reviewed here (Boekema et al., 2009)), in which 2D projections are acquired of a solution of purified macromolecules that are ideally randomly oriented on a carbon support film (when applied to negatively stained samples) or thin layer of amorphous ice (when using cryo-EM). Individual macromolecules are then classified and grouped based on their orientation and each group is averaged to obtain a final 3D reconstruction from the 2D projections. SPA has greatly contributed to resolving high-resolution structures, including the first structure solved by EM to date at atomic resolution of 1.25 Å (Yip et al., 2020).

However, these structures are derived from purified components that have been isolated from their native environment, thereby lacking important context. Transient or weak protein interactions with ligands, co-factors or lipids may thereby be lost as well as the cellular environment and information regarding localization within cellular compartments and interactions with cellular components. Moreover, structures derived from SPA rely on the acquisition of 2D projections from different angles and orientations of the macromolecule to obtain a complete 3D reconstruction. Macromolecular assemblies adopting preferred orientations on EM grids such as fibres thus provide limited datasets that result in anisotropic resolution of the final 3D volume. To overcome these limitations, (cryo-)electron tomography (ET) has been developed as a complementary technique to SPA. Initially used to study macromolecular complexes in isolation (reviewed here (Koehler, 1986)), it has increasingly been used to study the structure of bacteria and viruses (with the first cryo-ET study on viruses performed in 1993 (Dierksen et al., 1993)), cellular architecture, and the structure of macromolecular complexes in situ. In (cryo-)ET, an array of 2D projection images is acquired of the same sample by tilting it along a fixed axis. The individual projections of this so-called 'tilt series' are then computationally aligned to reconstruct a 3D volume of the sample (Fig. 8). The acquisition of tilt series requires the sample to be thin enough for electrons to penetrate even at high tilt angles, while exposing the sample cumulatively to the electron beam and thus to radiation damage (Cosslett, 1978; Glaeser and Taylor, 1978; Downing and Glaeser, 1986). Conventionally, the attainable resolution (d) for a tomographic reconstruction is evaluated by the Crowther criterion (Crowther et al., 1970) and depends

on the number of projections (m) acquired at equal angular spacing according to $m = \pi * {}^{D}/_{d}$, with D= diameter of the reconstructed particle (Yalisove et al., 2021). To maximize the number of images taken at different tilt angles while minimizing radiation damage, different tilt schemes have been developed. A commonly used scheme is the bidirectional acquisition scheme, in which the sample is rotated along a fixed axis in 0.5 to 5° increments, starting from 0° tilt (Hagen, Wan, and Briggs, 2017). By moving to higher tilts simultaneously in a rocking acquisition motion, the images acquired at low tilt angles, where the sample is the thinnest and thus provides the highest information, are acquired before radiation damage has accumulated. This is referred to as a "dose-symmetric" tilt scheme, specifically developed to maximize the transfer of high-resolution information (Hagen, Wan, and Briggs, 2017). The geometry of the sample and increased path of electrons at high angles reduces the usable tilt angle range from -60 to 60°. This results in a so-called "missing wedge" of information in Fourier space, which cannot be sampled. Hence, sample information is lost perpendicular to the tilt axis and the reconstructed volume suffers from anisotropic resolution and apparent elongation of features in Z-direction. To reduce the missing wedge in the final tomograms, two tilt series can be acquired along orthogonal tilt axes, also referred to as dual-axis tomography (Mastronarde, 1997). Both tilt series are processed and reconstructed similarly after acquisition to be combined into a final tomogram. Since the sample is exposed to the electron beam twice as much as during single axis acquisition, the total electron dose per tilt series is halved to minimize radiation damage. This leads to low signal-to-noise ratios in the individual tilt series and requires thin samples to allow enough contrast for image alignment. The image transfer at different tilts during dose-symmetric acquisition of dual-axis tilt series is schematically depicted in Figure 8. At low tilt angles, the information transfer is the highest and decreases symmetrically towards high tilt angles. As the electron dose accumulates over acquisition time, information transfer during the second tilt series acquisition is lower already at 0° tilt angle compared to the first tilt axis (here: tilt axis A). The final reconstructed dual-axis tomogram contains information from both angles acquired and approximately contains the same contrast as single axis tomograms (Winter and Chlanda 2021). By combining data obtained along orthogonal tilt axes, dual-axis tomography significantly reduces the missing wedge of information in the final tomograms.

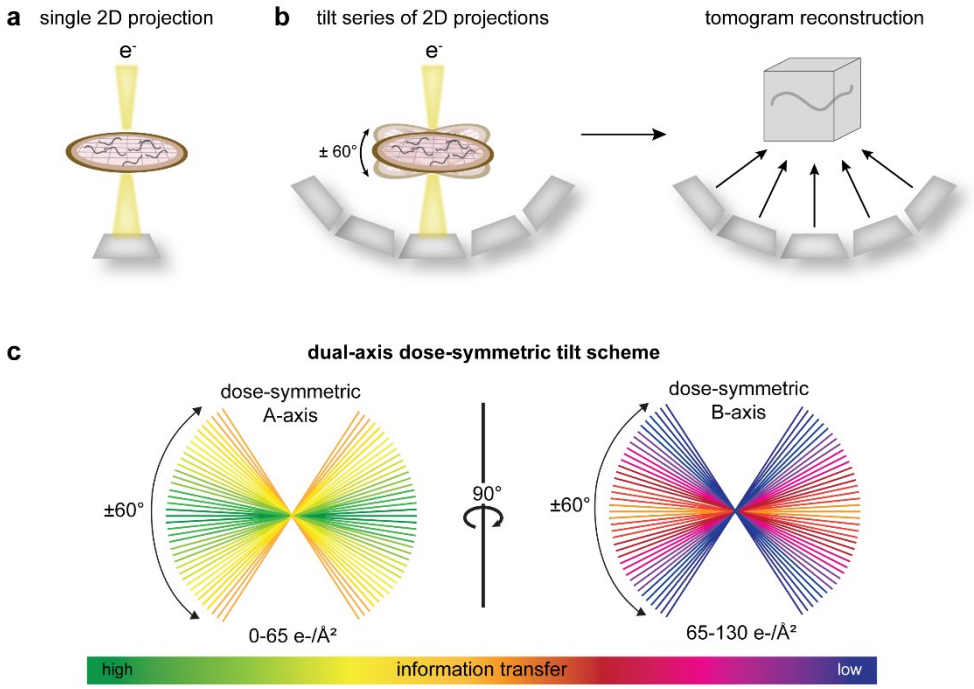

Figure 8: Principle of cryo-electron tomography. (a) Schematic of an EM grid containing filamentous specimens exposed to the electron beam during the acquisition of a 2D projection. Electrons transmitted through the sample are captured on a detector. **(b)** Schematic depicting the acquisition of a tilt series of 2D projections of filamentous specimens deposited on an EM grid. The sample is rotated from -60° to +60° degrees and at each tilt, a 2D projection image is acquired. The final 2D projections are then computationally recombined into a 3D volume, the tomogram. **(c)** Schematic showing the information transfer from 2D projection images obtained during dose-symmetric tilt series acquisition along axis A before rotating the axis by 90° and acquiring a second tilt series along axis B. The schematic in (c) is adapted from (Winter and Chlanda 2021).

Subtomogram averaging

Cryo-electron tomograms reveal the structural architecture of thin biological specimen, including the membrane-organization of cellular organelles, the localization of macromolecular complexes within the sample and lipid bilayers. Without further data processing, however, details that can be extracted from the tomograms are limited by missing wedge information and low signal-to-noise-ratio, and cryo-ET provides primarily snapshots of the biological specimen. To achieve higher resolution and reveal ultrastructural details of macromolecules occurring frequently in the sample, averaging approaches in analogy to SPA can be applied to fill in the missing wedge information and increase signal-to-noise ratio. To this end, subvolumes containing the macromolecule of interest are extracted from the tomograms and subjected to iterative alignment and averaging (Fig. 9). Since the molecules are often differently oriented in the tomogram, the missing wedge of information is reduced upon averaging (reviewed here (Hutchings and Zanetti, 2018)). Similar to SPA, the achievable resolution is determined by the number of averaged particles and the homogeneity of their structural organization, and details of highly flexible domains or disordered regions will be obscured during the averaging process. However, owing to recent developments in data acquisition (especially the development of DEDs) and processing pipelines, subtomogram averaging has become a powerful technique to extract structural details of macromolecules in their native environment at high-resolution (Obr et al., 2022). This has led to the highest resolution achieved to date by subtomogram

averaging of 2.8 Å of purified proteins in vitro (Tegunov et al., 2021; Ni et al., 2022), and 3.5 Å in cells (Tegunov et al., 2021), impressively demonstrating the potential of the technique.

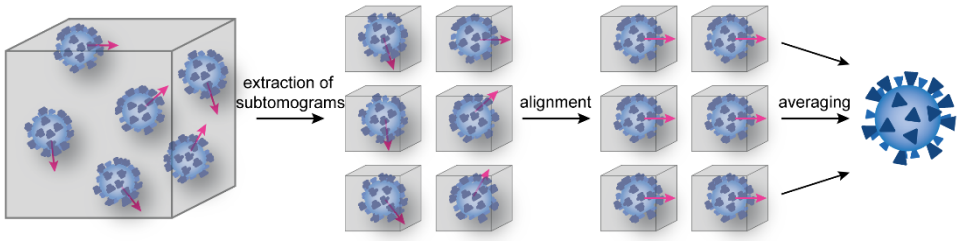

Figure 9: Principle of subtomogram averaging. Multiple subtomograms are extracted from initial tomograms and aligned to be similarly oriented. Averaging of all subtomograms reveals a final structure at high resolution.

Accessing cellular structures

As mentioned above, cryo-ET is especially powerful to reveal the structures of macromolecules in the context of their native environment. While thin biological samples such as bacteria and viruses are immediately accessible by cryo-ET, thicker samples such as cells or even tissue impede electron transmission and thus require substantial thinning prior to imaging. The first thinning technique developed called "cryo-electron microscopy of vitreous sections" (CEMOVIS) was based on cutting the samples with specifically designed diamond knives, further improved by preserving and cutting the samples at cryogenic temperatures (Al-Amoudi et al., 2004). Cryo-ultramicrotomy was routinely used to study specimen such as cell suspensions and tissue samples but resulting sections suffered from knife marks and compression of the specimen in the cutting direction, which caused artefacts that were difficult to compensate for and often obstructed structural details (Al-Amoudi et al., 2005). Inspired by a technique commonly used at the time in material sciences, sample thinning by successively ablating its top-most layers using a focused ion beam (FIB) was then introduced (Marko et al., 2007) and further optimized for routine sample preparation (Rigort et al., 2012; Schaffer et al., 2017). So-called "(cryo-)FIB-milling" is performed by subjecting the frozen sample to a beam of ions (typically gallium ions), which are focused on the sample surface at high currents to sputter off material. By iteratively reducing the ion beam current, sample layers are successively and gently removed until a thin section of approximately 150 nm, called lamella, remains. Integrated into the setup is a scanning electron microscope (SEM) that is used to image the sample during the sputtering process and monitor its progression without further ablating material. Cryo-FIB milling is typically performed to produce lamellae of cells grown on EM grids or applied on grids as a solution just before vitrification by plunge-freezing. EM grids containing multiple lamellae are then transferred to a TEM to acquire tomograms. Cryo-FIB milling thus "opens a window" into the cell's interior (Villa et al., 2013), enabling structural studies at high resolution without cutting and compression artefacts observed on samples thinned by cryo-ultramicrotomy. The power of cryo-ET performed on FIB-milled cells was demonstrated in 2016 when the complex cellular environment of the nuclear periphery in mammalian cells was visualized in 3D (Mahamid et al., 2016).

1.2.2 Unravelling virus-host cell interactions by cryo-ET

The continuous technological developments in sample preparation, data acquisition and data processing render cryo-ET gradually accessible to a wider scientific community. Especially enveloped viruses, which adopt heterogenous shapes and often lack symmetry or repetitive patterns that would allow analysis by SPA, are increasingly studied by cryo-ET. Subtomogram averaging has for example revealed the organization of matrix layers in pleiomorphic viruses such as respiratory syncytial virus (Sibert et al., 2021; Conley et al., 2022), influenza A virus (Peukes et al., 2020) and filoviruses (Wan et al., 2020). Other examples are studies of the organization and structure of flexible spike proteins on the surface of severe acute respiratory syndrome coronavirus-2 (SARS-CoV-2) (Turoňová et al., 2020b) and the structure of the mature human deficiency virus-1 (HIV-1) capsid within intact virions (Mattei et al., 2016). Furthermore, already before the advent of cryo-EM and high-resolution tomography of cellular compartments, TEM has revealed important steps during viral replication cycles including the first hints at different virus entry mechanisms (Helenius et al., 1980; Bousarghin et al., 2003; Kartenbeck et al., 1989). Since the recent establishment of cryo-FIB milling, this approach to access the cell's interior has been applied to study virus-host cell interactions of several viruses, revealing unprecedented details into their replication cycle (reviewed here (Quemin et al., 2020; Vankadari et al., 2022). One prominent example is the extensive host cell remodelling induced by SARS-CoV-2-infection; within one year of its emergence at the end of 2019, most steps of its replication cycle have been visualized by cryo-ET. These include the description of SARS-CoV-2-induced double-membrane vesicles (DMVs) as protected hubs of viral RNA replication (Klein et al., 2020a), assembly and budding of viral progeny at endoplasmic-reticulum–Golgi intermediate compartments (ERGIC) and the molecular architecture of intracellular virions (Mendonça et al., 2020; Klein et al., 2020a). A landmark in understanding the function of DMVs and how RNA is shuttled in and out of these compartments was the discovery of a DMV-spanning pore of the closely related β-coronavirus murine hepatitis coronavirus (Wolff et al., 2020a). This finding has implications not only for the replication of coronaviruses but potentially for the replication of other positive-strand RNA viruses inducing similar cellular replication compartments (reviewed here (Wolff et al., 2020b)). Beyond SARS-CoV-2, cryo-ET of FIB-milled infected cells has also been pivotal in understanding the steps of the replication cycle of other viruses: the assembly and egress of herpes simplex virus at the nuclear envelope was thereby visualized at molecular resolution (Hagen et al., 2015) and for the first time, intact capsids of HIV-1 have been visualized during their transport into the nucleus through nuclear pore complexes (Zila et al., 2021). These examples illustrate how cryo-EM, and cryo-ET in particular, increasingly develops into an invaluable tool to study virus structures and interactions with the host cell machinery during infection.

1.3 Aims of this thesis

As obligate intracellular pathogens, viruses rely on host cells for their replication and propagation. The viral replication cycle is initiated by virus attachment to the host cell, followed by virus uncoating and genome release into the cytoplasm, where the host cell machinery resides to enable virus replication or trafficking to replication compartments. These early steps of virus entry are pivotal, as they define the host range and tropism of the virus, i.e., the range of cell types and tissues that can be infected. Unravelling virus entry pathways in molecular detail provides invaluable insights into the role of viral, as well as host cell proteins and lipids, and offers strategies for early antiviral treatments.

The entry pathway of EBOV into host cells has been extensively studied, revealing the requirement of different host cell receptors and proteases. Furthermore, a mechanism of EBOV membrane fusion with the endosomal membrane, which concludes virus entry, has been proposed based on structural studies of the class I fusion protein GP. However, how uncoating of the remarkably long viruses is regulated to enable the timely genome release from the virus particles remains unknown. Moreover, EBOVs are shaped by a protein scaffold composed of the viral matrix protein VP40, which confers stability to the virions during transmission. Whether the VP40 scaffold must disassemble to enable virus uncoating, and how uncoating is regulated, remains unknown.

The aim of this work was to investigate EBOV uncoating during virus entry into host cells, with a focus on the fate of the VP40 matrix. To this end, I specifically aimed to

a) structurally characterize the VP40 matrix in virus-like particles (VLPs) and EBOV in vitro at neutral pH and in endosome-mimicking environments by cryo-ET
b) determine the role of acidic pH on virus morphology and virus entry by cryo-ET, light microscopy and virological assays
c) structurally characterize Ebola VLPs and EBOVs entering host cells by in situ cryo-ET

Inspired by the structural data, I further investigated

d) the presence of actin in VLPs
e) the interaction of the endosomal EBOV receptor NPC1 reconstituted in liposomes with GPs protruding from VLP surfaces
f) the global organization of the VP40 matrix in Marburg VLPs

"It is very easy to answer many of these fundamental biological questions; you just *look* at the thing!"

Richard P. Feynman (Feynman, 1960)

2 Results

2.1 Structural characterization of Ebola VLPs and virions at endosomal pH

Structural characterization of Ebola VLPs

To investigate endosomal EBOV uncoating during virus entry into host cells, I first structurally characterized virus particles in endosome-mimicking environments in vitro. Since EBOVs are BSL4 pathogens, their handling outside BSL4 facilities requires chemical fixation, which damages the particles' ultrastructure and impairs structural characterization. Therefore, I primarily used Ebola virus-like particles (VLPs), which closely resemble EBOVs (Noda et al., 2002; Bharat et al., 2012) but lack the infectious genome. To characterize the VLP morphology and protein composition by cryo-ET, I prepared VLPs by overexpressing the EBOV structural proteins VP40, GP, NP, VP24 and VP35 in HEK 293T cells. After purification of VLPs released into the cell culture media, filamentous VLPs were analysed by cryo-ET. All VLPs were enveloped and contained GPs protruding from the VLP surface (Fig. 10 a-f). The inner monolayer of the VLP envelope was lined by regular VP40 densities clearly discernible as an additional profile adjacent to the membrane from transverse cross-sections and as striations when viewed close to the VLP surface (Fig. 10 b, c, g). The nucleocapsids were poorly visible and were mostly loosely coiled (further discussed in Fig. 31-35).

To assess the morphology of VLPs in endosome-mimicking environments, I then incubated VLPs at pH 4.5 in vitro prior to performing cryo-ET. Strikingly, the VLPs retained their overall filamentous morphology, but no longer displayed distinct regular VP40 densities (Fig. 10 d-f, h). The VP40 matrix appeared detached from the membrane as particularly apparent from the empty space adjacent to the membrane (Fig. 10 e, white arrow), and disordered protein densities crowded the VLPs' lumina. To assess the presence or absence of the VP40 matrix, respectively, I determined line density profiles adjacent to the inner membrane monolayer (Fig. 10 g-i). VLPs subjected to pH 7.4 displayed regular VP40 densities with a spacing of 5-6 nm, which reflects the pitch of the VP40 matrix. In contrast, line density profiles in VLPs subjected to pH 4.5 revealed only background pixel densities. Despite having no effect on the overall filamentous shape of the particles, the absence of the VP40 matrix in VLPs subjected to pH 4.5 coincided with a more variable particle diameter as measured from membrane to membrane with a larger mean diameter of 116 nm (SD=54 nm, n=5) compared to 68 nm (SD= 9 nm, n=12) at pH 7.4 (Fig. 10 j).
To assess whether the VP40 phenotype is dependent on the presence of other viral proteins, I then prepared VLPs composed of VP40 alone and analysed them by cryo-ET. VP40-VLPs subjected to pH 7.4 displayed a uniform diameter and regular VP40 striations when viewed from near-to-surface tomographic slices (Fig. 10 k). However, similar to VLPs composed of all structural proteins, VP40-VLPs subjected to pH 4.5 did not contain ordered VP40 densities. This phenotype, as defined primarily by the presence or absence of an ordered VP40 matrix, was also observed for VLPs composed of VP40 and GP and quantified for all VLP compositions analysed by cryo-ET (Fig. 10 l). Accordingly, VLPs imaged at pH 4.5 primarily displayed

disassembled VP40 matrices ("disassembled"), while in some VLPs the VP40 matrix was partially attached ("intermediate") and few particles still displayed fully assembled VP40 matrices ("assembled").

Taken together, these data indicate that the integrity of the VP40 matrix in VLPs is sensitive to pH, irrespective of the protein composition of the viral particles. This suggests that low pH alone induces VP40 detachment from the viral membrane and disrupts VP40-lipid interactions.

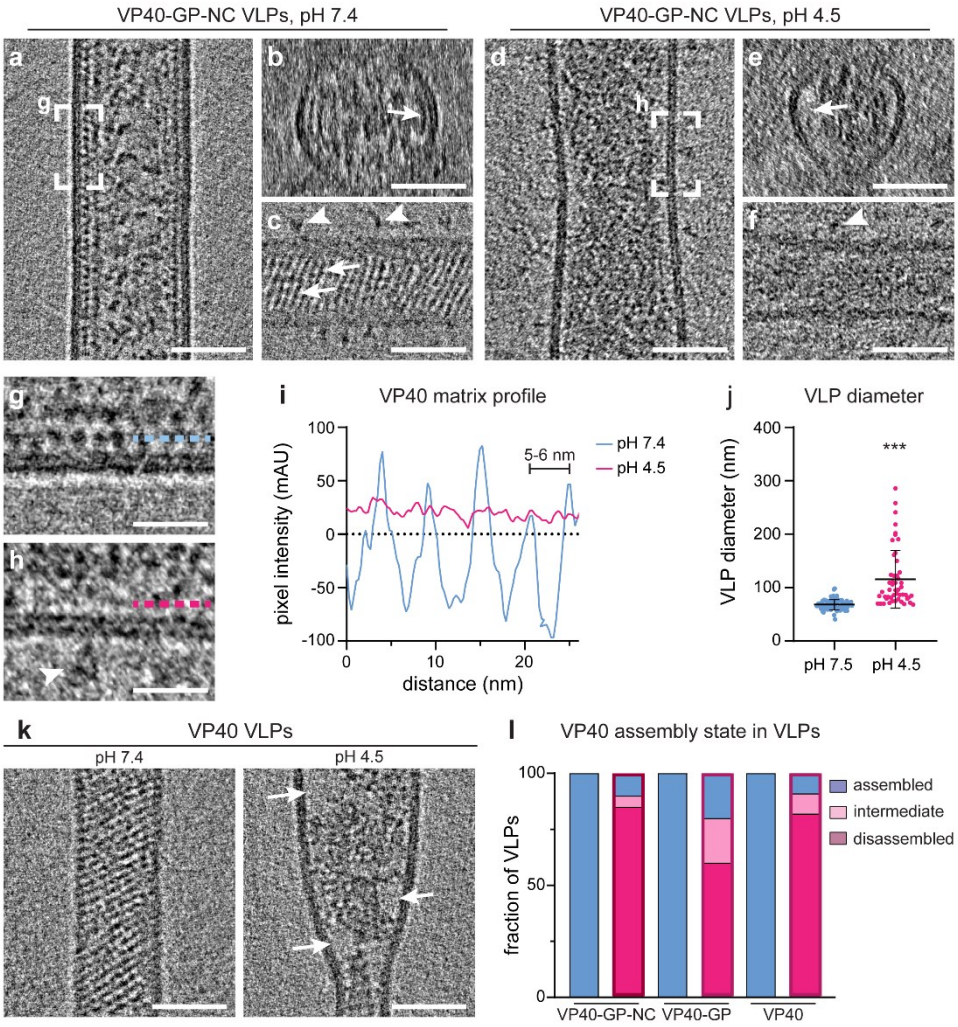

Figure 10: cryo-ET of Ebola VLPs at neutral and endosomal pH. (a) Slices through a tomogram showing the cross-section of a filamentous Ebola VLP composed of GP, VP40, and the nucleocapsid proteins NP, VP24 and VP35 at pH 7.4. **(b)** Transverse cross-section of the VLP shown in (a) displaying densities for the lipid bilayer surrounding the VLP and an additional profile of the VP40 matrix (white arrow) lining the inner membrane monolayer. **(c)** Near-to-surface tomographic slices of the tomogram shown in (a) displaying regular striations of the VP40 matrix spanning the width of the particle (white arrows). **(d)** Slices through a tomogram showing the cross-section of a filamentous VLP composed of GP, VP40, and the nucleocapsid proteins NP, VP24 and VP35 at pH 4.5. **(e)** Transverse cross-section of the VLP shown in (d) showing the densities for the lipid bilayer surrounding the VLP and disordered protein densities crowding the VLP lumen. The protein densities are detached from the membrane as apparent from the gap adjacent to the membrane (white arrow). **(f)** Near-to-surface tomographic slices of the tomogram shown in (d) showing the VLP membrane but lacking regular VP40 striations. **(g)** Area highlighted in (a) showing a magnified view of the lipid envelope of the VLP at pH 7.4 and regular densities adjacent to the inner membrane monolayer. **(h)** Area highlighted in (d) showing a magnified view of the lipid envelope of the VLP at pH 4.5. The space adjacent to the inner membrane monolayer is devoid of regular protein densities. **(i)** Line density profiles determined adjacent to the inner membrane monolayers of the VLPs shown in (g) and (h) showing the regular pitch of 5-6 nm of the VP40 matrix at pH 7.4 (blue line) and background densities at pH 4.5 (magenta line), respectively. **(j)** Quantification of the VLP diameter as measured from membrane to membrane of VLPs composed of GP, VP40, and the nucleocapsid proteins NP, VP24 and VP35. VLPs were imaged at pH 7.4 (mean diameter= 68 nm, SD= 9 nm, n=12 (90 measurements)) and at pH 4.5 (mean diameter= 116 nm, SD=54 nm, n=5 (50 measurements)). To account for heterogeneity in VLP diameter, each VLP was measured at approximately 8 random positions. Statistical significance was estimated using a two-tailed Student's t-test, *** $p<0.0001$. SD is standard deviation. **(k)** Slices through tomograms showing cross-sections of filamentous VLPs composed of VP40, incubated at pH 7.4 and pH 4.5 as indicated. **(l)** Quantification of the

assembly state of the VP40 matrix as assessed by cryo-ET. VLPs composed of GP, VP40, and the nucleocapsid proteins NP, VP24 and VP35 (n= 40 at pH 7.4 and n= 22 at pH 4.5); or GP and VP40 (n= 37 at pH 7.4 and n= 18 at pH 4.5); or VP40 alone (n= 22 at pH 7.4 and n= 8 at pH 4.5) were analysed after incubation at pH 7.4 and pH 4.5 (bars with magenta frame). VP40 matrices were either fully assembled (blue), partially attached to the VLP membrane (intermediate, pink) or disassembled (magenta). Scale bars: 50 nm (a-f, k), 20 nm (g,h).

Structural characterization of Ebola virions

Ebola VLPs closely resemble EBOV in terms of overall morphology, distribution of proteins and structure of the VP40 matrix. However, they lack the genome, which may contribute to the stability of the nucleocapsid that spans the entire length of the virions but is poorly visible and mostly loosely assembled in VLP preparations (Fig. 10 a) (further discussed in Fig. 31-35). Hence, I next aimed to verify the low pH phenotype observed in VLPs in infectious EBOVs. To this end, I collaborated with Thomas Hoenen (FLI, Greifswald- Insel Riems), who produced and purified EBOVs in BSL4 containment. He subjected the purified virions in BSL4 to buffers calibrated to pH 7.4 and pH 4.5, and chemically fixed the samples for 48 h using 4% paraformaldehyde and 0.1% glutaraldehyde following standard operating procedures. I then performed cryo-ET on the chemically fixed EBOVs and characterized their morphology as before. At neutral pH, EBOVs were characteristically filamentous and contained clearly visible nucleocapsids spanning the entire length of the particles (Fig. 11 a, n= 14). As for the VLPs (Fig. 10 a-c, g), the VP40 matrix was clearly apparent from both cross-sections and near-to-surface tomographic slices as an additional profile lining the inner membrane monolayer and regular striations, respectively (Fig. 11 b-d). In contrast to the VLPs, however, EBOVs subjected to low pH structurally resembled EBOV at neutral pH and did not show a striking phenotypic change (Fig. 11 e). The nucleocapsids appeared unaltered and the VP40 matrix did not seem detached from the membrane. When viewed close to the surface, however, regular striations were not detectable but disordered protein densities spanned the width of the particles (Fig. 11 f). Accordingly, when determining line density profiles close to the EBOV surface, the profile of the VP40 matrix was clearly detectable in samples incubated at pH 7.4 but was lacking in samples incubated at pH 4.5 (Fig. 11 g).

Chemical fixation cross-links neighbouring proteins to each other and nearby membrane lipids and thus leads to structural aberrations that impede structural characterization. To assess whether the low pH phenotype is indeed less pronounced in the context of authentic EBOVs, or is masked by the chemical fixation, I produced Ebola VLPs and subjected them to the same low pH-treatment followed by chemical fixation as used for the EBOVs. Similar to EBOVs, chemically fixed VLPs at both pH levels appeared dense with luminal proteins seemingly "glued" to the VLP membrane (Fig. 11 h-k). The typical striations of the VP40 matrix were visible in the sample incubated at pH 7.4 (Fig. 11 j) but were not unambiguously discernible in VLPs subjected to pH 4.5 (Fig. 11 k). As for the EBOVs, line density profiles determined close to the membrane revealed the regular spacing between neighbouring VP40 proteins at pH 7.4, and background pixel densities at pH 4.5. While chemical fixation did not influence the pitch of the VP40 matrix, i.e. the distance between the striations, at pH 7.4 (Fig. 11 m), it rendered the analysis of the low pH phenotype more difficult. Taken together, the VP40 matrix appears disassembled both in chemically fixed EBOVs and VLPs, while remaining attached to the particles' membrane presumably as a result from

chemical cross-linking. Although the structural details cannot be resolved due the chemical fixation, the nucleocapsid retained its overall condensed, cylindrical shape at low pH.

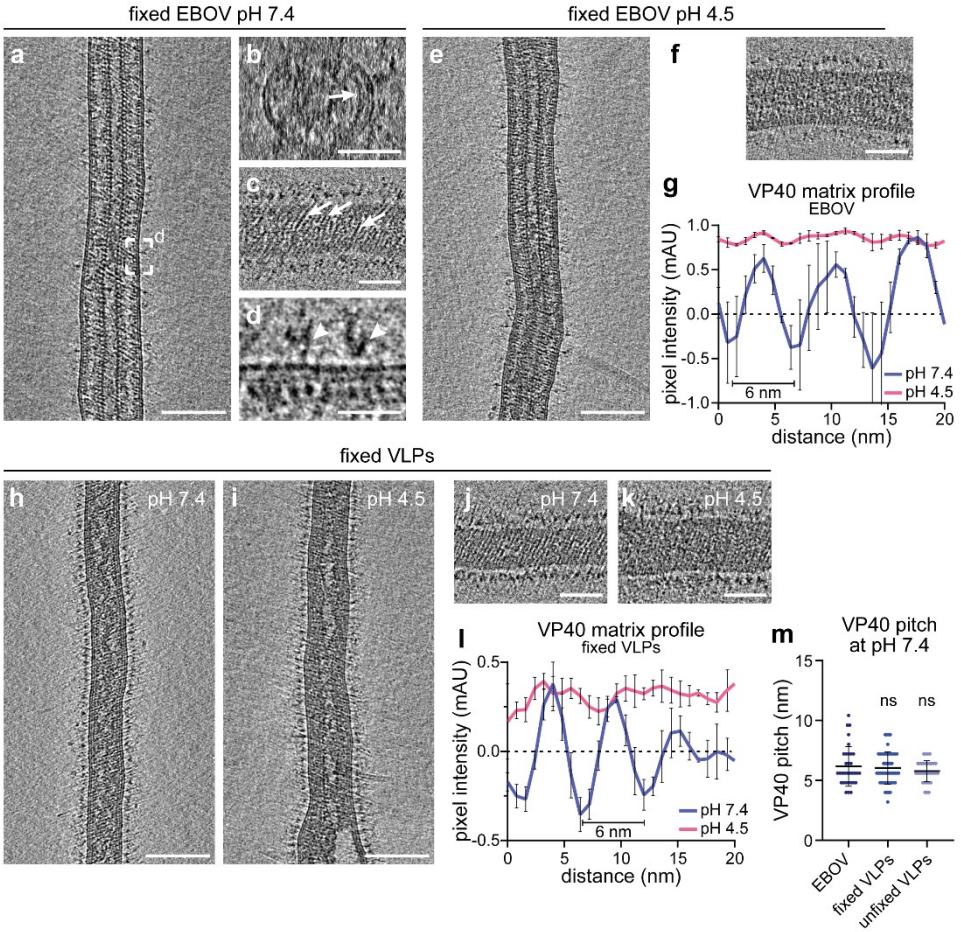

Figure 11: Structural characterization of chemically fixed EBOVs in comparison with chemically fixed Ebola VLPs. **(a-d)** Slices through a tomogram showing cross-sections of a filamentous EBOV at pH 7.4 after chemical fixation for biosafety reasons with 4% formaldehyde and 0.1% glutaraldehyde. **(b)** Transverse cross-section of the EBOV shown in (a) displaying densities of the VP40 matrix adjacent to the inner membrane monolayer of the viral envelope (white arrow). **(c)** Near-to-surface tomographic slices showing VP40 striations from the top view (white arrows). **(d)** Area shown in (a) showing the outer membrane monolayer studded with GPs (white arrowheads), the inner membrane monolayer, and regularly spaced VP40 densities. **(e)** Slices through a tomogram of a filamentous EBOV at pH 4.5 after chemical fixation. **(f)** Near-to-surface tomographic slices of the EBOV shown in (e). **(g)** Plot of line density profiles determined adjacent to the viral inner membrane monolayer to demonstrate the pitch of the VP40 matrix at pH 7.4. Line density profiles were determined in VLPs subjected to pH 7.4 and pH 4.5 (each sample: n= 3). Mean pixel densities and the standard error of the mean (SED) are plotted. **(h-i)** Slices of tomograms showing cross-sections of filamentous Ebola VLPs composed of VP40 and GP after chemical fixation according to the protocol applied to all EBOV samples. VLPs were incubated at pH 7.4 and pH 4.5 prior to chemical fixation as indicated. **(j-k)** Near-to-surface tomographic slices of the VLPs shown in (h) and (i), respectively. **(l)** Plot of line density profiles determined adjacent to the VLPs' inner membrane monolayer to demonstrate the pitch of the VP40 matrix. Line density profiles were determined in VLPs subjected to pH 7.4 and pH 4.5 (each sample: n= 3). Mean pixel densities and the standard error of the mean (SED) are plotted. **(m)** Pitch of the VP40 matrix determined for chemically fixed EBOV Ebola VLPs shown in comparison to the VP40 pitch determined from tomograms acquired from unfixed Ebola VLPs (EBOV: mean VP40 pitch= 6.2 nm, SD= 1.7 nm, n= 33; chemically fixed VLPs: mean VP40 pitch= 6 nm, SD= 1.3 nm, n= 52; unfixed VLPs: mean VP40 pitch= 5.8 nm, SD= 0.9 nm n= 34). Statistical significance between the means of the different samples was estimated using a two-tailed Student's t-test, ns= not significant. SD is standard deviation. Scale bars: (a, e, h, i): 100 nm, (b): 50 nm, (c, f, g, k): 50 nm, (d): 20 nm.

Characterization of VLP morphology at different pH

As visualized by cryo-ET, the VP40 matrix in Ebola VLPs and viruses disassembled upon exposure of the particles to low pH. In VLPs that were not subjected to chemical fixation, the disassembly of the VP40 matrix coincided with its detachment from the membrane (Fig. 10 d-e) and the concomitant release of steric restraints on the VLP envelope manifested in a more variable particle diameter (Fig 10 j). Therefore, we wondered whether VP40 matrix detachment from the membrane results in a global morphological change from filamentous to spherical particles. Since EBOVs are pleomorphic and comprise filamentous and spherical particles already at neutral pH (Feldmann and Klenk, 1996), I quantified the particle shape of Ebola VLPs subjected to both pH 7.4 and pH 4.5 after verifying the presence of the VP40 matrix in spherical VLPs. As shown in Figure 3, the envelope of spherical Ebola VLPs at pH 7.4 was decorated at the luminal side with VP40 proteins, that formed a flexible network spanning the entire surface. The VP40 proteins were clearly visible as distinct protein densities and the VP40 pitch was similar to the VP40 pitch observed in filamentous VLPs (Fig. 12 b, c). Similar to the phenotype observed in filamentous VLPs, the membranes of spherical VLPs subjected to pH 4.5 were devoid of protein densities at the luminal side and contained disordered protein densities that were detached from the membrane and accumulating at the particles' cores (Fig. 12 d, e, white arrows). Accordingly, only background densities were detected when measuring line density profiles proximal to the VLP inner membrane monolayer (Fig. 12 f). After confirming the presence of VP40 matrices in spherical VLPs, I quantified the particle shape from electron microscopy maps acquired at medium magnification (exemplarily shown at pH 7.4 for Ebola VLPs and EBOV in Fig. 12 g). At pH 7.4, the VLPs were predominantly filamentous, while at pH 4.5, they predominantly adopted spherical shapes (Fig. 12 i). However, the quantification was impeded by two factors: first, many cryo-EM maps were too crowded to unambiguously differentiate between overlapping VLPs. Second, even though the overall particle shapes could clearly be distinguished at the low magnification, the resolution was not sufficient to verify the presence of the VP40 matrix in these particles (as shown in tomograms at high magnification, Fig. 12 a-f). Hence, VLPs could not be differentiated from cellular debris remaining after VLP purification.

To automatically quantify VLP morphology of large datasets while confirming that quantified particles indeed contain VP40, I then decided to change to a fluorescence-based approach using Ebola VLPs containing GFP-tagged VP40. Since Ebola VLPs are longer than 1000 nm, the resolution limit of confocal light microscopy is sufficient to distinguish the shapes and the fluorescent tag enables exclusive visualization of VP40-containing particles. After acquiring overview images of VLPs expressing GFP-VP40 in excess over wild-type VP40 to avoid disrupting the architecture of the VP40 matrix (further verified in Fig. 17), I filtered and masked the data to allow automated segmentation (Fig. 12 j-l, Materials and Methods). The aspect ratio of the segmented particles was then measured using FiJi as the quotient from the long and short axes, with an aspect ratio of 1 defining a spherical shape. Remarkably, there was no significant difference in overall morphology of VLPs between either pH level (VLPs at pH 7.4: mean aspect ratio= 1.5 ± 0.8 (n=1701); VLPs at pH 4.5: mean aspect ratio= 1.5 ± 0.9 (n= 1087)).

These results indicate that, while the diameter of filamentous VLPs is more variable in the absence of an assembled VP40 matrix (Fig. 10 j), the overall EBOV particle shape is not affected by the disassembly of the VP40 matrix, at least in the timespan of low pH treatment performed in this experiment.

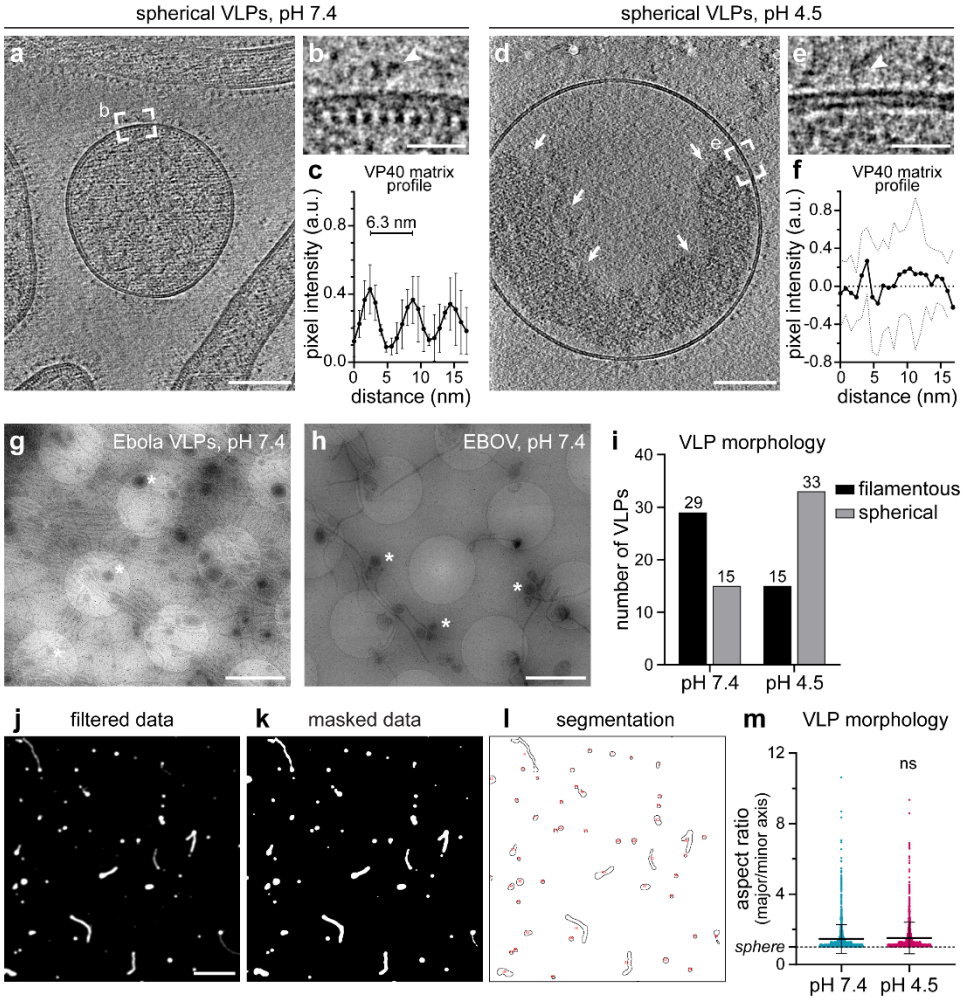

Figure 12: Quantification of the effect of acidic pH on Ebola VLP morphology. (a) Cross-sectional slices through a tomogram of a spherical Ebola VLP composed of GP, VP40 and the nucleocapsid proteins NP, VP24 and VP35 at pH 7.4. **(b)** Area highlighted in (a) showing a magnified view of the VLP membrane studded with GP (white arrowhead) and VP40 densities lining the inner membrane monolayer. **(c)** Line density profiles determined adjacent to the inner membrane monolayer using FiJiFiJi. Mean pixel values densities and standard deviations are plotted against distance measured at six independent positions along the membrane. The distance between neighbouring VP40 molecules was measured as distance between global maxima of the plotted profile (mean distance= 6.3 nm, SD= 1.8 nm, n= 27). SD is standard deviation. **(d)** Cross-sectional slices through a tomogram of a spherical Ebola VLP composed of GP, VP40 and the nucleocapsid proteins NP, VP24 and VP35 at pH 4.5. Disordered protein densities are crowding the VLP lumen (white arrows). **(e)** Area highlighted in (d) showing a magnified view of the VLP membrane studded with GP (white arrowhead). **(f)** Line density profiles determined adjacent to the inner membrane monolayer using FiJi. Mean pixel values densities and standard deviations are plotted against distance measured at five independent positions along the membrane. **(g-h)** cryo-EM map at medium magnification showing an overview of Ebola VLPs and EBOVs for comparison at pH 7.4. Spherical particles are indicated exemplarily with white asterisks. **(i)** Quantification of Ebola VLP morphology from cryo-EM maps shown exemplarily in (g) of VLPs incubated at pH 7.4 and pH 4.5. The number of particles analysed are indicated above each bar in the plot. **(j)** Fluorescence light microscopy image of Ebola VLPs fluorescently tagged with GFP to enable automated quantification of VLP morphology at different pH. **(k, l)** Image shown in (j) after masking the particles and automated segmentation. **(m)** Quantification of VLP morphology at pH 7.4 and pH 4.5 as measured by the aspect ratio of the particles from fluorescence light microscopy data. Particles with an aspect ratio of 1 are considered spheres, aspect ratios above 1 denote filamentous particles. Individual measurements are plotted with the mean aspect ratio and SD indicated (VLPs at pH 7.4: mean aspect ratio= 1.5, SD= 0.8, n= 1701; VLPs at pH 4.5: mean aspect ratio= 1.5, SD= 0.9, n= 1087). Scale bars: (a), (d)= 100 nm, (b), (e)= 20 nm, (g), (h)= 2 µm, (j)= 10 µm.

2.2 Structure of the VP40 matrix

Structure of the VP40 matrix in Ebola VLPs

The cryo-ET data indicate that VP40-lipid interactions in virus particles subjected to acidic environments are disrupted by low pH. To understand how VP40 interacts with the membrane and which protein domains are involved in membrane binding, I investigated the structure of the VP40 matrix in VLPs by subtomogram averaging. Several high-resolution structures of VP40 are available, including the dimeric structure of VP40 in solution and a hexameric structure, which was long postulated as the building block of the VP40 matrix in EBOVs (Bornholdt et al., 2013a). However, when I started this project, none of the structures was solved in the native context of virus particles and VP40-lipid interactions had been probed exclusively by mutagenesis studies and molecular dynamics simulations of the different oligomers (Bornholdt et al., 2013b; Del Vecchio et al., 2018; Nguyen et al., 2005; Scianimanico et al., 2000). Hence, I aimed to obtain a subtomogram average of the VP40 matrix in VLPs to investigate the VP40 oligomeric state and interaction interface with lipids in the inner viral membrane monolayer. To this end, I produced Ebola VLPs composed of GP and VP40 and a large dataset of tomograms was acquired at EMBL Heidelberg by Wim Hagen. Supervised by Petr Chlanda, I then extracted approximately 7800 subtomograms along the membrane of filamentous VLPs and applied subtomogram averaging (Fig. 13). The resulting average revealed that the VP40 matrix forms a quasi-helical scaffold underneath the VLP membrane and is composed of linearly arranged VP40 dimers that are closely connected to the inner membrane monolayer via their CTDs. The scaffold has a spacing of 5 nm and is tilted by 25° with respect to the VLP membrane (Fig. 13 c); however, the resolution was too low to identify secondary structures. To obtain more structural details, I fitted the available X-ray structure of the VP40 dimer into the average, which aligned well and further highlights the close contact of CTDs and the VLP lipids (Fig. 13 d). Importantly, the structure of the VP40 matrix in Ebola and Marburg VLPs and viruses was recently solved by subtomogram averaging (Wan et al., 2020) and is in agreement with the data presented here. Both the published and our subtomogram average show a direct connection between VP40 and membrane lipids, which is not covered by the crystal structure (Fig. 13 d, arrow). Since the VP40 dimer structure was solved in solution and is missing flexible C-terminal loops containing the basic patch of lysine residues that engages in electrostatic interactions, the VP40 dimers within the matrix likely conformationally re-arrange in contact with membrane lipids and neighbouring VP40 dimers. This is further discussed in Figure 6 and our preprint (Winter et al., 2022), for which we collaborated with Fabio Lolicato (Nickel lab, BZH Heidelberg), who ran MD simulations of the VP40 dimer and a synthetic membrane.

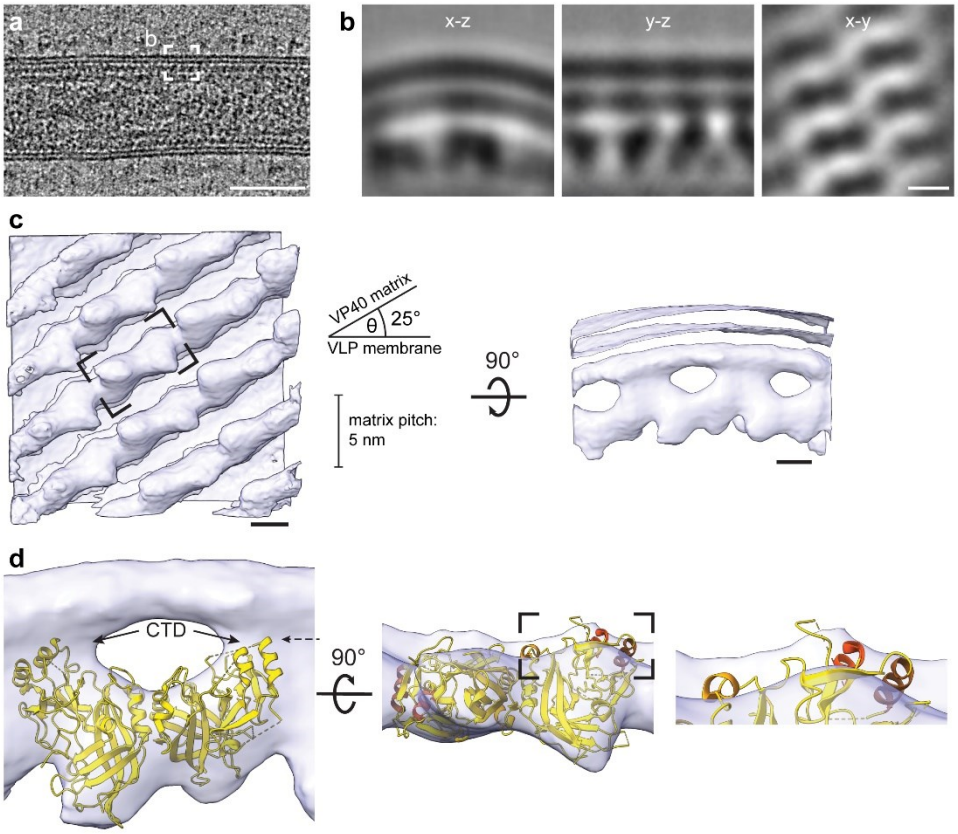

Figure 13: Structure of the VP40 matrix in Ebola VLPs. (a) Cross-sectional slices through a tomogram of a filamentous Ebola VLP composed of VP40 and GP. Subtomograms were picked along the VLP membrane as exemplarily indicated by the white rectangle and subjected to subtomogram averaging. **(b)** Subtomogram average of the VP40 densities lining the inner membrane monolayer of the Ebola VLPs, including all views along the three axes. **(c)** Surface representation of the subtomogram average shown in (b) showing the regular striations of the VP40 matrix from the bottom (X-Y view). A rectangle representing a single VP40 oligomer is indicated by a black dashed rectangle and shown after rotation of the surface by 90°. **(d)** Magnified view of the tilted surface highlighted in (c) overlayed with the crystal structure of the VP40 dimer (pdb: 7jzj). CTDs are indicated by arrows and unoccupied densities in the subtomogram average close to the membrane are indicated by a dotted arrow. Rotation of the overlayed structures by 90° reveals mismatching helical segments protruding from the subtomogram average (orange). Pixel spacing: 0.1701 nm, scale bars: 2.5 nm.

Despite several attempts to improve the resolution of the subtomogram average, the resolution did not exceed 30 nm. This likely results from considerable conformational flexibility of the VP40 dimers within the matrix, allowing the particles to adopt different shapes without breaking, including branched, U-shaped and spherical forms (Ellis et al., 1978; Feldmann and Klenk, 1996). This flexibility is exemplarily highlighted by 3D segmentation of the VP40 matrix within a bent Ebola VLP shown in Figure 14. To improve the contrast and reduce the missing wedge of information, which greatly facilitates 3D segmentation, tomograms were acquired with the help of Petr Chlanda using Volta-phase plate dual-axis tomography. At straight segments of Ebola VLPs, VP40 formed a quasi-helical scaffold characterized by regularly spaced striations (Fig. 13 c). However, when the VLPs adopted irregular shapes, the matrix displayed gaps and discontinuous VP40 stretches (Fig. 14 b, c), a finding we also published here (Winter and Chlanda, 2021).

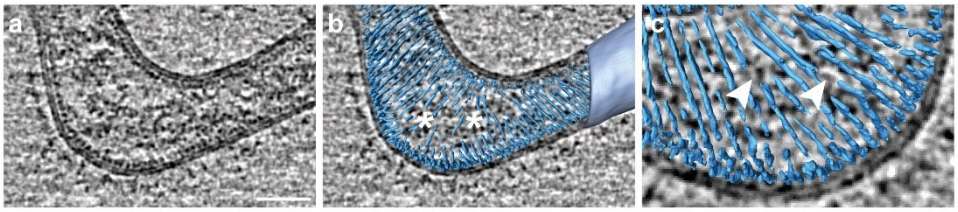

Figure 14: Conformational modularity of the VP40 matrix in Ebola VLPs. (a) Slices through a tomogram of a filamentous Ebola VLP composed of GP, VP40 and the nucleocapsid proteins NP, VP35 and VP24. The tomogram was acquired using dual-axis Volta phase plate cryo-ET to facilitate 3D segmentation of the VP40 matrix and has been published here (Winter and Chlanda, 2021a). **(b-c)** 3D segmentation of the VP40 matrix (blue) and parts of the Ebola VLP membrane (light blue) of the tomogram shown in (a). Gaps in the modular VP40 matrix are highlighted by white asterisks and discontinuous VP40 stretches by white arrowheads. Scale bar in (a): 50 nm.

Conformational modularity of the VP40 matrix

The subtomogram average presented here and the recently published structure of the VP40 matrix (Wan et al., 2020) do not reveal sufficient structural details to map the lipid interactions to specific amino acids or structural domains within the C-termini of the VP40 dimer. Hence, we collaborated with Fabio Lolicato (Nickel lab, BZH Heidelberg), who used the dimeric VP40 structure solved to high resolution by X-ray crystallography (Bornholdt et al., 2013b; Wan et al., 2020) and modelled the missing C-terminal residues located in flexible loops onto the structure. He then emulated a simplified membrane composed of 30% phosphatidylcholine, 40% cholesterol and 30% phosphatidylserine, and ran all-atom molecular dynamics (MD) simulations for a cumulative time of 10 microseconds. Initially oriented randomly towards the membrane, interactions with the membrane were established via one of the CTDs, before the second CTD was pulled towards the membrane (Fig. 15 a). To assess whether the conformation of the VP40 dimer changes upon lipid-binding, I aligned the VP40 dimer from the final state of the MD simulation with the published crystal structure (Fig. 15 b-c). While the core of the monomer aligned well (highlighted in Fig. 15 d), C-terminal helices were misaligned, presumably as a result from lipid interactions with the modelled loop (Fig. 15 c, green) and an additional rotation along the N-terminal dimerization domain upon lipid binding. Interestingly, when fitting the VP40 structure from the final state of the MD simulation into the subtomogram average (Fig. 15 d-f), no secondary structures apart from unstructured loops were protruding from the average (Fig. 15 f). This indicates that lipid-induced conformational changes of the VP40 dimer reflected in the MD simulation are in agreement with our structural data obtained from averaging the VP40 matrix. Furthermore, the modelled unstructured loop at the CTDs protruded into the inner membrane monolayer, confirming electrostatic interactions between lysine residues K224, K225, K274, and K275 and phosphatidylserines, which have previously been experimentally determined (Bornholdt et al., 2013b).

Finally, the lipid composition used here for the simulation is simplified and contains high levels of phosphatidylserine to mimic the net negative charge of the inner membrane monolayer of the plasma membrane, where VP40 dimers assemble to form budding virions during an infection (Panchal et al., 2003; Stahelin, 2014). To further refine the protein-lipid interactions, we determined the lipid profile of the Ebola VLP envelope in collaboration with Christian Lüchtenborg (Brügger lab, BZH Heidelberg) (Fig. 15 g). The

membrane of purified VLPs composed of EBOV GP, VP40 and the nucleocapsid proteins NP, VP35 and VP24 were enriched in cholesterol, sphingomyelin, phosphatidylcholine, and phosphatidylserine (39%, 25%, 9% and 9%, respectively). This reflects the lipid composition of the plasma membrane (Lingwood and Simons, 2010; Risselada, 2019) and corresponds well to the budding site of Ebola VLPs and viruses. Considering the asymmetry of the plasma membrane and by extension the VLP membrane, the phosphatidylserine concentration is even higher in the inner membrane monolayer and is responsible for its net negative charge.

Taken together, the lipidomics data indicate that phosphatidylserine is indeed enriched in the VLP membrane and thus majorly contributes to the electrostatic interactions with cationic C-terminal amino acids of VP40. To which extend other negatively charged lipids such as phosphatidylinositol phosphate contribute the VP40-binding remains to be elucidated.

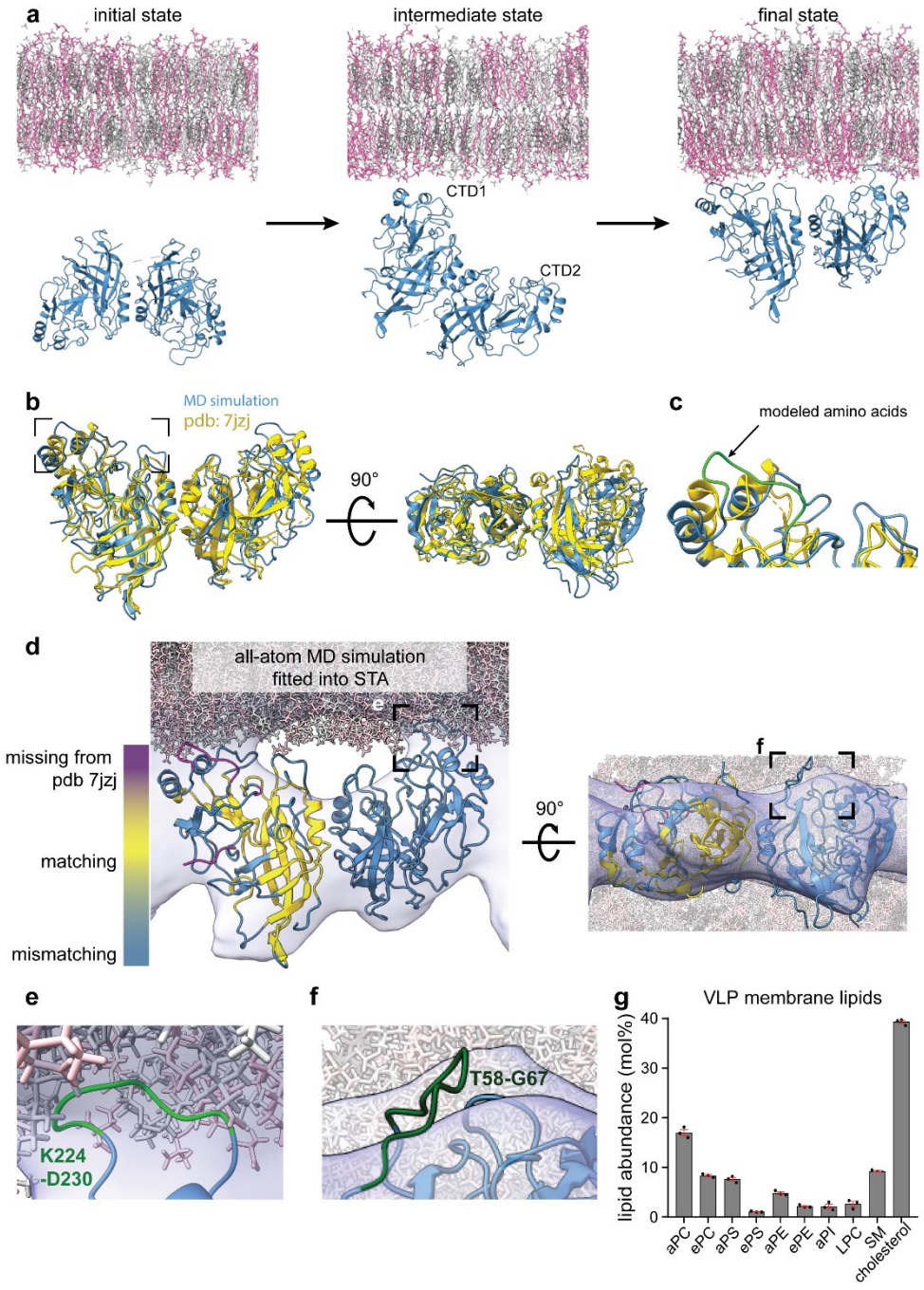

Figure 15: Molecular dynamics (MD) simulations of the VP40 dimer interacting with membrane lipids. The MD simulation was performed by Fabio Lolicato (Nickl lab, BZH Heidelberg) using the VP40 dimer crystal structure (pdb: 7jzj) and a simplified membrane composed of 30% phosphatidylcholine, 40% cholesterol and 30% phosphatidylserine. Missing unstructured regions from the VP40 dimer were modelled using GalxyFill software (Coutsias et al., 2004) within the CHARMM-GUI web server (Jo et al., 2008) . **(a)** Different frames of the MD simulation capturing the three main states of VP40-lipid binding: at the beginning of the MD simulation, VP40 is randomly oriented towards the membrane (initial state), before it starts interacting with lipids in the inner membrane monolayer via one CTD (CTD1) (intermediate state), before the second CTD (CTD2) is pulled towards the membrane (final state). **(b)** Alignment of the VP40 dimer from the final MD simulation state (blue) with the published crystal structure (pdb: 7jzj, yellow). The aligned structures are shown from the front and rotated by 90° to highlight mismatching secondary structures. **(c)** Area highlighted in (b) showing a flexible loop missing from the crystal structure. The adjacent alpha helices are shifted and do not align well. **(d)** Final state of the MD simulation shown in (a) fitted into the subtomogram average (Fig. 13). The colour code of the VP40 dimer structure reflects the alignment with the VP40 dimer crystal structure (pdb: 7jzj). Matching secondary structures are shown in yellow, while mismatching regions are shown in blue and unstructured regions missing from the crystal structure are shown in purple. **(e)** Area highlighted in (d) showing the flexible loop from K224-D230 missing from the crystal structure and extending into the inner membrane monolayer. **(f)** Area highlighted in (d) showing a flexible loop protruding from the subtomogram average. **(g)** Lipid profile of highly abundant lipids in the VLP membrane (n=3). Lipid abbreviations:

phosphatidylcholine (PC), phosphatidylserine (PS), phosphatidylethanolamine (PE), phosphatidylinositol (PI), lyso-phosphatidylcholine (LPC), sphingomyelin (SM). Prefix "a" indicates acyl-linked glycerophospholipids, prefix "e" indicates ether-linked (plasmanyl) or the presence of one odd and one even chain fatty acyl.

Structure of the VP40 matrix in Marburg VLPs

Since VP40 is solely responsible for the filamentous shape of EBOVs and related filoviruses and is indispensable for particle formation from infected cells, I was then wondering whether the structure and lipid interactions of the VP40 matrix are conserved among the filovirus family. The first members of the *Filoviridae* family were Ebola and Marburg viruses (MARVs) (Kiley et al., 1982). MARVs closely resemble EBOVs in overall morphology, but differ in length and distribution of the pleiomorphic virus shapes (Ellis et al., 1979; Geisbert and Jahrling, 1995). Despite a highly similar topology of the two VP40 proteins, MARV VP40 (mVP40) and EBOV VP40 (eVP40) share 42% sequence identity in their N-terminal domains (NTD) and only 16% sequence identity in their CTDs (Wan et al., 2020). Since the CTDs of eVP40 are strongly interacting with membrane lipids and likely define the conformational modularity of the matrix, I expected to detect differences in the organization of mVP40 within the mVP40 matrix. To structurally investigate the mVP40 matrix in VLPs, I expressed MARV GP and mVP40 in HEK 293T cells and analysed the VLPs released into the cell culture media by cryo-ET.

As expected, filamentous Marburg VLPs closely resembled Ebola VLPs in overall morphology and structural features, including the protrusion of MARV GP from the VLP membrane, the presence of mVP40 proteins decorating the inner membrane monolayer and actin filaments (Fig. 16 a-f), which I often observed in Ebola VLPs (further discussed in Figure 29-30). However, two differences stood out: first, the actin filaments were more prominently visible adjacent to the mVP40 matrix than in Ebola VLPs, where they were mostly observed from close-to-surface tomographic slices and diagonally spanned the VLP surface (Fig. 30) rather than running parallel to the membrane (Fig. 16 a, c and Fig. 29 c). Second, the mVP40 matrix appeared remarkably different compared to the eVP40 matrix when viewed from the top (Fig. 16 b, e). While still forming a helical scaffold, the helical turns formed doublets as apparent from the close-to-surface tomographic slices and line density profiles determined adjacent to the inner membrane monolayers (Fig 16 g). Accordingly, I obtained two distances from the peaks of the VP40 matrix profile: a doublet and inter-doublet spacing of 4-5 nm and 5-6 nm, respectively (Fig. 16 h). Interestingly, both spacings were narrower in the presence of actin within the VLPs. However, due to the limited dataset, the VP40 matrix was only analysed in one VLP lacking actin and thus requires further analysis. Lastly, the mVP40 matrix was organized perpendicular to the VLP membrane as opposed to the 25° tilt observed in the eVP40 matrix (Fig. 13 c and Fig. 16 i).

The structural differences between the VP40 matrices in Ebola and Marburg VLPs argue for differences in lipid-binding and potentially the overall stability and flexibility of the particles. Ultrastructural details at higher resolution are required to determine mVP40-lipid binding interfaces and assess whether they are similarly sensitive to external pH.

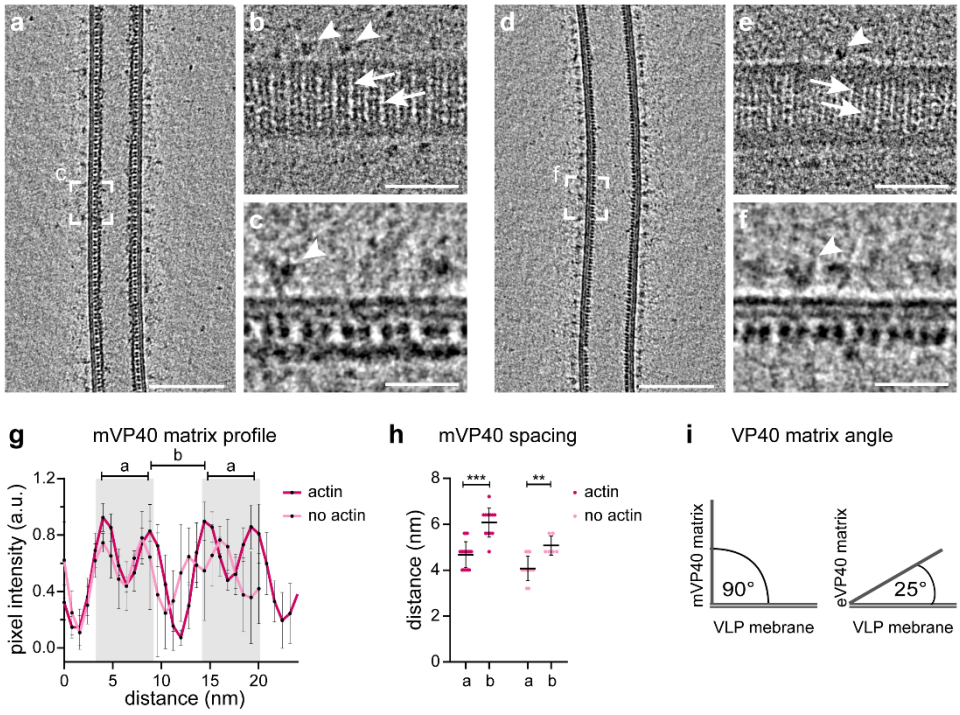

Figure 16: Characterization of the VP40 matrix in Marburg VLPs by cryo-ET. (a-f) Slices through tomograms showing filamentous Marburg VLPs composed of MARV VP40 (mVP40) and MARV GP. **(a)** Cross-sectional tomographic slices showing a filamentous Marburg VLP containing actin filaments lining the mVP40 matrix. **(b)** Near-to-surface tomographic slices of the tomogram shown in (a) highlighting the mVP40 striations underneath the VLP membrane (white arrows). GPs are exemplarily marked with white arrowheads. **(c)** Area highlighted in (a) showing a magnified view of the VLP membrane studded with GPs (white arrowheads), and globular VP40 densities between the inner monolayer leaflet and an actin filament. **(d)** Cross-sectional tomographic slices showing a filamentous Marburg VLP lacking actin filaments. **(e)** Near-to-surface tomographic slices of the tomogram shown in (d) highlighting the mVP40 striations underneath the VLP membrane (white arrows). GPs are exemplarily marked with white arrowheads. **(f)** Area highlighted in (d) showing a magnified view of the VLP membrane studded with GPs (white arrowheads), and globular VP40 densities lining the inner membrane leaflet. **(g)** Line density profiles determined at different positions adjacent to the inner membrane leaflet of the VLPs shown in (a) and (d) (n= 6 for each VLP) spanning four VP40 molecules each. Mean pixel intensities are plotted with the standard deviation (SD) against distance, and resulting profiles reflect the spacing of neighbouring mVP40 molecules. The profiles reveal mVP40 doublets with a spacing "a", which are separated by the inter-doublet spacing "b". **(h)** mVP40 spacing within the mVP40 matrix in Marburg VLPs determined from the line intensity profiles shown in (g). Individual measurements are shown with the mean distance and SD for the VLP containing actin or no actin (mean distance a (actin)= 4.7 nm, SD= 0.6, n= 18; mean distance b (actin)= 6.1 nm, SD= 0.6, n= 12; mean distance a (no actin) = 4.1 nm, SD= 0.5, n= 12; mean distance b (actin)= 5.1 nm, SD= 0.4, n= 6). Statistical significance between the means of the different spacings was estimated using a two-tailed Student's t-test, ** p= 0.001, *** p<0.0001. **(i)** Schematic of the estimation of the pitch of the VP40 matrix in Marburg VLPs in comparison to Ebola VLPs. The pitch is determined as the angle between the VLP membrane and mVP40 matrix or eVP40 matrix, respectively.

2.3 Acidification mechanism across the viral envelope

After structurally characterizing the VP40 matrix and pH-driven changes in its overall architecture, I next addressed the acidification mechanism across the viral membrane. Since the EBOV genome does not encode a known ion channel and, to date, acidification across the EBOV membrane has not been described or hypothesized, I aimed to determine acidification kinetics and measure the intraluminal pH of VLPs.

To this end, I cloned the pH-sensitive GFP variant pHluorin (Miesenböck et al., 1998) N-terminally to VP40 ((pH)VP40) and produced Ebola VLPs composed of EBOV GP, VP40 and (pH)VP40 (hereafter referred to as pHluorin-VLPs). I then analysed their fluorescence properties at different pH, expecting a decrease in fluorescence upon exposure of the VLPs to acidic pH levels and equilibration of the pH between the surrounding buffer and the VLPs' lumina (Fig. 17 a). pHluorin incorporation into VLPs was confirmed by Western blot analysis of purified pHluorin-VLPs using antibodies against VP40 and GFP, the latter of which bind to the structurally highly similar pHluorin fluorophore (Fig. 17 b). Similar to untagged VLPs, pHluorin-VLPs were pleomorphic in shape, including filamentous particles of uniform diameter and remarkable length as verified by both negative stain EM and fluorescence light microscopy (Fig. 17 c, d).

To measure the fluorescence properties of pHluorin-VLPs at different pH levels, I imaged the particles by time-lapse microscopy for 30 min in 15 second intervals (Fig. 17 e). The extent of bleaching during imaging was first assessed by imaging the particles at pH 7.4 (Fig. 17 e, f). I then imaged the particles at pH 7.4 for 2 min before dropping the pH of the surrounding buffer to approximately 4.5 by adding citric acid. The fluorescence intensity immediately decreased and gradually decayed to background fluorescence within several minutes. The slope of the fluorescence intensity curve obtained (Fig. 17 f) is indicative of the membrane permeability of the VLPs and demonstrates that the protons pass a membrane barrier. As a control to compare the fluorescence decrease over time in the absence of a membrane, I then incubated VLPs with the detergent Triton-100 (T-X^{100}) prior to imaging to permeabilize the VLP envelope. As expected, upon decreasing the pH of the surrounding buffer, the pHluorin fluorescence immediately decayed to background values within the 15 seconds imaging interval (Fig. 17 f).

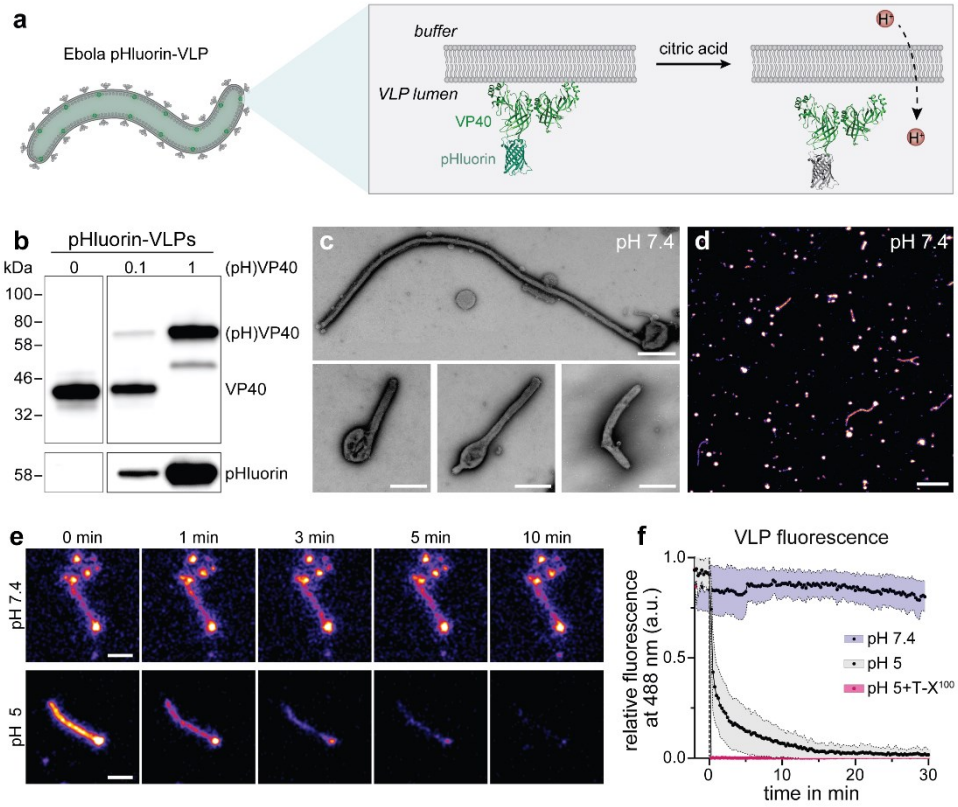

Figure 17: Determination of acidification kinetics of Ebola VLPs by time-lapse microscopy. (a) Schematic of a filamentous Ebola VLP composed of GP, VP40 and VP40 N-terminally tagged with pHluorin ((pH)VP40). At neutral pH, pHluorin exhibits fluorescent properties when excited at 488 nm. When VLPs are exposed to external low pH and protons get translocated across the VLP envelope, pHluorin fluorescence gradually decays in a pH-dependent manner**. (b)** Western blot of cells producing pHluorin-VLPs composed of GP, VP40 and (pH)VP40 in different molar ratios (1:1:0, 1:1:0.1 and 1:0:1). The amount of (pH)VP40 present in the sample is indicated. VP40 and pHluorin are detected with monoclonal antibodies against VP40 and GFP, respectively. **(c)** Negative stain images of filamentous pHluorin-VLPs at pH 7.4**. (d)** Confocal microscopy image of pHluorin-VLPs imaged at pH 7.4. **(e)** Confocal microscopy images of individual pHluorin-VLPs acquired during time-lapse imaging. Images are shown exemplarily 0 min, 1 min, 3 min, 5 min and 10 min after changing the external buffer to pH 7.4 or 4.5, respectively. **(f)** Quantification of the fluorescent signal acquired over the time-course of the experiment. Ebola pHluorin-VLPs were imaged for 30 min in 15 second intervals and the pH of the surrounding buffer was changed to pH 7.4 or 5 (n=42 and n=19, respectively) as indicated with the dotted line. As control, VLPs incubated in triton-100 (T-X100) prior to imaging were subjected to low pH (n=19). Mean fluorescent intensities and standard deviation are plotted. Scale bars: (c)= 500 nm, (e)= 2 µm.

Since Ebola VLPs bud from the plasma membrane, I next determined the acidification kinetics across the plasma membrane for comparison. To this end, I examined HEK 293T cells expressing pHluorin-VP40 and, to measure the effect of an additionally expressed well-described ion channel, the influenza ion channel M2. To enable measuring of several samples in parallel, I opted for an experimental setup using a 96 well plate and fluorescence readout by a plate-reader (Fig. 18 a). After reverse transfection of HEK 293T cells with the respective plasmids, the cells were seeded into fibronectin-coated 96 well plates and incubated overnight. Cells expressing pHluorin-VP40 exhibited bright fluorescence at 488 nm and were washed with buffer calibrated to pH 7.4. The buffer was then either kept at pH 7.4 or exchanged to pH 4.5, and plates were immediately imaged using a plate reader. Similar to VLPs, the fluorescence in cells remained constant when imaged at pH 7.4 but decayed gradually to background fluorescence when the external buffer was calibrated to pH 4.5 (Fig. 18 b). As expected, when expressing influenza M2, the fluorescence decayed more rapidly in a concentration-dependent manner (Fig. 18 c). These results indicate that similar to the VLP

membrane, the plasma membrane itself is permeable to protons already in the absence of exogenously expressed M2.

The fluorescence decay measured above directly correlates to membrane permeability, which can be determined numerically when the proton concentration, i.e. the pH level, on either side of the membrane barrier is known (here: the pH of the surrounding buffer and within the VLPs or cells). Since pHluorin fluorescence is pH-dependent (Miesenböck et al., 1998), I first determined a calibration curve by measuring the fluorescence intensity of pHluorin at different pH levels. To this end, HEK 293T cells were reverse transfected with pHluorin-VP40 and seeded into 96 well plates as before. After overnight incubation, the cells were then incubated in buffers at a range of pH levels from 3.5 to 8 (Fig. 18 a) and imaged with a plate reader after the pH had equilibrated across the cellular plasma membrane, approximately 1 h after buffer exchange. The fluorescence dropped linearly with decreasing pH only in a small range from pH 6 to pH 7.5 and decayed to background fluorescence at a pH below 5.5 (Fig. 18 d). The fluorescence properties of pHluorin at different pH hence need to be taken into account when determining membrane permeabilities.

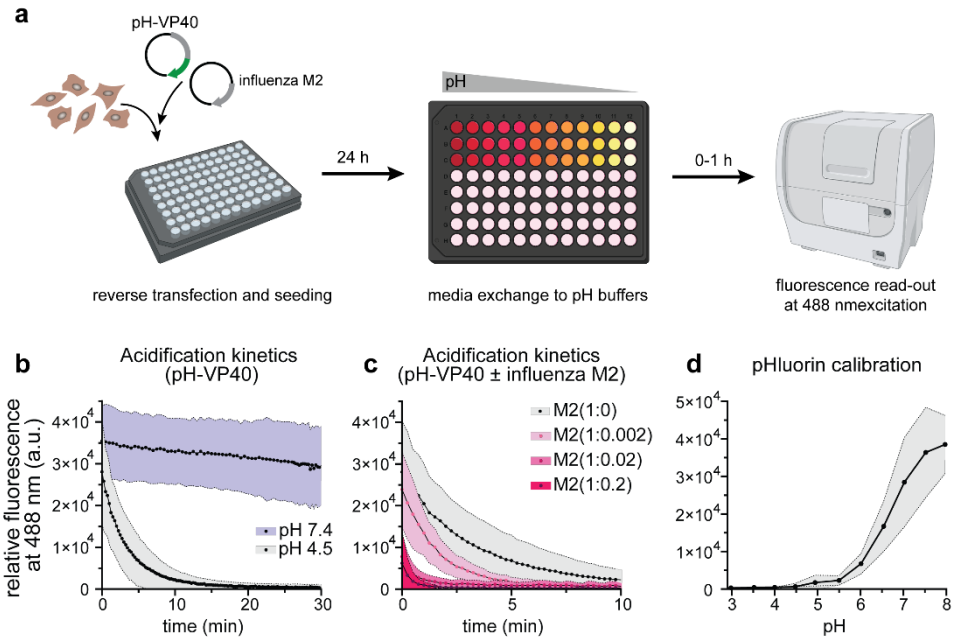

Figure 18: Calibration of pHluorin fluorescence at different pH. (a) Schematic of the experimental setup to determine the fluorescence properties of pHluorin at different pH. HEK 293T cells are mixed with transfection complexes containing the pHluorin-VP40 plasmid in combination with or without the M2 plasmid (reverse transfection) and seeded into 96 well plates. After 24 h, the media is exchanged with buffers at pH 3.5, 4, 4.5, 5, 5.5, 6, 6.5, 7, 7.5 and 8 and cells are incubated for 1 h before measuring fluorescence at 488 nm with a plate reader. To determine acidification kinetics across the plasma membrane, the cells are imaged immediately after exchanging the external buffer with acidified buffers**. (b)** Relative fluorescence of HEK 293T cells expressing (pH)VP40 after 488 nm excitation plotted against the pH of the external buffer solution. Mean values of 3 independent experiments (3 measurements each) and the standard deviation (SD) are plotted**. (c)** Relative fluorescence of HEK 293T cells expressing (pH)VP40 after exchanging the pH of the surrounding buffer to pH 7.4 or pH 4.5 plotted against time. Mean values of 3 independent experiments (3 measurements each) and the SD are shown. **(d)** Relative fluorescence of HEK 293T cells expressing (pH)VP40 and different amounts of the influenza ion channel M2 after exchanging the pH of the surrounding buffer to pH 7.4 or pH 4.5 plotted against time. (pH)VP40 and M2 were expressed in 1:0, 1:0.002, 1:0.02 and 1:2 molar ratios. Mean values of 3 independent experiments (3 measurements each) and the SD are shown.

To determine the luminal pH of the Ebola VLPs from the fluorescence data shown in Figure 17 using the calibration curve (Fig. 18 d), we collaborated with Gonen Golani (Schwarz lab, ITP Heidelberg). Based on the acidification kinetics and the geometry of the VLPs measured by cryo-ET (Fig. 10), he calculated the fluorescence decay time constant τ and proton permeability coefficient P_m (Deamer and Bramhall, 1986) as described in the Materials and Methods. Similarly, he determined the permeability of the plasma membrane of HEK 293T cells using the fluorescence data (Fig. 18 c) and cell geometry measured by fluorescence microscopy. The luminal pH of VLPs and cells dropped exponentially over time after lowering the pH of the surrounding buffers (Fig. 19 a). Since Ebola VLPs are pleomorphic (Fig. 12) and we expected differences in the permeability of spherical and filamentous VLPs, I divided the dataset of segmented VLPs into spherical and filamentous VLPs based on the length of their longest axes (spherical VLPs < 500 nm). The membrane of filamentous VLPs was significantly less permeable to protons compared to spherical VLPs (Fig. 19 b), and HEK 293T cells were more permeable to protons than spherical VLPs. Importantly, the proton permeability of the HEK 293T cells measured here is in line with previous measurements (Deamer and Bramhall, 1986; Deamer, 1987). As expected, expression of the influenza ion channel M2 increased the permeability of HEK 293T cells towards protons with increasing expression levels.

The low proton permeability of Ebola VLPs in comparison with the plasma membrane indicate that protons passively diffuse across the EBOV membrane, independent from a dedicated viral ion channel.

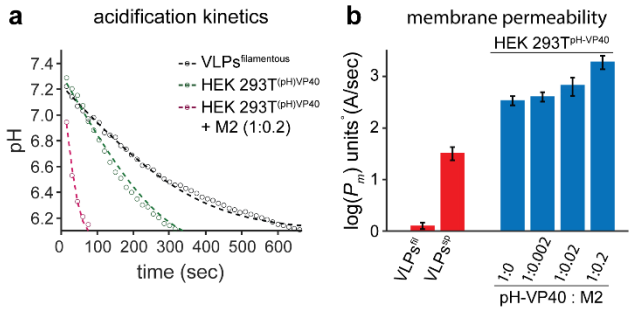

Figure 19: Membrane permeability of Ebola VLPs and the plasma membrane of HEK 293T cells. (a) Acidification kinetics of filamentous VLPs (VLPs^{filamentous}) and HEK 293T cells expressing pHluorin-VP40 ((pH)VP40) in the presence or absence of the influenza M2 ion channel (molar ratio (pH)VP40:M2 = 1:0.2). The luminal pH of VLPs and cells are plotted over time after changing the pH of the external buffer to pH 4-5. The dots represent mean values, and the dashed lines the theoretical fit to the data**. (b)** Membrane permeabilities determined for VLPs (red) and HEK 293T cells (blue) expressing (pH)VP40 and different amounts of influenza M2. The permeability is displayed on a logarithmic scale. Permeability coefficients: filamentous VLPs (VLPs^{fil})= 1.2 ± 0.2 Å ·sec^{-1}, spherical VLPs (VLPs^{sp})= 33 ± 9 Å ·sec^{-1}, cells expressing no M2= 345 ± 71 Å ·sec^{-1}, cells expressing (pH)VP40 and M2 at 1:0.002 molar ratio= 409 ± 85 Å ·sec^{-1}; at 1:0.02 molar ratio= 683 ± 263 Å ·sec^{-1} and at 1:0.2 molar ratio= 1940 ± 562 Å ·sec^{-1}. All plots and calculation shown here were provided by Gonen Golani (Schwarz lab, ITP, Heidelberg).

2.4 Characterization of EBOV entry into host cells

After demonstrating the effect of endosomal pH on the EBOV shape in vitro and establishing that acidification across the viral membrane occurs by passive diffusion, I investigated the impact of low pH and, indirectly, the integrity of the VP40 matrix on EBOV entry into host cells. To this end, I assessed entry of VLPs into target cells by fluorescence microscopy and using the well-established beta-lactamase (BlaM) entry assay. The VLPs used here can enter target cells but do not contain a genome and hence cannot replicate and establish an infection. For simplicity, however, I will refer to the addition of VLPs to target cells to monitor entry as "infection".

Timing of Ebola VLP entry into target cells

EBOV enter host cells via late endosomes and display remarkably late entry kinetics (Mingo et al., 2015). To investigate factors required for host cell entry and ultimately structurally characterize Ebola VLPs entering host cells, I first aimed to confirm the late entry kinetics by light microscopy. To this end, I produced Ebola VLPs composed of GP, VP40 and GFP-VP40 and infected target Huh7 cells exogenously expressing the mRFP-tagged endosomal EBOV receptor NPC1. At different time-points post infection, the samples were chemically fixed and imaged by confocal microscopy (exemplarily shown in Fig. 20 a and c at 3 hours post infection (hpi)). Each sample was then anonymized to determine the number of VLPs per cell in an unbiased manner (Fig. 20 b). The average number of VLPs found per cell was 6 (±5) at time-point 0, 9 (±8) at 1 hpi, 7 (±5) at 2 hpi, 10 (±) at 3 hpi and 2 (±3) at 6 hpi. In general, the high number of VLPs found per cell allowed rapid quantification but the large standard deviation per sample resulted in statistically less pronounced differences between the different time-points. The highest number of internalized VLPs was found at 1 and 3 hpi, with no statistical significance between the two time-points. Strikingly, the 2 hpi time-point showed a significantly lower average number of VLPs per cell than both 1 hpi and 3 hpi samples.

To avoid continuous VLP uptake from remaining VLPs in the cell culture media after removal of the VLP solution, which could skew the results, the target cells were washed extensively before incubation for 0-6 h. Since this might still have been insufficient, I next used the colocalization with the endosomal receptor NPC1 as a measure of VLP uptake. As NPC1 resides primarily in late endosomal compartments (Neufeld et al., 1999; Higgins et al., 1999; Garver et al., 2000), colocalization occurs after uptake by macropinocytosis and trafficking through the early endosomes and should remain for a short time until the VLPs successfully fuse with the endosomal membrane or end up in lysosomes to be degraded. As exemplarily shown 3 hpi (Fig. 20 c), internalized VLPs are encountered early after uptake (no colocalization, white asterisks) and in late endosomal compartments (colocalization with NPC1, white arrows). Quantification of colocalization events revealed the highest colocalization at 2 hpi, which is in line with previously determined entry kinetics (Mingo et al., 2015a).

Together with the previous data taking all VLPs into account that had entered target cells, these data indicate that VLP entry was likely not well synchronized in these experiments. VLPs either still bound to the cell surface or residing in early endosomes just after uptake from the surrounding media could account for the ambiguous results shown in Figure 20 b. Hence, co-localization with NPC1 provides a more robust measure to assess the timing of VLP entry into target cells.

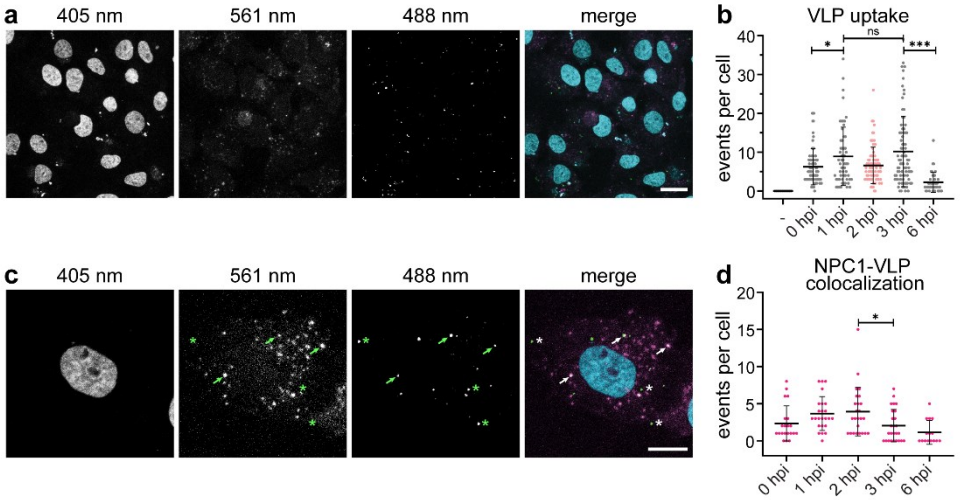

Figure 20: Entry kinetics of Ebola VLPs entering Huh7 cells. (a) Confocal fluorescence microscopy images of Huh7 cells expressing mRFP-NPC1 and challenged with GFP-labelled Ebla VLPs (time-point: 3 hours post addition of VLPs to the cells). The nuclei are stained with DAPI (405 nm excitation), NPC1 is detected by excitation at 561 nm and Ebola VLPs are detected by excitation at 488 nm**. (b)** Quantification of VLPs detected inside cells at different time-points post addition to the host cell media (indicated as "hpi"= hours post infection). To rule out false interpretation of background fluorescence, one sample without VLPs was included ("-") and all image files were anonymized prior to analysis to avoid bias. The mean number of VLPs detected per cell is plotted for each time-point together with the standard deviation. Statistical significance between the means of the different samples was estimated using a two-tailed Student's t-test, ns= not significant, * p= 0.0126, *** p<0.0001. Data is shown for three independent biological replicates with the total number of cells analysed: n(-)= 12, n(0 hpi)= 76, n(1 hpi)= 58, n(2 hpi)= 75, n(3 hpi)= 85 and n(6 hpi)=41**. (c)** Confocal fluorescence microscopy image of a Huh7 cell expressing mRFP-NPC1 3 hpi with GFP-VLPs. At this time-point, some internalized VLPs colocalize with NPC1 (white arrows), while others do not (white asterisks). **(d)** Quantification of co-localization between NPC1-mRFP and GFP-VLPs at different time-points post infection. The mean number of co-localization events is plotted for each time-point together with the standard deviation. Statistical significance between the means of the different samples was estimated using a two-tailed Student's t-test, * p= 0.0189. Data is shown for one biological replicate with the total number of cells analysed: n(0 hpi)= 21, n(1 hpi)= 24, n(2 hpi)= 25, n(3 hpi)= 26 and n(6 hpi)=15. Scale bars: (a)= 20 μm, (b)= 10 μm.

Impact of acidic environments on host cell entry of Ebola VLPs

Next, I assessed the impact of low pH on VLP entry into host cells. Several studies have shown that low pH is indispensable for EBOV entry to enable low pH-dependent proteolytic processing of GP by host cell cathepsin proteases (Brecher et al., 2012; Chandran et al., 2005). Only cleaved GP (GP_{CL}) can bind to the endosomal receptor NPC1 and enable membrane fusion, which is critical to conclude host cell entry. To measure entry of VLPs into host cells and decouple the requirement of low pH from GP processing, I performed BlaM entry assays using filamentous Ebola VLPs. BlaM assays are fluorescence-based assays in which target cells are loaded with a beta-lactamase substrate, which is composed of a FRET pair and emits green fluorescence when exited at 409 nm (Jones and Padilla-Parra, 2016). Upon successful cytosolic entry of VLPs containing beta-lactamase fused to the matrix protein, the beta-lactamase cleaves the substrate,

which as a result emits blue fluorescence when excited at 409 nm. Hence, VLP entry can be measured as a binary readout from the fluorescence of target cells.

I assessed the effect of several cellular inhibitors of endosomal low pH (bafilomycin and NH_4Cl) and the specific cathepsin B inhibitor E64d on VLP entry. Furthermore, to measure host cell entry of VLPs lacking an ordered VP40 matrix, I subjected the VLPs to different in vitro treatments prior to the experiment, including low pH and proteases. Proteases used here are cathepsin L, which requires activation at low pH, and thermolysin, which cleaves GP similarly to cathepsins (Schornberg et al., 2006) but is active at neutral pH. The different inhibitors and VLP treatments including their effect on virus entry are enlisted in Table 1.

Table 1: List of cellular inhibitors and Ebola VLP treatments and their effect on virus entry into host cells.

Cellular inhibitor	*Compound*	Bafilomycin	NH_4Cl	E64d
	Effect	inhibits cellular ATPases (Dröse and Altendorf, 1997)	neutralizes organellar low pH (Ohkuma and Poole, 1978)	inhibits cathepsin proteases (Brochmann Murray et al., 1997; Hook et al., 2011)
Mechanism of virus entry inhibition		inhibition of pH-dependent processing of the EBOV GP by host cell cathepsin proteases → no binding to the endosomal receptor NPC1 and membrane fusion		
Ebola VLP treatment	*Compound*	Cathepsin B and L	Thermolysin	Low pH
	Effect on VLPs	cleave EBOV GP at pH 4-5	cleaves EBOV GP in vitro at pH 7-8	potentially disassembles the EBOV VP40 matrix
Effect on virus entry		enhancement of virus entry (Kaletsky et al., 2007; Dube et al., 2009)		potential enhancement of virus entry

The experimental setup and initial experiments (Fig. 21 a-c) were performed by the master student Keerthihan Thiyagarajah under my supervision. VLPs composed of GP, VP40 and BlaM-VP40 (hereafter referred to as BlaM-VLPs) were produced and purified from HEK 293T cell media. They were then treated with cathepsin L at different pH and thermolysin in different concentrations before testing the efficiency of the proteolytic digest by Western blot analysis (Fig. 21 a). Cathepsin L treatment at pH 4-5 and thermolysin treatment at neutral pH resulted in similarly efficient cleavage of the EBOV GP as apparent from the reduced band intensity running at approximately 110-135 kDa. Proteolytic processing of EBOV GP produces a 19 kDa variant (Brecher et al., 2012) lacking the heavily glycosylated mucin-like domain. However, even after several attempts with different developing techniques, we could not resolve the respective band by Western blotting. We proceeded nonetheless with the BlaM-VLPs treated with thermolysin and compared their entry efficiency to untreated VLPs and VLPs additionally incubated at low pH. To this end, target Huh7 cells were infected with the different BlaM-VLPs, and entry was allowed to occur for 2 h at 37°C before loading the cells with the fluorescent BlaM substrate. After overnight incubation, fluorescence of the target cells was visually assessed by light microscopy (Fig. 21 b) and measured using a plate reader. In agreement with previous studies (Kaletsky et al., 2007; Mingo et al., 2015), thermolysin-treated VLPs entered target cells significantly more efficiently than untreated VLPs, irrespective of pH (Fig. 21 c). Entry of all VLPs tested was efficiently blocked by bafilomycin. To assess

entry of VLPs subjected to low pH alone in comparison to thermolysin-treated VLPs, I repeated the experiment using BlaM-VLPs subjected to pH 4.5 or thermolysin at pH 7.4. I further assessed the effect of ammonium chloride and the cathepsin inhibitor E64d on VLP entry (Fig. 21 d). Low pH treatment had no effect on VLP entry, while thermolysin treatment as before significantly enhanced VLP entry. Similar to bafilomycin, ammonium chloride and E64d both efficiently blocked VLP entry.

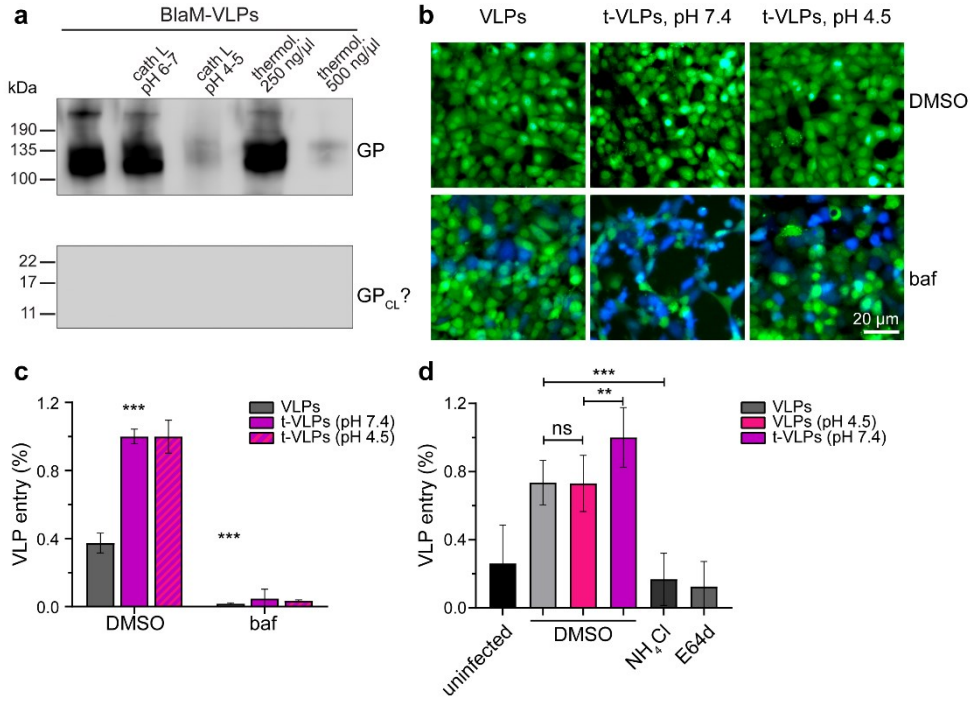

Figure 21: Set-up of beta-lactamase (BlaM) assays using Ebola VLPs to measure VLP entry into target cells. (a) Western blot analysis of purified Ebola VLPs composed of GP, VP40 and BlaM-VP40 using a monoclonal anti-GP antibody to assess the proteolytic cleavage of GP in vitro. As indicated on the blot, VLPs were either untreated; treated with 10 µg/µl cathepsin at pH 6-7 or pH 4-5; or treated with 250 ng/µl or 500 ng/µl thermolysin at pH 7.4. GP is detected by a band running at approximately 110 kDa, while the cleaved GP should be detected at approximately 19 kDa. **(b)** Wide-field light microscopy images of stained Huh7 target cells after incubation with BlaM-VLPs (untreated: VLPs, t-VLPs: thermolysin-treated VLPs) that were incubated at the indicated pH prior to infection. Target cells were either treated with DMSO or bafilomycin (baf) prior to incubating the cells with VLPs. Green cells indicate uninfected cells, blue cells indicated infected cells. **(c)** Quantification of the BlaM assay shown in (b) after measuring fluorescence intensities of the target cells using a plate-reader. Mean values are shown with the standard deviation (SD) (n= 3). Statistical significance between the means of the different samples was estimated using a two-tailed Student's t-test,*** $p<0.0001$. **(d)** Normalized entry of BlaM-VLPs into Huh7 target cells treated with DMSO, ammonium chloride (NH_4Cl) or E64d. Mean values are shown with the SD (n=3). Statistical significance between the means of the different samples was estimated using a two-tailed Student's t-test, ns= not significant, ** $p= 0.0037$, *** $p<0.0001$. Data shown in (a-c) were produced by Keerthihan Thiyagarajah under my supervision.

Despite fibronectin-coating of 96 well plates prior to cell seeding to improve cell attachment, and careful handling, some cells detached during sample handling, resulting in heterogeneous cell monolayers (Fig. 21 b). Since we used a plate-reader to measure bulk fluorescence intensity, which is sensitive to uniform cell growth, the partial detachment of cells caused inconsistencies in read-out, rendering some follow-up results irreproducible. Therefore, I opted for a single-cell FACS-based read-out, for which these differences in cell attachment or growth should not matter. Since the statistics are more robust at high cell numbers, I aimed for 10,000 cells per sample, which required significantly more BlaM-VLPs for a comprehensive study combining different VLP- and cell treatments. I thus used clarified supernatants of

BlaM-VLP-producing HEK 293T cells for the entry assays rather than purified BlaM-VLPs. They were more diluted than the purified VLPs and accordingly resulted in less entry but required less starting material and allowed me to parallelize the experiments. Additionally, to improve cell attachment and reduce cell loss after challenging target cells with thermolysin-treated VLPs, I inactivated thermolysin using phosphoramidon. In an initial experiment, I assessed the entry of BlaM-VLPs treated with thermolysin at both pH 7.4 and pH 4.5, and pH 4.5 alone. Target cells were either untreated or treated with ammonium chloride or E64d (Fig. 22).

Data acquisition was performed with Samy Sid Ahmed (Fackler lab, CIID Heidelberg). The FACS plots obtained after plotting fluorescence emission of the target cells at 450 nm against 510 nm revealed two main populations of uninfected cells and cells infected with all VLPs at pH 7.4. The populations shifted towards emission at 450 nm as apparent from the increase in cell counts in the gated window (black square, Fig. 22 a). In contrast, analysis of target cells infected with VLPs at pH 4.5 showed primarily one population that had shifted less dispersedly towards fluorescence emission at 450 nm. Consistent with the previous data, the quantification revealed enhanced cell entry of BlaM-VLPs treated with thermolysin at pH 7.4, which was 4-5-fold diminished in cells treated with ammonium chloride or E64d (Fig. 22 b). Strikingly, all BlaM-VLPs incubated at pH 4.5 showed a strong enhancement in cell entry already without cleavage of the GPs. Cell entry was not affected by ammonium chloride or E64 d treatment, which was unexpected at least for the VLPs treated with pH 4.5 alone, since they should still depend on intracellular GP cleavage by cathepsin proteases for cell entry. To visually confirm the high entry for BlaM-VLPs incubated at pH 4.5, I then analysed images taken by fluorescence light microscopy prior to detaching the cells for FACS analysis (Fig. 22 c). In contrast to uninfected cells and cells challenged with thermolysin-treated VLPs at pH 7.4, cells challenged with VLPs at pH 4.5 appeared to have partly lost the BlaM stain and I could not detect blue cells. To rule out that the low pH itself affects target cells during incubation, I then treated cells with media acidified to pH 4.5 using hydrochloric acid or citric acid, and directly compared their phenotype to cells incubated with unpurified VLPs that were similarly acidified. Target cells did not appear morphologically affected by the treatment of low pH alone and retained their dye (Fig. 22 d). In contrast, cells challenged with unpurified VLPs at pH 4.5 had partially lysed and lost their fluorescent dye (Fig. 22 e).

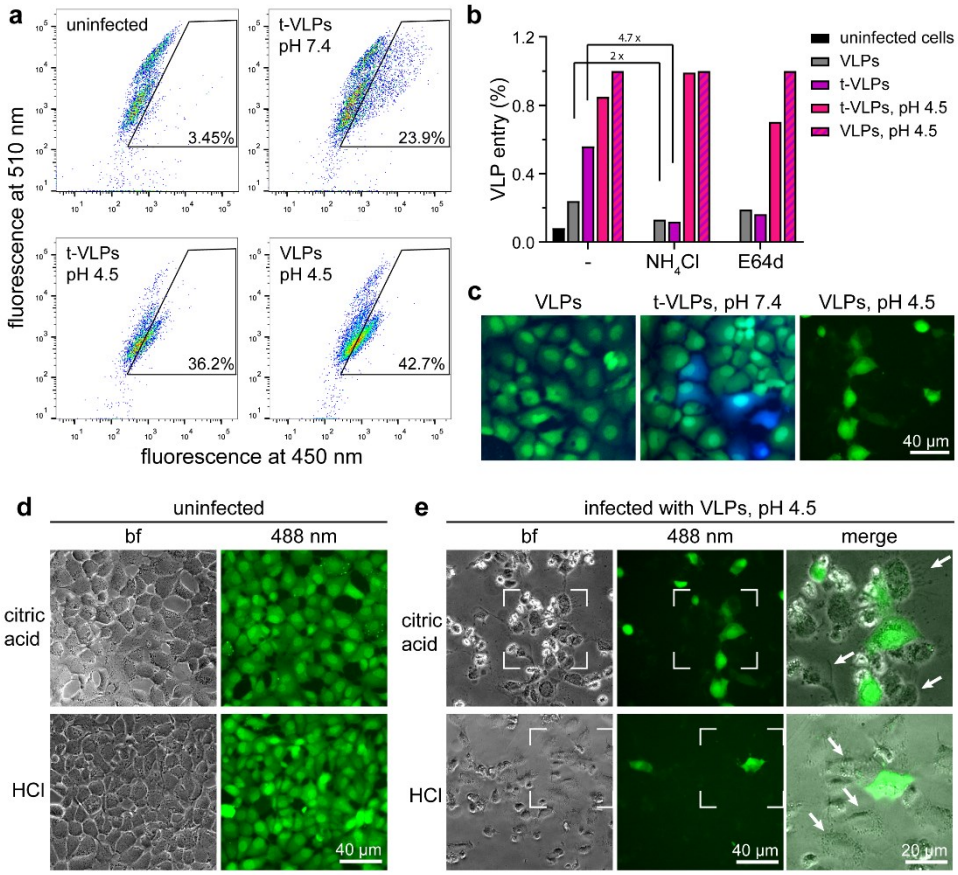

Figure 22: Optimization of experimental parameters for the BlaM assay. (a) Representative FACS plots showing the fluorescence intensity of target cells after performing BlaM assays. Data are shown for BlaM assays performed without infection (uninfected control), using VLPs treated with thermolysin (t-VLPs) at the indicted pH; and untreated VLPs subjected to pH 4.5. Fluorescence emission is detected at 510 nm and 450 nm, and the distribution of measured cells is shown in 2D scatter plots. A shift towards emission at 450 nm (productive VLP entry, blue cells) is measured by setting a gate on non-infected target cells, which is kept for all following experiments (black squares). The percentage of blue cells is indicated for each sample (n= 10,000 cells per sample). **(b)** Quantification of FACS data partially shown in (a) showing the normalized entry of VLPs treated with thermolysin (t-VLPs), and different pH as indicated. Target cells were either untreated or treated with ammonium chloride (NH_4Cl) or the cathepsin inhibitor E64d prior to adding the VLPs. Cell entry is inhibited two-fold for untreated VLPs when using NH_4Cl, while the entry of t-VLPs is inhibited 4-5-fold due to the higher entry into naïve target cells. **(c)** Wide-field light microscopy images of stained Huh7 target cells after incubation with BlaM-VLPs (untreated: VLPs, t-VLPs: thermolysin-treated VLPs) that were incubated at the indicated pH prior to infection. Green cells indicate uninfected cells, blue cells indicated infected cells. **(d)** Wide-field light microscopy images of stained Huh7 target cells after incubation in media acidified to pH 4.5 with either citric acid or hydrochloric acid (HCl). Both bright field (bf) images and fluorescence images at 488 nm excitation are shown. **(e)** Wide-field light microscopy images of stained Huh7 target cells after incubation with BlaM-VLPs that were subjected to buffer acidified to pH 4.5 using citric acid or HCl as indicated. Bright field (bf) and fluorescence images at 488 nm excitation are shown. Unstained cells (white arrows) are shown in the enlarged merged image on the right. FACS data shown in (a) were performed by Samy Sid Ahmed (Fackler lab, CIID).

Considering that cell lysis was exclusively observed when using unpurified VLPs treated at pH 4.5 (for comparison, see Fig. 21 b), I reverted to purifying BlaM-VLPs to perform the assay. The FACS data revealed similar distributions of cell populations for all conditions tested, and clear shifts towards fluorescence emission at 450 nm could be observed for untreated target cells challenged with differently treated BlaM-VLPs (Fig. 23 a). Consistent with the initial plate-reader based BlaM results (Fig. 21), entry of VLPs treated at pH 7.4 or pH 4.5 was similar, while entry of all thermolysin-treated VLPs was significantly enhanced (Fig. 23 b). Treatment of cells with ammonium chloride prior to and during infection efficiently inhibited entry of all VLPs except for VLPs treated with thermolysin and pH 4.5. The latter showed a significant rescue of infection, although entry was overall reduced compared to entry of the same sample

into untreated target cells. Finally, VLP entry as assessed by FACS could visually be confirmed from microscopy images taken prior to performing FACS (Fig. 23 c). All cells had grown into a uniform monolayer, no lysis was observed, and entry events were apparent from blue fluorescent cells.

In summary, endosomal pH is indispensable for Ebola VLP entry into target cells and can only be partially rescued by treating VLPs with proteases and low pH prior to infection. Pre-treatments of the VLPs were intended to decouple the low pH requirement from protease activation. The partial entry of VLPs pre-processed with thermolysin and low pH into cells lacking acidified endosomal compartments (i.e., treated with ammonium chloride) indicates that the timely GP processing and VP40 disassembly immediately before encountering the endosomal receptor NPC1 is not essential for efficient entry. However, whether VP40 disassembly or GP processing, or both, are rate-limiting during entry remains to be further investigated.

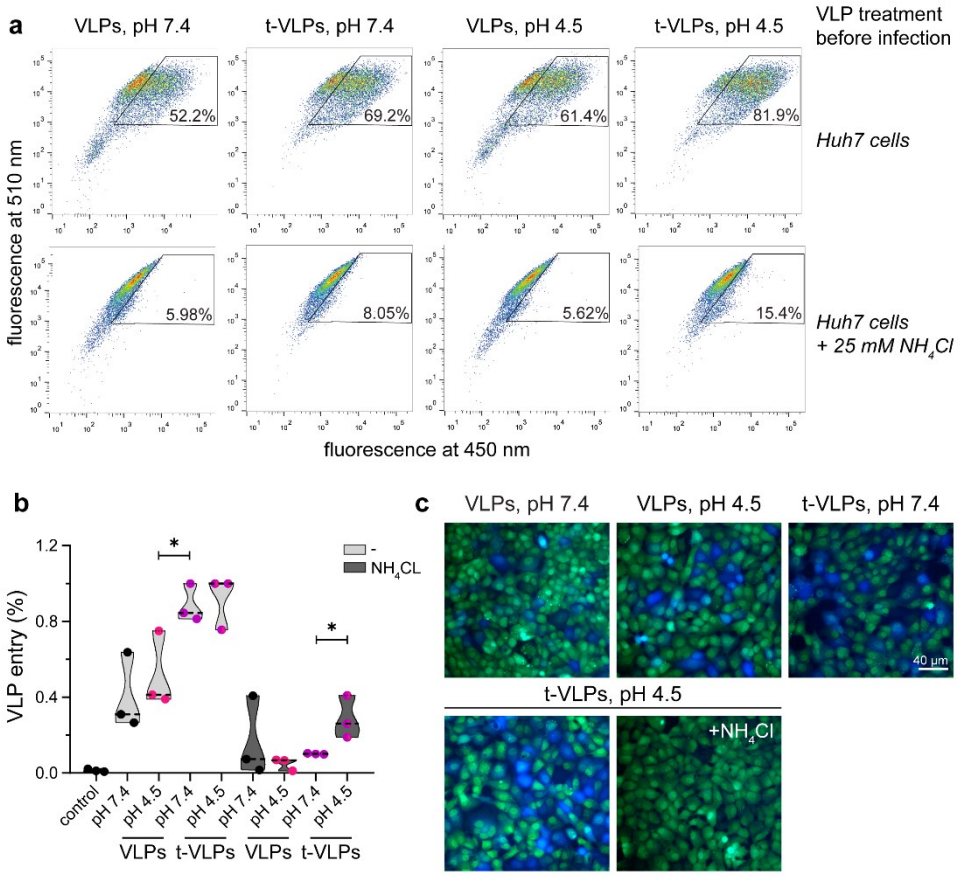

Figure 23: Effect of low pH on Ebola VLP entry into target cells. (a) FACS scatter plots of stained Huh7 cells after performing the BlaM assay using BlaM-VLPs (VLPs) that were either untreated (VLPs) or treated with thermolysin (t-VLPs) and incubated at the indicated pH. Huh7 cells were either untreated or treated with ammonium chloride (NH_4Cl) to block VLP entry prior to performing the assay (n= 10,000 cells per sample). **(b)** Violin plot quantifying the FACS data shown in (a) and two repetitions of the same experiments (10,000 cells measured for each sample). The normalized percentage of entry events (blue cells) per repetition and the means are shown. Statistical significance between the means of the different samples was estimated using a two-tailed Student's t-test, * p= 0.047. **(c)** Wide-field light microscopy images of stained Huh7 target cells after incubation with BlaM-VLPs (untreated: VLPs, t-VLPs: thermolysin-treated VLPs) that were incubated at the indicated pH prior to infection. Target cells were untreated or treated with NH_4Cl as indicated. Green cells indicate uninfected cells, blue cells indicated infected cells.

2.5 In vitro reconstitution of EBOV membrane fusion

To directly address whether low pH-driven structural remodelling of the VP40 matrix influences fusion of the viral with the endosomal membrane, I next reconstituted the fusion reaction in vitro. Prerequisite of EBOV membrane fusion is the presence of the endosomal EBOV receptor NPC1 and proteolytic processing of GP. To obtain purified NPC1, I initiated a collaboration with Chao Qi (Korkhov lab, PSI Villigen), who provided purified NPC1 and reconstituted the protein in liposomes in two different protein-to-lipid ratios.

To assess the NPC1 distribution on these liposomes composed of phosphatidylcholine, phosphatidylethanolamine and cholesterol (50%, 10%, 40%, respectively), I first characterized them by cryo-ET. NPC1 is a large transmembrane protein composed of 13 membrane-spanning domains and three large, flexible domains facing the endosomal lumen in cells (Gong et al., 2016). NPC1 densities are thus detectable by cryo-ET as densities protruding from the membrane surface. The sample containing NPC1-liposomes in a 1:100 protein-to-lipid ratio (hereafter referred to as NPC1-lipo100) contained multilamellar membrane sheets and vesicles that were devoid of protein densities (Fig. 24 a, b), as well as vesicles and membrane sheets decorated with NPC1 (Fig. 24 c-g). NPC1 distributed on either side of the membranes both on membrane sheets and on vesicles, indicating that its orientation is not influenced by membrane curvature. The sample was predominantly composed of decorated membrane sheets, which were on average 42.7 nm (SD=14.9 nm, n= 31) in length (Fig. 24 g, h).

In contrast, the sample containing NPC1-liposomes in a 1:1000 protein-to-lipid ratio (hereafter referred to as NPC1-lipo1000) was predominantly composed of protein-decorated vesicles and contained less multilamellar membrane sheets (Fig. 24 i-l). Both protein-decorated multilamellar and single vesicles were detected, and the average diameter of the latter was 44.3 nm, (SD= 15.1 nm, n= 59). When viewed from the top, the vesicle surfaces in all samples appeared occupied by a lattice of NPC1 proteins (Fig. 24 m). The distance between neighbouring NPC1 molecules was similar between the NPC1-lipo100 and NPC1-lipo1000 sample and differed only in large vesicles with diameters above 500 nm found in the NPC1-lipo1000 sample (Fig. 24 o).

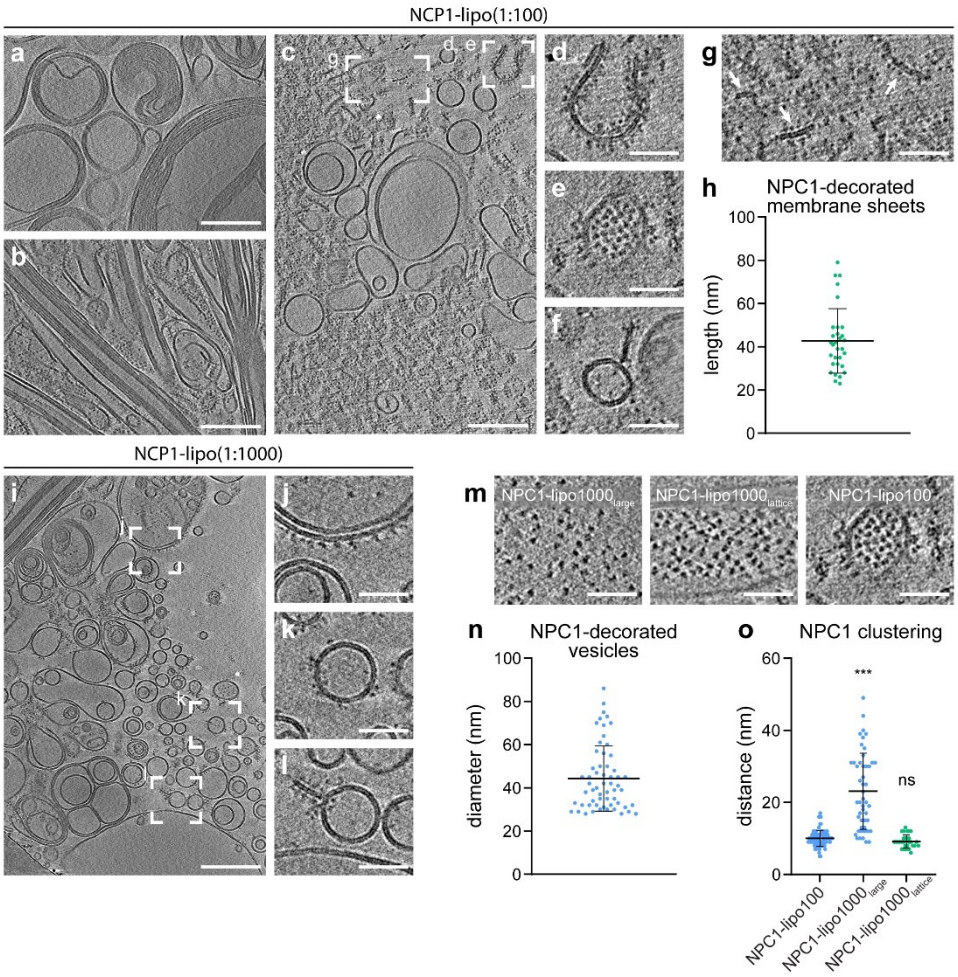

Figure 24: Characterization of liposomes containing purified NPC1 for in vitro reconstitution of EBOV membrane fusion. Human NPC1 was purified and reconstituted in liposomes composed of 50% phosphatidylcholine, 10% phosphatidylethanolamine and 40% cholesterol in a protein-to-lipid ratio of 1:100 and 1:1000 (NPC1-lipo100, NPC1-lipo1000), respectively, by Chao Qi (Korkhov lab, PSI Villigen). **(a-c)** Slices through tomograms showing the heterogeneous NPC1-lipo100 sample, including multilamellar membrane rings (a) and multilamellar membrane sheets (b) largely devoid of NPC1 molecules and a mixture of liposomes of different sizes and membrane fragments decorated by NPC1 (c). **(d)** Area highlighted in (c) showing a bent membrane sheet densely decorated with NCP1 on either side of the membrane. E) Near-to-surface tomographic slice of the same area shown in (d) displaying a lattice of NPC1 molecules. **(f)** Area highlighted in (c) displaying a NPC1-decorated liposome next to a membrane sheet. **(g)** Area highlighted in (c) containing NPC1-decorated membrane sheets. **(h)** Quantification of the length of NPC1-decorated membrane sheets accumulated in the NPC1-lipo100 sample (mean length= 42.7 nm, SD= 14.9 nm, n= 31). **(i)** Slices through a tomogram of the NPC1-lipo1000 sample showing primarily NPC1-decorated liposomes. **(j)** Area highlighted in (i) showing a membrane bilayer with an NPC1-decorated outer membrane. **(k-l)** Areas highlighted in (i) containing liposomes and a membrane sheet decorated with NPC1 molecules on either side of the membrane. **(m)** Near-to-surface slices through tomograms containing vesicles of different sizes decorated in different densities with NPC1 molecules. "Lattice" and "large" denote vesicles either densely or sparsely decorated with NPC1 found on large vesicles. **(n)** Quantification of the diameter of NPC1-decorated vesicles accumulated in the NPC1-lipo1000 sample (mean diameter= 44.3 nm, SD= 15.1 nm, n= 59). **(o)** Quantification of the distance between neighbouring NPC1 molecules on vesicles shown exemplarily in (m). Distances were measured using FiJi (NPC1-lipo100: mean distance= 9.2 nm, SD= 1.8 nm, n= 30; NPC1-lipo1000$_{lattice}$: mean distance= 10 nm, SD= 2.2 nm, n= 85; NPC1-lipo1000$_{large}$: mean distance= 23.1 nm, SD= 10.6 nm, n= 49). Statistical significance between the means of the different samples was estimated using a two-tailed Student's t-test, ns= not significant, * p= 0.04, *** p<0.0001. SD is standard deviation. Scale bars: (a-c), (i): 200 nm, (d-g), (j-m): 50 nm.

After characterizing both NPC1-lipo samples, I analysed the NPC1-lipo100 sample incubated with Ebola VLPs composed of GP and VP40 at pH 7.4. The sample was very crowded with filamentous VLPs in close proximity to NPC1-decorated membrane sheets and vesicles (Fig. 25 a-d). EBOV GP was clearly visible on the VLP surface as trimeric protein densities. In contrast, when the VLPs were treated with thermolysin

at pH 7.4 prior to mixing with NPC1-liposomes (hereafter referred to as VLPs(GP_{CL})), no GPs could be detected (Fig. 25 e-h) and predominantly membrane sheets containing NPC1 decorated the VLP surface.

I then analysed VLPs(GP_{CL}) incubated with the NPC1-lipo1000 sample and observed that they were similarly decorated by NPC1-containing membranes (Fig. 25 i-l). As expected from the characterization of the NPC1-liposome samples (Fig. 24), the VLPs were primarily bound by NPC1-containing membrane vesicles, which had partially deformed to increase contact with the VLP surface (Fig. 25 l). Since NPC1-decorated membranes and vesicles were found in the proximity of both VLPs and VLPs(GP_{CL}), I then quantified their distances as measured from NPC1-lipo membrane to VLP membrane. VLPs containing uncleaved GP were separated by approximately 27 nm from the NPC1-lipo membranes, while VLPs(GP_{CL}) were significantly closer with an average spacing of 14.2-16.5 nm (Fig. 25 n).

Together, these data indicate that NPC1 interacts with cleaved EBOV GP already at neutral pH, while fusion of the VLP membrane with the NPC1-containing liposomes appears inhibited as no fusion events were observed at this pH. Due to limited time, the experiment presented here is preliminary and the final sample of VLPs(GP_{CL}) incubated with NPC1-liposomes at pH 4.5, at which fusion is expected, still remains to be performed.

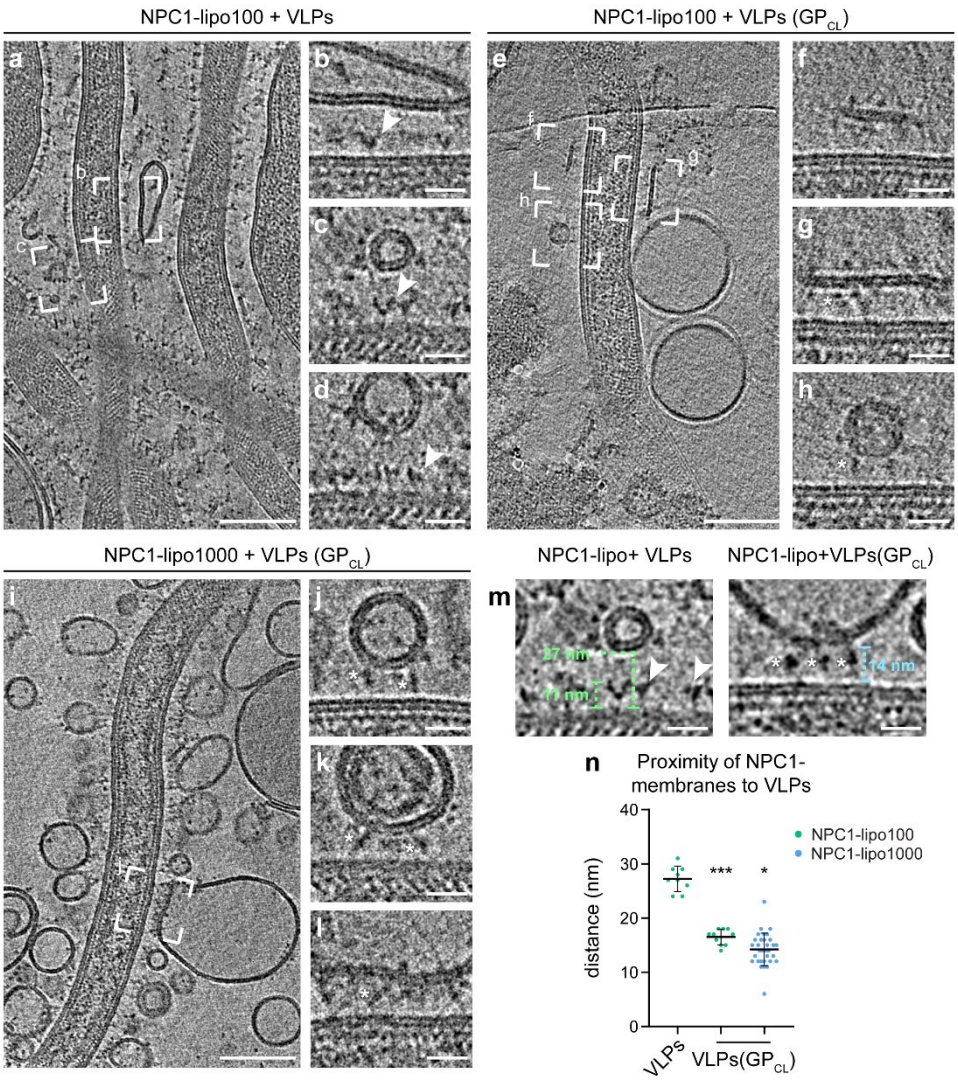

Figure 25: Characterization of the interaction of NPC1-containing liposomes with Ebola VLPs. (a) Slices through a tomogram showing NPC1-liposomes (protein-to-lipid ratio 1:100, NPC1-lipo100) incubated with Ebola VLPs composed of GP and VP40. **(b-d)** Areas highlighted in (a) showing examples of NPC1-decorated vesicles adjacent to the GP-decorated surface of Ebola VLPs (highlighted by white arrowheads). **(e)** Slices through a tomogram of NPC1-lipo100 incubated with Ebola VLPs composed of cleaved GP (GP_{CL}) and VP40. **(f-h)** Areas highlighted in (e) showing examples of membrane sheets and a vesicle (h) studded by NPC1 molecules (white asterisks) adjacent to the membrane of a VLP. **(i)** Slices through a tomogram of NPC1-lipo1000 incubated with Ebola VLPs composed of cleaved GP (GP_{CL}) and VP40. **(j-l)** Examples of liposomes studded by NPC1 molecules (white asterisks) adjacent to the membrane of a VLP with (j) highlighted in (i). **(m)** Slices through tomograms of NPC1-liposomes incubated with Ebola VLPs containing full-length GP or GP_{CL} demonstrating the measurements of the NPC1-liposome surface to the VLP surface, and the length of full-length GP (highlighted with white arrowheads). GPs protruding from the VLP surface in proximity to the vesicles were measured from membrane to crown using FiJi (mean length= 11.4 nm, SD= 1 nm, n= 14). **(n)** Quantification of the distance between NPC1-decorated membranes and the VLP surface as measured from outer membrane to outer membrane using FiJi (NPC1-lipo100+VLPs: mean distance= 27.2 nm, SD= 2.3 nm, n= 9; NPC1-lipo100+VLPs(GP_{CL}): mean distance= 16.5 nm, SD= 1.4 nm, n= 10; NPC1-lipo1000+VLPs(GP_{CL}): mean distance= 14.2 nm, SD= 3 nm, n= 32). Statistical significance between the means of the different samples was estimated using a two-tailed Student's t-test, * p= 0.03, *** p<0.0001. SD is standard deviation. Scale bars: (a), (e), (i): 100 nm, (b-d), (f-h), (j-m): 20 nm.

2.6 In situ cryo-ET of Ebola VLPs and virions entering host cells

In situ cryo-CLEM of Huh7 cells infected with Ebola VLPs

Since the BlaM assay revealed a clear impact of low endosomal pH on VLP entry but its requirement for VP40 disassembly rather than proteolytic GP processing was difficult to proof, I then structurally characterized Ebola VLPs and virions entering host cells by in situ cryo-ET. Entry events are difficult to find by cryo-EM, since they are rare and the VLPs or virions entering cells are small in comparison to intracellular structures. Hence, I first opted for a correlative approach using GFP-tagged VLPs to target cells displaying fluorescent signal with the correlative light and electron microscopy (CLEM) workflow established in the lab (Klein et al., 2020b, 2021). In brief, I incubated Huh7 target cells grown on electron microscopy grids and stained for lipid droplets with GFP-tagged VLPs. I then allowed the VLPs to enter for 1 h, before vitrifying the sample and mapping the fluorescence signal using a cryo-light microscope. The samples were transferred to a dual-beam microscope to perform focused ion beam (FIB) milling and thin cells displaying fluorescent signal to approximately 150 nm. Resulting lamellae were then transferred to a transmission electron microscope to acquire tomograms before imaging the targeted cells again by cryo-light microscopy. The last step served to computationally extract fluorescence information emanating specifically from the lamella and not from cellular features in different regions of the cell. I could thus correlate features of interest imaged by cryo-ET to fluorescent signal and identify VLP entry events.

Figure 26 shows an example of a lamella produced as described above after fluorescence correlation. Green fluorescence was observed throughout the cell, indicating that many VLPs had been taken up and probably fused with endosomal membranes as evident from the disperse fluorescent signal (Fig. 26 b). I targeted areas exhibiting green fluorescence and resembling endosomal compartments for tomography and could identify primarily post-fusion events as judged by the presence of EBOV GP-coated vesicles or organelles, where GPs were facing away from the cytoplasm (Fig. 26 c-f, h). The membranes were densely decorated by the trimeric proteins, and I could find one event where fusion was taking place as indicated by a GP-decorated membrane protrusion (Fig. 26 g). Additionally, two membrane-coated vesicles with disordered intralumenal densities residing in an otherwise empty organelle were observed. They closely resembled Ebola VLPs imaged from transverse cross-sections based on their GP-coat, with disassembled VP40 densities crowding the VLPs' lumina. Of 15 tomograms taken on 7 lamella, two showed fusion- and post-fusion events (Fig. 26), while 13 displayed cellular organelles without indication of Ebola VLP-infection.

These results have several implications. First, entry events can indeed be targeted using fluorescently labelled VLPs. However, most of the signal appeared disperse, indicating that fusion had already taken place. Considering that fusion is fast and the timing of entry difficult to predict precisely (Fig. 20), it is likely to catch mainly post-fusion events, which are also easier to detect by fluorescence due to the disperse signal. Second, the disassembled VP40 matrices observed in the two VLPs suggest an acidified environment and the VLPs likely reside in a late endosomal compartment. The presence of cellular membranes densely decorated with GPs additionally indicates that fusion with VLP membranes had taken place. Since GP-

mediated membrane fusion requires pH-driven proteolytic processing of GPs, the large number of trimeric GPs is surprising. Whether only a small number of GPs require processing to initiate fusion remains to be elucidated.

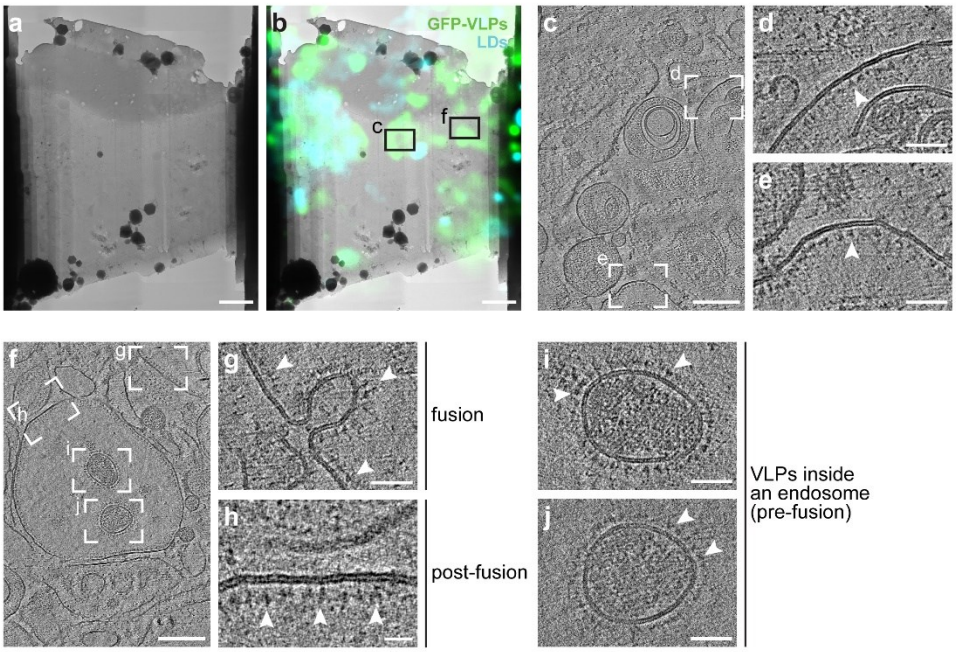

Figure 26: In situ cryo-CLEM of Ebola VLPs entering target Huh7 cells. (a) Overview of a lamella produced by cryo-FIB milling of a Huh7 cell stained with lipid droplets and infected with GFP-tagged Ebola VLPs for 1 h. **(b)** TEM map shown in (a) after correlation with the fluorescence signal of lipid droplets (stained with LipiBlue) and GFP-VLPs. **(c)** Slices through a tomogram taken on the lamella as indicated on (b) displaying intracellular vesicles decorated with EBOV GP at the luminal side. **(d-e)** Areas highlighted in (c) showing GP-decorated membranes. The GPs are facing the luminal sides of the organelles, indicating a post-fusion event. **(f)** Slices through a tomogram taken on the lamella as indicated in (b) displaying intracellular organelles decorated with EBOV GPs on the luminal sides and cross-sections of two VLPs inside a large, GP-decorated organelle. **(g)** Different tomographic slice of the area highlighted in (f) showing a fusion event, presumably in a late-endosomal compartment. The membrane of the intracellular compartment is decorated with GPs facing the luminal side (white arrowheads) and the membrane protrusion into the compartment's lumen indicates a fusion event. A globular density between the fusion pore is highlighted with a white arrow. **(h)** Area highlighted in (f) showing a GP-decorated membrane of an intracellular organelle indicativeof a post-fusion event. **(i-j)** Areas highlighted in (f) showing transverse cross-sections of VLPs, identified by their envelopes, which are studded with EBOV GPs facing the outside, and disordered protein densities crowding their lumina reminiscent of the VP40 densities observed in VLPs exposed to low pH. Scale bars: (a), (b): 5 µm, (c), (f): 200 nm, (d), (e), (g), (i), (j): 50 nm, (h): 20 nm.

In situ cryo-ET of EBOV-infected Huh7 cells

Targeting the correct time-point after VLP uptake to ensure encountering particles in endosomes before membrane fusion has taken place, is difficult, since entry takes place over a timespan of several hours (Fig. 20, (Spence et al., 2016; Aman, 2016; Mingo et al., 2015)) and membrane fusion happens fast. Hence, I next investigated infectious EBOVs entering target Huh7 cells at different time-points, including 48 h post infection, after which several rounds of infection had occurred. Studying late time-points during an EBOV infection increases the chances of finding entry events, since the continuous production of EBOV progeny from infected cells ensures an increasing number of virions (re-)infecting target cells. To perform the EBOV infection, I collaborated with Thomas Hoenen (FLI, Greifswald- Insel Riems) and prepared EM grids and seeding of Huh7 cells together with Melina Vallbracht from the Chlanda lab. The samples were then transferred to the BSL4 facility, where Thomas Hoenen infected the cells with Ebola virions and

chemically fixed them at different time-points post infection. After transferring the samples out of BSL4, I then continued with the in situ cryo-ET workflow, including cryo-preservation by plunge-freezing, FIB milling of target cells and tomogram acquisition (Fig. 27 a).

I targeted areas for tomogram acquisition that contained endosomal compartments characterized by membrane-delimited organelles crowded with cellular material including vesicles, crystalline lipidic structures and membrane fragments, which are presumably products of lysosomal degradation (Fig. 27 b, c, Fig. 28). Ebola virions could be identified by their characteristic filamentous shape and the presence of condensed nucleocapsids. In contrast to the VLPs found in endosomal compartments (Fig. 26 i, j), the membranes of endosomal virions were devoid of trimeric protein densities, which would indicate the presence of GPs. However, like the VLPs, they did not contain ordered VP40 densities. Instead, disordered protein densities crowded the virions' lumina and had detached from their membrane as particularly apparent from the cross-sections (Fig. 27 d-g). All virions displayed condensed nucleocapsids with a diameter of approximately 20 nm. For comparison, we also imaged virions found adjacent to the plasma membrane of infected cells (Fig. 27 h). They closely resembled purified EBOV particles (Fig. 11) with a uniform diameter, GPs studding their envelope and condensed nucleocapsids spanning the length of the particles. In contrast to virions found in endosomal compartments, extracellular virions contained ordered VP40 densities lining the inner membrane monolayer of the virions (Fig. 27 i-k).

This indicates that the imaged EBOV reside in late endosomal compartments and the low endosomal pH had equilibrated across the viral membrane as evident from the disassembled VP40 matrix layers. The presence of condensed nucleocapsids suggests that nucleocapsid de-condensation appears at a later time-point, possibly after membrane fusion has taken place. Taken together, the in situ cryo-ET data of both VLPs and EBOVs inside endosomal compartments confirm the low pH-phenotype described in purified particles in vitro.

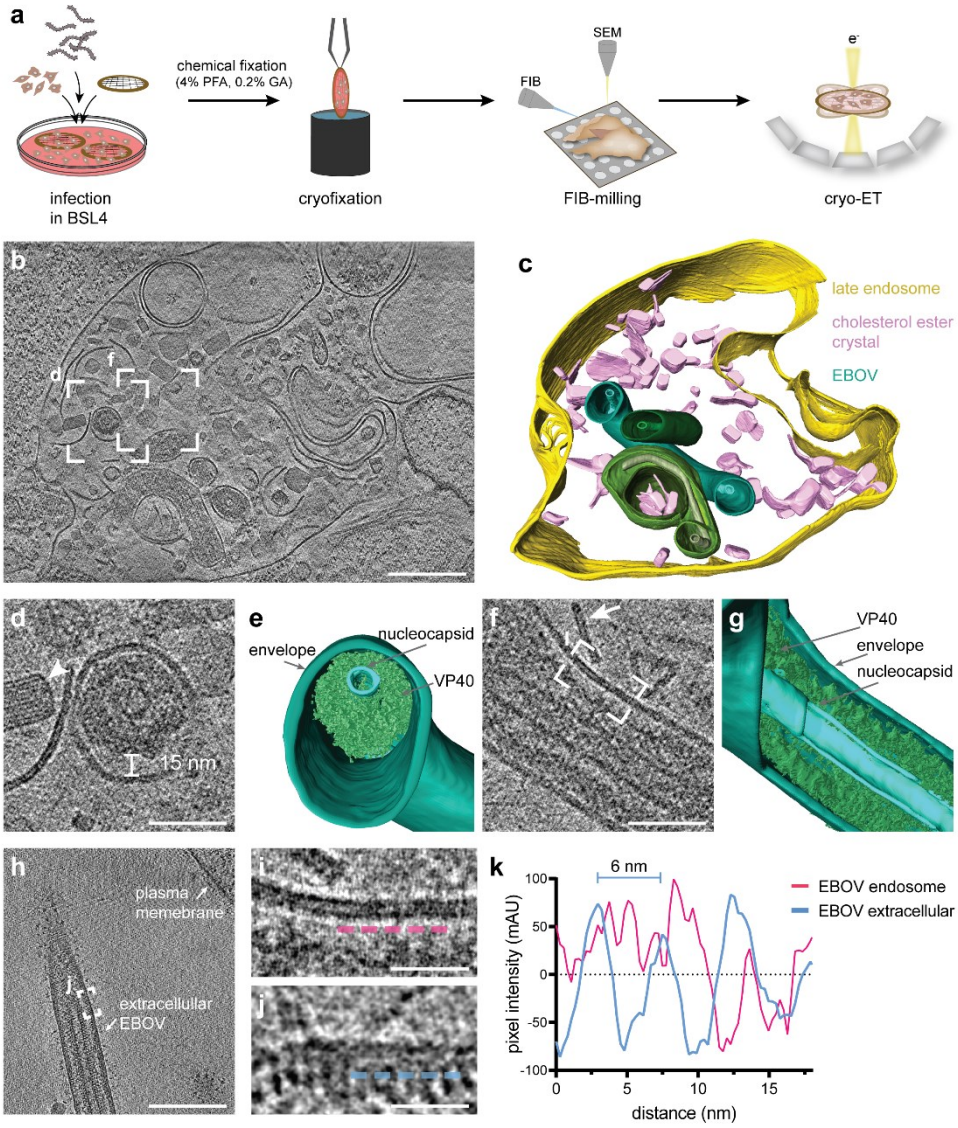

Figure 27: In situ cryo-ET of Ebola virions entering host cells. (a) Schematic of the in situ cryo-ET workflow to investigate EBOVs entering host cells. After seeding Huh7 cells on EM grids and infection with EBOVs in BSL4, the samples were chemically fixed at different time-points post infection, before continuing with the in situ cryo-ET workflow outside the BSL4 containment. The samples were plunge-frozen, cells were thinned by cryo-focused ion beam (FIB) milling and tomograms were acquired on lamellae of infected cells. **(b)** Slices through a tomogram showing a crowded endosomal compartment containing Ebola virions and lipidic crystalline structures reminiscent of cholesterol ester crystals. **(c)** 3D segmentation of the tomogram shown in (b) to highlight the endosomal membrane (yellow), cholesterol ester crystals (pink) and three EBOVs with segmented viral membranes (green) and nucleocapsids (light green). **(d-e)** Area highlighted in (b) with the corresponding 3D segmentation showing the transverse cross-section of a virion next to a cholesterol ester crystal (white arrowhead). The viral membrane (segmented in green) surrounds disordered protein densities and a condensed, cylindrical tube (presumably disassembled VP40 and the viral nucleocapsid, respectively). **(f-g)** Area highlighted in (b) with the corresponding 3D segmentation showing the longitudinal cross-section of the virion including the viral membrane, disordered VP40 densities and condensed nucleocapsid. A membrane fragment adjacent to the virion is highlighted by a white arrow. **(h)** Slices through a tomogram acquired adjacent to the plasma membrane of an infected cell showing the cross-section of a filamentous EBOV. **(i-j)** Magnified view of the membrane and adjacent protein densities of the virions highlighted in (f) and (h), respectively. Line density profiles were determined adjacent to the inner membrane monolayers as indicated by the dotted lines. **(k)** Line density profiles determined close to the membrane of virions found in an endosomal compartment (magenta), or extracellularly in close proximity to the plasma membrane of an infected cell (blue). Scale bars: (b), (h): 200 nm, (d), (f): 50 nm, (i), (j): 20 nm.

Characterization of crystalline lipidic structures in endosomal compartments

All EBOVs captured inside an infected cell were located in membrane-delimited compartments that were crowded with crystalline lipidic structures, with more than 50 structures found in the tomogram shown in Figure 27 alone (Fig. 28 a-c). To further characterize them, I determined line profiles across cross-sectional slices showing the regular membrane spacing, as well as Fourier-transform analysis (Fig. 28 d-f). They revealed a membrane spacing of 3.2 nm, consistent with the spacing found in cholesterol ester crystals previously described in studies of lamellar bodies, lipid droplets, and isolated low-density lipoprotein particles (van Niel et al., 2015; Mahamid et al., 2019; Klein et al., 2020b). Besides the crowded nature of the organelles and the presence of membrane fragments and vesicles, the large number of cholesterol ester crystals further confirms that the EBOVs analysed above reside within late endosomal/ lysosomal compartments.

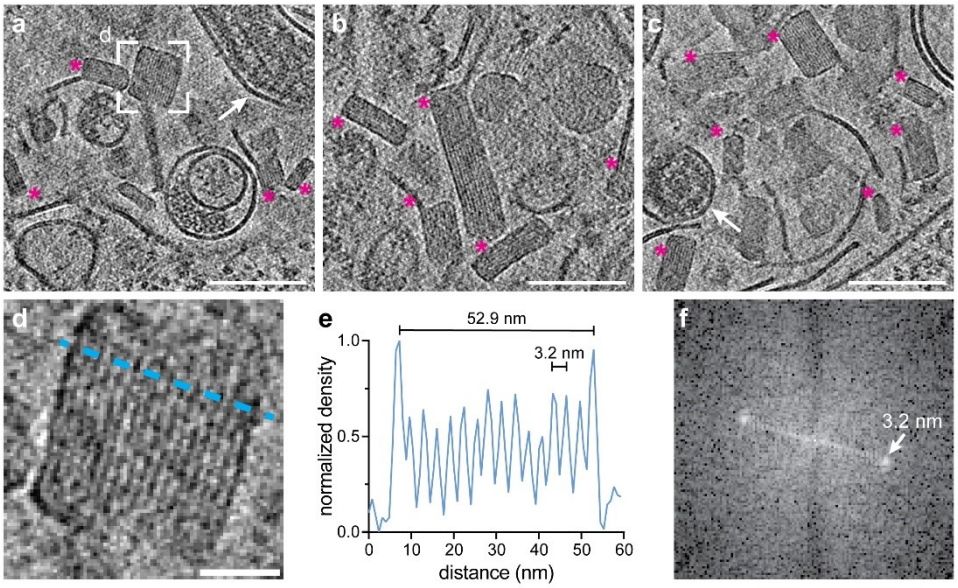

Figure 28: Characterization of crystalline lipidic structures in endosomal compartments. (a-c) Slices through the tomogram shown in Figure 18 showing examples of crystalline lipidic structures (magenta asterisks). Virions found adjacent to the structures are highlighted by white arrows. **(d)** Structure highlighted in (a) showing the regularly spaced organization of parallel membrane sheets. **(e)** Line density profile determined across the structure shown in (d) revealing its diameter (52.9 nm) and 3.2 spacing between adjacent membrane sheets. **(f)** Fourier-transform analysis of the tomogram shown in (d) confirming the 3.2 nm spacing between the membrane sheets. Scale bars: (a-c): 100 nm, (d): 20 nm.

2.7 Actin cytoskeleton in Filoviruses

As briefly mentioned before (Fig. 16), Ebola and Marburg VLPs were observed to contain actin filaments lining the VP40 matrix inside the VLPs. Actin is required for the trafficking of VP40 dimers in infected and transfected cells to the plasma membrane and is therefore indispensable for virion assembly (Kolesnikova et al., 2007; Adu-Gyamfi et al., 2012). However, whether the filaments interact with VP40 directly or via adaptor proteins, and how this interaction is modulated upon nucleocapsid incorporation into budding particles remains unknown. Furthermore, although the presence of actin in Ebola VLPs has been described by Western blotting of purified VLPs (Han and Harty, 2005), whether only traces are incorporated and whether they interact with viral proteins has not been structurally investigated. I thus analysed tomograms of Ebola and Marburg VLPs with respect to the localization of actin filaments within filamentous particles (Fig. 29). Interestingly, actin filaments exclusively lined the VP40 matrix as particularly apparent from near-to-surface tomographic slices of Ebola VLPs (Fig. 29 c). Remarkably, at branching points within the pleomorphic VLPs, the VP40 matrix had detached from the membrane but maintained the linear organization of the VP40 dimers that stayed attached to the actin filament (Fig. 29 b). Similarly, actin filaments in Marburg VLPs closely interacted with the mVP40 matrix, which appeared to "peel off" the membrane in bent VLP areas while maintaining their contact to actin (Fig 29 d-f). The proximity of actin filaments to the VP40 matrix in both Ebola and Marburg VLPs together with the absence of protein densities between the filaments suggests that the actin-VP40 interaction does not require additional adaptor proteins and that VP40 binds directly to actin.

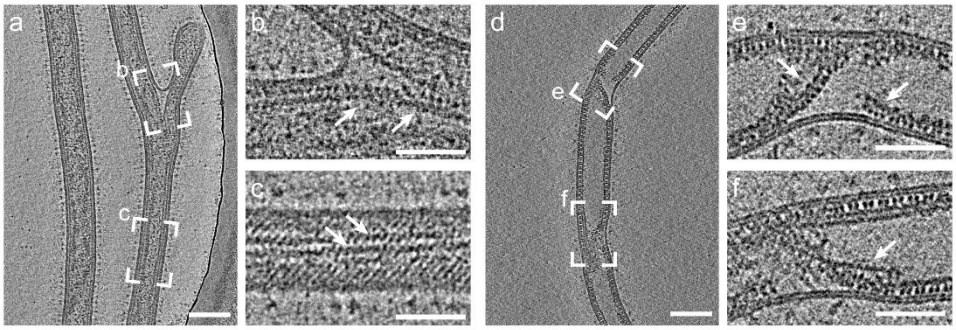

Figure 29: Imaging the actin cytoskeleton in Ebola and Marburg VLPs. (a) Slices through a tomogram showing filamentous Ebola VLPs composed of GP and VP40. **(b)** Area highlighted in (a) showing the branching point of a VLP with the VP40 matrix sitting tightly on an actin filament (white arrows). The VP40 matrix is detached from the VLP membrane as apparent from the void between membrane and VP40. **(c)** Near-to-surface tomographic slices of the area shown in (a) highlighting actin filaments underneath the VP40 matrix running parallel to the VLP membrane (white arrows). **(d)** Slices through a tomogram showing a filamentous Marburg VLP composed of GP and mVP40. **(e)** Area highlighted in (d) where the VLP bends and the mVP40 matrix appears to peel off the VLP membrane along an actin filament (white arrows). **(f)** Area highlighted in (d) where similar to the example in (e) the mVP40 matrix appears to peel off the VLP membrane and is in close contact with an actin filament (white arrow). Scale bars: (a), (d): 100 nm, (b), (c), (e), (f): 50 nm.

To facilitate visualization of the actin organization in VLPs in 3D, I then segmented both actin filaments and the VP40 matrix in Ebola VLPs imaged by dual-axis Volta phase plate cryo-ET (Fig 30). As described above (Fig. 29 a-c), actin filaments lined the VP40 matrix as apparent from cross-sections and near-to-surface tomographic slices (Fig. 30 a, b, d, e) and closely resembled actin filaments found outside the particles, presumably co-purified with the VLPs (Fig. 30 c, f). Accordingly, line density profiles determined

across the filaments revealed a similar spacing of approximately 7 nm. Importantly, the filaments closely resemble actin filaments imaged by cryo-ET in vitro and in cells (Galkin et al., 2015; Martins et al., 2020). The 3D segmentation further highlights that actin filaments are running along the VP40 matrix in Ebola VLPs and align diagonally to its helical arrangement (Fig. 30 h, i). Due to limited time, a similar segmentation of Marburg VLPs is still missing, which could reveal potential differences in the actin-VP40 organization.

The absence of compact nucleocapsids from the VLPs imaged here suggests that actin and nucleocapsids may interact with similar motifs within the VP40 NTDs, and thus compete for incorporation into VLPs. Whether the nucleocapsids replace actin during the budding of EBOVs, thereby explaining the absence of actin filaments from EBOVs (Fig. 11), remains to be elucidated.

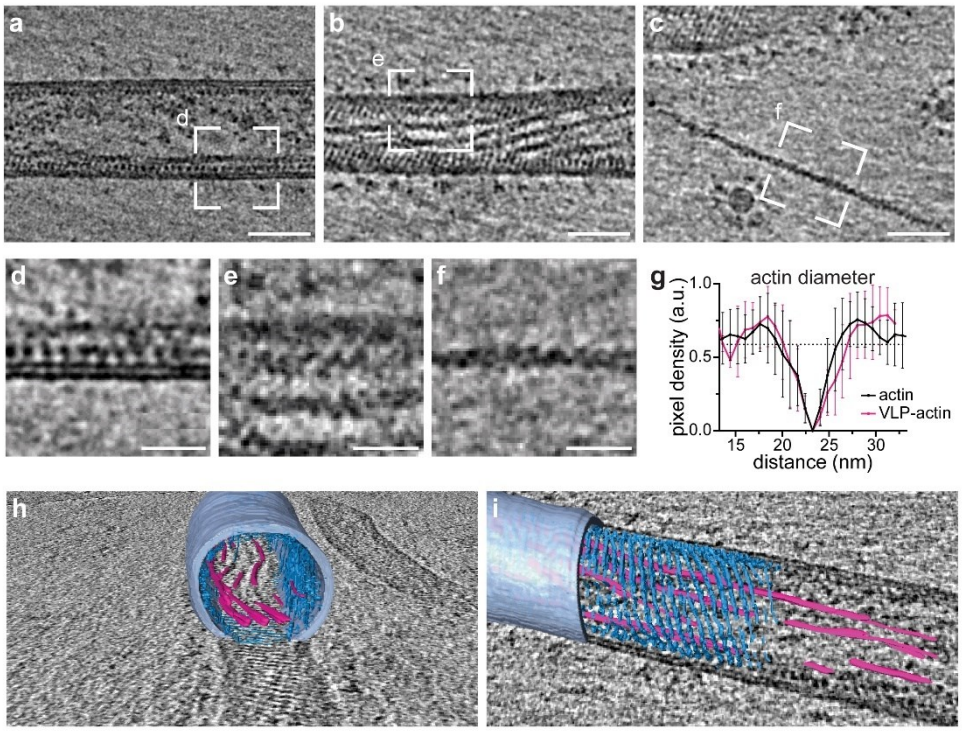

Figure 30: Dual-axis Volta phase plate cryo-ET of Ebola VLPs reveals the actin filaments inside VLPs. (a) Cross-sectional slices through a tomogram of a filamentous Ebola VLP composed of GP and VP40 and containing actin filaments. **(b)** Near-to-surface tomographic slices of the VLP shown in (a) displaying actin filaments running diagonally across the VLP width, just underneath the VP40 matrix. **(c)** Slices through a tomogram showing an actin filament co-purified with Ebola VLPs. **(d)** Area highlighted in (a) highlighting from top to bottom the VLP membrane, VP40 matrix lining the inner membrane monolayer and an actin filament running along the VP40 proteins. **(e)** Area highlighted in (b) illustrating actin filaments close to VLP surface. **(f)** Magnified view of the actin filament in (c) revealing its helical organization. **(g)** Line density profiles across actin filaments outside and inside VLPs (black and magenta profiles, respectively). The mean pixel density is shown with the standard deviation (n= 20 for actin outside a VLP, n = 13 for actin within a VLP). The dotted line indicates the average background pixel density. The diameter of actin filaments was determined as the distance between the intersects of the background line with the line density profiles and revealed a diameter of approximately 7 nm. Scale bars: (a-c): 50 nm, (d-f): 20 nm. The data presented in this figure are published (Winter and Chlanda, 2021b).

2.8 Incorporation of nucleocapsids into VLPs

Throughout this work, I primarily used Ebola VLPs instead of infectious EBOVs to facilitate the experimental setup, avoid chemical fixation for structural studies and study the effect of individual viral proteins on particle morphology. To resemble EBOVs as closely as possible, I initially used Ebola VLPs composed of GP, VP40 and the nucleocapsid proteins NP, VP35 and VP24, which have been reported to form particles with fully assembled nucleocapsids (Wan et al., 2017). However, in my hands, these VLPs rarely contained compact nucleocapsid structures, but loosely coiled assemblies. To study the fate of the nucleocapsid during virus entry and uncoating, I attempted to optimize the VLP production to obtain particles containing condensed nucleocapsids, as described in the following.

Ebola VLPs contain loosely coiled nucleocapsids

To structurally characterize Ebola VLPs containing nucleocapsids composed of NP, VP35 and VP24, I expressed these proteins along with EBOV GP and VP40 in equimolar ratios. After purification from the cell culture media, I imaged the VLPs by cryo-ET and analysed them with respect to the presence of nucleocapsid structures I expected to span the lengths of the particles as seen in purified Ebola virions (Fig. 11). The filamentous VLPs contained loosely coiled nucleocapsids spanning the length of the particles (Fig. 31 a, n= 33) but did not contain condensed nucleocapsid assemblies with the typical boomerang-shaped protrusions (Bharat et al., 2012; Wan et al., 2017). I then analysed VLPs directly from the cell culture media without prior purification to exclude that the ultracentrifugation steps during purification damage the particles. However, similar to the purified VLPs, unpurified VLPs contained loosely coiled structures spanning the length of the particles (Fig. 31 c, n=7) but did not show the typically condensed nucleocapsids. Altering the protein levels during VLP production from HEK 293T cells equally did not result in VLPs containing condensed nucleocapsids (data not shown).

Surprisingly, when investigating purified VLPs, I often found nucleocapsid structures in different assembly states outside the VLPs (Fig. 31 e-h). They were presumably co-purified from the cell culture media and formed clusters on the EM grids that contained loosely coiled and condensed nucleocapsids.

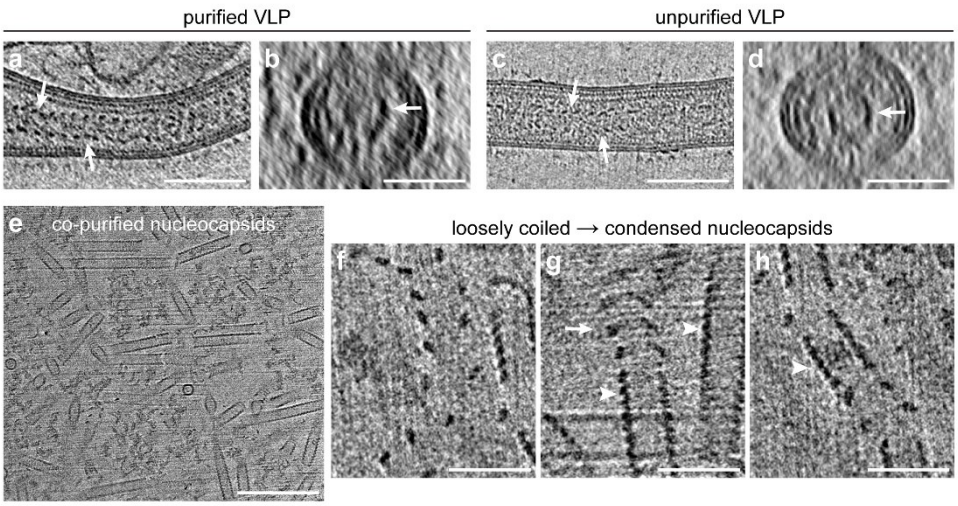

Figure 31: Nucleocapsid incorporation into Ebola VLPs. (a-b) Longitudinal and transverse cross-sections of a tomogram showing a purified, filamentous Ebola VLP composed of GP, VP40 and the nucleocapsid proteins NP, VP24 and VP35. The core of the particle is spanned by a loosely coiled nucleocapsid (white arrows, n= 33). **(c-d)** Longitudinal and transverse cross-sections of a tomogram showing a filamentous Ebola VLP composed of GP, VP40 and the nucleocapsid proteins NP, VP24 and VP35. The VLP was not purified but imaged directly from the supernatant of VLP-producing HEK 293T cells. As in purified VLPs, the nucleocapsid spans the length of the particle but is loosely coiled (white arrows, n=7). **(e)** Slices through a tomogram showing nucleocapsid assemblies that were co-purified from the supernatant of VLP-producing HEK 293T cells during the purification and enrichment of Ebola VLPs (exemplarily shown in (a-b). **(f-h)** Magnified views of loosely coiled (f) and condensed nucleocapsids shown in (e). The nucleocapsid shown in (g) is partially loosely coiled (white arrow) and transitions into a condensed state (white arrowhead). The nucleocapsid in (h) is condensed and kinked. Scale bars: (a), (c): 100 nm, (b), (d), (f-h): 50 nm, (e): 200 nm.

To increase the contrast of the cryo-ET images and reduce the missing wedge inherent in cryo-ET, I then imaged purified VLP preparations by dual-axis Volta phase plate cryo-ET. Clusters of co-purified nucleocapsid assemblies could thereby be analysed in 3D using isosurface renderings (Fig. 32 a-b). They revealed similar nucleocapsid assemblies as seen before (Fig. 31) clearly showing different condensation states including the helical coil of the loosely coiled nucleocapsid structures. Furthermore, I could identify three nucleocapsid assembly states by their level of condensation: loosely coiled nucleocapsids resembling a spring that is pulled apart, condensed nucleocapsids that form compact cylindrical structures, and "decorated-condensed" nucleocapsids which contain additional boomerang-shaped densities protruding from the condensed nucleocapsid helix (Fig. 32 c). These data are also published in our recent manuscript on the applicability of dual-axis Volta phase plate cryo-ET (Winter and Chlanda, 2021).

Together, these data suggest that condensed nucleocapsids are formed during VLP production in HEK 293T cells but are either insufficiently transported to VLP budding sites, poorly incorporated into VLPs, or decondense after incorporation into VLPs.

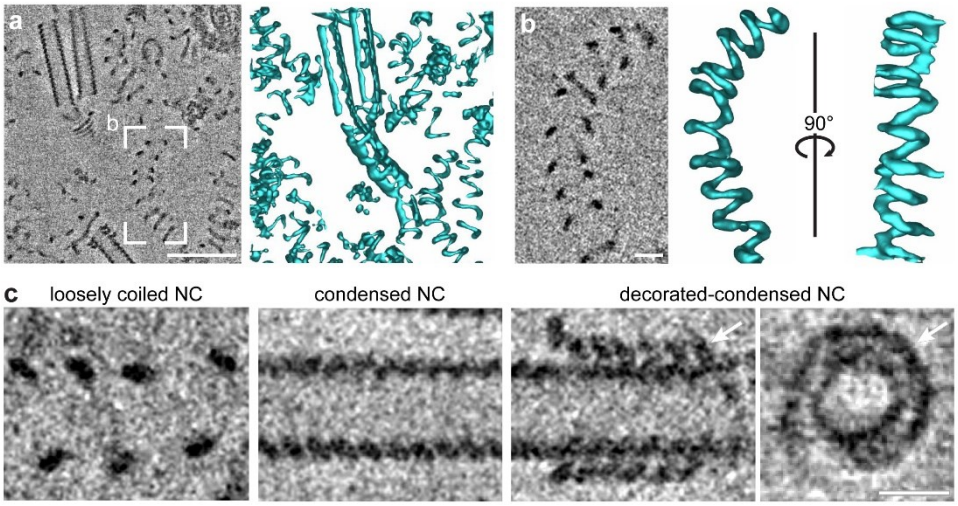

Figure 32: Analysis of nucleocapsid condensation states by dual-axis Volta phase plate cryo-ET. (a) Slices through a tomogram showing nucleocapsids that were co-purified during the preparation of Ebola VLPs composed of GP, VP40 and the nucleocapsid proteins NP, VP35 and VP24. The enhanced contrast achieved by using a Volta phase plate during cryo-ET acquisition enabled automatic isosurface rendering of the nucleocapsids in 3D. **(b)** Area highlighted in (a) showing a loosely coiled nucleocapsid with the respective isosurface rendering in 3D shown from two different angles. **(c)** Slices through tomograms showing three different nucleocapsid assembly states: loosely coiled, condensed and decorated-condensed. Decorated-condensed nucleocapsids display protrusions from the condensed helical structure (longitudinal cross-section) seen as an additional ring when viewed from the transverse cross-section (white arrows). Scale bars: (a): 100 nm, (b-c): 20 nm.

Characterization of transcription- and replication- competent Ebola VLPs

Since condensed nucleocapsids were observed in all EBOVs imaged by cryo-ET, I then assessed, whether the presence of viral RNA influences the formation and incorporation of condensed nucleocapsids into VLPs. To this end, I prepared VLPs using a reverse genetics system (Hoenen et al., 2014; Schmidt et al., 2018), in which the VLPs incorporate a truncated form of the EBOV genome (Fig. 33 a). The truncated so-called "minigenome" contains leader and trailer regions of the viral genome, and encodes for the structural proteins GP, VP40 and VP24 and soluble GFP as a fluorescent marker. Upon co-expression of the remaining viral proteins, the genomes of VLPs containing the minigenome are transcribed and replicated. Accordingly, VLPs incorporating this minigenome are referred to as tetracistronic transcription and replication-competent virus-like particle (trVLP). trVLPs are produced by expressing the minigenome and all proteins required for the viral transcription machinery and formation of the nucleocapsid on separate plasmids. By additionally expressing a T7 polymerase required to transcribe the DNA minigenome into RNA, trVLPs are produced that incorporate the truncated EBOV RNA genome. After harvesting the trVLPs from the cell culture media, they can then be used to infect target cells expressing the viral transcription machinery and – to increase EBOV uptake – the EBOV receptor TIM-1 (Figure 33 b). To increase the yield of trVLPs released into the cell culture media, I passaged the trVLPs for up to five rounds of infection before purifying the particles. The expression of GFP in the cytoplasm of infected cells served to estimate the increase in productive trVLP infection and consequently particle production over time (Fig. 33 c).

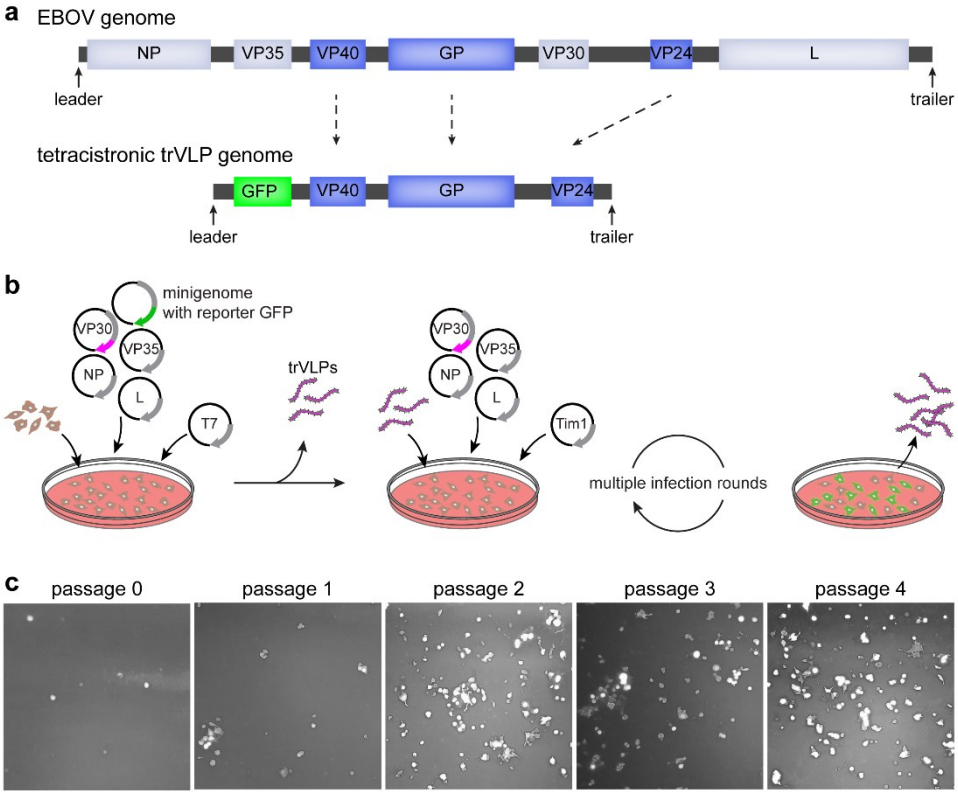

Figure 33: Production of transcription- and replication- competent VLPs (trVLPs) containing a minigenome. **(a)** Schematic of the EBOV genome in comparison with the trVLP genome. On the truncated minigenome, the EBOV matrix protein VP40, glycoprotein GP and minor matrix protein VP24 are encoded along with their leader, trailer and intergenic regions as well as a soluble GFP. **(b)** Schematic of the trVLP production workflow. trVLPs are generated by transfecting HEK 293T cells with plasmids encoding the EBOV transcription machinery (VP30, NP, VP35 and L), the tetracistronic minigenome, and a T7 promotor to initiate transcription by the host cell machinery. Second generation trVLPs are produced by infecting cells carrying the plasmids for the transcription machinery and the EBOV receptor TIM-1 with trVLPs. Multiple infection/ transfection rounds amplify the trVLP yield. **(c)** Widefield microscopy images acquired using a 488 nm filter of HEK 293T cells infected with trVLPs produced in several rounds of infection.

I aimed to structurally investigate trVLPs to assess whether they can be used as an alternative to VLPs that represent a more authentic system due to the presence of a genome. To visualize the nucleocapsid in future experiments, I produced trVLPs expressing fluorescently tagged VP30, which localizes to nucleocapsids (Groseth et al., 2009; Schudt et al., 2015) and was shown to have no influence on replication and transcription when tagged C-terminally (Bodmer and Hoenen, 2022). To visualize nucleocapsids and their assembly sites in viral inclusion bodies against the background of GFP expressed upon productive trVLP infection, I cloned mScarlet C-terminally to VP30. When expressed alone, VP30-mScarlet distributed evenly throughout the cytoplasm but re-localized to distinct inclusion bodies upon co-expression of the nucleocapsid proteins NP, VP35 and the polymerase L (Fig. 34 a). The inclusion bodies were well visible during progressive trVLP infection, as assessed by fluorescence light microscopy of Huh7 target cells infected with trVLPs and observed 5 hours post infection (hpi), 21 hpi and 48 hpi (Fig. 34 b). With progressive onset of infection, the expression of soluble GFP increased.

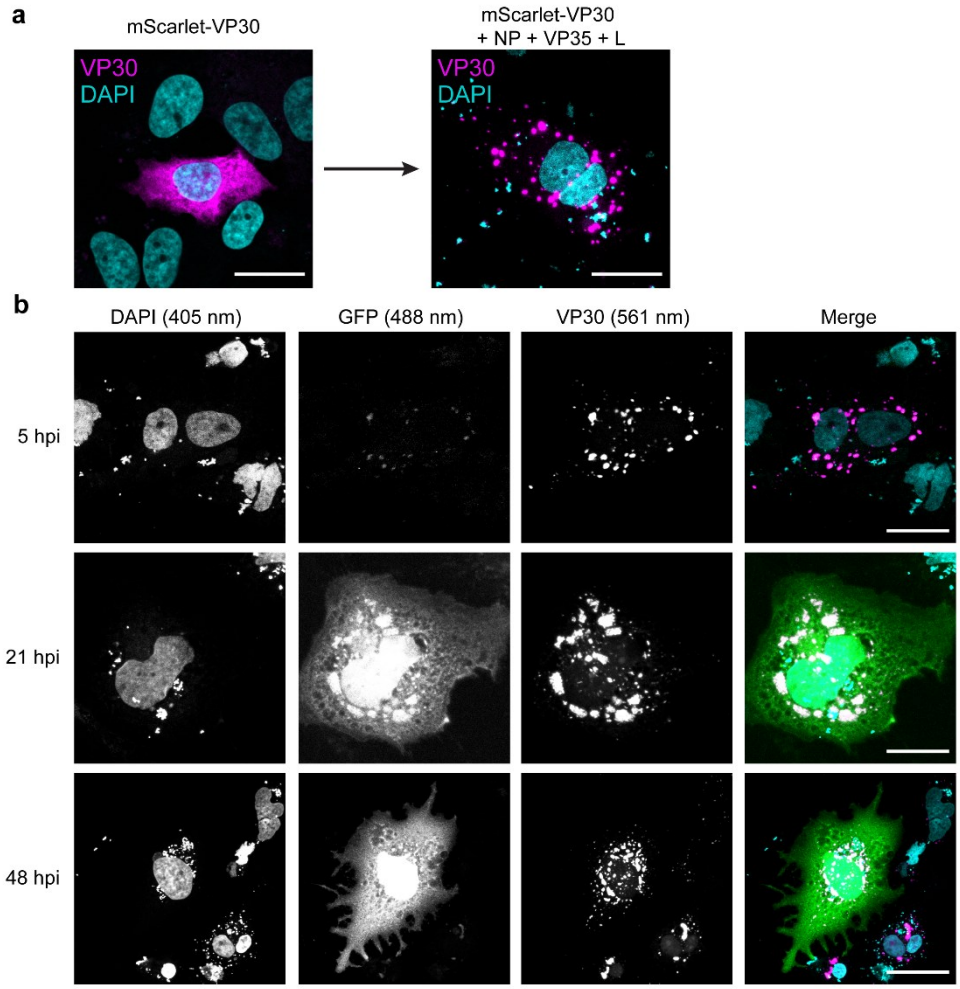

Figure 34: Propagation of trVLPs. (a) Maximum intensity projections of confocal light microscopy images of Huh7 cells expressing VP30-mScarlet alone, or VP30-mScarlet and the transcription machinery (NP, VP35 and L) to visualize inclusion bodies; sites of viral RNA replication and transcription. When expressed alone, VP30-mScarlet displays a cytosolic localization and re-localizes to discrete puncta upon co-expression of the transcription machinery. **(b)** Maximum intensity projections of confocal light microscopy images of Huh7 target cells expressing the EBOV transcription machinery (VP30-mScarlet, NP, VP35 and L) and the EBOV receptor TIM-1 at different time-points after infection with trVLPs. With increasing time after infection, the cytosolic GFP expression increases, indicating infection with trVLPs and expression of the minigenome. Scale bars: 20 µm (except for 48 hpi: 10 µm).

After three passages, trVLPs were purified from cell culture media and I structurally characterized them by cryo-ET (n= 24). The production and purification of the trVLPs was performed by Lisa Augenstein under my supervision.

Similar to VLPs lacking a minigenome, many trVLPs were filamentous with a uniform diameter and variable length of 2 µm ± 0.9 µm (n=11) as assessed by negative stain EM. The VLP surface was studded with GPs and the VP40 matrix was clearly visible from both transverse and longitudinal cross-sections (Fig. 35 a-c). The trVLP lumina appeared crowded and nucleocapsids could not unequivocally be identified (Fig. 35 d). However, nucleocapsids outside trVLPs, presumably co-purified from the supernatant of trVLP-producing cells, were identified easily (Fig. 35 e, f). Similar to the nucleocapsids co-purified during VLP preparations (Fig. 31-32), they were loosely coiled with a diameter of approximately 30 nm or condensed with a uniform diameter of approximately 25 nm.

Taken together, while the trVLP system is a promising tool to study EBOV replication in BSL1 conditions and viral spread (Fig. 33 and Fig. 34), the production of sufficient particles for structural analysis is time-consuming and so far, did not reveal improvements in nucleocapsid incorporation compared to VLPs. Since the particles were produced from HEK 293T cells and not from VeroE6 cells, which are commonly used for EBOV production, the influence of the producing cell line on particle assembly needs to be further assessed.

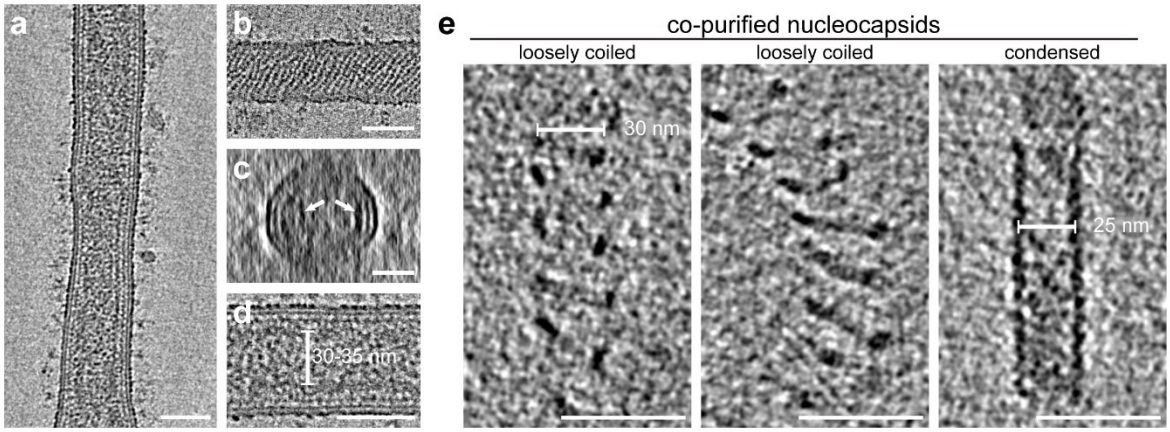

Figure 35: Characterization of trVLPs by cryo-ET. (a-d) Slices through a tomogram showing a filamentous trVLP including near-to surface tomographic slices showing the typical striations of the VP40 matrix (b) and longitudinal and transverse cross-sections (a) and (c), respectively. **(d)** Magnified view of the cross-section highlighted in (a) showing luminal densities parallel to the trVLP membrane with a spacing of 30-35 nm. **(e)** Tomographic slices showing co-purified nucleocapsid (nucleocapsid) assemblies, including loosely-coiled and condensed nucleocapsids of 30 nm and 25 nm diameter, respectively.

3 Discussion

EBOVs enter host cells via the endocytic route and release their genome into the cytoplasm after fusion of the viral with the endosomal membrane. To date, the mechanism of EBOV uncoating and the spatiotemporal regulation of genome release from the viral particles are poorly understood. Specifically, the role of the viral matrix protein VP40 that constitutes the scaffold underneath the viral envelope and is responsible for the EBOV shape and stability during virus transmission and entry is not known. Here, I investigated EBOV uncoating with a focus on the VP40 matrix. Using cryo-ET, I discovered that the VP40 matrix in Ebola virions disassembles in acidic environments and explored the extend of this disassembly and its implications for EBOV membrane fusion by complementary fluorescence-based techniques. These data show that EBOV uncoating is initiated inside late endosomes by low-pH driven disassembly of the VP40 matrix, followed by membrane fusion and concluded by nucleocapsid uncoating presumably in the cytoplasm by yet unknown mechanisms.

3.1 Low pH triggers disassembly of the EBOV VP40 matrix

The VP40 matrix disassembles at low pH in vitro

Since EBOV enter cells by fusion of the viral with the endosomal membrane in late endosomal compartments, I first investigated the structure of Ebola VLPs at the late endosomal pH of 4.5 in direct comparison with their structure at neutral pH. Irrespective of the protein composition of the VLPs, I found that the VP40 matrix detaches from the membrane and disassembles in low pH environments (Fig. 10). The detachment of the VP40 matrix from the membrane coincides with a more variable diameter of the particles, presumably as a result of released constraints imposed on the membrane. This suggested that the particles might relax altogether from filamentous to the energetically more favourable spherical shape. However, a global change of filamentous to spherical morphology was not observed (Fig. 12). Considering that the surface-to-volume ratio is higher for filamentous than for spherical shapes, a change to spherical morphologies would only be possible if the VLP membrane was permeable to allow the influx of water and increase the volume of the particles. Since the VLPs analysed in this work were subjected to low pH for 30 min, the time range might have been too short to allow passive diffusion of water molecules across the VLP membrane and thus observe an increase in the number of spherical particles. This indicates that EBOVs, which reside for a short time in acidic compartments during entry (Spence et al., 2016; Simmons et al., 2015; Mingo et al., 2015), likely do not undergo global morphological changes prior to membrane fusion. However, surface-to-volume ratio changes are likely to occur upon fusion pore formation. Surprisingly, the number of spherical particles in VLP preparations was high at both neutral and low pH (Fig. 12). In the context of MARV infection, spherical particles have been observed after prolonged infection and were less infectious than filamentous particles (Welsch et al., 2010). Accordingly, the number of spherical particles released from MARV-infected cells increased from 12% at early time points to 70% at late stages during infection. Similarly, the number of spherical Ebola VLPs may be caused by exhaustion

of the producing cell line due to the overexpression of proteins, ultimately resulting in the formation of aberrant, spherical particles.

To substantiate my observations on the low pH-phenotype of VLPs with respect to the VP40 matrix, I also studied isolated filamentous EBOV particles by cryo-ET. Compared to EBOVs subjected to neutral pH, the VP40 matrix appeared less ordered in EBOVs subjected to low pH, arguing for low pH-driven disassembly as observed in VLPs. In contrast to the phenotype in VLPs, however, the matrix stayed attached to the viral envelope. Since the EBOVs were inactivated after acidification by chemical fixation, which causes the cross-linking of proteins and membranes in close proximity to each other, the VP40 proteins were likely tethered to the membrane lipids. This is further supported by the structural characterization of Ebola VLPs at pH 4.5 after they had been chemically fixed according to the protocol employed for the fixation of EBOVs (Fig. 11). Similar to EBOVs, chemically fixed VLPs displayed disordered VP40 densities but remained apparently "glued" to the VLP membrane. Due to the need for EBOV inactivation by chemical fixation, it was impossible to verify the detachment of the VP40 matrix from the viral envelope at pH 4.5 using EBOVs. Other inactivation methods, such as cryo-UV illumination could be applied to circumvent chemical fixation (Depelteau et al., 2022), however, this method can only be used after plunge freezing, which would have to be performed under BSL4 conditions. Importantly, several studies have shown that VP40 proteins from both EBOVs and MARVs contain basic patches of lysine residues on their surface (Bornholdt et al., 2013b; Oda et al., 2016), which are engaged in electrostatic interactions with negatively charged membrane lipids (Bornholdt et al., 2013b; Del Vecchio et al., 2018; Bhattarai et al., 2017). As acidification neutralizes these charges, it is plausible that VP40 indeed detaches from the membrane concomitant with the disassembly of the VP40 matrix.

VP40 dimers form the VP40 matrix

The disassembly of the VP40 matrix at low pH and its detachment from the VLP membrane in the absence of chemical fixation suggests that VP40-membrane interactions are modified by acidic environments. To further elucidate these interactions in the context of virus particles, I investigated the structure of the VP40 matrix in VLPs composed of VP40 and GP at neutral pH. Subtomogram averaging revealed the linear arrangement of VP40 dimers (Fig. 13), which interact tightly with lipids in the inner VLP membrane monolayer. At the start of this project, several crystal structures of VP40 had been published including monomeric VP40, dimeric VP40, hexameric VP40 and octameric VP40 (Dessen, 2000; Ruigrok et al., 2000; Scianimanico et al., 2000; Gomis-Rüth et al., 2003; Bornholdt et al., 2013b; Landeras-Bueno et al., 2021). Based on these studies performed on purified VP40 proteins, the VP40 matrix was hypothesized to be composed of hexamers with the CTDs alternatingly facing the membrane (Bornholdt et al., 2013b). However, none of the structures was solved in the native context of virus particles and VP40-lipid interactions had been probed exclusively by mutagenesis studies and molecular dynamics (MD) simulations of the different oligomers (Bornholdt et al., 2013b; Del Vecchio et al., 2018; Nguyen et al., 2005; Scianimanico et al., 2000). In 2020, another cryo-ET study of Ebola VLPs, EBOVs and MARVs resolved

the VP40 matrix by subtomogram averaging (Wan et al., 2020), which is in agreement with the structure presented here. In the dimeric conformation, all VP40 C-termini, which interact with membrane lipids, are facing the inner membrane monolayer, arguing for strong electrostatic interactions. This was confirmed by all-atom MD simulations performed by Fabio Lolicato (Nickel lab, BZH Heidelberg) and shown here in direct comparison with the subtomogram average presented in this thesis. By comparing the known crystal structure of VP40 with the membrane bound state of the MD simulation and our subtomogram average, I could show the extension of flexible C-terminal loops inserted into the inner membrane monolayer and a rotation of the VP40 monomers along the N-terminal dimerization domain (Fig. 15) upon membrane binding. Together with the observation that the VP40 matrix accommodates different shapes including spherical particles and filamentous VLPs with kinks and bends (Fig. 12 and 14, respectively), this underlines the high conformational modularity of the VP40 matrix and illustrates how these particles can adopt pleiomorphic shapes without breaking.

Our lipidomics data on purified Ebola VLPs show that the VLP membrane, similar to the plasma membrane (Leventis and Grinstein, 2010; Lingwood and Simons, 2010; Risselada, 2019), is enriched in the anionic lipids phosphatidylserine and phosphatidylinositol (Fig. 15). Phosphatidylserine has long been identified as an important lipid involved in the recruitment of VP40 to the plasma membrane during budding (Adu-Gyamfi et al., 2015; Soni and Stahelin, 2014; Jeevan et al., 2017; Husby et al., 2022). Similarly, it engages in electrostatic interactions with matrix proteins of other viruses, such as influenza A virus M1 (Bobone et al., 2017), and is enriched in viral budding sites. Phosphatidylinositol is often phosphorylated and part of the membrane lipid phosphatidylinositol 4,5-bisphosphate (PIP2), which was shown to be specifically recruited and immobilized at HIV budding sites (Yandrapalli et al., 2016; Favard et al., 2019) and strongly promotes membrane association of the matrix proteins of Measles and Nipah virus (Norris et al., 2022). The role of PIP2 in EBOVs infection is less well characterized but was suggested to stabilize the VP40-membrane interaction (Jeevan et al., 2016). Since phosphatidylserines in the EBOV envelope are flipped to the outer leaflet (Nanbo et al., 2018; Nanbo and Kawaoka, 2019; Acciani et al., 2021), at least to some extent, PIP2 might be required to maintain the VP40 anchored to the viral envelope. In a recent MD simulation (Jeevan et al., 2017), PIP2 was shown to interact specifically with VP40. It would be interesting to expand the MD simulations presented here using a more comprehensive lipid composition. This could further be used to model VP40-membrane interactions at low pH to simulate the dissociation of VP40 upon interrupting the electrostatic interactions. We have shown this in a recent preprint, where we explored the role of pH-driven VP40 disassembly during virus entry (Winter et al., 2022). Fabio Lolicato (Nickel lab, BZH Heidelberg), who performed the MD simulations, determined the binding energies of VP40 dimers to a synthetic membrane containing 30% phosphatidylserine at neutral and low pH. Although the amount of phosphatdylserines used in the simulation exceeds physiological concentrations found in the plasma membrane to mimic the overall negative charge of the inner membrane monolayer, these data confirm a significant decrease in binding energy at low pH, further supporting the dissociation of VP40 from the membrane observed in this study.

3.2 Acidification of EBOV lumina occurs independently of a dedicated ion channel

The cryo-ET data of Ebola VLPs and virions presented in this work clearly show that the VP40 matrix in EBOVs is sensitive to low pH. This implies acidification of the viral lumina across the viral envelope, a process that has not been investigated for EBOVs yet. I show here in collaboration with Gonen Golani (Schwarz lab, ITP Heidelberg) that protons passively diffuse across the membrane of Ebola VLPs (Fig. 17-19), albeit at slower kinetics compared to the plasma membrane and protein-free liposomes (Deamer and Bramhall, 1986; Deamer, 1987). The plasma membrane has a complex protein composition that includes ion channels (DeCoursey, 2008), likely contributing to its higher permeability to protons. Due to the small radius of the Ebola virions, the pH equilibration across the viral envelope is nevertheless fast and takes place within minutes as shown in this study (Fig. 19). This suggests that acidification is not rate-limiting during virus entry into host cells. Since EBOVs do not encode a dedicated ion channel, passive proton diffusion is an important mechanism of acidification that has been neglected to date.

Several other enveloped viruses entering via acidic compartments encode virus-specific ion channels (reviewed here (Fischer and Sansom, 2002; Nieva et al., 2012)), called viroporins. They fulfil different functions during the viral replication cycle and interfere in a number of cellular pathways (Nieva and Carrasco, 2015; Xia et al., 2022), but only the influenza A viroporin M2 and the E protein of the β-coronaviruses SARS-CoV-1 and -2 (Cao et al., 2021) are known to incorporate into viral particles. It is well established that low endosomal pH equilibrates across the envelope of internalized influenza A viruses during host cell entry to facilitate virus uncoating. Acidification of the virus lumen is realized by M2 and is required to detach the M1 matrix from the viral membrane and allow vRNP release from the particles (Fontana and Steven, 2013). Unlike influenza viruses and as stated above, EBOVs do not express a dedicated ion channel and we show here that acidification occurs by passive diffusion in timescales well in line with the entry kinetics of Ebola virions. We nevertheless considered the possibility of an unknown viral ion channel that may accelerate acidification and play a role during infection. In this context, the only known viral protein that could fulfill this function is the delta-peptide produced during the maturation of EBOV sGP, which is secreted at high levels during EBOV infection. The viral gene encoding sGP contains several ORFs due to a poly-adenosine site that causes frequent stuttering of the viral polymerase. This leads to the primary expression of sGP (and by extension the delta peptide) and only secondary expression of the full-length membrane-bound GP that is incorporated into the viral membrane (Mehedi et al., 2013). Since the closely related MARVs lack the different ORFs found in EBOVs and exclusively express membrane bound full-length GP, they do not express the delta-peptide (Will et al., 1993; Feldmann et al., 2001). However, the delta-peptide is expressed in all EBOV species as well as Lloviu cuevavirus (Gallaher and Garry, 2015; Kuhn et al., 2019). Its CTD contains a stretch of highly conserved, hydrophobic amino acids, arguing for an important function during EBOV infection. The EBOV delta-peptide is composed of 40 amino acids that form an amphipathic helix. It was shown that it is inserted into the plasma membrane upon expression, where it forms small pores and increases the membrane permeability even at low concentrations for anionic

compounds and small molecules (He et al., 2017; Pokhrel et al., 2019). Whether the delta-peptide is selective towards specific ions still remains unknown, with only limited evidence pointing towards chloride ions (Pokhrel et al., 2019). Its ion-channel activity has been linked to its function as an enterotoxin (He et al., 2017; Melnik et al., 2022), which contributes to the pathogenesis of EVD. Another report demonstrates the ability of the delta-peptide to block entry of pseudotyped virions bearing EBOV- or MARV-GP by a yet unknown function, indicating that the delta-peptide may also be important for the EBOV replication cycle. However, it is not known whether the delta-peptide incorporates into the viral envelope, where it could increase the permeability of the viral envelope towards protons. To date, most EBOV studies including the study presented here have been performed using recombinant infectious viruses, trVLPs or VLPs that exclusively express the full-length transmembrane GP. In this case, the *GP* gene is modified at its poly-adenosine site to prevent the expression of other GP variants and increase the yield of produced particles (Alazard-Dany et al., 2006). It would be interesting to explore a potential incorporation of the delta-peptide into virus particles and investigate whether this would affect virus entry as a result of increased viral membrane permeability. To this end, the poly-adenosine site could either be restored in trVLPs such that they produce all GP variants, or the delta-peptide could be expressed from a separate plasmid during VLP production. Mass spectrometry of purified VLPs and targeted screening for EBOV proteins based on the published sequences could be used to assess the incorporation of the delta-peptide into the VLP membrane. If indeed incorporated into their membrane, these VLPs could then be used in the assay established here to investigate acidification kinetics across the VLP membrane. The data presented here show that the envelope of Ebola VLPs is less permeable to protons than the plasma membrane, indicating that host cell ion channels do not get incorporated into the VLP envelope. Mass spectrometry of virus particles would also reveal the host cell proteome and could provide direct proof of a potential incorporation – or lack – of host cell ion channels.

As shown here, the expression of dedicated viroporins is not necessary to allow acidification across the viral membrane. Passive proton diffusion could thus be an important mechanism for other late-penetrating viruses lacking viroporins.

3.3 Low pH is critical for membrane fusion

After showing that external pH equilibrates across the EBOV membrane and has a clear effect on EBOV particle morphology in vitro, I explored its role during the cytoplasmic entry of Ebola VLPs. Based on the structural organization of VP40 proteins into a helical scaffold tightly interacting with the viral membrane in VLPs and virions, we hypothesized that the fully assembled VP40 matrix would sterically hinder fusion pore formation. To address this and investigate entry of VLPs in the presence and absence of a VP40 matrix, I set up the BlaM assay together with a master student at the time in the lab, Keerthihan Thiyagarajah. We first tested important entry inhibitors that have been used in two other studies using Ebola VLPs (Shoemaker et al., 2013; Mingo et al., 2015) and confirmed that both endosomal acidification and proteolytic processing of the EBOV GP are indispensable for host cell entry. Since low pH is required

to activate endosomal cathepsin proteases involved in GP processing, these two processes are linked, and low pH has so far exclusively been associated with GP cleavage prior to membrane fusion. To elucidate whether low pH has an additional role in detaching VP40 from the viral membrane, we decoupled low pH treatment from protease activation by generating Ebola VLPs containing cleaved GP in vitro prior to infection. These experiments revealed two important observations: (1) Ebola VLPs containing cleaved GP cannot enter target cells after blocking endosomal acidification. This indicates that low pH is either still necessary to further prime GP and alter its conformation, or it is required to detach and disassemble the VP40 matrix. (2) Ebola VLPs containing cleaved GPs can enter host cells even after blocking endosomal acidification when they are treated at low pH prior to infection. This indicates that the timing of GP processing and VP40 disassembly immediately before encountering the endosomal receptor NPC1 is not essential for efficient entry. The late entry kinetics of EBOVs may therefore be caused by the need for the virus to encounter cathepsin proteases and the endosomal NPC1 receptor during infection, both of which reside in late endosomes (Higgins et al., 1999; Neufeld et al., 1999; Brix et al., 2008). Entry of cleaved and low pH treated VLPs is still less efficient when endosomal acidification is blocked compared to entry into untreated target cells, which could have several implications. First, blocking endosomal acidification by ammonium chloride or bafilomycin might interfere with the trafficking of the VLPs to NPC1-positive endosomes. This hypothesis has been explored by Mingo et al, showing that co-localization between Ebola VLPs and NPC1 is not affected by either inhibitor (Mingo et al., 2015). Second, even though I showed the membrane-detachment of VP40 in VLPs treated at low pH in vitro (Fig. 10), this phenotype may be reversible and VLPs entering target cells encounter neutral pH en route to late endosomal compartments. I addressed this by incubating purified VLPs successively in low pH and neutral pH buffers, but the results were inconclusive, and the experiment needs to be repeated (data not shown). Furthermore, it is important to unambiguously distinguish between low pH-requirements for GP processing and VP40-membrane detachment. Based on an NMR study, the fusion peptide of GP changes conformation at low pH from an extended loop to a kinked conformation, which may be important for insertion into the target membrane prior to fusion (Gregory et al., 2011). Thus, despite my attempt to decouple the low pH requirement from proteolytic GP processing, low pH may still be required to induce conformational re-arrangements of GP. To address this in future experiments, I considered expanding this study by generating Ebola VLPs, in which the VP40-membrane interaction is stabilized and cannot be disrupted by low pH. Mutating VP40 itself is difficult as it often leads to abrogated particle formation (Bornholdt et al., 2013b) and would require a mutant that still allows the formation of a VP40 matrix with similar structural properties as in wildtype EBOVs. I thus propose instead to produce VLPs with wildtype VP40 that incorporate a viral fusion protein, which initiates membrane fusion at neutral pH, such as the HIV Env protein. Since matrix proteins often interact with cytoplasmic tails of glycoproteins (Liljeroos and Butcher, 2013), and VP40 may interact with EBOV GPs (Wan et al., 2020), efficient incorporation of HIV Env into Ebola VLPs would have to be ensured. Previously, MARV VLPs composed of mVP40 and a chimeric glycoprotein have successfully been generated (Mittler et al., 2007). The chimeric glycoprotein contained the cytoplasmic tail and

transmembrane domain of MARV GP combined with the N-terminal ectodomain of the Lassa virus GP. In a similar manner, chimeric glycoproteins containing the EBOV GP cytoplasmic tail and transmembrane domain could be cloned to the Env ectodomain, and VLPs produced with EBOV VP40 and the chimeric GP-Env protein could be used in BlaM assays. Since Env mediates membrane fusion already at the plasma membrane, the need to detach the VP40 matrix at low pH to allow membrane fusion could thereby directly be tested.

Such chimeric Ebola VLPs could also be used to reconstitute EBOV membrane fusion in vitro. Here, I performed preliminary experiments to reconstitute the fusion of Ebola VLPs and liposomes containing NPC1. These experiments showed that NPC1-containing vesicles attach to the surface of VLPs containing cleaved GP already at neutral pH (Fig. 25). Since cleaved GP is mainly composed of a transmembrane domain and a truncated 19 kDa GP1 core, it is not detectable in tomograms. Thus, to confirm the interaction of NPC1 with cleaved GP, subtomogram averaging of NPC1 proteins bridging the liposome- and VLP membrane could be performed. At sufficient resolution, this would reveal conformational changes of cleaved GP upon binding to NPC1 at different pH. The next experiment, in which I intended to structurally characterize potential fusion events between Ebola VLPs bearing cleaved GP and NPC1-containing liposomes at low pH, would suffer from the same ambiguities encountered during the BlaM assay: since potential GP conformational changes induced by low pH and the VP40 detachment/ disassembly occur simultaneously, it will likely not be possible to distinguish between these events. Hence, using VLPs incorporating a chimeric GP-Env as suggested above would allow the unequivocal analysis of fusion events and reveal whether VP40 disassembly is indeed essential for membrane fusion.

In summary, I substantiated the previously established importance of endosomal pH during EBOV entry into target cells and provided further evidence that low pH is required for VP40 detachment beyond protease activation to cleave GP. The molecular details of the viral membrane fusion and the need to disassemble the VP40 matrix to allow fusion pore formation require further investigation, for which both the BlaM assay and cryo-ET analysis of in vitro reconstituted fusion events are promising experimental tools.

3.4 The VP40 matrix in EBOVs entering host cells is disassembled

The VP40 matrix clearly detaches from the viral membrane and disassembles upon exposure to acidic environments as shown by the in vitro experiments. I validated these findings further by structurally characterizing Ebola VLPs and virions entering host cells, which provided complementing structural details discussed separately in the following.

In situ cryo-CLEM of Ebola VLPs entering target cells

To study Ebola VLPs entering host cells, I employed a correlative approach using cryo-CLEM and structurally analysed entry events targeted by light microscopy (Fig. 26). I could show that VLPs residing in endosomal compartments display the typical coat of GPs protruding from the VLP envelope and have

disassembled VP40 matrices similar to VLPs subjected to low pH in vitro. The endosomal compartments appeared devoid of cellular structures, suggesting that fusion with other VLP(s) had already taken place and caused an increase of the surface of the endosome. This is further supported by the notion that many endosomal membranes were densely decorated with trimeric GPs facing away from the cytoplasm. While the presence of GP-decorated endosomal membranes clearly denotes post-fusion events, it was surprising to see such a large number of trimeric GPs. Considering that GP-mediated membrane fusion requires GP processing that results in the removal of the majority of the protein (Chandran et al., 2005; Schornberg et al., 2006; Brecher et al., 2012), I expected to observe fewer or no GPs inside late endosomal compartments and on the surface of internalized VLPs. Since Ebola VLPs are produced by overexpressing viral proteins in a timely uncontrolled manner, it is likely that they incorporate unphysiological amounts of GP. To compare the GP spacing on Ebola VLPs and virions, I attempted to analyse tomograms acquired of each; however, the chemical fixation employed on EBOVs to inactivate them prior to imaging impaired their analysis as discussed above. On VLPs, GPs had a spacing of 15 nm (Winter and Chlanda, 2021), which is larger than the approximately 9-10 nm spacing of HA spike proteins on filamentous influenza A viruses (Wasilewski et al., 2012). Owing to their remarkable length, Ebola VLPs carry many GPs on their surface and therefore likely saturate endosomal proteases. It was previously shown that influenza A virus membrane fusion requires only a few HAs, which are in close proximity to each other (Dobay et al., 2011), and influenza A virions incubated at low pH contain HAs at different conformations (Fontana et al., 2012). It is thus likely that EBOV GP-mediated membrane fusion also involves only a few GPs, and the remaining GPs may still be uncleaved.

In situ cryo-ET of EBOVs entering target cells

To further validate the cryo-ET data on entering Ebola VLPs, I structurally characterized EBOVs-infected target cells (Fig. 27, 28) in collaboration with Thomas Hoenen (FLI, Greifswald- Insel Riems) and together with Melina Vallbracht. We discovered that late endosomal compartments are often characterized by the accumulation of cholesterol ester crystals, membrane fragments and protein-decorated vesicles. These observations are consistent with their lysosomal function to degrade cellular material including membranes (Schulze et al., 2009). EBOVs in these compartments display characteristic filamentous morphologies and contain disassembled VP40 matrix layers, which are detached from the viral envelopes. This further supports the in vitro analysis of VLP particle shape at low pH (Fig. 12) and shows that global changes to spherical morphologies do not occur immediately upon VP40 matrix disassembly. In contrast to internalized VLPs, EBOVs in endosomes did not display proteins protruding from their envelope. In line with the discussion above, this might indicate either that EBOVs carry fewer GPs in comparison to VLPs, and thus do not saturate the proteases. Alternatively, the VLPs analysed in this work are located in earlier endosomes, while the virions are clearly located in late endosomal/ endolysosomal compartments, which are enriched in cathepsin proteases (Mingo et al., 2015; Brix et al., 2008).

Finally, we discovered that nucleocapsids in internalized EBOVs are still condensed, while the typical boomerang-protrusions corresponding to VP24 and VP35 observed in nucleocapsids in isolated virions (Fig. 11) are missing. The protrusions may either be obscured by the disordered VP40 proteins accumulated around the nucleocapsid or might be detached from the core structure in response to the acidic environment. In any case, the cylindrical nucleocapsid core appears to be stable at low pH and likely stays condensed during the delivery of the viral genome to the cytoplasm. In this context and in analogy to the cytoplasmic entry of influenza A viruses, the accumulated VP40 proteins around the nucleocapsid might recruit cellular factors to actively pull the encapsidated genome into the cytoplasm. In influenza A viruses entering cells through endosomes, the M1 matrix layer disassembles and aggregates similarly to the VP40 matrix described here around the vRNPs. The aggregates are suggested to engage the cellular aggresome machinery by mimicking misfolded proteins, which in turn facilitates cytoplasmic entry of the vRNPs (Banerjee et al., 2014).

Structural characterization of more EBOV entry events as described above would be desirable to confirm the nucleocapsid phenotype observed in entering virions and potentially capture intermediate fusion events. Screening the EBOV-infected samples for additional entry events is ongoing but has so far proven to be inefficient, since entry events are rare. If a VLP system with successfully incorporated nucleocapsid is established in the future (discussed below), one could implement a cryo-CLEM approach using fluorescently labelled VLPs. In preparation for this, dual-labelled VLPs containing fluorescently labelled VP40 and nucleocapsids have already been prepared by Lisa Augenstein under my supervision.

Together, the in situ cryo-ET data presented here indicate that EBOV uncoating occurs as a stepwise process initiated by low pH-mediated VP40 disassembly and concluded with the transport of encapsidated genomes into the cytoplasm.

3.5 The fate of the EBOV nucleocapsid during uncoating

In addition to matrix dissociation from the viral envelope, virus uncoating involves nucleocapsid decondensation, which is required to allow genome replication and transcription. In EBOVs, the fate of the nucleocapsid during cell entry is not known, including where and when decondensation takes place and whether nucleocapsids are required to transport the viral genome into the cytoplasm.

The in situ cryo-ET data presented in this work revealed that the nucleocapsids in internalized EBOVs remain condensed after VP40 matrix disassembly. To further investigate the fate of the nucleocapsid during entry and characterize its stability at different pH, VLP systems are well-suited tools; they allow structural analysis without chemical fixation, their protein composition can easily be modified, and they can be produced in large quantities. In this work, I produced and structurally characterized Ebola VLPs composed of all structural proteins as well as trVLPs, which additionally incorporate a minigenome.

The Ebola VLPs exclusively incorporated loosely coiled nucleocapsids, irrespective of the purification strategy and protein ratios used during VLP production. This suggested that maturation of nucleocapsids into the decorated and condensed state was impaired during VLP production. However, isolated

nucleocapsids of different condensation states were often co-purified along with the VLPs (Fig. 31-32). They were mostly condensed but also included condensed and decorated nucleocapsids (the mature state found in virions), and loosely coiled nucleocapsids as observed inside VLPs. During EBOV infection, nucleocapsids are formed in inclusion bodies, where NP forms loose coils around the viral RNA and further condenses in the presence of VP24 and VP35 (Bharat et al., 2012; Wan et al., 2017). The fully condensed nucleocapsids including the boomerang-shaped protrusions presumably formed by VP24 and VP35 are additionally associated with VP30 and L. They are mainly found at the periphery of the inclusion bodies surrounding the bulk of condensed and loosely coiled nucleocapsids (reviewed in (Dolnik and Becker, 2022)). According to the current model, nucleocapsids are transported only in this final state to budding sites at the plasma membrane, in an actin-dependent manner and independent from VP40 (Schudt et al., 2013, 2015; Takamatsu et al., 2018). The observation of clusters of co-purified nucleocapsids indicates that their production and maturation in the producing cell line successfully takes place. However, since I could not identify VLPs incorporating condensed nucleocapsids, this either indicates that these nucleocapsids are insufficiently transported to VLP budding sites, poorly incorporated into VLPs, or undergo decondensation after incorporation into VLPs. As shown for HIV (Wang et al., 2004) and postulated for EBOV based on MD simulations (Xu et al., 2020), the presence of RNA stabilizes nucleocapsid structures. RNA-interactions could therefore be relevant both for the transport and incorporation of condensed nucleocapsids into VLPs. To test this hypothesis, I thus produced and structurally characterized trVLPs containing truncated viral genomes.

During trVLP production, EBOV GP, VP40 and VP24 are encoded on the minigenome, which also encodes all viral leader, trailer and intergenic regions. Their genes are thereby transcribed and translated in a manner similar to that of EBOVs. All remaining viral proteins are expressed from plasmids in molar ratios observed in virions and get incorporated into newly formed viral progeny upon infection of the cells with trVLPs. As published (Schmidt et al., 2018), trVLP production increased with increasing passages, indicating that transcription and replication took place and that nucleocapsids were successfully incorporated into newly formed trVLPs. However, structural characterization by cryo-ET of the trVLPs revealed inconclusive results. While the overall particle shape including the organization of GPs and VP40 matrix in filamentous particles resembled the structures of EBOVs and VLPs, the core of the particles appeared too dense to recognize nucleocapsid structures unequivocally. This may have been caused by residual sucrose insufficiently removed during trVLP purification. Since trVLP production is time-consuming and the particle yield is low, it is difficult to analyse trVLPs directly from the media of producing cell lines similar to VLPs (Fig. 16, 31) and purification is mainly required to concentrate the sample. To reduce microscopy time and still characterize unpurified particles, I thus suggest performing whole-cell tomography on cells producing trVLPs. Due to the soluble GFP, which is encoded on the minigenome in addition to the structural proteins to monitor infection spread, infected cells can easily be identified by light microscopy (Fig. 34). By imaging the cell periphery of infected cells, budding VLPs incorporating nucleocapsids will be captured without prior purification. I show in this work that cells incubated at low

pH do not alter their morphology (Fig. 22). Therefore, this approach could also be performed on the trVLP-producing cells incubated at low pH, which would allow assessing the stability of nucleocapsids at endosomal pH.

Based on the data presented here (Fig. 27), I propose that nucleocapsids are released in a condensed state and that uncoating takes place in the cytoplasm. As discussed above, further validation could include (a) the analysis of nucleocapsids (either co-purified or within budding trVLPs) at low pH and (b) in situ screening for post-fusion events to identify released nucleocapsid structures.

3.6 Do actin and nucleocapsids compete for VP40 binding?

During virus assembly, dimeric VP40 and nucleocapsids are transported along actin filaments towards budding sites at the plasma membrane (Adu-Gyamfi et al., 2012; Schudt et al., 2015). Upon membrane interactions, VP40 proteins form a quasi-helical matrix and induce the formation of filamentous particles that incorporate one or more linearly arranged nucleocapsids (Beniac et al., 2012). Whether actin gets incorporated into the particles and how its interactions with VP40 and nucleocapsids are modulated to orchestrate virion assembly remains unknown.

Here, I characterized Ebola virions by cryo-ET and found that they contain condensed nucleocapsids but no traces of actin filaments (Fig. 11). In contrast, Ebola VLPs did not incorporate condensed nucleocapsids but contained multiple actin filaments in close contact with the VP40 matrix. Closer examination of both Ebola and Marburg VLPs revealed a direct contact between the actin filaments and the respective VP40 matrices (Fig. 29). In bent or kinked areas of the filamentous VLPs, the linearly arranged VP40 dimers had occasionally peeled off the membrane but stayed attached to actin filaments via their N-terminal domains like "pearls-on-a-string". No additional protein density could be identified between the VP40 dimers and actin, suggesting that the interaction does not involve additional adaptor proteins as previously suggested (Adu-Gyamfi et al., 2012).

For EBOVs, limited studies exist showing the transport of VP40 along actin filaments during assembly and incorporation of actin in virus particles (Han and Harty, 2005). Indirectly, VP40-actin interactions have been described for MARV by using inhibitors of actin polymerization and actin motor proteins, both of which abrogated particle formation (Kolesnikova et al., 2007). The only direct interaction of VP40 and actin-binding proteins has been shown for the cellular factor IQGAP1 (Lu et al., 2013), which regulates the assembly and dynamics of the actin network. Whether IQGAP1 gets incorporated into VLPs and whether its interaction with VP40 occurs while it is attached to actin has not been investigated yet. However, considering its large size of 190 kDa, which should be well visible in the tomograms, it is unlikely that IQGAP1 serves as an adaptor protein between VP40 and actin, at least inside VLPs.

The absence of nucleocapsids from VLPs containing actin filaments and, conversely, the absence of actin filaments in EBOVs containing condensed nucleocapsids suggests that their incorporation into virus particles is mutually exclusive. This would imply that actin detaches from VP40 at budding sites and "hands over" the nucleocapsids. Since VP40 interacts tightly with membrane lipids via its C-termini and the matrix

appears unaltered in VLPs and virions, I propose that actin- and nucleocapsid interactions are mediated by – potentially similar – motifs in the VP40 N-terminal domain. To reveal the VP40-actin interaction interface, I started a subtomogram averaging project of the VLPs displaying clear VP40-actin interactions, which is still ongoing. Interactions could further be confirmed by performing co-immunoprecipitation assays of exogenously expressed VP40. Since these interactions may be transient, cross-linking VP40 to proteins in the vicinity may be necessary.

Identifying amino acids involved in actin-binding could reveal motifs also involved in nucleocapsid-binding. VP40 interactions with both actin and nucleocapsids are pivotal for the formation of EBOVs and are therefore promising targets for antivirals.

3.7 Is VP40 disassembly during host cell entry conserved?

Finally, it remains to be elucidated whether the role of pH-mediated VP40 disassembly during virus entry is specific to EBOVs, or also important for other filoviruses. To address this, I first structurally investigated VLPs of the closely related MARVs and discovered some striking differences in the organization of the mVP40 matrix. Filamentous Marburg VLPs resemble Ebola VLPs in overall morphology and the mVP40 matrix appears to form a similar helical tube underneath the membrane (Fig. 16). However, adjacent helical turns clearly form doublets with a spacing of 4-5 nm and inter-doublet spacing of 5-6 nm. Additionally, the matrix is organized perpendicularly to the VLP membrane as opposed to the 25° angle of the eVP40 matrix in Ebola VLPs. These findings contradict the recently published structure of the VP40 matrix in Marburg VLPs and MARVs (Wan et al., 2020): In this study, the authors show mVP40 matrix layers which closely resemble the EBOVs VP40 matrix and differ only in their angle with respect to the viral/ VLP membrane. While the VP40 matrix in MARVs was shown to be almost perpendicular to the viral membrane in line with the observation here, the matrix in Marburg VLPs composed of mVP40 alone was shown to have a similar angle to the VP40 matrix in Ebola VLPs. Since the angle appears to depend on the protein composition of the VLPs, I suggest directly comparing the structure of Marburg VLPs composed of mVP40 and GP (as presented in this work, Fig. 16) and mVP40 alone (as used by (Wan et al., 2020)). Matrix proteins are known to interact with cytoplasmic tails of glycoproteins (Liljeroos and Butcher, 2013), which could alter their structural organization within virus particles. So far, specific VP40-GP interactions have not been described for filoviruses yet. Confirming the structural re-arrangement of the VP40 matrix in Marburg VLPs upon incorporation of MARV GP would therefore provide the first evidence for such an interaction.

Irrespective of the organization into doublets or helical arrangement resembling the EBOV VP40 matrix, the VP40 matrix in Marburg VLPs appears to be composed of dimers interacting via their C-termini with the inner membrane monolayer. Despite sequence similarities of only 16% in the C-terminal domains of eVP40 and mVP40, their surface properties and net positive charge are conserved. Hence, low pH may similarly abrogate mVP40-membrane interactions. In preliminary experiments, I assessed the effect of low pH on the morphology of unpurified Marburg VLPs. While the mVP40 membrane appeared to be

disassembled, the membranes of the VLPs were damaged and appeared "moth-eaten" (data not shown), a phenotype previously described in chemically fixed EBOVs (Ellis et al., 1979, 1978; Wan et al., 2020). I also observed this phenotype in unpurified Ebola VLPs subjected to low pH and cells incubated with low pH-treated unpurified VLPs (Fig. 22). In all examples, VLPs were directly harvested from the media of the producing cell line. Considering that the EBOV GPs are cytotoxic (Volchkov et al., 2001; Alazard-Dany et al., 2006) and induce apoptosis upon expression in target cells, VLP-producing cells might release low pH-activated enzymes into the surrounding media. Hence, upon low pH treatment, these enzymes might become activated and digest the VLP membranes. Accordingly, purified Ebola VLPs subjected to low pH exclusively displayed intact membranes (Fig. 10). The low pH experiments therefore will be repeated using purified Marburg VLPs.

Despite similar roles during the viral replication cycle, matrix proteins from different viruses are remarkably different in sequence and structure (Liljeroos and Butcher, 2013). However, their interaction with membrane lipids is often of electrostatic nature and therefore likely affected by low pH. We show in this work that the plasma membrane and Ebola VLP membrane are permeable to protons, indicating that other membranes of enveloped viruses budding from the plasma membrane may be similarly permeable. This expands the relevance of low pH-driven structural modifications of virus particles towards late-penetrating viruses in general beyond viruses that are known to encode viroporins.

4 Conclusion

Low pH has long been recognized as a trigger to initiate membrane fusion not only for filoviruses, but a wide diversity of enveloped viruses including arenaviruses, togaviruses, flavivirues, bunyaviruses, rhabdoviruses and hepadnaviruses (reviewed here (White et al., 1983, 2008; Yamauchi and Greber, 2016)). Most studies have focussed on the effect of low pH on the structure and fusion mechanism of fusion proteins of all classes (II-III), including EBOV GP. Only limited studies exist that examine the impact of low pH on overall virus particle morphology (Calder et al., 2010; Libersou et al., 2010; Fontana and Steven, 2013), and the best-studied virus in respect to particle morphology remains influenza A virus. Influenza A viruses, irrespective of their morphology at neutral pH (filamentous or spherical), undergo structural re-organization at pH 4.9, manifested in the disassembly of the M1 matrix layer and its detachment from the viral membrane (Calder et al., 2010; Fontana and Steven, 2013). This implies acidification of the viral lumen, which is realized by the M2 ion channel, located in the viral membrane and essential for several steps in the viral replication cycle (Manzoor et al., 2017). Here, I investigate the structure of Ebola VLPs and virions by cryo-ET and show that they display a similar low pH-phenotype despite lacking a dedicated viral ion channel. The detachment of the VP40 matrix occurs concomitantly with its disassembly and is likely pivotal for allowing membrane fusion in late endosomal compartments. Low pH-driven disassembly is therefore an integral part of the EBOV uncoating process beyond the proteolytic processing of the fusion protein.

Based on the results presented here, I propose that EBOV uncoating in late endosomal compartments is a stepwise process: First, low endosomal pH passively equilibrates across the viral membrane, leading to the disruption of electrostatic interactions between VP40 and lipids in the inner viral monolayer. The VP40 matrix thereby detaches from the viral membrane and disassembles, while the nucleocapsid remains compact around the viral genome. Second, VP40 detachment from the viral membrane releases steric constraints imposed by the assembled VP40 matrix at neutral pH, and the viral membrane can engage in GP-mediated fusion with the endosomal membrane. Third, membrane fusion results in the formation of a fusion pore that expands to release the compacted nucleocapsid into the cytoplasm. Finally, de-condensation of the nucleocapsid by a yet unknown mechanism occurs in the cytoplasm and allows genome replication and transcription.

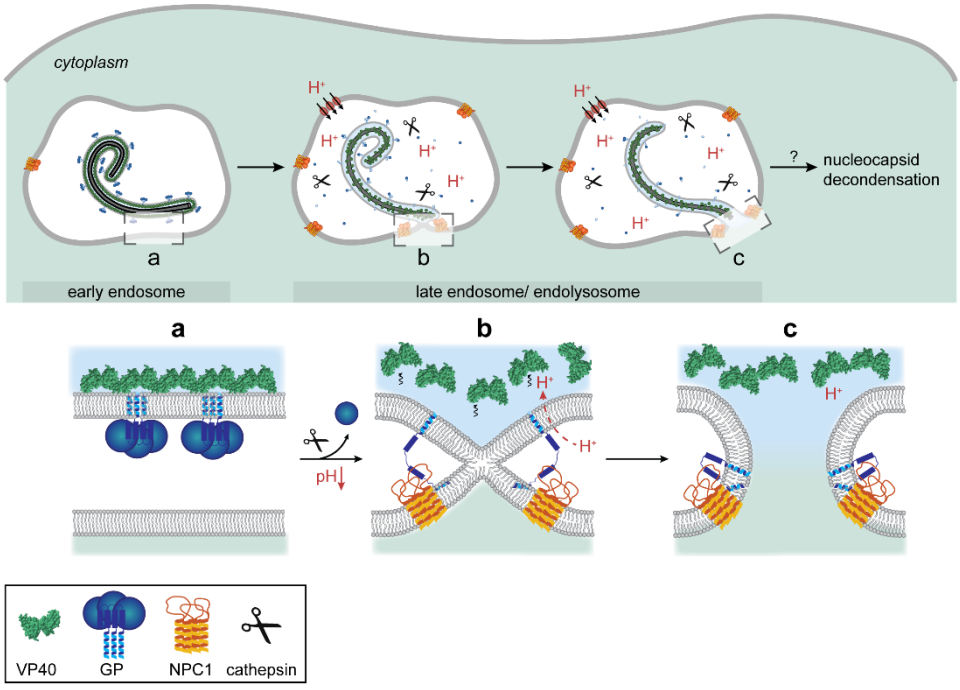

Figure 36: Model of EBOV uncoating during entry into host cells. After host cell attachment and internalization, EBOVs traffic through the endocytic machinery. **(a)** In early endosomes, the EBOV GPs and VP40 matrix remain structurally unchanged. **(b)** The low pH environment in late endosomal compartments activates cathepsin proteases that cleave the EBOV GP, while acidifying viral lumina by passive diffusion. In response to the low pH, the VP40 matrix detaches from the viral envelope and disassembles. **(c)** After binding to the endosomal receptor NPC1, the virions engage in membrane fusion, resulting in the release of the encapsidated genome into the cytoplasm. Nucleocapsid decondensation in the cytoplasm occurs by yet unknow mechanisms and concludes EBOV uncoating.

5 Materials and Methods

5.1 Materials

5.1.1 Cell culture

Table 2: List of cells and cell lines

Cells/ cell lines	Source	Use
Stellar chemically Competent Cells	Takara Bio Europe	plasmid amplification
HEK 293T	European Collection of Authenticated Cell Cultures (ECACC)	VLP production, membrane permeability measurements
Huh7	Prof. Dr. Ralf Bartenschlager	VLP/ EBOV infection

Table 3: List of chemicals, media and reagents for cell culture

Component	Supplier	Use
Ammonium chloride	ThermoFisher Scientific	Inhibition of VLP entry into cells (stock: 1 M in H2O, working solution: 25 mM in DMEM)
Bafilomycin A1, ready-made solution, 160 µM	Sigma-Aldrich	Inhibition of VLP entry into cells (working solution: 25 nM in DMEM)
Beta-lac loading solutions small kit DMSO	ThermoFisher Scientific	BlaM substrate
DMEM (1x) + GlutaMAX	Life Technologies	Maintenance of mammalian cells
E64d (stock: 500 µg/ml in Methanol:H2O (1:1))	Sigma-Aldrich	Inhibition of VLP entry into cells (working solution: 20 µM in DMEM
Fetal Bovine Serum (FBS)	Life Technologies	Maintenance of mammalian cells
Fibronectin, solution 1mg/ml in H2O (from: lyophilized powder)	Pan Biotech	Coating of 96-well plates for improved cell attachment
Lipi-Blue, stock solution in DMSO, 0.1 nmol/µl	Gerbu Biotechnik GmbH	Staining of lipid droplets
Opti-MEM I (1x) Reduced Serum Medium	Life Technologies	Transfection media
PBS with Ca2+/Mg2+, Dulbecco's	Promo Cell	Buffer used for mammalian cells
PenStrep (10.000 Units/ml Penicillin, 10.000 µg/ml Streptomycin)	Life Technologies	Maintenance of mammalian cells
Polyethylenimine, Linear, MW 25000	Polysciences	Transfection reagent for HEK 293T cells
Trans IT-LT1 transfection reagent	Mirus	Transfection reagent for Huh7 and VeroE6 cells

Table 4: List of instruments

Instrument	Manufacturer
Optima L-90K ultracentrifuge (SW32 Ti rotor)	Beckmann
Optima TLX ultracentrifuge (TLA 120.2 rotor)	Beckmann
Infinite 200 plate reader	Tecan
Trans-Blot® Turbo™ Transfer Starter System, Midi PVDF	Bio-Rad
ChemoStar Touch ECL and Fluorescence imager	Intas

5.1.2 Molecular biology

Table 5: List of chemicals and reagents and kits

Component	Manufacturer
Agar Bacto	BD
Agarose LE	Biozym
Ampicillin sodium salt	Sigma-Aldrich
Bacto Agar	BD
Bacto Tryptone	BD
Bacto Yeast extract	BD
Citric acid monohydrate	Carl Roth
CloneAmp HiFi PCR Premix	Takara Bio Europe
Cloning Enhancer	Takara Bio Europe
Clarity Western ECL Substrate	Bio-Rad
Color Prestained Protein Standard Broad Range 10-250 kDa (#P7712, replaced now by #P7719)	New England Biolabs
D(+)-Saccharose	Carl Roth
DAPI (4',6-Diamidino-2-phenyl-indol -dihydrochlorid, 2-(4-Amidinophenyl)-6-indolcarbamidin -dihydrochlorid)	Sigma-Aldrich
Dimethyl sulfoxide, DMSO	Sigma-Aldrich
Dithiothreitol (DTT), 1M solution	Bio-Rad
DNA loading dye 6x	Thermo Scientific
DpnI, recombinant	New England Biolabs
E64d	ThermoFisher Scientific
EcoRI-HF	New England Biolabs
EDTA 0,5 M pH 8.0	Invitrogen
EGTA	Sigma-Aldrich
Gene Ruler 1 kb DNA ladder	Thermo Scientific
HEPES	Carl Roth
Hydrochlorid acid solution, 1M	Zentrallager
In-Fusion HD cloning kit	Takara Bio Europe
Laemmli 4x sample buffer	Bio-Rad
Magnesium chloride	Carl Roth
Midori green direct	NIPPON
Milk powder, blotting grade	Carl Roth
Mini-Protean TGX Gels 4-15%, 10 well comb, 50 µl	Bio-Rad
Phosphoramidon (R7385-1MG)	Sigma-Aldrich
Pierce BCA Protein Assay Kit	ThermoFisher Scientific
PIPES	
Probenecid, 100x stock in H2O	Invitrogen
Prolong Glass mounting medium	Life Technologies
EDTA-free Protease Inhibitor tablets (cOmplete™)	Sigma Aldrich/ Roche
Qiagen Plasmid Maxi Kit (25)	Qiagen
QIAprep Spin Miniprep Kit (50)	Qiagen
Shrimp Alkaline Phosphatase (rSAP)	New England Biolabs
Sodium chloride	Carl Roth
Sodium hydroxide	Carl Roth
Thermolysin from Geobacillus	Sigma-Aldrich
Trans-Blot Turbo Mini PVDF Transfer Pack, 0.2 µm	Bio-Rad
TransIT-LT1 transfection reagent	Mirus
Tris	Carl Roth
Triton X-100	Sigma-Aldrich
Trypsin-EDTA Solution 1x	Sigma-Aldrich
Tryptone Bacto	BD
Tween-20	Roth
Yeast extract Bacto	BD

Table 6: List of buffers, media and solutions

Name	Composition
Agar plates	10 g tryptone, 5 g yeast extract, 10 g NaCl, 15 g agar
HNE buffer	10 mM HEPES, 100 mM NaCl, 1 mM EDTA
Lysgeny Broth (LB) medium	10 g tryptone, 5 g yeast extract, 10 g NaCl
Lysis buffer	2% SDS in Tris buffer, pH 8
PHEM buffer, 4 x	60 mM PIPES, 25 mM HEPES, 2 mM MgCl2, 10 mM EGTA, pH 6.9
Tris/acetate/EDTA (TAE) buffer, 10 x	Sigma-Aldrich
Tris-buffered saline with 0.1% Tween20 (TBS-T)	20 mM Tris, 150 mM NaCl, 0.1% (w/v) Tween 20 detergent
Tris/Glycine/SDS (10 x)	Bio-Rad

Table 7: List of plasmids

Plasmid identifier and name	Organism	Origin/ provided by
EBO_002: pCAGGS_GP	species *Zaire ebolavirus*, strain Mayinga	Petr Chlanda
EBO_003: pCAGGS_VP40	species *Zaire ebolavirus*, strain Mayinga	Petr Chlanda
EBO_004: pCAGGS_GFP-VP40	species *Zaire ebolavirus*, strain Mayinga	Petr Chlanda
EBO_008a: pCAGGS_pHluorin-VP40	species *Zaire ebolavirus*, strain Mayinga	This work
EBO_013: EBOV_BlaM-VP40	species *Zaire ebolavirus*, strain Mayinga	Kartik Chandran (lab)
pCAGGS_flag-VP24	species *Zaire ebolavirus*, strain Mayinga	Petr Chlanda
EBO_007: pCAGGS_VP24	species *Zaire ebolavirus*, strain Mayinga	This work
EBO_006: pCAGGS_VP35	species *Zaire ebolavirus*, strain Mayinga	Petr Chlanda
EBO_001: pCAGGS_NP	species *Zaire ebolavirus*, strain Mayinga	Petr Chlanda
MARV_001: pCAGGS-MARV-VP40	species *Marburg marburgvirus*, strain Musoke	Thomas Hoenen (FLI, Greifswald-Insel Riems)
MARV_002: pCAGGS-MARV-GP	species *Marburg marburgvirus*, strain Musoke	Thomas Hoenen (FLI, Greifswald-Insel Riems)
INF_005: pCAGGS-M1-phluorin	Influenza A virus strain A/Hong Kong/01/1968 (H3N2)	Hans-Dieter Klenk
CEL_017: pcDNA3.1-IFITM3-IRES-mScarlet	human	Steffen Klein
INF_004: pCAGGS-M2	A/Udorn/307/1972 (H3N2)	Hans-Dieter Klenk

All plasmids used for trVLP production (Fig. 33-35) were kindly provided by Thomas Hoenen (FLI, Greifswald-Insel Riems) and listed below.

Table 8: List of plasmids used for trVLP production

Plasmid name	Organism	Origin/ provided by
pCAGGS_EBOV_TH-4ciseGFP	species *Zaire ebolavirus*, strain Mayinga	Thomas Hoenen (FLI, Greifswald-Insel Riems)
pCAGGS_EBOV_TH-VP35		Thomas Hoenen (FLI, Greifswald-Insel Riems)
pCAGGS_EBOV_TH-VP30		Thomas Hoenen (FLI, Greifswald-Insel Riems)
pCAGGS-VP30-GFP		Thomas Hoenen (FLI, Greifswald-Insel Riems)
pCAGGS_VP30-mScarlet		Cloned in this work

pCAGGS_EBOV_TH-NP		Thomas Hoenen (FLI, Greifswald-Insel Riems)
pCAGGS_EBOV_TH-L		Thomas Hoenen (FLI, Greifswald-Insel Riems)
pCAGGS_EBOV_TH-TIM-1	human	Thomas Hoenen (FLI, Greifswald-Insel Riems)
pCAGGS_EBOV_TH-T7	human	Thomas Hoenen (FLI, Greifswald-Insel Riems)

Table 9: List of primers

Primer name	Use	Sequence
SW01	forward (fwd) sequencing primer	CTGCTAACCATGTTCATGCC
SW02	reverse (rev) sequencing primer	CCAGAAGTCAGATGCTCAAGG
SW03	VP24 fwd primer (flag-removal)	GCTAAAGCTACGGGACGATAC
SW04	VP24 rev primer (flag removal)	CATGGTACCCTCGAGGAATTC
SW011	pHluorin fwd	TTTTGGCAAAGAATTATGAGTAAAGGAGAAGAACTTTTCA
SW012	pHluorin-linker_rev	GCCTCATGGTGAATTCTGCTTTGTATAGTTCATCCATGCC
SW042	VP30-mScarlet vector fwd	TAGACGAGACGGAGCTCTTAATTAG
SW043	VP30-mScarlet vector rev	AGGGGTACCCTCATCAGAC
SW044	VP30-mScarlet insert fwd	GAGGGTACCCCTGGATCTGGCATGGTGAGCAAG
SW045	VP30-mScarlet insert rev	GCTCCGTCTCGTCTATTACTTGTACAGCTGGTCCATGC

Table 10: List of antibodies

Antibody	Supplier	Working concentration for Western blotting
anti-VP40 (rabbit)	IBT Bioservices (Catalog #: 0301-010)	stock conc.: 0.789 mg/ml, used in 1:5,000 dilution
anti-GFP (mouse)	Clontech (632381)	stock conc.: 1 mg/ml, used in 1:1,000 dilution
anti-GP (rabbit)	IBT Bioservices (Catalog #: 0301-015)	Stock conc.:), 1 mg/ml, used in 1:10,000 dilution
anti-mouse-HRP	Santa-Cruz (sc-516102)	Used in 1:1,000 dilution
anti-rabbit-HRP	Santa-Cruz (sc-2357	Used in 1:1,000 dilution

5.1.3 Light and Electron microscopy

Table 11: List of chemicals and reagents used for EM

Chemical/ reagent	Supplier
Glutaraldehyde, 25% in H2O, EM-grade	Sigma-Aldrich
Paraformaldehyde, 16%	Science Services
Phosphotungstic acid hydrate (PTA), 2%	Sigma-Aldrich
Protein A 10 nm, Immunogold	Aurion
Whatman filter paper, grade 1, diameter 55 mm	Merck

Table 12: List of EM grids

Grids	Manufacturer	Use
Formvar/Carbon 200 Mesh, Copper	Sigma-Aldrich	Negative stain EM
Holy Carbon, R2/1 Cu, 200 mesh	Quantifoil	Cryo-ET of VLPs and viruses
SiO_2 R1/4 and R1.2/20 on Au 200 mesh	Quantifoil	Cryo-ET of infected cells

Table 13: List of tools and instruments for EM and LM

Tool/ instrument	Supplier
Automatic Plunge Freezer EM GP2	Leica Microsystems
Aquilos cryo-FIB/SEM	Thermo Fisher Scientific
Cryo-CLEM wide-field fluorescent microscope (with a 60×/0.9 NA objective)	Leica Microsystems
(FIB) Autogrids and autogrid loading and clipping tools	Thermo Fisher Scientific
Glow discharger, Solarus Model 950, Advanced Plasma System	Gatan
Grid holders, 3D printed	Custom made
Leica SP8 DLS Laser Scanning Confocal SPIM	Leica Microsystems
Krios cryo-TEM equipped with GIF-K3 (Gatan, Pleasanton, CA, USA)	Thermo Fisher Scientific
Solarus Plasma Cleaner	Gatan
Tecnai F20 transmission electron microscope	ThermoFisher Scientific
Eclipse Ts2 inverse fluorescent microscope	Nikon

Table 14: List of software

Name	Developer/ Source
Amira	ThermoFisher Scientific
ChimeraX	(Pettersen et al., 2021)
Etomo (IMOD version 4.10.49)	(Kremer et al., 1996)
Dynamo	(Castaño-Díez et al., 2012)
ImageJ/FiJi (referred to as Fiji throughout this work)	(Schindelin et al., 2012)
icy	(De Chaumont et al., 2012)
LAS X	Leica Microsystems
MAPS	(Schorb and Sieckmann, 2017)
SerialEM	(Mastronarde, 2005)

5.2 Methods

5.2.1 Cell culture

Cell lines used in this work include Huh7 cells and VeroE6 cells (kindly provided by Prof. Dr. Ralf Bartenschlager (Heidelberg University Hospital)) as target cells to investigate entry of Ebola VLPs and EBOV, and HEK 293T cells (ECACC General Cell Collection) to produce Ebola VLPs and for assays to determine the proton permeability of the plasma membrane. All cell lines were maintained in DMEM media (ThermoFisher Scientific) supplemented with 10% (v/v) FBS and 100 U/ml penicillin-streptomycin (ThermoFisher Scientific) at 37°C and 5% CO_2. All cells were tested for Mycoplasma contamination every three months and passaged for a maximum of 30 times.

5.2.2 Production and purification of Ebola VLPs

Ebola VLPs were produced by expressing pCAGGS plasmids encoding the EBOV proteins GP, VP40, VP35, VP24 and NP (species *Zaire ebolavirus*, Mayinga strain) in HEK 293T cells. HEK 293T cells were grown in 10 cm dishes and seeded at a density of 2.5 x 10^6 cells per dish 24 h prior to transfection. As indicated for each experiment, different combinations of plasmids were used, while keeping the total amount of transfected DNA identical (Table 15). Reporter VLPs composed of GP and VP40 were prepared by additionally expressing VP40 variants N-terminally linked to GFP, pHluorin or beta-lactamase (BlaM). To maintain the overall filamentous shape of the particles, untagged VP40 was expressed in excess over tagged VP40 with a molar ratio of 1:0.1.

In preliminary experiments, Marburg VLPs were produced composed of MARV GP and MARV VP40 similar to Ebola VLPs. All plasmids used for VLP production are listed in Table 8.

Table 15: Transfection mixtures for the production of different Ebola VLPs. Pipetting schemes are shown for the transfection of 1×10 cm dishes. All plasmids are concentrated to 1 µg/µl and per dish, 15 µg DNA are transfected.

Component	Volume in µl (VLPs: GP, VP40, VP35, VP24, NP)	Volume in µl (VLPs: GP, VP40)	Volume in µl (VLPs: VP40)
OptiMEM	1000	1000	1000
pCAGGS-GP	3	7.5	-
pCAGGS-VP40	3	7.5	15
pCAGGS-VP35	3	-	-
pCAGGS-VP24	3	-	-
pCAGGS-NP	3	-	-
Polyethyleneimine	45	45	45

The protocol for the purification of Ebola VLPs was adapted from (Nanbo et al., 2018). Ebola VLPs released into the supernatant of transfected cells were harvested 48 h post transfection and supernatants were clarified by centrifugation at 398 g for 10 min, and 2168 g for 15 min (JA-10 rotor, Beckmann). Clarified supernatants were then layered over a 30% (w/v) sucrose cushion in HNE buffer (10 mM HEPES, 100 mM NaCl, 1 mM EDTA, pH 7.4) and centrifuged for 2.5 h at 11,400 rpm (SW32 Ti rotor, Optima L-90K ultracentrifuge, Beckmann). To remove residual sucrose, pellets containing Ebola VLPs were resuspended in HNE buffer and centrifuged for 30 min at 19,000 rpm (TLA 120.2 rotor, Optima TLX ultracentrifuge (Beckmann)). Final pellets were dissolved in HNE buffer and the morphology of VLPs was verified by negative stain electron microscopy. To ensure reproducibility of the experiments, the protein concentration of each VLP preparation was determined and equal amounts of VLPs were used.

5.2.3 trVLP production

trVLPs were produced according to the protocol published by Hoenen et al (Hoenen et al., 2014) and schematically depicted in Fig. 33. HEK 293T cells were seeded in 10 cm dishes at a seeding density of 2.7 x 10^6 cells per dish and grown for 24 h at 37°C, 5% CO_2. They were then transfected with plasmids encoding the EBOV transcription and replication machinery as well as the T7 polymerase according to the scheme below (Table 16). Since these cells are producing the first trVLPs from plasmid expression exclusively, they are referred to as p0 cells.

Table 16: Pipetting scheme for the production of trVLPs from p0 cells.

Component	Plasmid ratio/ final amount in ng	Volume for 1 x 10 cm dish in µl
OptiMEM		950
pT1.4-cis-vRNA-eGFP	2/ 1750	1.75
NP	1/ 875	0.875
VP35	1/ 875	0.875
VP30	0.6/ 525	0.525
L	8/ 7000	7
pCAGGS-T7	2/1750	1.75
pCAGGS-TIM-1	-	-
PEI		40

Two days post transfection, a fresh batch of HEK 293T cells was seeded in 10 cm dishes similar as before (referred to as p1 cells). They were incubated for 24 h at 37°C, 5% CO2, and transfected according to the scheme below.

Table 17: Pipetting scheme for the production of trVLPs from p1 cells.

Component	Plasmid ratio/ final amount in ng	Volume for 1 x 10 cm dish in µl
OptiMEM		950
pT1.4-cis-vRNA-eGFP	-	-
NP	1/ 875	0.875
VP35	1/ 875	0.875
VP30	0.6/ 525	0.525
L	8/ 7000	7
pCAGGS-T7	-	-
pCAGGS-TIM-1	2/1750	1.75
PEI		40

Approximately 4 h post transfection, the p1 cells were infected with trVLPs harvested from the supernatant of p0 producer cells. Cell culture media was removed from p1 cells and replaced with the trVLP solution. The dishes were then incubated for 2 h at 37°C, 5% CO2, before the trVLP solution was replaced with fresh cell culture media and p1 cells were incubated for 4 days. To increase the yield of trVLPs, fresh batches of HEK 293T cells were iteratively transfected and infected with trVLP cells collected from the previous generation as previously described (Hoenen et al., 2014).

5.2.4 Production and purification of EBOVs and EBOV-infected cells

EBOVs (species *Zaire ebolavirus*, strain Mayinga) were kindly provided by Thomas Hoenen (FLI, Greifswald-Insel Riems), who produced the viruses in VeroE6 cells in the BSL4 facility at the FLI (Insel Riems, Greifswald), following approved standard operating procedures. He then harvested and purified the viruses from supernatants of infected cells 5 days post infection according to the protocol described above for the purification of VLPs. After chemical fixation of the viruses for 24 h in final concentrations of 4% paraformaldehyde and 0.1% glutaraldehyde in HNE buffer (10 mM HEPES, 100 mM NaCl, 1 mM EDTA), they were aliquoted and transferred out of BSL4.

EBOV-infected cells were prepared according to our protocol published as a preprint (Winter et al., 2022). All BSL4 work was carried out by Thomas Hoenen (FLI, Greifswald- Insel Riems).

"For structural characterization of EBOV- infected cells, Huh7 cells were seeded on 200 mesh Quantifoil™ SiO2 R1.2/20 EM grids placed on 3D-printed grid holders in a 96-well plate. 0.0075 x 10^6 cells were seeded, and the plates were transferred to the BSL4 laboratory after 4-5 h. Cells were infected with unpurified EBOVs at an MOI of 0.1 and incubated for 48 h before chemical fixation for 24 h with 4% paraformaldehyde and 0.1% glutaraldehyde in PHEM buffer (60 mM PIPES, 25 mM HEPES, 2 mM MgCl2, 10 mM EGTA, pH 6.9). After transfer of the samples out of BSL4, the grids were kept in PHEM buffer and plunge-frozen within three days."

5.2.5 Protein determination

The total protein concentration in purified Ebola VLP solutions was determined using the Pierce BCA Protein Assay Kit (ThermoFisher Scientific) according to the manual provided by the manufacturer. In brief, different dilutions of bovine serum albumin (BSA) used as protein standard were prepared. 200 µl BCA solution were then added to 25 µl BSA dilution or VLP sample of unknown protein concentration and the samples were incubated for 2 h at RT. Fluorescence was measured using an Infinite 200 plate reader (Tecan) at 562 nm excitation. A standard calibration curve was determined for the BSA stock solutions of known concentration, and the VLP concentration was deduced from the slope of the curve.

5.2.6 Cloning

All constructs used in this work were cloned into pCAGGS vectors using the In-Fusion HD cloning kit (Takara Bio Europe) according to the protocol provided with the manufacturer. Lists of plasmids and primers used in this work are provided in Table 7 and 9. For the data presented here, cloning was mainly used to introduce fluorescent tags and create fusion proteins. These include pHluorin, which was cloned N-terminally to EBOV VP40 (VP40-pHluorin) and mScarlet, which was cloned C-terminally to EBOV VP30 (mScarlet-VP30). The plasmid encoding for EBOV VP24 was obtained with an N-terminal flag tag (amino acid sequence: DYKDDDDK), which I removed for the production of VLPs.

To create fusion protein construct, target plasmids were either linearized by restriction enzyme digestion using EcoRI-HF (NEB) following the protocol provided with the provider or by PCR-amplification using the CloneAmp HiFi PCR Premix (Takara Bio Europe). Digested plasmids were further treated for 1 h at 37°C using shrimp alkaline phosphatase (rSAP, NEB) to dephosphorylate undigested parental plasmids and prevent their re-ligation. rSAP was then inactivated by heating for 5 min at 65°C. DNA sequences encoding fluorescent tags were amplified by PCR from parental plasmids using the CloneAmp HiFi PCR Premix (Takara Bio Europe). Linearized target vectors and DNA inserts were analysed on 1% agarose gels prepared in TAE buffer. Since in all cases, only single products were produced, purification of the respective bands from the gels was not necessary. Instead, target plasmids and inserts were ligated directly using Cloning Enhancer and the In-Fusion HD cloning kit (Takara Bio Europe) according to the protocol provided with the manufacturer. The products were then transformed into chemically competent Stellar cells by heat shock for 45 seconds at 42°C and the bacteria were grown on agar plates supplemented with ampicillin. Plasmids from single colonies were prepared using the QIAprep Spin Miniprep Kit (Qiagen)

and verified by Sanger sequencing (Microsynth Seqlab). Correct plasmids were further amplified in 200 ml bacterial cultures grown in LB media supplemented with ampicillin and isolated using the Qiagen Plasmid Maxi Kit (Qiagen).

To generate pCAGGS_pHluorin-VP40, pHluorin was amplified by PCR from the parental INF_005 plasmid using the SW011 and SW012 primers. The target vector (EBO_003) was linearized by EcoRI-HF (NEB) digestion. To generate pCAGGS_VP30-mScarlet, mScarlet was amplified by PCR from the parental plasmid CEL_017 using the SW042 and SW043 primers. The target vector (pCAGGS_EBOV_TH-VP30) was linearized by PCR using the SW044 and SW045 primers. To generate pCAGGS-VP24 without the flag tag (EBO_007), the vector containing VP24 was amplified using primers SW03 and SW04 and religated.

5.2.7 Western Blotting

Western Blotting was performed to verify the expression of viral proteins (shown in Fig. 17) and incorporation of viral proteins into VLPs (shown in Fig. 21). Cell lysates from HEK 293T cells expressing viral proteins were prepared by gently detaching the cell monolayer in lysis buffer (2% SDS in Tris) supplemented with protease inhibitors (Sigma Aldrich/ Roche). After 30 min incubation on ice, the lysates were transferred to Eppendorf tubes, centrifuged for 10 min at 8°C at 14,000 × g and supernatants were used for Western Blot analysis.

Cell lysates and purified VLPs were mixed with 4 x Laemmli sample buffer (Bio-Rad) supplemented with DTT and separated by SDS-PAGE using pre-cast 4-15% gradient gels (Bio-Rad). To ensure equal amounts of proteins detected, cell lysates were added in equal volumes and VLP solutions in equal protein concentrations determined by the BCA assay. The samples were run along with a pre-stained protein marker (NEB) at 120 V for 60 min. Proteins were then transferred to polyvinylidene difluoride (PVDF) membranes using the Trans-Blot Turbo Transfer System (Bio-Rad) operated at 2.5 A for 7 min. After washing the membranes with TBS-T (Table 6), they were incubated for 1 h at RT in 5% milk in TBS-T, before adding primary antibody solutions prepared in 5% milk in TBS-T in dilutions displayed in Table 10. After overnight incubation at 4°C, the membranes were thoroughly washed in TBS-T before adding secondary antibody solutions for 1 h at RT. The membranes were washed again in TBS-T and signal was detected after incubating the membranes in Enhanced Chemiluminescence (ECL) solutions (Bio-Rad). The secondary antibodies used in this work are conjugated to horse radish peroxidase (HRP) and ECL serves as a luminol-based substrate that upon conversion by the antibody-coupled HRP becomes chemiluminescent. After 5 min incubation in the dark, the membranes were placed between two sheets of transparent foil and signal was detected with the ChemoStar Touch ECL and Fluorescence imager (Intas).

5.2.8 Lipidomics

To determine the lipid composition of Ebola VLP membranes, Ebola VLPs composed of the structural GP, VP40, NP, VP35 and VP24 were produced and purified according to the protocol provided above. They were used at a final protein concentration of 880 ng/µl. Lipid extraction and lipidomics analysis were

performed by Christian Lüchtenborg and Britta Brügger (Brügger lab, BZH Heidelberg) according to the protocol published as a preprint (Winter et al., 2022):

"VLPs were subjected to lipid extractions using an acidic liquid-liquid extraction method (Blight and Dyer, 1959) as described in Malek et al., 2021 (Malek et al., 2021). In order to ensure that similar amounts of lipids were extracted, a test extraction was performed to determine the concentration of PC as a bulk membrane lipid. Quantification was achieved by adding 1-3 internal lipid standards for each lipid class, with the standards resembling the structure of the endogenous lipid species. Of note, sample volumes were adjusted to ensure that all lipid standard to lipid species ratios were in a linear range of quantification. Typically, the standard to species ratios were within a range of >0.1 to <10. Following this approach, a relative quantification of lipid species was performed. Lipid standards were added prior to extractions, using a master mix consisting of 50 pmol phosphatidylcholine (PC, 13:0/13:0, 14:0/14:0, 20:0/20:0; 21:0/21:0, Avanti 575 Polar Lipids), 50 pmol sphingomyelin (SM, d18:1 with N-acylated 13:0, 17:0, 25:0, semi-synthesized (Özbalci et al., 2013), 100 pmol deuterated cholesterol (D7-cholesterol, Cambridge Isotope Laboratory), 30 pmol phosphatidylinositol (PI, 17:0/ 20:4, Avanti Polar Lipids), 25 pmol phosphatidylethanolamine (PE) and 25 pmol phosphatidylserine (PS) (both 14:1/14:1, 20:1/20:1, 579 22:1/22:1, semi-synthesized (Özbalci et al., 2013), 25 pmol diacylglycerol (DAG, 17:0/17:0, Larodan), 25 pmol cholesteryl ester (CE, 9:0, 19:0, 24:1, Sigma), and 24 pmol triacylglycerol (TAG, LM-6000/D5- 581 17:0,17:1,17:1, Avanti Polar Lipids), 5 pmol ceramide (Cer, d18:1 with N-acylated 14:0, 17:0, 25:0, semi-synthesized (Özbalci et al., 2013) or Cer d18:1/18:0-D3, Matreya) and 5 pmol glucosylceramide (HexCer) (d18:1 with N-acylated 14:0, 19:0, 27:0, semi-synthesized or GlcCer d18:1/17:0, Avanti Polar 584 Lipids), 5 pmol lactosylceramide (Hex2Cer, d18:1 with N-acylated C17 fatty acid), 10 pmol phosphatidic acid (PA, 17:0/20:4, Avanti Polar Lipids), 10 pmol phosphatidylglycerol (PG, 586 14:1/14:1, 20:1/20:1, 22:1/22:1, semi-synthesized (Özbalci et al., 2013) and 5 pmol lysophosphatidylcholine (LPC, 587 17:1, Avanti Polar Lipids). The final chloroform phase was evaporated under a gentle stream of nitrogen at 37 °C. Samples were either directly subjected to mass spectrometric analysis, or were stored at -20 °C prior to analysis, which was typically done within 1-2 days after extraction. Lipid extracts were resuspended in 10 mM ammonium acetate in 60 µl methanol. Two µl aliquots of the resuspended lipids were diluted 1:10 in 10 mM ammonium acetate in methanol in 96-well plates (Eppendorf twin tec 96) prior to measurement. For cholesterol determinations, the remaining lipid extract was again evaporated and subjected to acetylation as previously described (Liebisch et al., 2006). Samples were analysed on an QTRAP 6500+ mass spectrometer (Sciex) with chip-based (HD-D ESI Chip, Advion Biosciences) electrospray infusion and ionization via a Triversa Nanomate (Advion Biosciences). Data evaluation was done using LipidView (Sciex) and an in-house-developed software (ShinyLipids)."

5.2.9 Negative stain EM

Negative stain electron microscopy was used to verify the morphology of Ebola VLPs prior to using them for experiments (shown in Fig. 17). Formvar/Carbon grids (Table 12) were glow-discharged for 10 seconds

with a hydrogen/oxygen mixture using a Solarus plasma cleaner (Gatan), before being placed for 5 seconds on approximately 5 µl VLP solution (diluted to 10-20 ng/µl). After three successive washing steps in water, the grids were briefly blotted on Whatman Type 1 paper and placed for 30 seconds on 3 µl 2% phosphotungstic acid. Grids were then briefly blotted again and air-dried for several hours before imaging.

Data were acquired on a Tecnai F20 transmission electron microscope (ThermoFisher Scientific) equipped with a field emission gun and operated at 200 kV. Images shown in Figure 17 were acquired at 25 kx magnification, corresponding to a pixel size of 0.4459 nm.

5.2.10 cryo-CLEM of VLP-infected target cells

For the cryo-CLEM experiment of Ebola VLP-infected target cells (Fig. 26), Huh7 cells were seeded at a density of 0.0075 x 10^6 on R1/4 EM grids (Table 12) placed on 3D-printed grid holders in 96 well plates. They were then incubated for 24 h at 37°C, 5% CO_2. For the infection, all liquid was carefully removed and 50 µl GFP-VLPs (90 ng/µl) were directly added onto the grids. After 20 min incubation at 8°C, the VLP solutions were removed and replaced with 100 µl media supplemented with Lipi-blue (to stain lipid droplets) per well. After 1 h incubation at 37°C, the grids were plunge-frozen as described below for virus-infected cells.

The cryo-CLEM workflow employed in this work followed the protocol established in the lab and published in Methods in Cell Biology (Klein et al., 2021) closely. To map the fluorescence of GFP-VLPs and lipid droplets, the vitrified grids were inserted to a wide-field fluorescent microscope equipped with a cryo-stage (Leica) at -190°C. Fluorescent maps were acquired with Z-stacks covering 30 µm in step sizes of 300 nm using the Las X software (Leica). The grids were then transferred to an Aquilos dual-beam FIB-SEM microscope (ThermoFisher Scientific) to produce lamellae of 150-250 nm thickness. To target cells displaying signal from GFP-VLPs for cryo-FIB milling, the fluorescent maps were stitched using the "Stitch TileScan" function of the CryoCLEM FIJI plugin (Wachsmuth-Melm and Klein, 2020) and loaded into the MAPS software (ThermoFisher Scientific). Targeted cells were milled as described in detail (Wagner et al., 2020; Klein et al., 2021). The samples were then transferred to a Krios TEM microscope (ThermoFisher Scientific) to map the resulting lamellae and acquire tomograms at potential sites showing VLP entry events. To validate these entry events by fluorescence, the grids were transferred back to the wide-field fluorescent microscope (Leica) after data collection and fluorescence maps of FIB-milled cells were acquired using similar parameters as before. Since the lamellae were exposed to the electron beam, which damages the sample such that fluorescence is lost, they do not display any fluorescence, while the remaining cell body retains its fluorescence. Hence, by correlating both fluorescence maps acquired before and after FIB-milling and TEM, the fluorescence emanating from the plane of the lamellae can be precisely extracted as described by Klein et al (Klein et al., 2021). The correlation was performed using the icy software (De Chaumont et al., 2012). Lipid droplets, which were fluorescently stained and are easily identified by TEM, were used as correlation markers.

5.2.11 Sample preparation for cryo-ET

Sample preparation of VLPs and viruses

VLPs were either purified and diluted to approximately 10-20 ng/µl or used undiluted after harvesting from supernatants of VLP-producing cells (unpurified). Viruses were diluted 1:10 in HNE buffer (10 M HEPES, 100 mM NaCl, 1 mM EDTA, pH 7.4).

EM grids (200 mesh, R 2/1, Quantifoil, Table 12) were glow-discharged for 10 seconds with a hydrogen/oxygen mixture using a Solarus plasma cleaner (Gatan). VLP/ virus solutions were then mixed with 10 nm protein A-coated colloidal gold (Aurion) and applied onto the grids prior to vitrification by plunge-freezing with an EM GP2 automatic plunge-freezer (Leica). The plunge-freezer was operated as indicated by the manufacturer at a sample chamber environment of 25°C and 95% humidity, liquid ethane temperature of -183°C and using one-sided blotting on Whatman Type 1 paper with a blotting time of 3 seconds. Vitrified grids were clipped into Autogrids (ThermoFisher Scientific) and stored in liquid nitrogen until data acquisition.

Sample preparation of EBOV-infected cells

Grids containing VLP- or virus-infected cells were placed into the sample chamber of an EM GP2 automatic plunge-freezer (Leica). 3-5 µl growth medium or PHEM buffer (Table 6) were then added to the grids before blotting them from the back with Whatman Type 1 paper for 3 sec. After plunge-freezing, the vitrified grids were clipped into specifically designed AutoGrids™ (Thermo Fisher). The grids were then transferred to an Aquilos dual-beam FIB-SEM microscope (ThermoFisher Scientific) and cryo-FIB milling was performed after deposition of a thin organometallic platinum layer to minimize charging effects during milling. A focussed gallium-ion beam was used at an acceleration voltage of 30 eV to successively ablate cellular material as described in detail (Wagner et al., 2020; Klein et al., 2021) and to produce lamellae of approximately 200-250 nm thickness. The grids were then transferred to a Krios TEM microscope (ThermoFisher Scientific) for tomogram acquisition.

5.2.12 Tilt series acquisition and tomogram reconstruction

Tilt series were acquired on a Krios TEM microscope (ThermoFisher Scientific) operated at 300 kV in nanoprobe mode and equipped with a K3 direct electron detector (Gatan) using a 50 µm C2 aperture. Data acquisition was performed using the SerialEM software (Mastronarde, 2005). To identify regions of interest, grids containing either VLPs/ viruses or infected cells containing lamellae were first mapped at a low magnification of 135×, before acquiring maps at 8,700× magnification. Tilt series were acquired at 33,000× magnification, corresponding to a pixel size of 0.2671 nm, using a dose-symmetric acquisition scheme covering tilt ranges from 60° to -60° in 3° increments (Hagen et al., 2017). The target defocus was -4 µm, projections were acquired using the Quantum energy filter (Gatan) with a filter slit at 20 eV and the electron dose per projection image was kept constant at approximately 3 e^-/A^2, accumulating to a total dose of 120 e^-/A^2 per tilt series. Since the planes of the lamellae are tilted with respect to the grid by 8° due to the milling

angle, tilt series acquired on lamellae were performed with the stage tilted to 8° using a dose-symmetric scheme covering tilt ranges from 68° to -52°. For tilt series acquired both on VLPs/viruses and on lamellae, each projection was acquired in counting mode using dose fractionation and 20 – 40 individual frames.

Dual-axis tomography

Dual-axis tomography was performed using the same data acquisition scheme described above but using approximately half the electron dose per projection image, resulting in a cumulative dose of 60 e^-/A^2 per tilt series. After acquiring data along one axis, the stage was rotated by 90°, the region of interest was re-aligned, and a second tilt series was acquired.

Volta phase plate tomography

To acquire tilt series with the Volta phase plate instead of defocus phase contrast, data were collected as previously described (Winter and Chlanda, 2021):

"Tilt series were acquired using the dose-symmetric tilt schema with an angular range ±60◦, an increment of 3◦, and a projection dose of ~0.8–3.2 $e^-/Å^2$ using SerialEM 3.8.0 beta (Mastronarde, 2005). Each record projection was acquired as a movie composed of 10–15 frames which were aligned and summed on-fly using the SerialEM SEMCCD plugin. Beam-tilt angle for focus determination was set to 10 mrad and no defocus offset was used. Beam shift pivot points were aligned for both microprobe and nanoprobe modes. Objective astigmatism correction and coma-free alignment were per- formed in Sherpa 1.12.3 (ThermoFisher Scientific, USA). An objective aperture with a diameter of 100 μm was used for the defocus phase- contrast cryo-ET. The VPP on-plane position at the back focal plane and the C2 condenser astigmatism were corrected using a Ronchigram with 150 μm diameter C2 aperture. VPP conditioning was done at a magnification 33,000×, beam diameter ~2.5 μm and screen current ~0.3 nA, and the phase shift of 0.5 π was verified using the Sherpa tool 1.12.3 before starting each tilt series acquisition."

Tomogram reconstruction

Tilt series alignment and tomogram reconstruction was performed using Etomo (IMOD version 4.10.49) (Kremer et al., 1996). Alignment of tilt series acquired on VLPs/ viruses was performed using 10-15 fiducial markers, while tilt series acquired on lamellae were aligned using 3-5 spots of platinum sprinkled on the lamellae during FIB-milling as fiducial markers. Prior to tomogram reconstruction, CTF correction was performed by phase flipping for tilt series acquired with defocus phase contrast. Dose filtration was performed for all tilt series and final tomograms were reconstructed by weighted back-projection using a SIRT-like filter equivalent to 10 iterations.

Dual-axis tomograms were described as above but using 20-40 fiducial markers for precise alignment. Tomogram combination was performed as previously described (Winter and Chlanda, 2021):

"Two tomograms were combined in IMOD using fiducial markers on one side, fiducial markers with high residual errors were excluded to keep the mean residual error below 8 pixels. The final rotation between

the axis of the two tomograms was approximately 87◦. Local cross-correlation values of overlapping patches (400×400×200 pixels) were calculated using kernel filtering with sigma 3, and linear interpolation for both initial registration and the final match. Large residual patch vectors corresponding to areas with low cross-correlation values were removed from the patch vector model to minimize the warping residuals."

5.2.13 Subtomogram averaging

For subtomogram averaging, tomograms were acquired at a Krios TEM microscope (ThermoFisher Scientific) equipped with a K2 direct electron detector (Gatan) at EMBL Heidelberg by Wim Hagen. As briefly described above, data were collected using the SerialEM software (Mastronarde, 2005) and tomograms were acquired at 81,000× magnification, which corresponds to a pixel size of 0.17005 nm. Subtomogram averaging including particle picking, alignment and averaging was performed using the Dynamo software package (Castaño-Díez et al., 2012) as previously described (Winter et al., 2022):
"Particles were automatically picked using the filament model and subtomograms were extracted with a cubic side length of 128 voxels from 23 tomograms. A reference template was obtained by iteratively aligning and averaging of 50 subtomograms using a mask permitting alignments of only membrane and VP40 matrix. The initial average was then used as a template for the final averaging of approximately 7,800 particles."

5.2.14 Data visualization and Volume rendering

Data visualization

For visualization, tomograms were binned 3× when overview data are shown (for example Fig. 11 a, e) and binned 1× when details such as VP40 proteins along a membrane are shown (for example Fig. 11 b-d, f). Additionally, 10 slices were averaged, and the final projection was low-pass filtered.

Volume rendering

The subtomogram average was shown as a surface view rendered in ChimeraX (Pettersen et al., 2021). 3D-renderings shown in Figures 14, 27 and 30 were performed using the Amira software (ThermoFisher Scientific). For membrane segmentations, the data was binned 3×, low-pass filtered and a Membrane Enhancement Filter was applied. The membranes were then manually segmented in several tomogram slices and the segmentation was interpolated. Other features, such as nucleocapsids and the VP40 matrix were manually segmented after filtering the 3× binned data using a Gaussian Filter. The isosurface rendering shown in Figure 32 was performed in IMOD (Kremer et al., 1996).

5.2.15 Fluorescence light microscopy

Time-lapse confocal microscopy

In this work, time-lapse microscopy was performed on purified pHluorin-labelled VLPs to monitor changes in fluorescent properties of the VLPs upon exposure to different pH (Fig. 17). Ebola VLPs composed of

GP, VP40 and pHluorin-VP40 were produced and purified as described above. VLP solutions were diluted in HNE buffer (10 mM HEPES, 100 mM NaCl, 1 mM EDTA) calibrated to pH 7.4 to 10-20 ng/µl. µ-Slide 8 well dishes (ibidi) were glow-discharged for 10 seconds using a Solaris plasma cleaner (Gatan) to improve VLP attachment to the bottom of the microscopy dish, 150 µl of the VLP solutions were added to the microscopy dishes and the VLPs were allowed to settle for approximately 20 min at RT. Time-lapse microscopy was performed using a Leica SP8 confocal microscope (Leica) with a 63× oil immersion objective. VLPs that had settled at the bottom of the microscopy dish were imaged using a 488 nm excitation laser and emission range of 500-600 nm. Z-stacks covering 1 µm were acquired in 300 nm step sizes in 15 second intervals and time-lapse movies were acquired for 30 min. To monitor the fluorescence properties of the VLPs as the external pH changes, a 20 mM citric acid solution was prepared in HNE buffer and added at a final citric acid concentration of 2.6 mM during data acquisition. To assess the acidification kinetics in the absence of the VLP membrane, VLPs were incubated for 5 min in 0.1% TritonX-100 prepared in HNE buffer prior to imaging.

Data processing and analysis was performed in FiJi (Schindelin et al., 2012). After generating maximum image projections of the Z-stacks, the movie frames of the time-lapse series were aligned using the MultiSteckReg plugin in FiJi. VLPs were then manually segmented, and their mean fluorescence was measured at each time-point. Fluorescence data for were normalized for every segmented VLP by dividing the fluorescence intensity at each time-point by the maximum fluorescence intensity. Normalized data were then plotted against time.

Confocal light microscopy

Confocal microscopy was performed in this work using a Leica SP8 confocal microscope (Leica) with a 63× oil immersion objective. To localize GFP-labelled VLPs in target cells (Fig. 20), Huh7 cells were grown on coverslips in 35 mm dishes at seeding densities of 0.02 x 10^6 cells per dish for 24 h at 37°C, 5% CO_2. They were then transfected with plasmids encoding NPC1-mRFP using TransIT-LT1 transfection reagent (Mirus) according to the protocol provided with the manufacturer. After 16 h, the coverslips were taken out of the cell culture dishes, placed on parafilm in a clean plastic dish next to a Kimwipe paper soaked in PBS to prevent drying. 50 µl purified GFP-VLP solution were added to the coverslips such that they were completely covered in liquid. The plastic dish was then closed with a plastic lid and incubated for 30 min at 8°C. The coverslips were briefly washed in fresh cell culture media (Table 3) and incubated in media for 0-6 h at 37°C, 5% CO_2. At different time-points post infection, the coverslips were then removed from the incubator, washed in PBS and chemically fixed for 20 min at RT using 4% paraformaldehyde in PBS. To visualize the cells' nuclei, DAPI was added to the media 30 min before fixation. After fixation, the dishes were briefly rinsed in water, mounted on microscopy slides using Prolong Glass mounting medium (Life Technologies) and kept at RT overnight before imaging. Data were acquired as Z-stacks covering 6 µm at 300 nm step sizes by exciting the samples in a sequential scan at 561 nm (emission range: 580-720 nm), at 488 nm (emission range: 500-575 nm) and at 405 nm (emission range 415-470 nm). To quantify internalized VLPs, the final stacks were anonymized using the "Blind Analysis Tools" plugin in FiJi. GFP-signal was

then manually counted in 3D for each cell. Co-localization events with NPC1-mRFP were quantified in a similar manner.

To monitor trVLP replication (Fig. 34), Huh7 cells were grown on coverslips in 35 mm dishes at seeding densities of 0.02 x 10^6 cells per dish and infected with trVLPs (produced according to the protocol described above). At different time-points post infection, the coverslips were briefly washed in PBS and fixed in 4% paraformaldehyde in PBS. They were then mounted on microscopy slides using Prolong Glass with nucblue (Life Technologies), which is a mounting media supplemented with a dye intercalating into DNA to visualize nuclei. Data were acquired as Z-stacks covering 6 µm at 300 nm step sizes by exciting the samples in a sequential scan at 561 nm (emission range: 580-720 nm), at 488 nm (emission range: 500-575 nm) and at 405 nm (emission range 415-470 nm).

Wide-field microscopy

Wide-field microscopy was used to assess BlaM-VLP infection (Fig. 21-23). Representative images were taken using a Nikon Eclipse Ts2 fluorescent microscope equipped with a DS-Fi3 camera, 20× / 0.4 NA lens and a custom filter cube optimized for acquisition of the beta-lactamase fluorescence resonance energy transfer (FRET) substrate CCF4-AM (ThermoFisher Scientific, Invitrogen™).

5.2.16 Calibration of pHluorin fluorescence

pHluorin fluorescence was calibrated at different pH using an Infinite 200 plate reader (Tecan). 96 well plates were coated with 2 µg fibronectin diluted in PBS per well by covering the surface of the wells with 50 µl of the fibronectin solution. After 1 h incubation at RT, the wells were rinsed with water and air-dried for 2 h at RT under the laminar flow hood. HEK 293T cells were reverse transfected with plasmids encoding pHluorin-VP40 and seeded into the 96 well plates at a seeding density of 0.02 x 10^6 cells per well. To this end, transfection mixes were prepared according to the pipetting scheme below and incubated for 20 min at RT. Cells were detached using trypsin-EDTA, mixed with the transfection mixes and seeded into the fibronectin-coated 96 well plates. After 24 h incubation at 37°C, 5% CO2, cells expressing pHluorin-VP40 exhibited bright fluorescence when excited at 488 nm. The cells were washed with HNE buffer (10 mM HEPES, 100 mM NaCl, 1 mM EDTA) calibrated to pH 7.4 and incubated in triplicates in HNE buffers calibrated to a range of pH levels including 3, 3.5, 4, 4.5, 5, 5.5, 6, 6.5, 7, 7.5, 8. They were incubated for 1 h at 37°C, 5% CO_2 and fluorescence was measured using an Infinite 200 plate reader (Tecan) at 488 nm excitation. The experiment was repeated three independent times and the fluorescence data was pooled and plotted against pH.

Table 18: Pipetting scheme for reverse transfection of HEK 293T cells

Component	Stock concentration	Volume in µl (for 1 well of a 96 well plate)
OptiMem		9
Ebo_008 (pHluorin-VP40)	1 µg/µl	0.1
PEI		0.3

5.2.17 Time-lapse measurement of cells

To determine the acidification kinetics across the plasma membranes, HEK 293T cells were reverse transfected with plasmids encoding pHluorin-VP40 and influenza A virus M2 as described above and seeded into fibronectin-coated 96 well plates. After 24 h incubation at 37°C, 5% CO2, the cells were washed with HNE buffer (10 mM HEPES, 100 mM NaCl, 1 mM EDTA) calibrated to pH 7.4 and fluorescence was measured at 488 nm excitation using an Infinite 200 plate reader (Tecan). The buffer was then exchanged to HNE buffer calibrated to pH 4.5 and fluorescence was immediately measured in 15 second intervals for 30 min using the plate reader. All measurements were performed in triplicates and the experiment was repeated three independent times.

5.2.18 Determination of the membrane permeability of VLPs and cells

The membrane permeability of the VLPs was determined by Gonen Golani (Schwarz lab, ITP Heidelberg) based on the fluorescence time-lapse data (Methods 5.2.15 and 5.2.17) as previously described (Winter et al., 2022):

"We estimate the membrane permeability based on the geometry and pH equilibrium time of the VLPs. The membrane total proton flux, I, is proportional to the area of the VLPs, A_{VLP}, ion concentration difference between the buffer, C_B, and VLPs, C_{VLP}, $\Delta C(t) = C_B - C_{VLP}(t)$, and membrane permeability coefficient P_m (Deamer and Bramhall, 1986),

$$I = P_m \cdot A_{VLP} \cdot \Delta C(t) \tag{1}$$

It is easy to show that the protons concentration difference decays exponentially with time t,

$$\Delta C(t) = \Delta C_0 \cdot e^{-\frac{t}{\tau}} \tag{2}$$

With the decay time constant $\tau = \frac{V_{VLP}}{P_m \cdot A_{VLP}}$, V_{VLP} the volume of the VLPs and ΔC_0 the initial concentration difference. The pH level is the logarithm of the proton concentration and is related to the concentration difference as follows:

$$\mathrm{pH_{VLP}}(t) = \mathrm{pH_{Buffer}} - \log_{10}\left[1 - \frac{\Delta C_0}{C_B} \cdot e^{-\frac{t}{\tau}}\right] \tag{3}$$

Next, we use a least-squares minimization procedure to fit the measured pH to Eq. 3. We find the three minimization parameters $\mathrm{pH_{Buffer}}$, $\frac{\Delta C_0}{C_B}$ and τ. Since the VLPs are either spherical or filamentous, we can derive the membrane permeability coefficient $P_m = \frac{R}{n \cdot \tau}$, with R the respective radius and n is either 2 for filamtoues VLPs or 3 for spherical VLPs and cells. The fitted decay times τ are presented in Fig. S3 B and the VLPs radii are found using cryo-ET (Fig. S3). In line with previous measurements of Ebola VLPs and virions (Wan et al., 2020b), the filamentous VLPs had an average radius of 34 ± 4.5 nm (n = 90), while spherical particles are more heterogeneous in size, with a radius of 426 ± 100 nm (n = 12). A similar analysis

was also performed on HEK 293T cells. The cells had a round shape. The radius was estimated using fluorescence microscopy to be 17.5 ± 2.5 nm."

5.2.19 Beta-lactamase (BlaM) entry assay

The BlaM assay is a fluorescence-based assay to monitor entry of VLPs or viruses that carry beta-lactamase enzymes usually fused to their matrix proteins (Jones and Padilla-Parra, 2016). Upon successful entry into target cells, which are loaded with a beta-lactamase substrate composed of a FRET dye, the beta lactamase distributes in the cytoplasm and cleaves the FRET dye. This results in a shift in fluorescence that is measured and used to assess cell entry.

Preparation of cells

96 well plates were coated with 2 µg fibronectin in PBS per well. After incubating the wells for 1 h at RT in the fibronectin solution, they were washed with water and air-dried for 2 h at RT. Huh7 cell were seeded at a seeding density of 0.02 x 10^6 cells per well and incubated overnight at 37°C, 5% CO_2. Before infection, the cell culture media was replaced with media supplemented with DMSO or the entry inhibitors ammonium chloride (25 mM), bafilomycin (25 nM) or E64d (20 µM) and the cells were incubated for 1-2 h at 37°C, 5% CO_2.

Preparation of VLPs

BlaM VLPs composed of GP, VP40 and BlaM-VP40 were produced in HEK 293T cells and purified as described above. Same amounts of purified BlaM-VLPs were either kept untreated or treated with protease, low pH, or a combination of both. Protease-treatment was performed for 30 min at 37°C with 500 µg/ml thermolysin (ThermoFisher Scientific), reconstituted in H_2O and filtered through a 0.22 µm membrane filter. The reaction was stopped using 300 µg/ml phosphoramidon (Sigma-Aldrich) for 10 min at 37°C. Low-pH treatment was performed by adding citric acid at a final concentration of 1.6 mM prepared in HNE buffer (10 mM HEPES, 100 mM NaCl, 1 mM EDTA) for 30 min at 37°C. When a combination of protease- and low pH-treatment was used, the VLPs were first incubated with thermolysin and phosphoramidon as described above at neutral pH before lowering the pH with citric acid. VLPs were immediately placed on ice until infection.

Infection and readout

The media was removed from each well and replaced with 50 µl purified (pre-treated) BlaM-VLPs. The 96-well plates were then centrifuged for 30 min at 200 × g at 20°C (Beckmann), after which the BlaM-VLP solutions were removed and replaced with 100 µl media supplemented with DMSO or entry inhibitors. After 2 h incubation at 37°C, 5% CO2, the BlaM dye from the LiveBLAzer™ FRET-B/G Loading Kit with CCF4-AM (ThermoFisher Scientific) supplemented with probenecid (Invitrogen) was prepared according to the instructions from the manufacturer. 20 µl BlaM dye were added to each well and the plates were incubated for 12-14 h at 11°C. The cells were then harvested by trypsinization for 5-10 min at 37°C

and washed with three times with PBS and placed on ice. Single-cell fluorescence was measured at 410 nm excitation and emission at 450 nm and 510 nm by fluorescence-activated cell sorting (FACS) using a BD FACS Celesta Cell Analyzer (BD Biosciences). Per sample, 10,000 cells were analysed, and each experiment was repeated three times. FACS measurements and data processing were performed by Samy Sid Ahmed (Fackler lab, CIID Heidelberg).

5.2.20 In vitro reconstitution of membrane fusion

To reconstitute the membrane fusion between Ebola VLP membranes and endosomal membranes in vitro, Ebola VLPs composed of GP and VP40 were produced and purified as described above. Since EBOV fusion requires the presence of the endosomal receptor NPC1, liposomes composed of phosphatidylcholine, phosphatidylethanolamine and cholesterol (50%, 10%, 40%, respectively), incorporating purified human NPC1 were prepared by Chao Qi (Korkhov lab, PSI Villigen). The NPC1-containing liposomes were prepared in protein-to-lipid ratios of 1:100 and 1:1000. They were mixed with 10 nm protein A-coated colloidal gold (Aurion), plunge-frozen and analysed by cryo-ET.

To reconstitute the fusion reaction, 50 ng/µl VLPs were either kept untreated, or were treated with 500 µg/ml thermolysin (ThermoFisher Scientific), which was reconstituted in H_2O and filtered through a 0.22 µm membrane filter, for 30 min at 37°C. The VLPs were then mixed with NPC1-liposomes at a 1:1 ratio, immediately plunge-frozen with 10 nm protein A-coated colloidal gold (Aurion) and analysed by cryo-ET.

5.5.21 MD simulation and structure comparison

MD simulations presented in this work were performed by Fabio Lolicato (Nickel lab, BZH Heidelberg) as previously described (Winter et al., 2022):

"We used the truncated (residues 45-311) crystallographic structure of the VP40 dimer deposited by Norris, M.J. et al. (pdb: 7jzj) for atomistic molecular dynamics simulations. The missing CTD loops were modeled using the GalxyFill software(Coutsias et al., 2004) within the CHARMM-GUI web server (Jo et al., 2008). The protonation states of the proteins at pH 7.4 and 4.5 were calculated through the PROPKA web server (Søndergaard et al., 2011), which indicated a change in the protonation state at pH 4.5 for the following residues: E76, E325, H61, H124, H210, H269, H315. First, the proteins were simulated in water with a 0.1 M NaCl for 1 microsecond. Next, the final structures were placed at a distance of 2 nm from a previously built model membrane surface containing POPC:POPS:CHOL (30:30:40) at ten different random orientations. The model membrane was made using the CHARMM-GUI membrane builder (Jo et al., 2009). Since the percentage of POPS charged molecules at pH 4.5 is 10% (Tsui et al., 1986), we modelled the membrane at pH 4.5 by randomly replacing 90% of POPS molecules with its protonated model (POPSH). Then, each of the ten repeats was solvated with 40913 water molecules and 0.1 M NaCl. Next, charges were neutralized by adding or removing the needed amount of Na^+- or Cl^--ions. Finally, each system was simulated for 1 microsecond under NpT conditions. Four out of ten simulations, at both pH conditions,

showed VP40 dimer binding to the membrane with the experimentally known binding residues, K224, K225, K274 and K275. These simulations were used for the analysis. For the production run, we employed the Parrinello-Rahman barostat (Parrinello and Rahman, 1981) with a semi-isotropic pressure coupling scheme and a time constant set to 5.0 ps to maintain the pressure constant. The pressure was set to 1.0 bar and the isothermal compressibility to 4.5 × 10–5 bar–1. The temperature was maintained at 310 K using the Nose-Hoover thermostat (Hoover, 1985) with a time constant of 1.0 ps. Electrostatic interactions were handled using the PME method (Essmann et al., 1995). The cut-off length of 1.2 nm was used for electrostatic (real space component) and van der Waals interactions. Hydrogen bonds were constrained using the LINCS algorithm (Hess et al., 1997). Finally, periodic boundary conditions were applied in all directions. The simulations were carried out using an integration time step of 2 fs with coordinates saved every 100 ps. All simulations have been carried out with the GROMACS-2021 software (Abraham et al., 2015). Protein, lipids, and salt ions were described using the CHARMM36m force field (Pastor and MacKerell, 2011; Huang and Mackerell, 2013; Huang et al., 2016). For water, we used the TIP3 model (Jorgensen et al., 1983). All pictures, snapshots, and movies were rendered with the Visual Molecular Dynamics (VMD) software (Humphrey et al., 1996)."

For visualization (Fig. 15), the final frame of the MD simulation performed at pH 7.4 was loaded into ChimeraX (Pettersen et al., 2021) and overlayed with the subtomogram average presented in this work. The alignment between the published X-ray structure of the VP40 dimer (pdb: 7jzj) and the VP40 dimer interacting with the simulated membrane in the MD simulation was performed using the Matchmaker tool in ChimeraX.

References

Abbe, E. 1873. Beiträge zur Theorie des Mikroskops und der mikroskopischen Wahrnehmung: I. Die Construction von Mikroskopen auf Grund der Theorie. *Arch. für mikroskopische Anat.* 9:413–418. doi:10.1007/BF02956173.

Abraham, M.J., T. Murtola, R. Schulz, S. Páll, J.C. Smith, B. Hess, and E. Lindah. 2015. Gromacs: High performance molecular simulations through multi-level parallelism from laptops to supercomputers. *SoftwareX*. 1–2:19–25. doi:10.1016/j.softx.2015.06.001.

Acciani, M.D., M.F. Lay Mendoza, K.E. Havranek, A.M. Duncan, H. Iyer, O.L. Linn, and M.A. Brindley. 2021. Ebola Virus Requires Phosphatidylserine Scrambling Activity for Efficient Budding and Optimal Infectivity. *J. Virol.* 95. doi:10.1128/jvi.01165-21.

Adrian, M., J. Dubochet, J. Lepault, and A.W. McDowell. 1984. Cryo-electron microscopy of viruses. *Nature*. 308:32–36. doi:10.1142/9781848164666_0001.

Adu-Gyamfi, E., M.A. Digman, E. Gratton, and R. V. Stahelin. 2012. Single-particle tracking demonstrates that actin coordinates the movement of the Ebola virus matrix protein. *Biophys. J.* 103. doi:10.1016/j.bpj.2012.09.026.

Adu-Gyamfi, E., K.A. Johnson, M.E. Fraser, J.L. Scott, S.P. Soni, K.R. Jones, M.A. Digman, E. Gratton, C.R. Tessier, and R. V. Stahelin. 2015. Host Cell Plasma Membrane Phosphatidylserine Regulates the Assembly and Budding of Ebola Virus. *J. Virol.* 89:9440–9453. doi:10.1128/JVI.01087-15.

Al-Amoudi, A., J.J. Chang, A. Leforestier, A. McDowall, L.M. Salamin, L.P.O. Norlén, K. Richter, N.S. Blanc, D. Studer, and J. Dubochet. 2004. Cryo-electron microscopy of vitreous sections. *EMBO J.* 23:3583. doi:10.1038/SJ.EMBOJ.7600366.

Al-Amoudi, A., D. Studer, and J. Dubochet. 2005. Cutting artefacts and cutting process in vitreous sections for cryo-electron microscopy. *J. Struct. Biol.* 150:109–121. doi:10.1016/J.JSB.2005.01.003.

Alazard-Dany, N., V. Volchkova, O. Reynard, C. Carbonnelle, O. Dolnik, M. Ottmann, A. Khromykh, and V.E. Volchkov. 2006. Ebola virus glycoprotein GP is not cytotoxic when expressed constitutively at a moderate level. *J. Gen. Virol.* 87:1247–1257. doi:10.1099/vir.0.81361-0.

Aman, M.J. 2016. Chasing Ebola through the endosomal labyrinth. *MBio*. 7:e00346-16. doi:10.1128/mBio.00346-16.

Amman, B.R., S.A. Carroll, Z.D. Reed, T.K. Sealy, S. Balinandi, R. Swanepoel, A. Kemp, B.R. Erickson, J.A. Comer, S. Campbell, D.L. Cannon, M.L. Khristova, P. Atimnedi, C.D. Paddock, R.J. Kent Crockett, T.D. Flietstra, K.L. Warfield, R. Unfer, E. Katongole-Mbidde, R. Downing, J.W. Tappero, S.R. Zaki, P.E. Rollin, T.G. Ksiazek, S.T. Nichol, and J.S. Towner. 2012. Seasonal Pulses of Marburg Virus Circulation in Juvenile Rousettus aegyptiacus Bats Coincide with Periods of Increased Risk of Human Infection. *PLoS Pathog.* 8:1002877. doi:10.1371/journal.ppat.1002877.

Anthony, S.J., J.H. Epstein, K.A. Murray, I. Navarrete-Macias, C.M. Zambrana-Torrelio, A. Solovyov, R. Ojeda-Flores, N.C. Arrigo, A. Islam, S.A. Khan, P. Hosseini, T.L. Bogich, K.J. Olival, M.D. Sanchez-Leon, W.B. Karesh, T. Goldstein, S.P. Luby, S.S. Morse, J.A.K. Mazet, P. Daszak, and W.I. Lipkin. 2013. A strategy to estimate unknown viral diversity in mammals. *MBio.* 4. doi:10.1128/MBIO.00598-13/SUPPL_FILE/MBO004131613S1.DOCX.

De Arellano, E.R., M. Sanchez-Lockhart, M.J. Perteguer, M. Bartlett, M. Ortiz, P. Campioli, A. Hernández, J. Gonzalez, K. Garcia, M. Ramos, M.Á. Jiménez-Clavero, A. Tenorio, M.P. Sánchez-Seco, F. González, J.E. Echevarría, G. Palacios, and A. Negred. 2019. First evidence of antibodies against lloviu virus in schreiber's bent-winged insectivorous bats demonstrate a wide circulation of the virus in spain. *Viruses*. 11. doi:10.3390/v11040360.

Banerjee, I., Y. Miyake, S. Philip Nobs, C. Schneider, P. Horvath, M. Kopf, P. Matthias, A. Helenius, and Y. Yamauchi. 2014. Influenza A virus uses the aggresome processing machinery for host cell entry. *Science (80-.).* 346:473–477. doi:10.1126/science.1257037.

Baseler, L., D.S. Chertow, K.M. Johnson, H. Feldmann, and D.M. Morens. 2017. The Pathogenesis of Ebola Virus Disease. *Annu. Rev. Pathol. Mech. Dis.* 12:387–418. doi:10.1146/annurev-pathol-052016-100506.

Beniac, D.R., and T.F. Booth. 2017. Structure of the Ebola virus glycoprotein spike within the virion envelope at 11 Å resolution. *Sci. Rep.* 7:1–8. doi:10.1038/srep46374.

Beniac, D.R., P.L. Melito, S.L. deVarennes, S.L. Hiebert, M.J. Rabb, L.L. Lamboo, S.M. Jones, and T.F. Booth. 2012. The organisation of Ebola virus reveals a capacity for extensive, modular polyploidy.

PLoS One. 7. doi:10.1371/journal.pone.0029608.
Bharat, T.A.M., T. Noda, J.D. Riches, V. Kraehling, L. Kolesnikova, S. Becker, Y. Kawaoka, and J.A.G. Briggs. 2012. Structural dissection of Ebola virus and its assembly determinants using cryo-electron tomography. *Proc. Natl. Acad. Sci.* 109:4275–4280. doi:10.1073/pnas.1120453109.
Bhattarai, N., J.B. Gc, B.S. Gerstman, R. V. Stahelin, and P.P. Chapagain. 2017. Plasma membrane association facilitates conformational changes in the Marburg virus protein VP40 dimer. *RSC Adv.* 7:22741–22748. doi:10.1039/C7RA02940C.
Biek, R., P.D. Walsh, E.M. Leroy, and L.A. Real. 2006. Recent common ancestry of Ebola Zaire virus found in a bat reservoir. *PLoS Pathog.* 2:0885–0886. doi:10.1371/journal.ppat.0020090.
Blight, E.G., and W.J. Dyer. 1959. A rapid method of total lipid extraction and purification. *Can. J. Biochem. Physiol.* 37:911–917. doi:10.1139/o59-099.
Bobone, S., M. Hilsch, J. Storm, V. Dunsing, A. Herrmann, and S. Chiantia. 2017. Phosphatidylserine Lateral Organization Influences the Interaction of Influenza Virus Matrix Protein 1 with Lipid Membranes. *J. Virol.* 91:1–15. doi:10.1128/jvi.00267-17.
Bodmer, B.S., and T. Hoenen. 2022. Assessment of Life Cycle Modeling Systems as Prediction Tools for a Possible Attenuation of Recombinant Ebola Viruses. *Viruses*. 14. doi:10.3390/v14051044.
Boekema, E.J., M. Folea, and R. Kouřil. 2009. Single particle electron microscopy. *Photosynth. Res.* 102:189. doi:10.1007/S11120-009-9443-1.
Bornholdt, Z.A., T. Noda, D.M. Abelson, P. Halfmann, M. Wood, Y. Kawaoka, and E.O. Saphire. 2013a. Structural basis for ebolavirus matrix assembly and budding; protein plasticity allows multiple functions. doi:10.1016/j.cell.2013.07.015.
Bornholdt, Z.A., T. Noda, D.M. Abelson, P. Halfmann, M.R. Wood, Y. Kawaoka, and E.O. Saphire. 2013b. Structural rearrangement of ebola virus vp40 begets multiple functions in the virus life cycle. *Cell.* 154:763–774. doi:10.1016/j.cell.2013.07.015.
von Borries, B., E. Ruska, and H. Ruska. 1938. Bakterien und Virus in übermikorskopischer Aufnahme. *Klin. Wochenschr.*
Bousarghin, L., A. Touzé, P.-Y. Sizaret, and P. Coursaget. 2003. Human Papillomavirus Types 16, 31, and 58 Use Different Endocytosis Pathways To Enter Cells. *J. Virol.* 77:3846–3850. doi:10.1128/jvi.77.6.3846-3850.2003.
Bowen, E.T.W., G. Lloyd, W.J. Harris, G.S. Platt, A. Baskerville, and E.E. Vella. 1977. VIRAL HÆMORRHAGIC FEVER IN SOUTHERN SUDAN AND NORTHERN ZAIRE. Preliminary Studies on the Aetiological Agent. *Lancet*. 309:571–573. doi:10.1016/S0140-6736(77)92001-3.
Brecher, M., K.L. Schornberg, S.E. Delos, M.L. Fusco, E.O. Saphire, and J.M. White. 2012. Cathepsin Cleavage Potentiates the Ebola Virus Glycoprotein To Undergo a Subsequent Fusion-Relevant Conformational Change. *J. Virol.* 86:364–372. doi:10.1128/JVI.05708-11.
Brenner, S., and R.W. Horne. 1959. A negative staining method for high resolution electron microscopy of viruses. *BBA - Biochim. Biophys. Acta*. 34:103–110. doi:10.1016/0006-3002(59)90237-9.
Brix, K., A. Dunkhorst, K. Mayer, and S. Jordans. 2008. Cysteine cathepsins: Cellular roadmap to different functions. *Biochimie*. 90:194–207. doi:10.1016/J.BIOCHI.2007.07.024.
Brochmann Murray, E.J., M.S. Grisanti, G. V. Bentley, and S.S. Murray. 1997. E64d, a membrane-permeable cysteine protease inhibitor, attenuates the effects of parathyroid hormone on osteoblasts in vitro. *Metabolism.* 46:1090–1094. doi:10.1016/S0026-0495(97)90284-5.
Burleigh, L.M., L.J. Calder, J.J. Skehel, and D.A. Steinhauer. 2005. Influenza A Viruses with Mutations in the M1 Helix Six Domain Display a Wide Variety of Morphological Phenotypes. *J. Virol.* 79:1262–1270. doi:10.1128/jvi.79.2.1262-1270.2005.
Calder, L.J., S. Wasilewski, J.A. Berriman, and P.B. Rosenthal. 2010. Structural organization of a filamentous influenza A virus. *Proc. Natl. Acad. Sci. U. S. A.* 107:10685–10690. doi:10.1073/pnas.1002123107.
Cao, Y., R. Yang, I. Lee, W. Zhang, J. Sun, W. Wang, and X. Meng. 2021. Characterization of the SARS-CoV-2 E Protein: Sequence, Structure, Viroporin, and Inhibitors. *Protein Sci.* 30:1114–1130. doi:10.1002/pro.4075.
Carette, J.E., M. Raaben, A.C. Wong, A.S. Herbert, G. Obernosterer, N. Mulherkar, A.I. Kuehne, P.J. Kranzusch, A.M. Griffin, G. Ruthel, P.D. Cin, J.M. Dye, S.P. Whelan, K. Chandran, and T.R. Brummelkamp. 2011. Ebola virus entry requires the cholesterol transporter Niemann-Pick C1. *Nature*. 477:340–343. doi:10.1038/nature10348.
Castaño-Díez, D., M. Kudryashev, M. Arheit, and H. Stahlberg. 2012. Dynamo: A flexible, user-friendly

development tool for subtomogram averaging of cryo-EM data in high-performance computing environments. *J. Struct. Biol.* 178:139–151. doi:10.1016/j.jsb.2011.12.017.
Chamberland, C. 1884. Sur Un Filtre Donnant de l'eau Physiologiquement Pure. *C. R. Hebd. Acad. Sci. Paris,*. 247–248.
Chandran, K., N.J. Sullivan, U. Felbor, S.P. Whelan, and J.M. Cunningham. 2005. Endosomal proteolysis of the Ebola virus glycoprotein is necessary for infection. *Science.* 308:1643–5. doi:10.1126/science.1110656.
De Chaumont, F., S. Dallongeville, N. Chenouard, N. Hervé, S. Pop, T. Provoost, V. Meas-Yedid, P. Pankajakshan, T. Lecomte, Y. Le Montagner, T. Lagache, A. Dufour, and J.C. Olivo-Marin. 2012. Icy: an open bioimage informatics platform for extended reproducible research. *Nat. Methods 2012 97.* 9:690–696. doi:10.1038/nmeth.2075.
Chua, K.B., E.M.H. Wong, B.C. Cropp, and A.D. Hyatt. 2007. Role of electron microscopy in Nipah virus outbreak investigation and control. *Med. J. Malaysia.* 62:139–142.
Conley, M.J., J.M. Short, A.M. Burns, J. Streetley, J. Hutchings, S.E. Bakker, B.J. Power, H. Jaffery, J. Haney, G. Zanetti, P.R. Murcia, M. Stewart, R. Fearns, S. Vijayakrishnan, and D. Bhella. 2022. Helical ordering of envelope-associated proteins and glycoproteins in respiratory syncytial virus. *EMBO J.* 41. doi:10.15252/embj.2021109728.
Cosslett, V.E. 1978. Radiation damage in the high resolution electron microscopy of biological materials: A review. *J. Microsc.* 113:113–129. doi:10.1111/j.1365-2818.1978.tb02454.x.
Côté, M., J. Misasi, T. Ren, A. Bruchez, K. Lee, C.M. Filone, L. Hensley, Q. Li, D. Ory, K. Chandran, and J. Cunningham. 2011. Small molecule inhibitors reveal Niemann-Pick C1 is essential for Ebola virus infection. *Nature.* 477:344–348. doi:10.1038/nature10380.
Coutsias, E.A., C. Seok, M.P. Jacobson, and K.A. Dill. 2004. A Kinematic View of Loop Closure. *J. Comput. Chem.* 25:510–528. doi:10.1002/jcc.10416.
Crowther, R.A., L.A. Amos, J.T. Finch, D.J. De Rosier, and A. Klug. 1970. Three Dimensional Reconstructions of Spherical Viruses by Fourier Synthesis from Electron Micrographs. *Nature.* 226:421–425. doi:10.1038/226421a0.
Curry, S. 2015. Interdisciplinary Science Reviews Structural Biology: A Century-long Journey into an Unseen World. doi:10.1179/0308018815Z.000000000120.
Dahl, R., and L.A. Staehelin. 1989. Highpressure freezing for the preservation of biological structure: Theory and practice. *J. Electron Microsc. Tech.* 13:165–174. doi:10.1002/jemt.1060130305.
Danev, R., B. Buijsse, M. Khoshouei, J.M. Plitzko, and W. Baumeister. 2014. Volta potential phase plate for in-focus phase contrast transmission electron microscopy. *Proc. Natl. Acad. Sci. U. S. A.* 111:15635–15640. doi:10.1073/pnas.1418377111.
Danev, R., and K. Nagayama. 2001. Transmission electron microscopy with Zernike phase plate. *Ultramicroscopy.* 88:243–252. doi:10.1016/S0304-3991(01)00088-2.
Davey, R.A., O. Shtanko, M. Anantpadma, Y. Sakurai, K. Chandran, and W. Maury. 2017. Mechanisms of filovirus entry. *In* Current Topics in Microbiology and Immunology. 323–352.
Deamer, D.W. 1987. Proton permeation of lipid bilayers. *J. Bioenerg. Biomembr.* 19:457–479. doi:10.1007/BF00770030.
Deamer, D.W., and J. Bramhall. 1986. Permeability of lipid bilayers to water and ionic solutes. *Chem. Phys. Lipids.* 40:167–188. doi:10.1016/0009-3084(86)90069-1.
DeCoursey, T.E. 2008. Voltage-Gated Proton Channels. *Cell. Mol. Life Sci.* 65:2554. doi:10.1007/S00018-008-8056-8.
Depelteau, J.S., L. Renault, N. Althof, C.K. Cassidy, L.M. Mendonça, G.J. Jensen, G.P. Resch, and A. Briegel. 2022. UVC inactivation of pathogenic samples suitable for cryo-EM analysis. *Commun. Biol.* 5. doi:10.1038/s42003-021-02962-w.
Dessen, A. 2000. Crystal structure of the matrix protein VP40 from Ebola virus. *EMBO J.* 19:4228–4236. doi:10.1093/emboj/19.16.4228.
Dierksen, K., D. Typke, R. Hegerl, and W. Baumeister. 1993. Towards automatic electron tomography II. Implementation of autofocus and low-dose procedures. *Ultramicroscopy.* 49:109–120. doi:10.1016/0304-3991(93)90217-L.
Dobay, M.P., A. Dobay, J. Bantang, and E. Mendoza. 2011. How many trimers? Modeling influenza virus fusion yields a minimum aggregate size of six trimers, three of which are fusogenic. *Mol. Biosyst.* 7:2741–2749. doi:10.1039/c1mb05060e.
Dolnik, O., and S. Becker. 2022. Assembly and transport of filovirus nucleocapsids. *PLOS Pathog.*

18:e1010616. doi:10.1371/JOURNAL.PPAT.1010616.
Downing, K.H., and R.M. Glaeser. 1986. Improvement in high resolution image quality of radiation-sensitive specimens achieved with reduced spot size of the electron beam. *Ultramicroscopy*. 20:269–278. doi:10.1016/0304-3991(86)90191-9.
Dröse, S., and K. Altendorf. 1997. Bafilomycins and concanamycins as inhibitors of V-ATPases and P-ATPases. *J. Exp. Biol.* 200:1–8. doi:10.1242/jeb.200.1.1.
Dube, D., M.B. Brecher, S.E. Delos, S.C. Rose, E.W. Park, K.L. Schornberg, J.H. Kuhn, and J.M. White. 2009. The Primed Ebolavirus Glycoprotein (19-Kilodalton GP 1,2): Sequence and Residues Critical for Host Cell Binding. *J. Virol.* 83:2883–2891. doi:10.1128/jvi.01956-08.
Dubochet, J., M. Adrian, J.-J. Chang, J.-C. Homo, J. Lepault, A.W. McDowall, and P. Schultz. 1988. Cryo-electron microscopy of vitrified specimens. *Q. Rev. Biophys.* 21:129–228. doi:10.1017/S0033583500004297.
Ellis, D.S., D.I.H. Simpson, D.P. Francis, J. Knobloch, E.T. Bowen, P. Lolik, and I.M. Deng. 1978. Ultrastructure of Ebola virus particles in human liver. *J. Clin. Pathol.* 31:201–208. doi:10.1136/jcp.31.3.201.
Ellis, D.S., S. Stamford, G. Lloyd, E.T.W. Bowen, G.S. Platt, and H. Way. 1979. Ebola and Marburg Viruses: 1. Some UItrastructural Differences Between Strains When Grown in Vero Cells. *Microscopy*. 211:201–211.
Essmann, U., L. Perera, M.L. Berkowitz, T. Darden, H. Lee, and L.G. Pedersen. 1995. A smooth particle mesh Ewald method. *J. Chem. Phys.* 103:8577–8593. doi:10.1063/1.470117.
Faruqi, A.R., and G. McMullan. 2011. Electronic detectors for electron microscopy. 44. 357–390 pp.
Favard, C., J. Chojnacki, P. Merida, N. Yandrapalli, J. Mak, C. Eggeling, and D. Muriaux. 2019. HIV-1 Gag specifically restricts PI(4,5)P2 and cholesterol mobility in living cells creating a nanodomain platform for virus assembly. *Sci. Adv.* 5. doi:10.1126/sciadv.aaw8651.
Feldmann, H., and H.D. Klenk. 1996. Marburg and Ebola viruses. *Adv. Virus Res.* 47:1–52. doi:10.1016/s0065-3527(08)60733-2.
Feldmann, H., V.E. Volchkov, V.A. Volchkova, U. Ströher, and H.D. Klenk. 2001. Biosynthesis and role of filoviral glycoproteins. *J. Gen. Virol.* 82:2839–2848. doi:10.1099/0022-1317-82-12-2839/CITE/REFWORKS.
Feynman, R.P. 1960. There's Plenty of Room at the Bottom. *Eng. Sci.* 22–36. doi:10.1201/9780429500459.
Fischer, W.B., and M.S.P. Sansom. 2002. Viral ion channels: Structure and function. *Biochim. Biophys. Acta - Biomembr.* 1561:27–45. doi:10.1016/S0304-4157(01)00009-0.
Fontana, J., G. Cardone, J.B. Heymann, D.C. Winkler, and A.C. Steven. 2012. Structural Changes in Influenza Virus at Low pH Characterized by Cryo-Electron Tomography. *J. Virol.* 86:2919–2929. doi:10.1128/jvi.06698-11.
Fontana, J., and A.C. Steven. 2013. At Low pH, Influenza Virus Matrix Protein M1 Undergoes a Conformational Change Prior to Dissociating from the Membrane. *J. Virol.* 87:5621–5628. doi:10.1128/jvi.00276-13.
Galkin, V.E., A. Orlova, M.R. Vos, G.F. Schröder, and E.H. Egelman. 2015. Near-Atomic Resolution for One State of F-Actin. *Structure*. 23:173–182. doi:10.1016/J.STR.2014.11.006.
Gallaher, W.R., and R.F. Garry. 2015. Modeling of the ebola virus delta peptide reveals a potential lytic sequence motif. *Viruses*. 7:285–305. doi:10.3390/v7010285.
Garoff, H., R. Hewson, and D.-J.E. Opstelten. 1998. Virus Maturation by Budding. *Microbiol. Mol. Biol. Rev.* 62:1171–1190. doi:10.1128/mmbr.62.4.1171-1190.1998.
Garver, W.S., R.A. Heidenreich, R.P. Erickson, M.A. Thomas, and J.M. Wilson. 2000. Localization of the murine Niemann-Pick C1 protein to two distinct intracellular compartments. *J. Lipid Res.* 41:673–687. doi:10.1016/S0022-2275(20)32376-2.
Geisbert, T.W., and P.B. Jahrling. 1995. Differentiation of filoviruses by electron microscopy. *Virus Res.* 39:129–150. doi:10.1016/0168-1702(95)00080-1.
Glaeser, R.M., and K.A. Taylor. 1978. Radiation damage relative to transmission electron microscopy of biological specimens at low temperature: a review. *J. Microsc.* 112:127–138. doi:10.1111/j.1365-2818.1978.tb01160.x.
Goldsmith, C.S., and S.E. Miller. 2009. Modern uses of electron microscopy for detection of viruses. *Clin. Microbiol. Rev.* 22:552–563. doi:10.1128/CMR.00027-09.
Goldstein, T., S.J. Anthony, A. Gbakima, B.H. Bird, J. Bangura, A. Tremeau-Bravard, M.N. Belaganahalli,

H.L. Wells, J.K. Dhanota, E. Liang, M. Grodus, R.K. Jangra, V.A. DeJesus, G. Lasso, B.R. Smith, A. Jambai, B.O. Kamara, S. Kamara, W. Bangura, C. Monagin, S. Shapira, C.K. Johnson, K. Saylors, E.M. Rubin, K. Chandran, W.I. Lipkin, and J.A.K. Mazet. 2018. Discovery of a new ebolavirus (Bombali virus) in molossid bats in Sierra Leone. *Nat. Microbiol.* 3:1084. doi:10.1038/S41564-018-0227-2.

Gomis-Rüth, F.X., A. Dessen, J. Timmins, A. Bracher, L. Kolesnikowa, S. Becker, H.-D. Klenk, and W. Weissenhorn. 2003. The Matrix Protein VP40 from Ebola Virus Octamerizes into Pore-like Structures with Specific RNA Binding Properties. *Structure*. 11:423–433. doi:10.1016/S0969-2126(03)00050-9.

Gong, X., H. Qian, X. Zhou, J. Wu, T. Wan, P. Cao, W. Huang, X. Zhao, X. Wang, P. Wang, Y. Shi, G.F. Gao, Q. Zhou, and N. Yan. 2016. Structural insights into the Niemann-Pick C1 (NPC1)-mediated cholesterol transfer and ebola infection. *Cell.* 165:1467–1478. doi:10.1016/j.cell.2016.05.022.

Greber, U.F., I. Singh, and A. Helenius. 1994. Mechanisms of virus uncoating. *Trends Microbiol.* 2.

Gregory, S.M., E. Harada, B. Liang, S.E. Delos, J.M. White, and L.K. Tamm. 2011. Structure and function of the complete internal fusion loop from Ebolavirus glycoprotein 2. *PNAS*. 108:11211–11216. doi:10.1073/pnas.1104760108.

Groseth, A., J.E. Charton, M. Sauerborn, F. Feldmann, S.M. Jones, T. Hoenen, and H. Feldmann. 2009. The Ebola virus ribonucleoprotein complex: A novel VP30–L interaction identified. *Virus Res.* 140:8. doi:10.1016/J.VIRUSRES.2008.10.017.

Hagen, C., K.C. Dent, T. Zeev-Ben-, M. Plitzko, T.C. Mettenleiter, and K. Grü Newald Correspondence. 2015. Structural Basis of Vesicle Formation at the Inner Nuclear Membrane. *Cell.* 163. doi:10.1016/j.cell.2015.11.029.

Hagen, W.J.H., W. Wan, and J.A.G. Briggs. 2017. Implementation of a cryo-electron tomography tilt-scheme optimized for high resolution subtomogram averaging. *J. Struct. Biol.* 197:191–198. doi:10.1016/J.JSB.2016.06.007.

Han, Z., and R. Harty. 2005. Packaging of actin into Ebola virus VLPs. *Virol. J.* 2:92. doi:10.1186/1743-422X-2-92.

Hanssen, E. 2018. Cellular Imaging. Electron Tomography and Related Techniques. 319 pp.

Harty, R.N. 2009. No exit: targeting the budding process to inhibit filovirus replication. *Antiviral Res.* 81. doi:10.1016/j.antiviral.2008.12.003.

He, J., L.I. Melnik, A. Komin, G. Wiedman, T. Fuselier, C.F. Morris, C.G. Starr, P.C. Searson, W.R. Gallaher, K. Hristova, R.F. Garry, and W.C. Wimley. 2017. Ebola Virus Delta Peptide Is a Viroporin. *J. Virol.* 91. doi:10.1128/JVI.

Helenius, A., J. Kartenbeck, K. Simons, and E. Fries. 1980. On the entry of semliki forest virus into BHK-21 cells. *J. Cell Biol.* 84:404–420. doi:10.1083/jcb.84.2.404.

Hess, B., H. Bekker, H.J.C. Berendsen, and J.G.E.M. Fraaije. 1997. LINCS: A linear constraint solver for molecular simulations. *J. Comput. Chem.* 18:1463–1472. doi:10.1002/(sici)1096-987x(199709)18:12<1463::aid-jcc4>3.3.co;2-l.

Higgins, M.E., J.P. Davies, F.W. Chen, and Y.A. Ioannou. 1999. Niemann–Pick C1 Is a Late Endosome-Resident Protein That Transiently Associates with Lysosomes and the Trans-Golgi Network. *Mol. Genet. Metab.* 68:1–13. doi:10.1006/MGME.1999.2882.

Hoenen, T., N. Biedenkopf, F. Zielecki, S. Jung, A. Groseth, H. Feldmann, and S. Becker. 2010a. Oligomerization of Ebola Virus VP40 Is Essential for Particle Morphogenesis and Regulation of Viral Transcription. *J. Virol.* 84:7053–7063. doi:10.1128/jvi.00737-10.

Hoenen, T., S. Jung, A. Herwig, A. Groseth, and S. Becker. 2010b. Both matrix proteins of Ebola virus contribute to the regulation of viral genome replication and transcription. *Virology*. 403:56–66. doi:10.1016/j.virol.2010.04.002.

Hoenen, T., R.S. Shabman, A. Groseth, A. Herwig, M. Weber, G. Schudt, O. Dolnik, C.F. Basler, S. Becker, and H. Feldmann. 2012. Inclusion Bodies Are a Site of Ebolavirus Replication. *J. Virol.* 86:11779–11788. doi:10.1128/JVI.01525-12/SUPPL_FILE/ZJV999096756SO2.PDF.

Hoenen, T., A. Watt, A. Mora, and H. Feldmann. 2014. Modeling the lifecycle of Ebola virus under biosafety level 2 conditions with virus-like particles containing tetracistronic minigenomes. *J. Vis. Exp.* 52381. doi:10.3791/52381.

Holik, A.S. 2001. Optical microscopy. *Encycl. Mater. Sci. Technol.* doi:doi:10.1016/b0-08-043152-6/01142-6.

Hook, G., V. Hook, and M. Kindy. 2011. The cysteine protease inhibitor, E64d, reduces brain amyloid-β

and improves memory deficits in alzheimer's disease animal models by inhibiting cathepsin B, but not BACE1, β-secretase activity. *J. Alzheimer's Dis.* 26:387–408. doi:10.3233/JAD-2011-110101.
Hoover, W.G. 1985. Canonical dynamics: Equilibrium phase-space distributions. *Phys. Rev. A.* 31:1695–1697. doi:10.1103/PhysRevA.31.1695.
Huang, J., and A.D. Mackerell. 2013. CHARMM36 all-atom additive protein force field: Validation based on comparison to NMR data. *J. Comput. Chem.* 34:2135–2145. doi:10.1002/jcc.23354.
Huang, J., S. Rauscher, G. Nawrocki, T. Ran, M. Feig, B.L. De Groot, H. Grubmüller, and A.D. MacKerell. 2016. CHARMM36m: An improved force field for folded and intrinsically disordered proteins. *Nat. Methods.* 14:71–73. doi:10.1038/nmeth.4067.
Humphrey, W., A. Dalke, and K. Schulten. 1996. VMD: Visual molecular dynamics. *J. Mol. Graph.* 14:33–38. doi:10.1016/0263-7855(96)00018-5.
Husby, M.L., S. Amiar, L.I. Prugar, E.A. David, C.B. Plescia, K.E. Huie, J.M. Brannan, J.M. Dye, E. Pienaar, and R. V Stahelin. 2022. Phosphatidylserine clustering by the Ebola virus matrix protein is a critical step in viral budding. *EMBO Rep.* e51709. doi:10.15252/EMBR.202051709.
Hutchings, J., and G. Zanetti. 2018. Fine details in complex environments: the power of cryo-electron tomography. *Biochem. Soc. Trans.* 46:807–816. doi:10.1042/BST20170351.
Ivanovsky, D. 1903. Über die Mosaikkrankheit der Tabakpflanze. *Zeitschrift für Pflanzenkrankheiten.* 13:1–41.
Janesick, J.R. 2001. Scientific Charge-coupled Devices. SPIE Press.
Jeevan, B.G., B.S. Gerstman, and P.P. Chapagain. 2017. Membrane association and localization dynamics of the Ebola virus matrix protein VP40. *Biochim. Biophys. Acta - Biomembr.* 1859:2012–2020. doi:10.1016/j.bbamem.2017.07.007.
Jeevan, B.G., B.S. Gerstman, R. V. Stahelin, and P.P. Chapagain. 2016. The Ebola virus protein VP40 hexamer enhances the clustering of PI(4,5)P2 lipids in the plasma membrane. *Phys. Chem. Chem. Phys.* 18:28409–28417. doi:10.1039/c6cp03776c.
Jo, S., T. Kim, V.G. Iyer, and W. Im. 2008. CHARMM-GUI: A web-based graphical user interface for CHARMM. *J. Comput. Chem.* 29:1859–1865. doi:10.1002/jcc.20945.
Jo, S., J.B. Lim, J.B. Klauda, and W. Im. 2009. CHARMM-GUI membrane builder for mixed bilayers and its application to yeast membranes. *Biophys. J.* 97:50–58. doi:10.1016/J.BPJ.2009.04.013.
Johnson, K.A., M.R. Budicini, S. Urata, N. Bhattarai, B.S. Gerstman, P.P. Chapagain, S. Li, and R. V Stahelin. 2018. PI(4,5)P2 Binding Sites in the Ebola Virus Matrix Protein Modulate Assembly and Budding. *bio*R*xiv*. 341248. doi:10.1101/341248.
Johnson, K.A., G.J.F. Taghon, J.L. Scott, and R. V. Stahelin. 2016. The Ebola Virus matrix protein, VP40, requires phosphatidylinositol 4,5-bisphosphate (PI(4,5)P 2) for extensive oligomerization at the plasma membrane and viral egress. *Sci. Rep.* 6:1–14. doi:10.1038/srep19125.
Johnson, K.M., J.V. Lange, P.A. Webb, and F.A. Murphy. 1977. Isolation and partial characterization of a new virus causing acute haemorrhagic fever in Zaire. *Lancet.* 569–571.
Jones, D.M., and S. Padilla-Parra. 2016. The β-lactamase assay: Harnessing a FRET biosensor to analyse viral fusion mechanisms. *Sensors (Switzerland).* 16. doi:10.3390/s16070950.
Jorgensen, W.L., J. Chandrasekhar, J.D. Madura, R.W. Impey, and M.L. Klein. 1983. Comparison of simple potential functions for simulating liquid water. *J. Chem. Phys.* 79:926–935. doi:10.1063/1.445869.
Kaletsky, R.L., G. Simmons, and P. Bates. 2007. Proteolysis of the Ebola Virus Glycoproteins Enhances Virus Binding and Infectivity. *J. Virol.* 81:13378–13384. doi:10.1128/jvi.01170-07.
Kartenbeck, J., H. Stukenbrok, and A. Helenius. 1989. Endocytosis of Simian virus 40 into the endoplasmic reticulum. *J. Cell Biol.* 109:2721–2729. doi:10.1083/jcb.109.6.2721.
Kausche, G.A., E. Pfankuch, and H. Ruska. 1939. Die Sichtbarmachung von pflanzlichem Virus im Übermikroskop. *Naturwissenschaften.* 27:292–299. doi:10.1007/BF01493353.
Kemenesi, G., K. Kurucz, B. Dallos, B. Zana, F. Földes, S. Boldogh, T. Görföl, M.W. Carroll, and F. Jakab. 2018. Re-emergence of Lloviu virus in Miniopterus schreibersii bats, Hungary, 2016. *Emerg. Microbes Infect.* 7:1–4. doi:10.1038/s41426-018-0067-4.
Kiley, M.P., E.T.W. Bowen, G. Eddy, M. Isaäcson, K.M. Johnson, J.B. McCormick, F. Murphy, S.R. Pattyn, D. Peters, O.W. Prozesky, R.L. Regnery, D.I. Simpson, W. Slenczka, P. Sureau, G. van der Groen, P. Webb, and H. Wulff. 1982. Filoviridae: A taxonomic home for marburg and ebola viruses? *Intervirology.* 18:24–32. doi:10.1159/000149300.
Klein, S., M. Cortese, S. Winter, M. Wachsmuth-Melm, C. Neufeldt, B. Cerikan, M. Stanifer, S. Boulant,

R. Bartenschlager, and P. Chlanda. 2020a. SARS-CoV-2 structure and replication characterized by in situ cryo-electron tomography. *Nat. Commun.* 1–10. doi:10.1101/2020.06.23.167064.

Klein, S., M. Wachsmuth-Melm, S.L. Winter, A. Kolovou, and P. Chlanda. 2021. Cryo-correlative light and electron microscopy workflow for cryo-focused ion beam milled adherent cells. *In* Methods in Cell Biology. Academic Press. 273–302.

Klein, S., B. Wimmer, S.L. Winter, A. Kolovou, V. Laketa, and P. Chlanda. 2020b. Post-correlation on-lamella cryo-CLEM reveals the membrane architecture of lamellar bodies. doi:10.1101/2020.02.27.966739.

Knoll, M., and E. Ruska. 1932. Das Elektronenmikroskop. *Zeitschrift für Phys.* 78:318–339. doi:10.1055/s-0028-1122268.

Koehler, J.K. 1986. Advanced Techniques in Biological Electron Microscopy III.

Kolesnikova, L., E. Ryabchikova, A. Shestopalov, and S. Becker. 2007. Basolateral budding of marburg virus: VP40 retargets viral glycoprotein GP to the basolateral surface. *J. Infect. Dis.* 196. doi:10.1086/520584.

Kordyukova, L. V., P. V. Konarev, N. V. Fedorova, E. V. Shtykova, A.L. Ksenofontov, N.A. Loshkarev, L.A. Dadinova, T.A. Timofeeva, S.S. Abramchuk, A. V. Moiseenko, L.A. Baratova, D.I. Svergun, and O. V. Batishchev. 2021. The cytoplasmic tail of influenza a virus hemagglutinin and membrane lipid composition change the mode of m1 protein association with the lipid bilayer. *Membranes (Basel).* 11. doi:10.3390/membranes11100772.

Kordyukova, L. V., E. V. Shtykova, L.A. Baratova, D.I. Svergun, and O. V. Batishchev. 2019. Matrix proteins of enveloped viruses: a case study of Influenza A virus M1 protein. 37. Taylor & Francis. 671–690 pp.

Kremer, J.R., D.N. Mastronarde, and J.R. McIntosh. 1996. Computer Visualization of Three-Dimensional Image Data Using IMOD. *J. Struct. Biol.* 116:71–76. doi:10.1006/JSBI.1996.0013.

Kruger, D.H., P. Schneck, and H.R. Gelderblom. 2000. Helmut Ruska and the visualisation of viruses. *Lancet*. 355:1713–1717. doi:10.1016/S0140-6736(00)02250-9.

Ksiazek, T.G., D. Erdman, C.S. Goldsmith, S.R. Zaki, T. Peret, S. Emery, S. Tong, C. Urbani, J.A. Comer, W. Lim, P.E. Rollin, S.F. Dowell, A.-E. Ling, C.D. Humphrey, W.-J. Shieh, J. Guarner, C.D. Paddock, P. Rota, B. Fields, J. DeRisi, J.-Y. Yang, N. Cox, J.M. Hughes, J.W. LeDuc, W.J. Bellini, and L.J. Anderson. 2003. A Novel Coronavirus Associated with Severe Acute Respiratory Syndrome. *N. Engl. J. Med.* 348:1953–1966. doi:10.1056/NEJMOA030781/SUPPL_FILE/NEJM_KSIAZEK_1953SA1.PDF.

Kuhn, J.H., G.K. Amarasinghe, C.F. Basler, S. Bavari, A. Bukreyev, K. Chandran, I. Crozier, O. Dolnik, J.M. Dye, P.B.H. Formenty, A. Griffiths, R. Hewson, G.P. Kobinger, E.M. Leroy, E. Mühlberger, S. V Netesov, G. Palacios, B. Palyi, J.T. Pawęska, S.J. Smither, A. Takada, J.S. Towner, V. Wahl, E.J. Lefkowitz, A.J. Davison, S.G. Siddell, P. Simmonds, S. Sabanadzovic, D.B. Smith, and R.J. Orton. 2019. ICTV virus taxonomy profile: Filoviridae. *J. Gen. Virol.* 100:911–912. doi:10.1099/jgv.0.001252.

De La Vega, M.A., G. Wong, G.P. Kobinger, and X. Qiu. 2015. The Multiple Roles of sGP in Ebola Pathogenesis. *Viral Immunol.* 28:3. doi:10.1089/VIM.2014.0068.

Landeras-Bueno, S., H. Wasserman, G. Oliveira, Z.L. VanAernum, F. Busch, Z.L. Salie, V.H. Wysocki, K. Andersen, and E.O. Saphire. 2021. Cellular mRNA triggers structural transformation of Ebola virus matrix protein VP40 to its essential regulatory form. *Cell Rep.* 35. doi:10.1016/j.celrep.2021.108986.

Lecoq, H. 2001. Discovery of the first virus, Tobacco mosaic virus: 1892 or 1898? *Comptes Rendus l'Academie des Sci. - Ser. III*. 324:929–933. doi:10.1016/S0764-4469(01)01368-3.

Lee, J.E., M.L. Fusco, A.J. Hessell, W.B. Oswald, D.R. Burton, and E.O. Saphire. 2008. Structure of the Ebola virus glycoprotein bound to an antibody from a human survivor. *Nature*. 454:177–182. doi:10.1038/nature07082.

Lee, J.E., and E.O. Saphire. 2009. Ebolavirus glycoprotein structure and mechanism of entry. *Future Virol.* 4:621–635. doi:10.2217/fvl.09.56.

Lefkowitz, E.J., D.M. Dempsey, R.C. Hendrickson, R.J. Orton, S.G. Siddell, and D.B. Smith. 2018. Virus taxonomy: the database of the International Committee on Taxonomy of Viruses (ICTV). *Nucleic Acids Res.* 46:D708–D717. doi:10.1093/NAR/GKX932.

Leroy, E.M., B. Kumulungui, X. Pourrut, P. Rouquet, A. Hassanin, P. Yaba, A. Délicat, J.T. Paweska, J.P. Gonzalez, and R. Swanepoel. 2005. Fruit bats as reservoirs of Ebola virus. *Nat. 2005 4387068*. 438:575–576. doi:10.1038/438575a.

Leventis, P.A., and S. Grinstein. 2010. The distribution and function of phosphatidylserine in cellular membranes. *Annu. Rev. Biophys.* 39:407–427. doi:10.1146/annurev.biophys.093008.131234.
Li, S., C. Sieben, K. Ludwig, C.T. Höfer, S. Chiantia, A. Herrmann, F. Eghiaian, and I.A.T. Schaap. 2014. PH-ontrolled two-step uncoating of influenza virus. *Biophys. J.* 106:1447–1456. doi:10.1016/J.BPJ.2014.02.018/ATTACHMENT/9582977A-3A24-4C9B-A561-A3A1127995F4/MMC1.PDF.
Li, X., P. Mooney, S. Zheng, C. Booth, M.B. Braunfeld, S. Gubbens, D.A. Agard, and Y. Cheng. 2013. Electron counting and beam-induced motion correction enable near atomic resolution single particle cryoEM. *Nat. Methods.* 10:584–590. doi:10.1038/nmeth.2472.Electron.
Libersou, S., A.A.V. Albertini, M. Ouldali, V. Maury, C. Maheu, H. Raux, F. De Haas, S. Roche, Y. Gaudin, and J. Lepault. 2010. Distinct structural rearrangements of the VSV glycoprotein drive membrane fusion. *J. Cell Biol.* 191:199–210. doi:10.1083/jcb.201006116.
Liebisch, G., M. Binder, R. Schifferer, T. Langmann, B. Schulz, and G. Schmitz. 2006. High throughput quantification of cholesterol and cholesteryl ester by electrospray ionization tandem mass spectrometry (ESI-MS/MS). *Biochim. Biophys. Acta - Mol. Cell Biol. Lipids.* 1761:121–128. doi:10.1016/J.BBALIP.2005.12.007.
Liljeroos, L., and S.J. Butcher. 2013. Matrix proteins as centralized organizers of negative-sense RNA virions. *Front. Biosci.* 15:1–40.
Lingwood, D., and K. Simons. 2010. Lipid Rafts As a Membrane-Organizing Principle. *Science (80-.).* 327:46–50. doi:10.1126/SCIENCE.1174621.
Loeffler, F., and P. Frosch. 1898. Berichte der Kommission zur Erforschung der Maul-und Klauenseuche bei dem Institut für Infektionskrankheiten in Berlin. *Zentralblatt für Bakteriol. Parasitenkd. und Infekt.* 23:371–391.
Lu, J., Y. Qu, Y. Liu, R. Jambusaria, Z. Han, G. Ruthel, B.D. Freedman, and R.N. Harty. 2013. Host IQGAP1 and Ebola Virus VP40 Interactions Facilitate Virus-Like Particle Egress. *J. Virol.* 87:7777–7780. doi:10.1128/jvi.00470-13.
Mahamid, J., S. Pfeffer, M. Schaffer, E. Villa, R. Danev, L.K. Cuellar, F. Förster, A.A. Hyman, J.M. Plitzko, and W. Baumeister. 2016. Visualizing the molecular sociology at the HeLa cell nuclear periphery. *Science (80-.).* 351:969–972. doi:10.1126/science.aad8857.
Mahamid, J., D. Tegunov, A. Maiser, J. Arnold, H. Leonhardt, J.M. Plitzko, and W. Baumeister. 2019. Liquid-crystalline phase transitions in lipid droplets are related to cellular states and specific organelle association. *Proc. Natl. Acad. Sci. U. S. A.* 116:16866–16871. doi:10.1073/PNAS.1903642116/VIDEO-4.
Malek, M., A.M. Wawrzyniak, P. Koch, C. Lüchtenborg, M. Hessenberger, T. Sachsenheimer, W. Jang, B. Brügger, and V. Haucke. 2021. Inositol triphosphate-triggered calcium release blocks lipid exchange at endoplasmic reticulum-Golgi contact sites. *Nat. Commun.* 12. doi:10.1038/S41467-021-22882-X.
Manzoor, R., M. Igarashi, and A. Takada. 2017. Influenza A virus M2 protein: Roles from ingress to egress. *Int. J. Mol. Sci.* 18. doi:10.3390/ijms18122649.
Marko, M., C. Hsieh, R. Schalek, J. Frank, and C. Mannella. 2007. Focused-ion-beam thinning of frozen-hydrated biological specimens for cryo-electron microscopy. *Nat. Methods.* 4:215–217. doi:10.1038/nmeth1014.
Martines, R.B., D.L. Ng, P.W. Greer, P.E. Rollin, and S.R. Zaki. 2015. Tissue and cellular tropism, pathology and pathogenesis of Ebola and Marburg viruses. *J. Pathol.* 235:153–174. doi:10.1002/path.4456.
Martins, B., S. Sorrentino, W.-L. Chung, M. Tatli, O. Medalia, M.E. Correspondence, and M. Eibauer. 2020. Unveiling the polarity of actin filaments by cryo-electron tomography ll Unveiling the polarity of actin filaments by cryo-electron tomography. *Structure.* 29. doi:10.1016/j.str.2020.12.014.
Mastronarde, D.N. 1997. Dual-axis tomography: An approach with alignment methods that preserve resolution. *In* Journal of Structural Biology. 343–352.
Mastronarde, D.N. 2005. Automated electron microscope tomography using robust prediction of specimen movements. *J. Struct. Biol.* 152:36–51. doi:10.1016/J.JSB.2005.07.007.
Mattei, S., B. Glass, W.J.H. Hagen, H.G. Kräusslich, and J.A.G. Briggs. 2016. The structure and flexibility of conical HIV-1 capsids determined within intact virions. *Science (80-.).* 354:1434–1437. doi:10.1126/science.aah4972.
Mattei, S., A. Tan, B. Glass, B. Müller, H.G. Kräusslich, and J.A.G. Briggs. 2018. High-resolution structures of HIV-1 Gag cleavage mutants determine structural switch for virus maturation. *Proc.*

Natl. Acad. Sci. U. S. A. 115:E9401–E9410. doi:10.1073/PNAS.1811237115/SUPPL_FILE/PNAS.1811237115.SM01.MOV.
McCarthy, S.E., R.F. Johnson, Y.-A. Zhang, J.O. Sunyer, and R.N. Harty. 2007. Role for Amino Acids 212 KLR 214 of Ebola Virus VP40 in Assembly and Budding . *J. Virol.* 81:11452–11460. doi:10.1128/JVI.00853-07/FORMAT/EPUB.
Mehedi, M., T. Hoenen, S. Robertson, S. Ricklefs, M.A. Dolan, T. Taylor, D. Falzarano, H. Ebihara, S.F. Porcella, and H. Feldmann. 2013. Ebola Virus RNA Editing Depends on the Primary Editing Site Sequence and an Upstream Secondary Structure. *PLoS Pathog.* 9:1003677. doi:10.1371/JOURNAL.PPAT.1003677.
Melnik, L.I., S. Guha, J. Ghimire, A.R. Smither, B.J. Beddingfield, A.R. Hoffmann, L. Sun, N.A. Ungerleider, M.C. Baddoo, E.K. Flemington, W.R. Gallaher, W.C. Wimley, and R.F. Garry. 2022. Ebola virus delta peptide is an enterotoxin. *Cell Rep.* 38:110172. doi:10.1016/j.celrep.2021.110172.
Mendonça, L., A. Howe, J.B. Gilchrist, D. Sun, M.L. Knight, L.C. Zanetti-Domingues, B. Bateman, A.-S. Krebs, L. Chen, J. Radecke, Y. Sheng, V.D. Li, T. Ni, I. Kounatidis, M.A. Koronfel, M. Szynkiewicz, M. Harkiolaki, M.L. Martin-Fernandez, W. James, and P. Zhang. 2020. SARS-CoV-2 Assembly and Egress Pathway Revealed by Correlative Multi-Modal Multi-Scale Cryo-Imaging. *SSRN Electron. J.* doi:10.2139/ssrn.3733984.
Mercer, J., and A. Helenius. 2008. Vaccinia virus uses macropinocytosis and apoptotic mimicry to enter host cells. *Science (80-.).* 320:531–535. doi:10.1126/science.1155164.
Miesenböck, G., D.A. De Angelis, and J.E. Rothman. 1998. Visualizing secretion and synaptic transmission with pH-sensitive green fluorescent proteins.
Milazzo, A.C., A. Cheng, A. Moeller, D. Lyumkis, E. Jacovetty, J. Polukas, M.H. Ellisman, N.H. Xuong, B. Carragher, and C.S. Potter. 2011. Initial evaluation of a direct detection device detector for single particle cryo-electron microscopy. *J. Struct. Biol.* 176:404–408. doi:10.1016/j.jsb.2011.09.002.
Miller, E.H., G. Obernosterer, M. Raaben, A.S. Herbert, M.S. Deffieu, A. Krishnan, E. Ndungo, R.G. Sandesara, J.E. Carette, A.I. Kuehne, G. Ruthel, S.R. Pfeffer, J.M. Dye, S.P. Whelan, T.R. Brummelkamp, and K. Chandran. 2012. Ebola virus entry requires the host-programmed recognition of an intracellular receptor. *EMBO J.* 31:1947–1960. doi:10.1038/emboj.2012.53.
Mingo, R.M., J.A. Simmons, C.J. Shoemaker, E.A. Nelson, K.L. Schornberg, R.S. D'Souza, J.E. Casanova, and J.M. White. 2015a. Ebola Virus and Severe Acute Respiratory Syndrome Coronavirus Display Late Cell Entry Kinetics: Evidence that Transport to NPC1 $^{+}$ Endolysosomes Is a Rate-Defining Step. *J. Virol.* 89:2931–2943. doi:10.1128/JVI.03398-14.
Mittler, E., L. Kolesnikova, T. Strecker, W. Garten, and S. Becker. 2007. Role of the Transmembrane Domain of Marburg Virus Surface Protein GP in Assembly of the Viral Envelope. *J. Virol.* 81:3942–3948. doi:10.1128/jvi.02263-06.
Moor, H., and K. Mühlethaler. 1963. Fine structure in frozen-etched yeast cells. *J. Cell Biol.* 17:609–628. doi:10.1083/jcb.17.3.609.
Moreira, E.A., Y. Yamauchi, and P. Matthias. 2021. How Influenza Virus Uses Host Cell Pathways during Uncoating. *Cells 2021, Vol. 10, Page 1722*. 10:1722. doi:10.3390/CELLS10071722.
Nanbo, A., and Y. Kawaoka. 2019. Molecular Mechanism of Externalization of Phosphatidylserine on the Surface of Ebola Virus Particles. *DNA Cell Biol.* 38:115–120. doi:10.1089/dna.2018.4485.
Nanbo, A., J. Maruyama, M. Imai, M. Ujie, Y. Fujioka, S. Nishide, A. Takada, Y. Ohba, and Y. Kawaoka. 2018. Ebola virus requires a host scramblase for externalization of phosphatidylserine on the surface of viral particles. *PLoS Pathog.* 14:1–25. doi:10.1371/journal.ppat.1006848.
Negredo, A., G. Palacios, S. Vázquez-Morón, F. González, H. Dopazo, F. Molero, J. Juste, J. Quetglas, N. Savji, M. de la Cruz Martínez, J.E. Herrera, M. Pizarro, S.K. Hutchison, J.E. Echevarría, W.I. Lipkin, and A. Tenorio. 2011. Discovery of an ebolavirus-like filovirus in europe. *PLoS Pathog.* 7. doi:10.1371/journal.ppat.1002304.
Neufeld, E.B., M. Wastney, S. Patel, S. Suresh, A.M. Cooney, N.K. Dwyer, C.F. Roff, K. Ohno, J.A. Morris, E.D. Carstea, J.P. Incardona, J.F. Strauss, M.T. Vanier, M.C. Patterson, R.O. Brady, P.G. Pentchev, and E.J. Blanchette-Mackie. 1999. The Niemann-Pick C1 Protein Resides in a Vesicular Compartment Linked to Retrograde Transport of Multiple Lysosomal Cargo. *J. Biol. Chem.* 274:9627–9635. doi:10.1074/JBC.274.14.9627.
Nguyen, T.L., G. Schoehn, W. Weissenhorn, A.R. Hermone, J.C. Burnett, R.G. Panchal, C. McGrath, D.W. Zaharevitz, M.J. Aman, R. Gussio, and S. Bavari. 2005. An all-atom model of the pore-like structure of hexameric VP40 from Ebola: Structural insights into the monomer-hexamer transition.

J. Struct. Biol. 151:30–40. doi:10.1016/j.jsb.2005.02.013.
Ni, T., T. Frosio, L. Mendonça, Y. Sheng, D. Clare, B.A. Himes, and P. Zhang. 2022. High-resolution in situ structure determination by cryo-electron tomography and subtomogram averaging using emClarity. *Nat. Protoc. 2022 172*. 17:421–444. doi:10.1038/s41596-021-00648-5.
van Niel, G., P. Bergam, A. Di Cicco, I. Hurbain, A. Lo Cicero, F. Dingli, R. Palmulli, C. Fort, M.C. Potier, L.J. Schurgers, D. Loew, D. Levy, and G. Raposo. 2015. Apolipoprotein E Regulates Amyloid Formation within Endosomes of Pigment Cells. *Cell Rep.* 13:43–51. doi:10.1016/J.CELREP.2015.08.057.
Nieva, J.L., and L. Carrasco. 2015. Viroporins: Structures and functions beyond cell membrane permeabilization. *Viruses*. 7:5169–5171. doi:10.3390/v7102866.
Nieva, J.L., V. Madan, and L. Carrasco. 2012. Viroporins: structure and biological functions. *Nat. Rev. Microbiol.* 10:563–574. doi:10.1038/nrmicro2820.
Noda, T., H. Sagara, E. Suzuki, A. Takada, H. Kida, and Y. Kawaoka. 2002b. Ebola virus VP40 drives the formation of virus-like filamentous particles along with GP. *J. Virol.* 76:4855–65. doi:10.1128/JVI.76.10.4855-4865.2002.
Norris, M.J., M.L. Husby, W.B. Kiosses, J. Yin, R. Saxena, L.J. Rennick, A. Heiner, S.S. Harkins, R. Pokhrel, S.L. Schendel, K.M. Hastie, S. Landeras-Bueno, Z.L. Salie, B. Lee, P.P. Chapagain, A. Maisner, W. Paul Duprex, R. V. Stahelin, and E.O. Saphire. 2022. Measles and Nipah virus assembly: Specific lipid binding drives matrix polymerization. *Sci. Adv.* 8. doi:10.1126/sciadv.abn1440.
O'Reilly, F.J., L. Xue, A. Graziadei, L. Sinn, S. Lenz, D. Tegunov, C. Blötz, N. Singh, W.J.H. Hagen, P. Cramer, J. Stülke, J. Mahamid, and J. Rappsilber. 2020. In-cell architecture of an actively transcribing-translating expressome. *Science (80-.).* 369:554–557. doi:10.1126/SCIENCE.ABB3758/SUPPL_FILE/ABB3758_TABLE_S3.XLSX.
Obr, M., W.J.H. Hagen, R.A. Dick, L. Yu, A. Kotecha, and F.K.M. Schur. 2022. Exploring high-resolution cryo-ET and subtomogram averaging capabilities of contemporary DEDs. *J. Struct. Biol.* 214. doi:10.1016/j.jsb.2022.107852.
Oda, S., T. Noda, K.J. Wijesinghe, P. Halfmann, Z.A. Bornholdt, D.M. Abelson, T. Armbrust, R. V. Stahelin, Y. Kawaoka, and E.O. Saphire. 2016. Crystal Structure of Marburg Virus VP40 Reveals a Broad, Basic Patch for Matrix Assembly and a Requirement of the N-Terminal Domain for Immunosuppression. *J. Virol.* 90:1839–1848. doi:10.1128/jvi.01597-15.
Ohkuma, S., and B. Poole. 1978. Fluorescence probe measurement of the intralysosomal pH in living cells and the perturbation of pH by various agents. *Proc. Natl. Acad. Sci. U. S. A.* 75:3327–3331. doi:10.1073/PNAS.75.7.3327.
Olival, K.J., A. Islam, M. Yu, S.J. Anthony, J.H. Epstein, S.A. Khan, S.U. Khan, G. Crameri, L.F. Wang, W.I. Lipkin, S.P. Luby, and P. Daszak. 2013. Ebola virus antibodies in fruit bats, bangladesh. *Emerg. Infect. Dis.* 19:270–273. doi:10.3201/eid1902.120524.
Orlova, E. V., and H.R. Saibil. 2011a. Structural analysis of macromolecular assemblies by electron microscopy. *Chem. Rev.* 111:7710–7748. doi:10.1021/cr100353t.
Özbalci, C., T. Sachsenheimer, and B. Brügger. 2013. Quantitative analysis of cellular lipids by nano-electrospray ionization mass spectrometry. *Methods Mol. Biol.* 1033:3–20. doi:10.1007/978-1-62703-487-6_1/COVER/.
Panchal, R.G., G. Ruthel, T.A. Kenny, G.H. Kallstrom, D. Lane, S.S. Badie, L. Li, S. Bavari, and M.J. Aman. 2003. In vivo oligomerization and raft localization of Ebola virus protein VP40 during vesicular budding. *Proc. Natl. Acad. Sci. U. S. A.* 100:15936–15941. doi:10.1073/PNAS.2533915100/SUPPL_FILE/3915MOVIE5.MOV.
Parrinello, M., and A. Rahman. 1981. Polymorphic transitions in single crystals: A new molecular dynamics method. *J. Appl. Phys.* 52:7182–7190. doi:10.1063/1.328693.
Pastor, R.W., and A.D. MacKerell. 2011. Development of the CHARMM force field for lipids. *J. Phys. Chem. Lett.* 2:1526–1532. doi:10.1021/jz200167q.
Pease, D.C., and R.F. Baker. 1948. Sectioning Techniques for Electron Microscopy Using a Conventional Microtome. *Proc. Soc. Exp. Biol. Med.* 67:470–474. doi:10.3181/00379727-67-16344.
Pettersen, E.F., T.D. Goddard, C.C. Huang, E.C. Meng, G.S. Couch, T.I. Croll, J.H. Morris, and T.E. Ferrin. 2021. UCSF ChimeraX: Structure visualization for researchers, educators, and developers. *Protein Sci.* 30:70–82. doi:10.1002/PRO.3943.
Peukes, J., X. Xiong, S. Erlendsson, K. Qu, W. Wan, L.J. Calder, O. Schraidt, S. Kummer, S.M.V. Freund,

H.G. Kräusslich, and J.A.G. Briggs. 2020. The native structure of the assembled matrix protein 1 of influenza A virus. *Nature*. 587:495–498. doi:10.1038/s41586-020-2696-8.

Pokhrel, R., E. Pavadai, B.S. Gerstman, and P.P. Chapagain. 2019. Membrane pore formation and ion selectivity of the Ebola virus delta peptide. *Phys. Chem. Chem. Phys.* 21:5578–5585. doi:10.1039/c8cp07323f.

Pourrut, X., M. Souris, J.S. Towner, P.E. Rollin, S.T. Nichol, J.P. Gonzalez, and E. Leroy. 2009. Large serological survey showing cocirculation of Ebola and Marburg viruses in Gabonese bat populations, and a high seroprevalence of both viruses in Rousettus aegyptiacus. *BMC Infect. Dis.* 9:159. doi:10.1186/1471-2334-9-159.

Quemin, E.R.J., E.A. MacHala, B. Vollmer, V. Pražák, D. Vasishtan, R. Rosch, M. Grange, L.E. Franken, L.A. Baker, and K. Grünewald. 2020. Cellular Electron Cryo-Tomography to Study Virus-Host Interactions. *Annu. Rev. Virol.* 7:239–262. doi:10.1146/annurev-virology-021920-115935.

Radoshitzky, S.R., K.L. Warfield, X. Chi, L. Dong, K. Kota, S.B. Bradfute, J.D. Gearhart, C. Retterer, P.J. Kranzusch, J.N. Misasi, M.A. Hogenbirk, V. Wahl-Jensen, V.E. Volchkov, J.M. Cunningham, P.B. Jahrling, M.J. Aman, S. Bavari, M. Farzan, and J.H. Kuhn. 2011. Ebolavirus Δ-Peptide Immunoadhesins Inhibit Marburgvirus and Ebolavirus Cell Entry. *J. Virol.* 85:8502–8513. doi:10.1128/jvi.02600-10.

Richert-Pöggeler, K.R., K. Franzke, K. Hipp, and R.G. Kleespies. 2019. Electron microscopy methods for virus diagnosis and high resolution analysis of viruses. *Front. Microbiol.* 10. doi:10.3389/fmicb.2018.03255.

Rigort, A., F.J.B. Bäuerlein, E. Villa, M. Eibauer, T. Laugks, W. Baumeister, and J.M. Plitzko. 2012. Focused ion beam micromachining of eukaryotic cells for cryoelectron tomography. *Proc. Natl. Acad. Sci. U. S. A.* 109:4449–4454. doi:10.1073/pnas.1201333109.

Risselada, H.J. 2019. Cholesterol: The Plasma Membrane's Constituent that Chooses Sides. *Biophys. J.* 116:2235. doi:10.1016/J.BPJ.2019.05.003.

Rivers, T.M. 1932. The nature of viruses. *Physiol. Rev.* 12. doi:10.1152/physrev.1932.12.3.423.

Ruigrok, R.W.H., G. Schoehn, A. Dessen, E. Forest, V. Volchkov, O. Dolnik, H.D. Klenk, and W. Weissenhorn. 2000. Structural characterization and membrane binding properties of the matrix protein VP40 of Ebola virus. *J. Mol. Biol.* 300:103–112. doi:10.1006/jmbi.2000.3822.

Ruska, H., B. v. Borries, and E. Ruska. 1939. Die Bedeutung der Ubermikroskopie fiir die Virusforsehung. *Arch. gesamte Virusforsch.* 1:155–169.

Sanchez, A., M.P. Kiley, B.P. Holloway, and D.D. Auperin. 1993. Sequence analysis of the Ebola virus genome: organization, genetic elements, and comparison with the genome of Marburg virus. *Virus Res.* 29:215–240. doi:10.1016/0168-1702(93)90063-S.

Sankaran, N. 2018. On the historical significance of Beijerinck and his contagium vivum fluidum for modern virology. *Hist. Philos. Life Sci.* 40:1–25. doi:10.1007/s40656-018-0206-1.

Schaffer, M., J. Mahamid, B.D. Engel, T. Laugks, W. Baumeister, and J.M. Plitzko. 2017. Optimized cryo-focused ion beam sample preparation aimed at in situ structural studies of membrane proteins. *J. Struct. Biol.* 197:73–82. doi:10.1016/j.jsb.2016.07.010.

Schindelin, J., I. Arganda-Carreras, E. Frise, V. Kaynig, M. Longair, T. Pietzsch, S. Preibisch, C. Rueden, S. Saalfeld, B. Schmid, J.Y. Tinevez, D.J. White, V. Hartenstein, K. Eliceiri, P. Tomancak, and A. Cardona. 2012. Fiji - an Open Source platform for biological image analysis. *Nat. Methods*. 9:676–682. doi:10.1038/NMETH.2019.

Schmidt, M.L., B.A. Tews, A. Groseth, and T. Hoenen. 2018. Generation and Optimization of a Green Fluorescent Protein-Expressing Transcription and Replication-Competent Virus-Like Particle System for Ebola Virus. *J. Infect. Dis.* 360:218. doi:10.1093/infdis/jiy405.

Schorb, M., and F. Sieckmann. 2017. Matrix MAPS—an intuitive software to acquire, analyze, and annotate light microscopy data for CLEM. *Methods Cell Biol.* 140:321–333. doi:10.1016/BS.MCB.2017.03.012.

Schornberg, K., S. Matsuyama, K. Kabsch, S. Delos, A. Bouton, and J. White. 2006. Role of Endosomal Cathepsins in Entry Mediated by the Ebola Virus Glycoprotein Role of Endosomal Cathepsins in Entry Mediated by the Ebola Virus Glycoprotein. *J. Virol.* 80:4174–4178. doi:10.1128/JVI.80.8.4174.

Schudt, G., O. Dolnik, L. Kolesnikova, N. Biedenkopf, A. Herwig, and S. Becker. 2015. Transport of Ebolavirus Nucleocapsids Is Dependent on Actin Polymerization: Live-Cell Imaging Analysis of Ebolavirus-Infected Cells. *J. Infect. Dis.* 212:S160–S166. doi:10.1093/infdis/jiv083.

Schudt, G., L. Kolesnikova, O. Dolnik, B. Sodeik, and S. Becker. 2013. Live-cell imaging of Marburg virus-infected cells uncovers actin-dependent transport of nucleocapsids over long distances. *Proc. Natl. Acad. Sci. U. S. A.* 110:14402–14407. doi:10.1073/PNAS.1307681110/SUPPL_FILE/SM07.AVI.

Schulze, H., T. Kolter, and K. Sandhoff. 2009. Principles of lysosomal membrane degradation. Cellular topology and biochemistry of lysosomal lipid degradation. *Biochim. Biophys. Acta - Mol. Cell Res.* 1793:674–683. doi:10.1016/j.bbamcr.2008.09.020.

Schur, F.K.M., M. Obr, W.J.H. Hagen, W. Wan, A.J. Jakobi, J.M. Kirkpatrick, C. Sachse, H.G. Kräusslich, and J.A.G. Briggs. 2016. An atomic model of HIV-1 capsid-SP1 reveals structures regulating assembly and maturation. *Science (80-.).* 353:506–508. doi:10.1126/science.aaf9620.

Scianimanico, S., G. Schoehn, J. Timmins, R.H.W. Ruigrok, H.D. Klenk, and W. Weissenhorn. 2000. Membrane association induces a conformational change in the Ebola virus matrix protein. *EMBO J.* 19:6732–6741. doi:10.1093/emboj/19.24.6732.

Shoemaker, C.J., K.L. Schornberg, S.E. Delos, C. Scully, H. Pajouhesh, G.G. Olinger, L.M. Johansen, and J.M. White. 2013. Multiple Cationic Amphiphiles Induce a Niemann-Pick C Phenotype and Inhibit Ebola Virus Entry and Infection. *PLoS One.* 8. doi:10.1371/journal.pone.0056265.

Sibert, B.S., J.Y. Kim, J.E. Yang, Z. Ke, C.C. Stobart, M.M. Moore, and E.R. Wright. 2021. Respiratory syncytial virus matrix protein assembles as a lattice with local and extended order that coordinates the position of the fusion glycoprotein. *bioRxiv.* 2021.10.13.464285. doi:10.1101/2021.10.13.464285.

Siegert, R., H.L. Shu, W. Slenczka, D. Peters, and G. Müller. 1967. Zur Ätiologie einer unbekannten, von Affen ausgegangenen menschlichen Infektionskrankheit. *DMW - Dtsch. Medizinische Wochenschrift.* 92:2341–2343. doi:10.1055/S-0028-1106144.

Simmons, J.A., R.S. D'Souza, M. Ruas, A. Galione, J.E. Casanova, and J.M. White. 2015. Ebolavirus Glycoprotein Directs Fusion through NPC1- Endolysosomes. *J. Virol.* 90:605–610. doi:10.1128/JVI.01828-15.

Søndergaard, C.R., M.H.M. Olsson, M. Rostkowski, and J.H. Jensen. 2011. Improved treatment of ligands and coupling effects in empirical calculation and rationalization of p K a values. *J. Chem. Theory Comput.* 7:2284–2295. doi:10.1021/ct200133y.

Soni, S.P., and R. V Stahelin. 2014. The Ebola Virus Matrix Protein VP40 Selectively Induces Vesiculation from Phosphatidylserine-enriched Membranes. *J. Biol. Chem.* 289:33590–33597. doi:10.1074/jbc.M114.586396.

Spence, J.S., T.B. Krause, E. Mittler, R.K. Jangra, and K. Chandran. 2016. Direct visualization of Ebola virus fusion triggering in the endocytic pathway. *MBio.* 7:e01857-15. doi:10.1128/mBio.01857-15.

Stahelin, R. V. 2014. Membrane binding and bending in Ebola VP40 assembly and egress. *Front. Microbiol.* 5. doi:10.3389/fmicb.2014.00300.

Staples, J.E., and T.P. Monath. 2008. Yellow fever: 100 Years of discovery. *J. Am. Med. Assoc.* 300:960–962. doi:10.1001/jama.300.8.960.

Studer, D., B.M. Humbel, and M. Chiquet. 2008. Electron microscopy of high pressure frozen samples: Bridging the gap between cellular ultrastructure and atomic resolution. *Histochem. Cell Biol.* 130:877–889. doi:10.1007/S00418-008-0500-1/FIGURES/5.

Takamatsu, Y., L. Kolesnikova, and S. Becker. 2018. Ebola virus proteins NP, VP35, and VP24 are essential and sufficient to mediate nucleocapsid transport. *Proc. Natl. Acad. Sci. U. S. A.* 115:1075–1080. doi:10.1073/pnas.1712263115.

Tegunov, D., L. Xue, C. Dienemann, P. Cramer, and J. Mahamid. 2021. Multi-particle cryo-EM refinement with M visualizes ribosome-antibiotic complex at 3.5 Å in cells. *Nat. Methods.* 18:186–193. doi:10.1038/s41592-020-01054-7.

Thon, F. 1966. Zur defokussierungsabhängigkeit des phasen- kontrastes bei der elektronenmikroskopischen abbildung. *Zeitschrift fur Naturforsch. - Sect. A J. Phys. Sci.* 21:476–478. doi:10.1515/zna-1966-0417.

Towner, J.S., B.R. Amman, T.K. Sealy, S.A. Reeder Carroll, J.A. Comer, A. Kemp, R. Swanepoel, C.D. Paddock, S. Balinandi, M.L. Khristova, P.B.H. Formenty, C.G. Albarino, D.M. Miller, Z.D. Reed, J.T. Kayiwa, J.N. Mills, D.L. Cannon, P.W. Greer, E. Byaruhanga, E.C. Farnon, P. Atimnedi, S. Okware, E. Katongole-Mbidde, R. Downing, J.W. Tappero, S.R. Zaki, T.G. Ksiazek, S.T. Nichol, and P.E. Rollin. 2009. Isolation of genetically diverse Marburg viruses from Egyptian fruit bats. *PLoS Pathog.* 5:1000536. doi:10.1371/journal.ppat.1000536.

Trinick, J., and J. Berriman. 1987. Zero-loss electron microscopy with the Zeiss EM902. *Ultramicroscopy.*

21:393–397. doi:10.1016/0304-3991(87)90039-8.
Tsui, F.C., D.M. Ojcius, and W.L. Hubbell. 1986. The intrinsic pKa values for phosphatidylserine and phosphatidylethanolamine in phosphatidylcholine host bilayers. *Biophys. J.* 49:459–468. doi:10.1016/S0006-3495(86)83655-4.
Turoňová, B., W.J.H. Hagen, M. Obr, S. Mosalaganti, J.W. Beugelink, C.E. Zimmerli, H.G. Kräusslich, and M. Beck. 2020a. Benchmarking tomographic acquisition schemes for high-resolution structural biology. *Nat. Commun.* 11. doi:10.1038/s41467-020-14535-2.
Turoňová, B., M. Sikora, C. Schürmann, W.J.H. Hagen, S. Welsch, F.E.C. Blanc, S. von Bülow, M. Gecht, K. Bagola, C. Hörner, G. van Zandbergen, J. Landry, N.T.D. de Azevedo, S. Mosalaganti, A. Schwarz, R. Covino, M.D. Mühlebach, G. Hummer, J.K. Locker, and M. Beck. 2020b. In situ structural analysis of SARS-CoV-2 spike reveals flexibility mediated by three hinges. *Science (80-.).* 370:203–208. doi:10.1126/science.abd5223.
Twort, F.W. 1915. An investigation on the nature of ultramicroscopic viruses. *Lancet.* 186:1241–1243. doi:10.1016/S0140-6736(01)20383-3.
Vankadari, N., D.C. Shepherd, S.D. Carter, and D. Ghosal. 2022. Three-dimensional insights into human enveloped viruses in vitro and in situ. *Biochem. Soc. Trans.* 50:95–105. doi:10.1042/BST20210433.
Del Vecchio, K., C.T. Frick, B. Gc Jeevan, S. Oda, Bernard S. Gerstman, X. Erica Ollmann Saphire, Prem P. Chapagain, and Robert V. Stahelin. 2018. A cationic, C-terminal patch and structural rearrangements in Ebola virus matrix VP40 protein control its interactions with phosphatidylserine. doi:10.1074/jbc.M117.816280.
Villa, E., M. Schaffer, J.M. Plitzko, and W. Baumeister. 2013. Opening windows into the cell: Focused-ion-beam milling for cryo-electron tomography. *Curr. Opin. Struct. Biol.* 23:771–777. doi:10.1016/j.sbi.2013.08.006.
Volchkov, V.E., V.A. Volchkova, E. Mühlberger, L. V. Kolesnikova, M. Weik, O. Dolnik, and H.D. Klenk. 2001. Recovery of infectious Ebola virus from complementary DNA: RNA editing of the GP gene and viral cytotoxicity. *Science (80-.).* 291:1965–1969. doi:10.1126/SCIENCE.1057269/SUPPL_FILE/105726S4_THUMB.GIF.
Volchkova, V.A., H.-D. Klenk, and V.E. Volchkov. 1999. Delta-Peptide Is the Carboxy-Terminal Cleavage Fragment of the Nonstructural Small Glycoprotein sGP of Ebola Virus. *Virology.* 265:164–171. doi:10.1006/VIRO.1999.0034.
Wachsmuth-Melm, M., and S. Klein. 2020. cryoCLEM FIJI plugin.
Wagner, F.R., R. Watanabe, R. Schampers, D. Singh, H. Persoon, M. Schaffer, P. Fruhstorfer, J. Plitzko, and E. Villa. 2020. Preparing samples from whole cells using focused-ion-beam milling for cryo-electron tomography. *Nat. Protoc.* 15:2041–2070. doi:10.1038/s41596-020-0320-x.
Walker, P.J., S.G. Siddell, E.J. Lefkowitz, · Arcady, R. Mushegian, · Evelien, M. Adriaenssens, P. Alfenas-Zerbini, · Donald, M. Dempsey, · Bas, E. Dutilh, · María, L. García, · R Curtis Hendrickson, S. Junglen, M. Krupovic, J.H. Kuhn, · Amy, J. Lambert, M. Łobocka, · Hanna, and M. Oksanen. 2022. Recent changes to virus taxonomy ratified by the International Committee on Taxonomy of Viruses (2022). *Arch. Virol.* doi:10.1007/s00705-022-05516-5.
Wan, W., M. Clarke, M.J. Norris, L. Kolesnikova, A. Koehler, Z.A. Bornholdt, S. Becker, E.O. Saphire, and J.A.G. Briggs. 2020. Ebola and marburg virus matrix layers are locally ordered assemblies of VP40 dimers. *Elife.* 9:1–22. doi:10.7554/eLife.59225.
Wan, W., L. Kolesnikova, M. Clarke, A. Koehler, T. Noda, S. Becker, and J.A.G. Briggs. 2017. Structure and assembly of the Ebola virus nucleocapsid. *Nature.* 551:394–397. doi:10.1038/nature24490.
Wang, H.W., and X. Fan. 2019. Challenges and opportunities in cryo-EM with phase plate. *Curr. Opin. Struct. Biol.* 58:175–182. doi:10.1016/j.sbi.2019.06.013.
Wang, S.-W., K. Noonan, and A. Aldovini. 2004. Nucleocapsid-RNA Interactions Are Essential to Structural Stability but Not to Assembly of Retroviruses. *J. Virol.* 78:716–723. doi:10.1128/jvi.78.2.716-723.2004.
Wasilewski, S., L.J. Calder, T. Grant, and P.B. Rosenthal. 2012. Distribution of surface glycoproteins on influenza A virus determined by electron cryotomography. *Vaccine.* 30:7368–7373. doi:10.1016/j.vaccine.2012.09.082.
Welsch, S., L. Kolesnikova, V. Krähling, J.D. Riches, and S. Becker. 2010. Electron Tomography Reveals the Steps in Filovirus Budding. *PLoS Pathog.* 6:1000875. doi:10.1371/journal.ppat.1000875.
White, J., M. Kielian, and A. Arihelenius. 1983. Membrane fusion proteins of enveloped animal viruses. *Q. Rev. Biophys.* 16:151–195. doi:10.1017/S0033583500005072.

White, J.M., S.E. Delos, M. Brecher, and K. Schornberg. 2008. Structures and mechanisms of viral membrane fusion proteins: Multiple variations on a common theme. *Crit. Rev. Biochem. Mol. Biol.* 43:189–219. doi:10.1080/10409230802058320.

Will, C., E. Mühlberger, D. Linder, W. Slenczka, H.D. Klenk, and H. Feldmann. 1993. Marburg virus gene 4 encodes the virion membrane protein, a type I transmembrane glycoprotein. *J. Virol.* 67:1203–1210. doi:10.1128/jvi.67.3.1203-1210.1993.

Winter, S.L., and P. Chlanda. 2021a. Dual-axis Volta phase plate cryo-electron tomography of Ebola virus-like particles reveals actin-VP40 interactions. *J. Struct. Biol.* 213:107742. doi:10.1016/j.jsb.2021.107742.

Winter, S.L., and P. Chlanda. 2021b. Dual-axis Volta phase plate cryo-electron tomography of Ebola virus-like particles reveals actin-VP40 interactions. *J. Struct. Biol.* 213:107742. doi:10.1016/j.jsb.2021.107742.

Winter, S.L., G. Golani, F. Lolicato, M. Vallbracht, S. Sid Ahmed, C. Lüchtenborg, O.T. Fackler, B. Brügger, T. Hoenen, W. Nickel, U.S. Schwarz, and P. Chlanda. 2022. The Ebola virus VP40 matrix undergoes endosomal disassembly essential for membrane fusion. *bioRxiv*. doi:10.1101/2022.08.24.505067.

Wolff, G., R.W.A.L. Limpens, J.C. Zevenhoven-Dobbe, U. Laugks, S. Zheng, A.W.M. de Jong, R.I. Koning, D.A. Agard, K. Grünewald, A.J. Koster, E.J. Snijder, and M. Bárcena. 2020a. A molecular pore spans the double membrane of the coronavirus replication organelle. *Science.* doi:10.1126/SCIENCE.ABD3629

Wolff, G., C.E. Melia, E.J. Snijder, and M. Bárcena. 2020b. Double-Membrane Vesicles as Platforms for Viral Replication. *Trends Microbiol.* 28:1022–1033. doi:10.1016/J.TIM.2020.05.009.

Xia, X., A. Cheng, M. Wang, X. Ou, D. Sun, S. Mao, J. Huang, Q. Yang, Y. Wu, S. Chen, S. Zhang, D. Zhu, R. Jia, M. Liu, X.X. Zhao, Q. Gao, and B. Tian. 2022. Functions of Viroporins in the Viral Life Cycle and Their Regulation of Host Cell Responses. *Front. Immunol.* 13. doi:10.3389/fimmu.2022.890549.

Xu, C., N. Katyal, T. Nesterova, and J.R. Perilla. 2020. Molecular determinants of Ebola nucleocapsid stability from molecular dynamics simulations. *J. Chem. Phys.* 153:155102. doi:10.1063/5.0021491/5.0021491.MM.ORIGINAL.V3.MP4.

Yalisove, R., S.H. Sung, P. Ercius, and R. Hovden. 2021. Limits of Three-Dimensional Resolution and Dose for Aberration-Corrected Electron Tomography. *Phys. Rev. Appl.* 15:14003. doi:10.1103/PhysRevApplied.15.014003.

Yamauchi, Y., and U.F. Greber. 2016. Principles of Virus Uncoating: Cues and the Snooker Ball. *Traffic.* 17:569–592. doi:10.1111/tra.12387.

Yandrapalli, N., Q. Lubart, H.S. Tanwar, C. Picart, J. Mak, D. Muriaux, and C. Favard. 2016. Self assembly of HIV-1 Gag protein on lipid membranes generates PI(4,5)P2/Cholesterol nanoclusters. *Sci. Rep.* 6:1–13. doi:10.1038/srep39332.

Yang, X. Lou, C.W. Tan, D.E. Anderson, R. Di Jiang, B. Li, W. Zhang, Y. Zhu, X.F. Lim, P. Zhou, X.L. Liu, W. Guan, L. Zhang, S.Y. Li, Y.Z. Zhang, L.F. Wang, and Z.L. Shi. 2019. Characterization of a filovirus (Měnglà virus) from Rousettus bats in China. *Nat. Microbiol.* 4:390–395. doi:10.1038/s41564-018-0328-y.

Yip, K.M., N. Fischer, E. Paknia, A. Chari, and H. Stark. 2020. Atomic-resolution protein structure determination by cryo-EM. *Nat. 2020 5877832*. 587:157–161. doi:10.1038/s41586-020-2833-4.

Zhang, J., G.P. Leser, A. Pekosz, and R.A. Lamb. 2000. The Cytoplasmic Tails of the Influenza Virus Spike Glycoproteins Are Required for Normal Genome Packaging. *Virology*. 269:325–334. doi:10.1006/VIRO.2000.0228.

Zhao, Y., J. Ren, K. Harlos, and D.I. Stuart. 2016. Structure of glycosylated NPC1 luminal domain C reveals insights into NPC2 and Ebola virus interactions. *FEBS Lett.* 590:605–612. doi:10.1002/1873-3468.12089.

Zila, V., E. Margiotta, B. Turoňová, T.G. Müller, C.E. Zimmerli, S. Mattei, M. Allegretti, K. Börner, J. Rada, B. Müller, M. Lusic, H.G. Kräusslich, and M. Beck. 2021. Cone-shaped HIV-1 capsids are transported through intact nuclear pores. *Cell.* 184:1032-1046.e18. doi:10.1016/j.cell.2021.01.025.